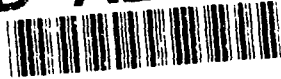AD-A258 718

AEOSR-TR· 2 0983

(2)

WAVE PROPAGATION AND DYNAMIC LOAD TRANSFER DUE TO EXPLOSIVE LOADING IN HETEROGENOUS GRANULAR MEDIA WITH MICROSTRUCTURE
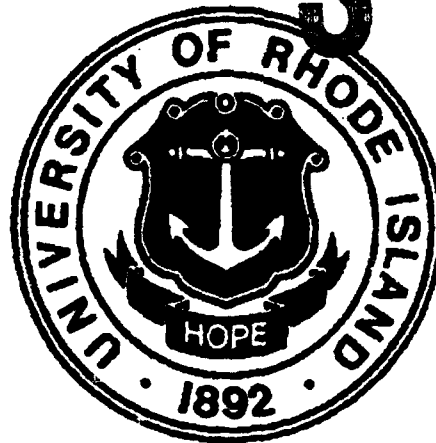
(FINAL REPORT)

by

Arun Shukla and Matin H. Sadd

Prepared for U.S. Air Force Office of Scientific Research
Under Contract No. F49620-89-C-0091
Bolling Air Force Base.

DTIC
ELECTE
DEC 0 4 1992
S A D

92-30773

Department of Mechanical Engineering & Applied Mechanics
University of Rhode Island
Kingston, RI 02881

September 1992

WAVE PROPAGATION AND DYNAMIC LOAD-TRANSFER DUE TO EXPLOSIVE LOADING IN HETEROGENOUS GRANULAR MEDIA WITH MICROSTRUCTURE
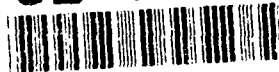
(FINAL REPORT)

by

Arun Shukla and Matin H. Sadd
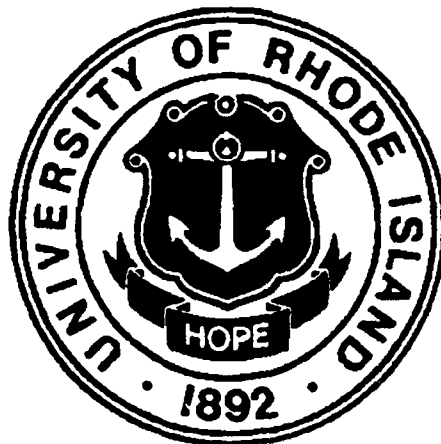
Accesion For	
NTIS CRA&I	✓
DTIC TAB	
Unannounced	
Justification	
By	
Dist ib tio /	
Avail l /	
Dist	Special

A-1

Department of Mechanical Engineering & Applied Mechanics
University of Rhode Island
Kingston, RI 02881

September 1992

I

REPORT DOCUMENTATION PAGE

Form Approved
OMB No. 0704-0188

1a. REPORT SECURITY CLASSIFICATION UNCLASSIFIED		1b. RESTRICTIVE MARKINGS		
2a. SECURITY CLASSIFICATION AUTHORITY		3. DISTRIBUTION/AVAILABILITY OF REPORT Approved for Public Release; Distribution Unlimited		
2b. DECLASSIFICATION/DOWNGRADING SCHEDULE				
4. PERFORMING ORGANIZATION REPORT NUMBER(S) ME – 92 – 01		5. MONITORING ORGANIZATION REPORT NUMBER(S)		
6a. NAME OF PERFORMING ORGANIZATION University of Rhode Island	6b. OFFICE SYMBOL (If applicable)	7a. NAME OF MONITORING ORGANIZATION AFOSR/NA		
6c. ADDRESS (City, State, and ZIP Code) Kingston, RI 02881		7b. ADDRESS (City, State, and ZIP Code) Bldg. 410 Bolling AFB, DC 20332-6448		
8a. NAME OF FUNDING/SPONSORING ORGANIZATION AFOSR	8b. OFFICE SYMBOL (If applicable) NA	9. PROCUREMENT INSTRUMENT IDENTIFICATION NUMBER F49620-89-C-0091		

| 8c. ADDRESS (City, State, and ZIP Code) Bldg. 410 Bolling AFB, DC 20332-6448	10. SOURCE OF FUNDING NUMBERS			
	PROGRAM ELEMENT NO. 6.1102F	PROJECT NO. 2302	TASK NO. C1	WORK UNIT ACCESSION NO.

11. TITLE (Include Security Classification)   (U) Wave Propagation and Dynamic Load Transfer due to Explosive Loading in the Heterogeneous Granular Media with Microstructure (Final Report)

12. PERSONAL AUTHOR(S)
A. Shukla and M.H. Sadd

13a. TYPE OF REPORT Final	13b. TIME COVERED FROM 8/15/89 TO 8/15/92	14. DATE OF REPORT (Year, Month, Day) 92/9/30	15. PAGE COUNT 255

16. SUPPLEMENTARY NOTATION

17. COSATI CODES			18. SUBJECT TERMS (Continue on reverse if necessary and identify by block number)
FIELD	GROUP	SUB-GROUP	Granular media, dynamic contact load, wave propagation,
			dynamic photoelasticity, distinct element method, finite
			element method, explosive loading, strain gages, wave velocity

19. ABSTRACT (Continue on reverse if necessary and identify by block number)
An experimental and numerical investigation has been conducted to study wave propagation and load transfer due to dynamic loading in granular materials. Systematic as well as random aggregates of particles of different material properties as well as shapes were used to simulate the granular media. These assemblies were loaded either with explosives or projectiles driven by a gas gun to generate short duration pulses. The resulting dynamic phenomenon was experimentally studied by using the optical technique of photo-elasticity and dynamic strain gage equipment. Of particular attention was the effect of local microstructure on the wave propagation process. The effect of the loading pulse wavelength as well as the material hetrogeniety on the wave propagation phenomenon was evlauated. The effect of the particle shape and size on the load transfer process was also studied. Initial experiments were also conducted to investigate the effect of prestress as well as interstitial moisture on the wave propagation process. The experimental results elucidated the basic mechanisms of load transfer, provided the duration and

(OVER)

20. DISTRIBUTION/AVAILABILITY OF ABSTRACT ☒ UNCLASSIFIED/UNLIMITED ☐ SAME AS RPT. ☐ DTIC USERS	21. ABSTRACT SECURITY CLASSIFICATION UNCLASSIFIED	
22a. NAME OF RESPONSIBLE INDIVIDUAL Major M.D. LEWIS	22b. TELEPHONE (Include Area Code) (202) 767-6963	22c. OFFICE SYMBOL AFOSR/NA

DD Form 1473, JUN 86   Previous editions are obsolete.   SECURITY CLASSIFICATION OF THIS PAGE

BLOCK 19 (ABSTRACT CONTINUED)

magnitude of the dynamic contact stresses, wave propagation velocities, envelope
of load transfer and wave attenuation.

The computational work employed two different numerical techniques to simulate
dynamic load transfer in the granular materials under study. The first technique
used the distinct element method whereby the dynamic behavior of an assembly of
particles is modeled with Newtonian rigid-body mechanics using prescribed
interparticle contact laws to account for stiffness and damping interactions.
New dynamic contact law models have been develped for use in the distinct element
wave propagation code. The second method employed the concept of replacing the
granular assembly with an equivalent elastic network which was then analyzed by
the finite element method using one-dimensional dynamic bar elements. Boundary
and finite element methods were also used to investigate the basic dynamic
interaction mechanisms between particles in contact. Experimental data was used
to characterize modeling parameters used in the wave propagation codes and to
validate numerical predictions.

ACKNOWLEDGEMENTS

TABLE OF CONTENTS

SUMMARY

This final report presents the progress and accomplishments of the three-year research program sponsored by the *Air Force Office of Scientific Research* under contract F49620-89-C-0091 to the *University of Rhode Island*. This research program has been involved with wave propagation and dynamic load transfer in heterogeneous granular materials. The overall objectives of the program were to provide a basic understanding of the dynamic load transfer processes in particulate media, and how local microstructure or fabric effect the overall wave propagation through the material.

The research program focused on the dynamic response of particulate media when they are subjected to explosive loadings with typical duration times of 30 to 500μs. Such loadings produce propagating stress waves moving with distinct speeds and attenuating with propagational distance. In such materials, these mechanical signals are transmitted locally along a series of complex and discrete paths, established by the media microstructure. In order to investigate the local microstructural or fabric effects on dynamic load transfer, a comprehensive experimental and theoretical research program was established. Studies were conducted on dynamically loaded model granular materials composed of two-dimensional assemblies of circular disks arranged in a wide variety of packing geometries. Both particle size and material were systematically varied to study the effects of heterogeneity and fabric.

The experimental program employed methods of dynamic photoelasticity and electrical resistance strain gages. Dynamic photoelasticity is an optical technique in which full-field stress data may be collected at various instants of time using high speed photography. The method was applied to the present research program by constructing model granular assemblies of birefringent disks which were dynamically loaded by exploding a small charge of PETN directly on top of one of the disks. These model media along with the loading apparatus were placed in the optical bench of a high-speed, multiple-spark gap camera. This high-speed photographic system operates as a series of high intensity, extremely short duration pulses of light and provides 20 photoelastic images at discrete times during the dynamic event. Framing rates of up to 10^6 frames per second are attainable using this system, and the collected experimental data are photographs of isochromatic fringe patterns at different times as the stress wave passes

1

through the model granular assembly. Such photographic data provides full-field qualitative and quantitative information on the nature of dynamic stress distribution, and allows determination of the wave speed, interparticle contact load transfer, and the wave spreading characteristics. Because certain segments of our research required opaque particulate media or very long assemblies of granules, the optical photoelastic technique was replaced by dynamic strain gage instrumentation. Electrical resistance strain gages were bonded to predetermined particles in particular model assemblies. The dynamic signal from the gage gives the transient strain response at that location on the particle. Although this technique does not give full-field data, it does provide sufficient information to calculate the wave speed and amplitude attenuation (intergranular contact load).

The theoretical program conducted in this study employed several numerical techniques including finite, boundary and distinct element methods. Dynamic intergranular contact was analyzed using both finite element and boundary element schemes which investigated the details of the dynamic load transfer between idealized granular particles. In addition, finite element methods were also used in our elastic network modeling in which granular media were replaced by equivalent elastic networks. Each link in the network was a one-dimensional, tension-only finite element, and a nonlinear solution strategy was developed to calculate the dynamic response of the network at various time steps.

A large portion of our theoretical work involved the use of the *distinct element method* to simulate or model the behavior of large assemblies of circular disks. In this method, the contact forces and displacements of an assembly of disks are determined through a series of calculations tracing the movements of each of the individual disks. For applications to wave propagation, the movements of each of the disks are a result of the propagation through the medium of disturbances originating at the loading points. Newtonian rigid-body mechanics is used to model the translational and rotational motion of each disk in a model assembly. The technique establishes a discretized time stepping numerical routine, in which it is assumed that during each time step, disturbances cannot propagate from any disk further than its immediate neighbors. Under these assumptions, the method becomes explicit, and therefore at any time increment the resultant forces on

any disk are determined solely by its interactions with the disks it is in contact. Major contributions of our distinct element studies were in the development new dynamic intergranular contact laws which accurately predicted the load transfer in a wide variety of model particulate materials. We have found that this intergranular contact behavior establishes the dynamic constitutive response of particulate media under loading rates of short duration.

Significant coupling of the experimental and theoretical segments of our research program occurred in which the theoretical modeling provided direction as to what data would be the most useful to understand the dynamic material response. Experiments provided important data needed in the characterization (i.e. modeling parameter determinations) of the developed numerical models. Finally, experimental data has been collected on numerous model granular assemblies, and this has been used to verify the predictive capabilities of the numerical simulations.

We have found that local microstructural effects in particulate media do influence the dynamic load transfer and the resulting wave propagation. Several important fabric measures have been determine which affect wave propagation and these include: the relative positions of neighboring particles (normally measured by the so-called branch vectors); the location and direction of the contact normal vectors between particles; and the interparticle contact force-deformation laws. The first two of these fabric measures are *kinematical* in nature because they are determined by the particle shapes and packing geometries. The final fabric measure dealing with the contact mechanics is *kinetic*, being determined by the particle material and shape properties and by the contact surface conditions.

Therefore our studies have determined new and fundamental knowledge of the dynamic load transfer between particles. Numerous heterogeneous and fabric influences have been studied including the effects of:

- contact angle or branch vector
- wavelength and pulse duration
- particle material, size and shape
- intergranular contact law
- random granular anisotropy

3

In addition, we have developed several modeling tools which include dynamic contact simulators, particulate media generators, and finite and distinct element wave propagation codes. Details of these accomplishments will be presented in the following sections of this report.

BRIEF REVIEW OF RESULTS

During the course of our studies a number of interesting and fundamental developments were found as related to wave propagation in granular and particulate materials. Some new experimental and numerical approaches were created to understand and explain the basic mechanisms of dynamic load transfer in such materials. A brief review of the important results are listed below which is then followed by detailed descriptions in the appendix.

Prediction of Dynamic Contact Loads in Granular Assemblies Using Load Transfer Coefficients

An experimental-numerical hybrid technique was developed to predict the intergranular contact load transfer in granular media subjected to explosive loading. The granular media was simulated by assemblies of circular disks in contact. The peak contact load transfer coefficients (i.e. the ratio of the maximum output contact load to the input contact load as a function of the contact angles) of a given particle were obtained through controlled experimental studies. These coefficients, along with the principle of superposition, were then used to predict the peak contact loads in several regular as well as irregular assemblies of disks. The predicted results compared favorably with the experimental data for several different assemblies.

Granular Contact Law Effects

The microstructural wave propagation behavior of a granular medium was modeled using the distinct element method. This technique simulates the discrete behavior of the medium by assuming that the motion of each particle may be modeled using Newtonian rigid-body mechanics with particular force-deformation and force-deformation rate contact laws. The present work provided a comparison of the effects of various contact laws on the wave propagational behaviors including wave attenuation and dispersion characteristics. Specific cases which were studied include linear, non-linear and non-linear hysteretic force-deformation contact laws along with velocity proportional damping. Numerical results were compared with experimental data from dynamic photoelastic and strain gage experiments. Since velocity dependent contact damping is not a reasonable model for dry cohesionless granular media, it was desired to determine if a non-linear hysteretic contact law could be used to replace the velocity damping. Results indicate

5

that such a non-linear law does provide a damping mechanism which can predict experimental attenuation data, and that the dispersion characteristics are modeled more accurately with this hysteretic model.

Effects of Particle Size and Loading Pulse Duration on Dynamic Load Transfer

An experimental and numerical investigation was conducted to study the dynamic response of granular media when subjected to loadings with different wavelengths. The granular media was simulated by an assembly of circular disks arranged in a long straight single chain. The dynamic loading was produced by either an explosive or by impacting a projectile from a gas gun onto one end of the granular assembly. It was found from the experiments that an input wave with a short period of 90μs (wavelength to diameter ratio of four) will propagate in this granular media with a steady amplitude attenuation. On the other hand, the long wave (period about 650 μs to 900 μs) will propagate through this granular media with first an increase of amplitude (up to 40% higher than the input) which is then followed by a decrease of amplitude. In addition, oscillation behavior was found within the main wave pulse indicating significant dispersion of the input signal. Numerical distinct element analyses also predicted the same behavior observed in the experiments. Thus there exists a fundamental change in the local propagational behavior of waves in granular media for waves with different wave length.

Preliminary Studies on the Effect of the Particle Shape on Wave Propagation Phenomenon

Preliminary experimental and numerical investigations have been conducted to investigate the effect of particle shape and size on the inter-granular load transfer.Studies include the velocity and wavelength behavior of a stress wave transmitted through granular media subjected to explosive loading. Dynamic photoelasticity and distinct element modeling were used to study this stress wave propagation through granular media simulated by assemblies of elliptical particles in contact. The results indicate that the shape of the particle has considerable effect on both velocity as well as attenuation of the stress wave.

The Effect of Preloading on Dynamic Response of Granular Media

A series of experiments were conducted in which an initial biaxial prestress was applied to the granular assembly before it was subjected to dynamic loading. A biaxial

loading fixture was designed which could exert a variety of biaxial loadings on the granular assembly. The effect of several different ratios of the biaxial stress on wave propagation in granular assemblies was studied. The results indicate that the initial load on the granular media effects both the velocity as well as the attenuation of the stress wave.

Dynamic Simulation of Granular Media Using Elastic Networks

A microstructural wave propagation model was developed for cohesionless granular media in which the dynamic load transfer between adjacent particles is simulated through a special finite element scheme. The particulate media is modeled by an equivalent elastic network which is constructed by connecting all adjacent particle mass centers with an elastic load-carrying link. The link behavior is modeled with a one dimensional finite element that is tensionless and carries end moments and axial and shear forces. The resulting solution procedure is nonlinear, and model stiffness and damping parameters were obtained from dynamic photoelastic experiments. Several types of two-dimensional assemblies were studied, and these numerical results compared favorably with experimental data.

Dynamic Interparticle Load Transfer Studies Using Boundary and Finite Element Methods

The dynamic interparticle load transfer plays a primary role in the propagation of waves in granular materials, and this contact behavior is an important parameter in our modeling efforts using distinct and elastic network element methods. In order to obtain a more complete understanding of this phenomena, theoretical boundary and finite element analyses were applied to the problem. The dynamic interaction of two or more elastic particles in contact represents a nonlinear initial/boundary-value problem of elastodynamics. These problems were attacked using boundary discretization schemes (boundary element methods) and interior discretization schemes (finite element methods) applied to model the dynamic interaction between two or more idealized circular disk particles. A dynamic input was applied to one of the disks, and the transient load transfer through the contact point(s) was computed. Load transfer profiles for circular and elliptical particles were calculated, and the results compared favorably with experimental data.

7

Influence of Local Heterogeneities on Dynamic Stress History in Granular Assemblies

An experimental-numerical study was conducted to investigate the effects of microstructural defects, such as inclusions and voids, on the wave propagation phenomena in granular materials. The granular materials as well as the defects were simulated using circular disks in both one-and two-dimensional experiments. The defects were of two types, namely, inclusions and voids. Dynamic photoelasticity and high-speed photography and numerical distinct element modeling were used to study the effects of these defects on the local stress field during wave propagation. Results indicate that both inclusions and voids produce local wave scattering through various reflection mechanisms. Inclusions increase the wavelength of the loading pulse and produce local attenuation while voids change the local energy-transfer paths.

Wave Propagation in Heterogenous Granular and Layered Media

Dynamic load transfer due to explosive loading in layered and heterogenous granular assemblies was studied using dynamic photoelasticity. The heterogenous granular assemblies consisted of circular discs fabricated from photoelastic materials such as Homalite 100, PSM1, PSM4, PSM9, CR-39 and nonphotoelastic materials such as steel, rock and aluminum. The experimental results showed that the local microstructure controls the magnitude of load transferred in any given direction. The load transfer depends not only on the angle between the branch vectors drawn from the mass center of the contacting granules but also on the acoustic impedance of the contacting granules. The wave dispersion and scattering produced by the mismatch of acoustic impedance in the heterogenous assemblies resulted in more peak contact load attenuation than in a homogenous granular medium. Systematic experiments were also conducted to quantify the load transferred from one granule to the other as a function of branch angle as well as material properties. This information was used to propose an empirical load transfer model to predict peak contact loads in heterogenous assemblies.

Dynamic Load Transfer in Virgin and Damaged Particles

An experimental investigation was conducted to study dynamic load transfer in granular rock media. The granular rock media was modeled as a one-dimensional chain of disks fabricated from four different types of white Vermont marble. The study focused

on the effect of microstructure on transient pulse propagation generated by explosive loading. During wave propagation dynamic contact strains were recorded using electrical resistance strain gages. This information was used to calculate wave velocity and attenuation as a function of the cumulative damage in the disk assembly. The results indicate a considerable influence of the microstructure and prior loading history on the wave propagation process. A correlation exists between the stress wave velocity and the microstructure of the rock material. Also the wave velocity increases initially and then decreases with the repeated explosive loading.

Wave Propagation in Saturated Granular Media

Some preliminary experiments were conducted to investigate the effect of interstitial fluid on wave propagation phenomenon. The experiments were conducted with circular discs and the space between discs was filled by different fluids such as water and Dow Corning 200 fluids with different viscosities. High speed photographs of the dynamic event showed that both wave velocity and attenuation are affected by the fluid. The effect is more prominent on wave attenuation.

Studies of Large Random Assemblies

Distinct element simulations were conducted on large random assemblies in order to investigate the effects of granular anisotropy on the wave propagational characteristics. Special granular assemblies were computationally constructed by random particulate media generators. These generators used special algorithms to construct assemblies with varying degrees of anisotropy as measured by the distributions of local branch vectors between adjacent particles. Anisotropy was characterized with respect to two orthogonal directions in the media. Distinct element results compared wave propagation along these orthogonal directions, and the findings indicated that media anisotropy does significantly effect the wave speed and attenuation.

PERSONNEL ASSOCIATED WITH THE RESEARCH

1. Professor Martin H. Sadd

2. Professor Arun Shukla

3. Dr. Changyi Zhu, Ph.D awarded Aug. 1990. Currently working at Texas A&M

University

4. Dr. Lun Qiu, Post Doctoral Fellow

5. Dr. Yi Xu, Ph.D awarded Aug. 1991. Currently working at Brown and Associates, Houston, Texas

6. Mr. Qiming Tai, Ph.D student

7. Dr. M. Adley, Ph.D awarded May 1991. Currently working at Waterways Experiment Station, Vicksburg, Mississippi

8. Mr. W. Boardman, M.S awarded May 1990. Currently working at Department of Transportation, Providence, Rhode Island

9. Mr. Raman Pal Singh, M.S. student

10. Mr. S. Vishwanathan, M.S. student

PUBLICATIONS

Journal Publications

1. Zhu, C. Y., Shukla, A. and Sadd, M.H. "Prediction of Dynamic Contact Loads in Granular Assemblies", J. of Applied Mechanics, Vol. 58, No. 2., June 1991, pp. 341-346.

2. Prakash, V. and Shukla, A. "Dynamic Load Transfer in Virgin and Damaged Granular Rock Media", J. of Engineering Mechanics, Vol. 117, No. 3, March 1991, pp. 498-512.

3. Xu, Y. and Shukla, A. "Stress Wave Velocity in Granular Medium", Mechanics Research Communications, Vol. 17, No. 6, 1990, pp. 383-391.

4. Sadd, M.H., Tai, Q.M. and Shukla, A. "Contact Law Effects on Wave Propagation in Particulate Media Using Distinct Element Modeling", submitted to Intl. Journal of Nonlinear Mechanics.

5. Sadd, M.H., Qiu, L., Boardman, W. and Shukla, A. "Modelling Wave Propagation in Granular Media Using Elastic Networks", Intl. J. Rock Mech. and Mining Sci., Vol. 29, No. 2, 1992, pp. 161-170.

6. Xu, Y. and Shukla, A. "Application of Strain Gages to Study Static and Dynamic Contact Loads in Granular Particles", submitted to Experimental Techniques, Jour. of Testing and Evaluation.

7. Shukla, A., Zhu, C.Y. and Xu, Y. "Dynamic Stresses in Granular Assemblies with Microstructural Defects", J. of Engineering Mechanics, Vol. 118, No. 1, Jan. 1992, pp. 190-201.

8. Shukla A. and Sadd, M. H., Singh, R. P., Tai, Q. M., And Vishwanathan, S., "Role of Particle Shape and Contact Profile on the Dynamic Response of Particulate Materials", to appear in J. of Optics and Laser in Engineering

9. Adley, M.D. and Sadd, M.H. "Continuum Models for Material with Latticelike Microstructure", J. of Computers and Structures, Vol.43, p13, 1992.

Thesis and Dissertations

1. Dr. Changyi Zhu, Ph.D. awarded Aug. 1990. Title of Dissertation: "An Experimental and Numerical Study of the Wave Propagation Phenomenon in Granular Media."

2. Dr. Yi Xu, Ph.D. awarded Aug. 1991. Title of Dissertation: "Study of Wave Propagation and Dynamic Load Transfer in Heterogeneous Granular Media."

3. Dr. M. Adley, Ph.D. awarded May 1991. Title of Dissertation: "Computation of the Effective Properties of Materials with Microstructure."

4. Mr. W. Boardman, M.S. awarded May 1990. Title of Thesis: "Wave Propagation in Granular Media Simulated by Elastic Networks".

5. Mr. J. Toth, M.S. awarded Aug. 1992. Title of Thesis:"Development of A Tensile Loading Apparatus and Its Use in Determining the Dynamic Fracture Toughness of Geological Materials", M.S. student

6. Mr. Qiming Tai, Title of Dissertation: "Computational Studies of Wave Propagation in Granular Media", Ph.D. student

7. Mr. Raman Pal Singh, Title of Thesis: "Effect of Particle Shape on Stress Wave Propagation in Granular Media", M.S. student

8. Mr. S. Vishwanathan, Title of Thesis: " Study of Static and Dynamic Field in One, Two, and Three Dimensional Media Using Different Optical Techniques", M.S. student

EQUIPMENT AND SOFTWARE

During the course of this research several experimental facilities and numerical codes were also developed. These include

Experimental Facilities

1. Electromagnetic Plane Wave Generator

11

2. Gas Gun (0.5 in bore) For Compressive Loading

3. Gas Gun (2 in bore) For Tensile Loading

4. Lecroy Ultra High Speed Data Acquisition System

5. Ectron High Speed Strain Gage Amplifier System

6. Optical Bench For Fiber Optic Sensor Development And Use

7. Image Processing System

Software Codes

1. Ray / Branch Path Generator

2. Random Fabric Granular Media Generator

3. WAPRIPM - Wave Propagation In Particulate Media

INTERACTION AND COUPLING ACTIVITIES

Papers Presented at Meetings and Conferences

1. "Experimental Studies of Wave Propagation in Granular Media," A. Shukla, seminar given at Rensselaer Polytechnic Institute, Feb. 20, 1990. Interacted ,ith Prof. Dobry, Prof. Petrakis and others at Civil Engineering Department.

2. "Influence of the Microstructural Defects on Dynamic Stress History in Granular Assemblies," Shukla, A., Zhu, C.Y. and Xu, Y., presented at the 1990 Spring Conference on Experimental Mechanics, Albuquerque, NM, Proceedings pp. 63-38.

3. "Dynamic Load Transfer in Heterogenous Granular Assemblies," Shukla, A. and Xu, Y., accepted for presentation at 9th International Conference on Experimental Mechanics, Aug. 1990, Copenhagen, Denmark.

4. "Micromechanical Constitutive Behavior of Granular Media Under Dynamic Loading Conditions", accepted for presentation at 3rd International Conference on Constitutive Laws for Engineering Materials, Univ. of Arizona, January, 1991.

5. "Dynamic Load Transfer in Granular Materials," Shukla, A., seminar given at University of Connecticut, April 8, 1991. Interacted with several members of their faculty.

6. "Using Strain Gages to Study Static and Dynamic Contact Stress Problems", Y. Xu and A. Shukla, presented at the 1991 SEM Spring Conference, Milwaukee, June 1919.

7. "Micromechanical Constitutive Behavior of Granular Media Under Dynamic Loading Conditions", M.H. Sadd, A. Shukla, Q.M. Tai and Y. Xu, presented at the 3rd International Conference on Constitutive Laws for Engineering Materials, Univ. of Arizona, January, 1991, pp. 539-542.

8. "Wave Propagation in Granular Materials - Microstructural Connections", M.H. Sadd, presented to the Department of Civil Engineering, University of Rhode Island, Kingston, RI, April, 1991.

9. "Wave Propagation and Dynamic Load Transfer Due to Explosive Loading in Herterogeneous Granular Media with Microstructure", A. Shukla and M. H. Sadd presented at AFOSR grantees meeting, Albuquerque NM, January 1992

10. "Influence of Particle Shape on Stress Wave Propagation in Granular Media", A. Shukla and R. Singh presented in the VII International Congress on Experimental Mechanics, Las Vegas, Nevada, June 8-11, 1992

Interactions with Other Personnel

1. Our research group hosted a workshop on Stress Wave Propagation in Random Media with Microstructure, August 17-18, 1989, at U.R.I. Attenders included: Bob Rohani/WES, John Gill/AFWL, Otis Walton/LLNL, and Martin Ostaja Starzewski/Purdue Univ.

2. Major Steven Boyce from AFOSR visited our group in February 1990. Various issues related to our research project were discussed in detail.

3. Dr. L.D. Miller of the U.S. Army Foreign Science and Technology Center visited our laboratory in March 1990. During his two day visit, we discussed in general about wave motion in granular assemblies and in particular about the possibility of propagating soliton waves in such materials.

4. Our research group hosted a visit by Major John Gill of the USAF, Geologic Response Section, Phillips Laboratory, Kirtland Air Force Base, on March 26, 1991. He gave us a seminar dealing with his research on micro-geomechanics, and we presented and discussed several issues related to our research.

5. Prof. J.W. Dally from the University of Maryland visited our research group on Feb. 15, 1991. We discussed different aspects of experimental mechanics approaches related to our research.

6. Major Martin Lewis from AFOSR visited our group in March 1992. In depth discussions on various topic related to particulate material were held.

7. Prof. C. S. Chang from the University of Massachusetts visited our group on September 22, 1992. We discussed different aspects of our work as related to AFOSR.

APPENDICES

CHAPTER 1

EXPERIMENTAL-NUMERICAL PREDICTION OF DYNAMIC CONTACT LOADS

1.1 INTRODUCTION

Numerical methods model the behavior of an idealized granular particle by calculating the motion of individual grains in the assembly as they interact with each other. There is no assumed constitutive relation between stress and strain in the bulk material. Instead, the bulk behavior is determined from space and time averages of the loads on individual granules and their resulting movements. These methods are more flexible in application than theoretical ones.

Cundall and Strack (1979, 1983) pioneered the distinct element method for handling large number of particles of any shape. In this method, the interaction of particles is viewed as a transient problem with states of equilibrium developing whenever the internal forces balance. An explicit numerical scheme is used to monitor the interaction of particles contact by contact and to model the motion of the media particle by particle. Extensions of this method have been made by Walton (1982), Thornton (1985), Sadd (1989a) and Ting (1989). Swrrano and Rodrigue-Ortiz (1973) and Rodrigue-Ortiz (1974) developed a numerical model for assemblies of discs and spheres. Contact forces and displacements are calculated for equilibrium conditions. Hertzian-type contact compliances are used for normal forces. Theories of Mindlin and Deresiewicz are used for tangential forces. In this modelling, the matrix representing the contact stiffnesses must be reformulated whenever a contact is made or broken and shape changes are assumed negligible. Inelasticity and friction effects are modeled via a collision operator that determines post collisional trajectories and rotations for particles involved in instantaneous, binary, impacts. Hopkins (1985) simulated the effects of particle collisions in uniform shearing flows by randomly selecting two particles from a large ensemble of particles representing a statistically meaningful sample of the particles in the flow. One of the selected particles is temporarily located at the origin and the other is assigned a

14

random pre-collision position on a sphere whose radius equals the expected mean separation for a system at the modeled solid concentration.

An experimental-numerical hybrid technique has been developed in this study. A transfer function, i.e. the ratio of the maximum output contact load to the maximum input contact load of a given particle, determined from controlled experiments has been used to predict the dynamic intergranular contact load transfer in granular media. The granular materials with systematic as well as irregular packing microstructure as shown in Fig.1.1 were simulated by assemblies of circular discs. It has been verified by experiments that at most of the contact points the tangential load is less than 15 % of the normal load. Thus in this investigation only normal contact loads were considered. Initially a series of calibration experiments of controlled microstructure were conducted in which the contact angles between the granules were systematically varied. The data obtained from each experiment was analyzed to get a load transfer coefficient for a given disc. This coefficient was obtained for several contact angles and number of contacts per disc. With various load transfer coefficients determined, a numerical scheme was developed using the experimental data and based on the principle of superposition. Predictions were made of the intergranular contact loadings for several model assemblies with different microstructure as shown in Fig.1.1. Numerical predictions were compared with experimental data for these models. Although the numerical scheme is very simple, the predicted results compared fairly well with the photoelastic experimental data.

1.2 LOAD TRANSFER FORMULATION

The microstructure of a granular medium can be characterized by branch vectors drawn between the mass centers of adjacent discs as shown in Fig.1.2. The angle θ is that between any two neighboring branch vectors and is denoted as the contact angle. It has been shown by Shukla et al. (1988) that the dynamic load transfer phenomena in granular media are strongly dependent on the contact angles made by the adjacent branch vectors. Experimental fringe patterns from their work obtained in a hexagonal closed packing (HCP) granular assembly for the geometry of Fig.1.1b are shown in Fig.1.3b. Normal contact load profiles of a typical disc, A, in this HCP model are shown in Fig.1.4. Wave energy entering at point 1 shows maximum transfer across point 2 which is directly ahead of point 1. Although contact points 3 and 4 make the same angles with the input point

15

1, the contact load is higher at point 4 than point 3 due to the superposition of loads from the other discs. No load transfer occurs across points 5 and 6 as the contact angles are larger than $(\pi/2)$ for these points. It is apparent that load transfer in a granular medium occurs primarily through contact mechanisms between adjacent particles, and thus various discrete load transfer paths will be established through the space that the media occupies. These load transfer paths are a result of the geometry of the granular assembly, and are especially related to the locations of the contacts of the various particles. For the dynamic case, inertia becomes significant and the location of the mass centers of the particles will also be important in the load transfer process. For the cases under study with circular discs, the branch vectors defined in Fig.1.2 completely describe the relative location of both the contact points and the particle mass centers. Thus it seems reasonable to develop a load transfer theory based upon the use of the branch vectors to predict the transmission of dynamic signals from disc to disc. The theory to be proposed is intended to predict the peak inter-granular load transfer between discs in model assemblies of granular media.

Referring to Fig.1.2, the peak load transfer through the j-th contact of any arbitrary disc may be written in the form,

$$P_{oj} = C_j P_i \qquad (1.1)$$

where P_{oj} is the peak output load at the j-th contact, P_i is the peak input load to this disc, and C_j is defined to be the load transfer coefficient which relates these peak inter-granular loads. Clearly, this load transfer coefficient depends on various contact angles made by the branch vectors of this disc. For discs of equal diameter, the maximum number of possible contacts is limited to six. Furthermore, as mentioned previously, experiments have shown that when the contact angle is greater than or equal to $90°$, no load transfer will occur and thus C_j will be zero for these cases. Therefore for equal diameter discs, the range of the index j will be limited from one to three, and the load transfer coefficient will be a function of at most three relative contact angles, i.e. $C_j = C_j(\theta_1, \theta_2, \theta_3)$, where the angles θ_1, θ_2, θ_3 are defined in Fig.1.5 relative to the input direction of the disc. If in any particular assembly one of these angles becomes larger than $90°$, then this contact is removed from the analysis. Consequently, for a given input point, at most only three

output contacts will be able to transmit the dynamic signal to adjacent discs.

1.3 EXPERIMENTAL DETERMINATION OF LOAD TRANSFER COEFFICIENTS

In order to determine the peak contact load transfer coefficients, $C_j(\theta_1, \theta_2, \theta_3)$, experiments were conducted on the three groups of models, that is, the two, three and four contact point models. A general four contact point model is shown in Fig.1.5. In experiments of the two contact point model, contact angles θ_1 and θ_3 were kept at 90°. Only contact angle θ_2 was systematically varied from 0° to 90°. In experiments of the three contact point model, contact angle θ_3 was kept at 90°, and both contact angles θ_1 and θ_2 were systematically varied. In experiments of the four contact point model, all three contact angles θ_1, θ_2 and θ_3 were systematically varied. For simplicity the granular materials were simulated by assemblies of 25.4 mm, 6.35 mm thick discs of Homalite-100. The experimental models were placed in the optical bench of a high speed multiple spark gap camera. The camera was triggered at some prescribed delay time after igniting the explosive. The high speed photographic system operated as a series of high intensity, extremely short duration pulses of light and provided 20 isochromatic fringe images at discrete times during the dynamic event.

The isochromatic fringes photographed during the experiments were analyzed by the numerical method developed by Shukla and Nigam (1985) to determine the contact length and friction factor from the full field photoelastic fringe patterns. These obtained values were substituted in the Hertz stress field equations and the contact stresses were numerically integrated along the contact length to obtain the normal and tangential contact loads.

For a two contact point model, contact angles θ_1 and θ_3 are 90° and C_1 and C_3 are therefore identically equal to zero. For a three contact point model, θ_3 is taken to be 90° and hence C_3 is identically zero.

The transfer coefficients C_j thus obtained from the three groups of experiments were plotted as a function of the contact angles θ_1, θ_2 and θ_3, as shown in Figs.1.6 to 1.8. In Fig.1.6, curve 1 represents the ratio of P_{o2}/P_i vs. contact angle θ_2 when both the contact angles θ_1 and θ_3 are equal to 90°. Since both P_{o1} and P_{o3} are zero, it actually represents the transfer coefficient C_2 of the two contact point model. The remaining curves in Fig.

17

1.6 represent the transfer coefficients C_2 vs. contact angle θ_2 of the three contact point model when contact angle θ_3 is $90°$ and θ_1 is also a constant but less than $90°$ (it is equal to $30°$, $45°$, $60°$ and $75°$ respectively). Fig.1.7 shows the transfer coefficients C_2 vs. contact angle θ_3 for the four contact point model when the contact angles $\theta_2=0°$ with various values of θ_1, while Fig.1.8 shows the transfer coefficient C_3 vs. contact angle θ_3 for the same four contact point model. The transfer coefficient C_1 for the four contact point model can be obtained easily using Figs.1.6 and 1.8 and the property that $C_1(\theta_1,\theta_2,90°) = C_2(\theta_2,\theta_1,90°)$ and $C_1(\theta_1,0°,\theta_3) = C_3(\theta_3,0°,\theta_1)$.

1.4 NUMERICAL IMPLEMENTATION

The experimentally determined peak contact load transfer coefficients were used to construct a numerical scheme capable of predicting dynamic load transfer in granular aggregate assemblies of discs. Several assumptions were used in this numerical method. First, only normal contact loading was considered in this study. The tangential contact loads were assumed to be zero. Next the speed of propagation of the mechanical signal is assumed to be constant, a fact which has been observed from the experiments. The load transfer coefficients are taken to be independent of the loading amplitude. Finally, simple superposition of loading, as shown in Fig.1.9, is used when more than one input contact load occurs on a given disc. Figs.1.6 to 1.8 combined with a Lagrangian interpolation method have been used to obtain all the necessary transfer coefficients to predict the peak contact loads in granular media. As an example consider the transfer coefficients for a four contact point model ($\theta_1=60°$, $\theta_2=0°$ and $\theta_3=65°$) as shown in Fig.1.5. Since θ_1 and θ_2 are equal to the two contact angles of curve 4 in Fig.1.8, the transfer coefficient C_3 can be obtained directly and is equal to 0.273. In contrast, the transfer coefficient C_1 can not be obtained directly. However it can be obtained by using the curves in Fig.1.8 combined with the Lagrangian interpolation method and the symmetrical property $C_1(60°,0°,65°) = C_3(65°,0°,60°)$. Using the values $C_3(60°,0°,60°) = 0.28$, $C_3(70°,0°,60°) = 0.294$, $C_3(80°,0°,60°) = 0.32$ and our Lagrangian interpolation method, we get $C_1(60°,0°,65°) = C_3(65°,0°,60°) = 0.286$. The transfer coefficients C_2 can be obtained directly from curve 3 in Fig.1.7, $C_2 = C_2(60°,0°,65°) = 0.775$.

After the three transfer coefficients have been obtained, the relevant output peak contact loads for the four contact point model can be computed easily. According to the

definition of the peak contact load transfer coefficient, the three output peak contact loads P_{o1}, P_{o2} and P_{o3} at contact points 1, 2 and 3 are calculated as follows,

$$P_{o1} = C_1 P_1$$
$$P_{o2} = C_2 P_1 \quad\quad\quad\quad\quad (1.2)$$
$$P_{o3} = C_3 P_1$$

1.5 RESULTS AND DISCUSSION

The experimental-numerical hybrid method was used to predict peak contact loads at every contact point in various models of granular media. Four different microstructural packings illustrated in Fig.1.1 were used in this study. Experimental fringe patterns obtained for each of the microstructures are shown in Fig.1.3. The comparison of the numerical and experimental results are shown in Figs.1.10 to 1.13.

Fig.1.3a shows a sequence of seven photographs obtained as the wave travels in a single chain of granular media as shown in Fig.1.1a. In this geometry each particle has two contact points, hence only one transfer coefficient is needed to model this geometry. This transfer coefficient is obtained from Fig.1.6, $C_2 = C_2(90°,0°,90°) = 0.97$. The peak contact loads at each contact point can be determined as follows,

$$P_2 = C_2 P_1$$
$$P_3 = C_2 P_2 = C_2^2 P_1 \quad\quad\quad\quad\quad (1.3)$$
$$\cdot$$
$$\cdot$$
$$\cdot$$
$$P_n = C_2^{n-1} P_1$$

The comparison of numerical and experimental peak contact loads in the single chain is shown in Fig.1.10. The average peak contact load error, $\{(P_{exp}-P_{num})/P_{exp}*100\}$, for this model is computed to be 5%. The results are in very good agreement because most of the assumptions made in our numerical model are satisfied.

Fig.1.3b shows a photograph obtained as the wave travels in a hexagonal closed packing (HCP) granular medium as shown in Fig. 1.1b. In this geometry each particle has

six contact points. The major load in this assembly is transferred by two primary chains, 1 and 2, shown in Fig.1.1b. Experimental data showed that the tangential contact loads were very close to zero for the primary chains, hence they behaved similar to the single chain assemblies. In the HCP model there are only two independent contact angles, $\theta_1 = \theta_3 = 60°$ and $\theta_2 = 0°$, with respect to the input load. Thus only two transfer coefficients were needed for the HCP model. From Figs.1.7 and 1.8, we obtain the two transfer coefficients, $C_1(60°,0°,60°) = C_3(60°,0°,60°) = 0.28$, $C_2(60°,0°,60°) = 0.75$. These coefficients were used to determine the peak contact loads throughout the assembly. The comparison of numerical and experimental results of the peak contact loads for the HCP model is shown in Fig.1.11. The average error of the peak contact loads for this model is 13%, with the average error along the center line of the primary chain being only 6%.

Fig.1.3c shows a photograph obtained as the wave travels in the geometry of Fig.1.1c, which will be referred to as a half hexagonal closed packing (HHCP) granular medium. In this geometry a particle has either four or five contact points. It is observed that most of the energy was transferred through a vertical column consisting of the HHCP cells under the explosive and several horizontal chains as shown in Figs.1.3c and 1.12. The peak contact loads were obtained by the same method discussed previously. The comparison of numerical and experimental peak contact loads is shown in Fig.1.12. It was found that the average error for this model is 12%. However the average error along the center line of the horizontal chains is only 7.5%.

Fig.1.3d shows a photograph obtained as the wave travels in an irregular packing granular medium as shown in Fig.1.1d. In this geometry particles have contact points ranging from two to six. The fringes in Fig.1.3d reveal a complex nature of load transfer phenomenon. The energy transfer showed no preferential direction in this model. In the former three models, the tangential contact loads, especially along the main path of the energy transfer, were quite small. However in this irregular model, at the contacts near the explosive point, the fringes appeared unsymmetrical with respect to the contact points. So it appears that sizable tangential loadings existed in this case. Away from the explosive point, the fringes showed the tendency to become symmetric with respect to the contact points. Again from Figs.1.6 to 1.8 all the transfer coefficients necessary for the determination of the peak contact loads in the irregular packing granular medium were

obtained. The comparison of numerical and experimental peak contact loads is shown in Fig.1.13. The tangential contact loads tend to increase the average error in the peak contact loads. This error was computed to be 19.0% for this model.

1.6 SUMMARY

A hybrid experimental-numerical technique has been developed to predict dynamic intergranular contact loads due to explosive loading in different assemblies of circular discs. For a known geometrical arrangement of discs the technique can predict contact loads at any point in the assembly for a given input loading. The method utilizes experimentally generated load transfer coefficients along with simple linear superposition in space. The results from this scheme are compared with those obtained experimentally using the method of dynamic photoelasticity. In general, the results are in good agreement for regular packings of the discs. However, for an irregular packing the agreement is marginal, and this is primarily due to the fact that the numerical scheme currently does not take into account tangential contact loads which were quite large in random arrangement. Further, the superposition method does not account for any angular dependence of wave length of the loading pulse. It was shown by Shukla et al. (1988) that the duration of contact loads is dependent on the contact angles. Thus to obtain better predictions, superpositions must be used both in space as well as time.
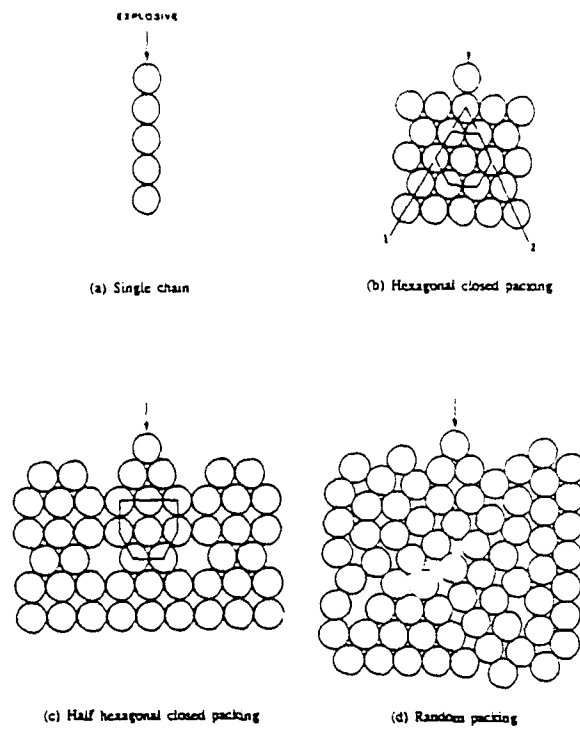
(a) Single chain

(b) Hexagonal closed packing

(c) Half hexagonal closed packing

(d) Random packing

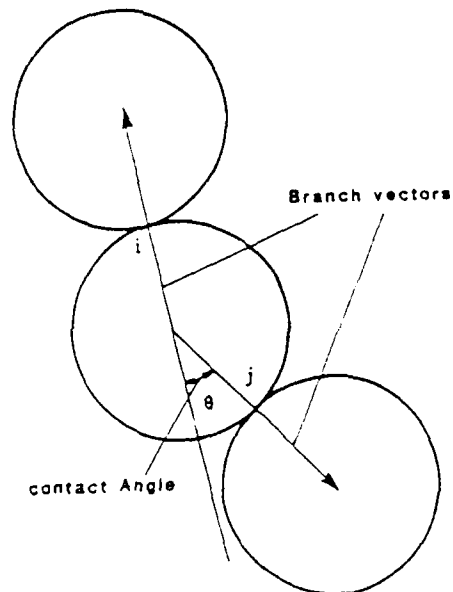Fig. 1.1 Microstructural arrangements used in different experiments·

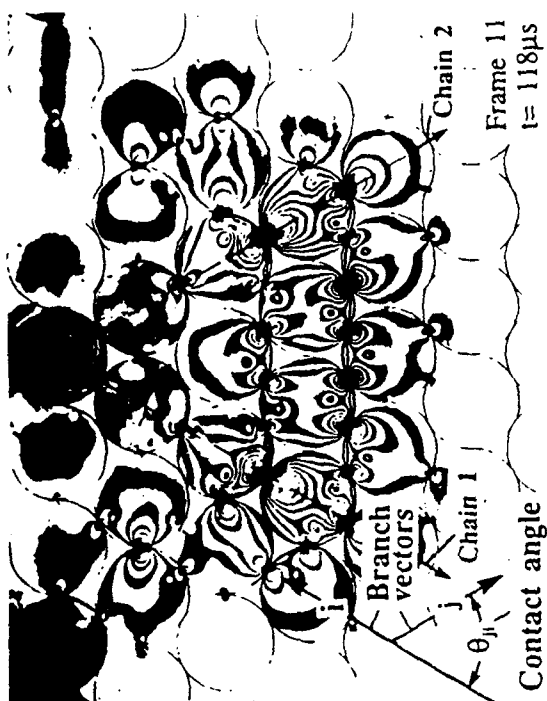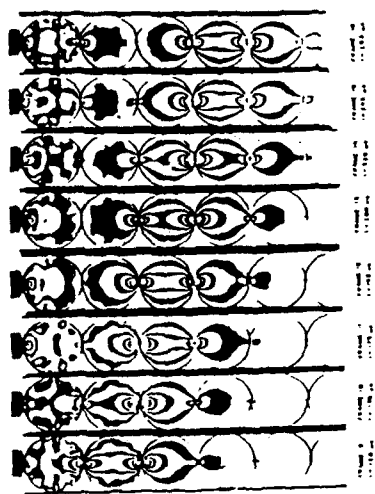Fig. 1.2 Branch vectors and contact angle, Θ_{ij}

22

Fig. 1.3a Dynamic isochromatic fringes obtained in a single chain arrangement for the geometry of Fig.1.1a

Fig. 1.3b Dynamic isochromatic fringes obtained in a HHCP arrangement for the geometry of Fig.1.1b

Frame 9
t= 96µs

Fig. 1.3d Dynamic isochromatic fringes obtained in an irregular arrangement for the geometry of Fig.1.1d

Frame 10
t= 119µs

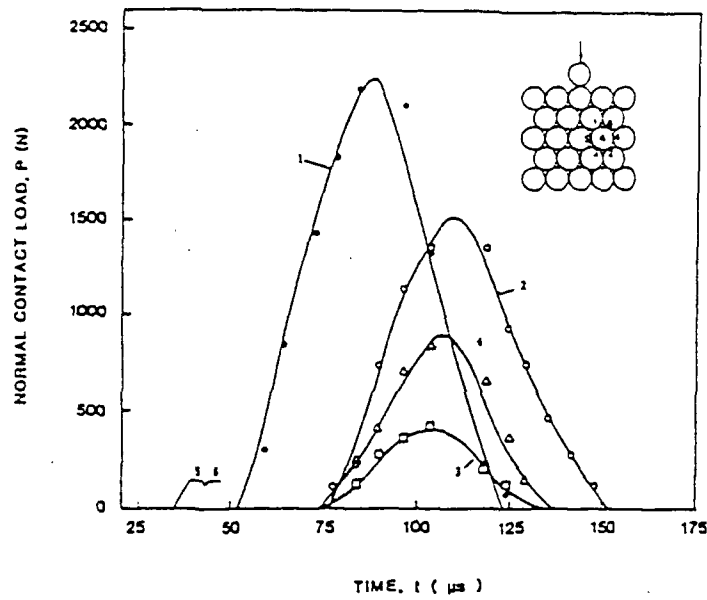Fig. 1.3c Dynamic isochromatic fringes obtained in a HHCP arrangement for the geometry of Fig.1.1c

23

Fig. 1.4 Normal contact load tansfer profiles for disc A in a HCP arrangement
for the geometry of Fig.1.1b.

(a)

(b)

$\theta_1 = 90°, \theta_3 = 90°$
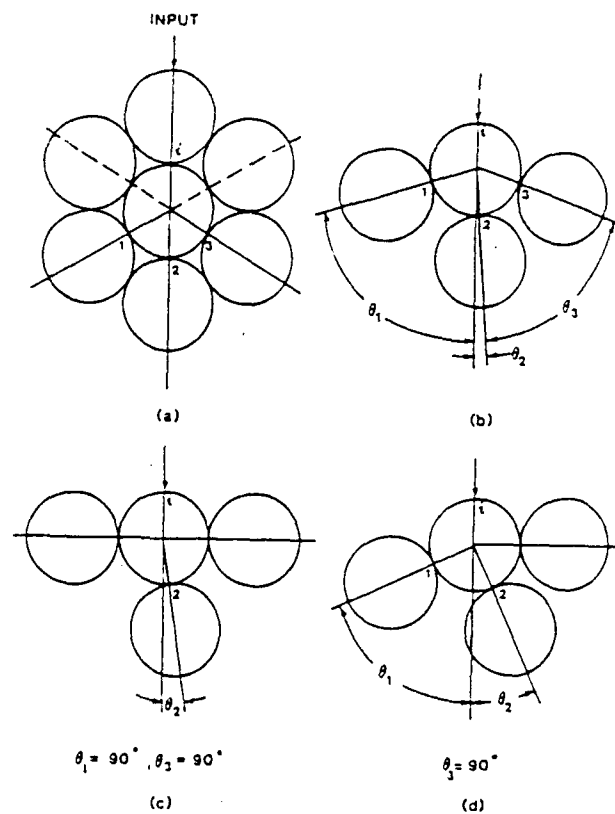
(c)

$\theta_3 = 90°$

(d)

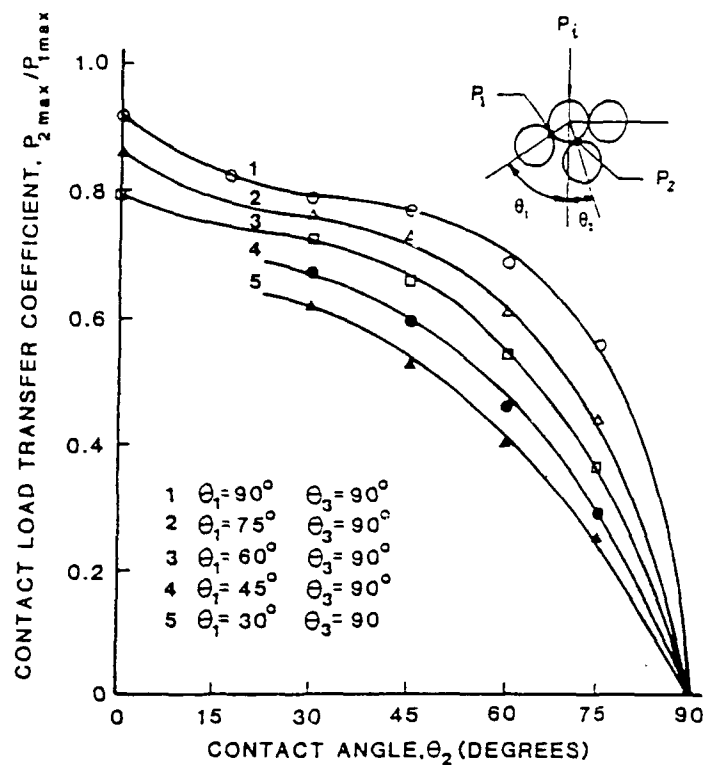Fig. 1.5 General four contact point model

24

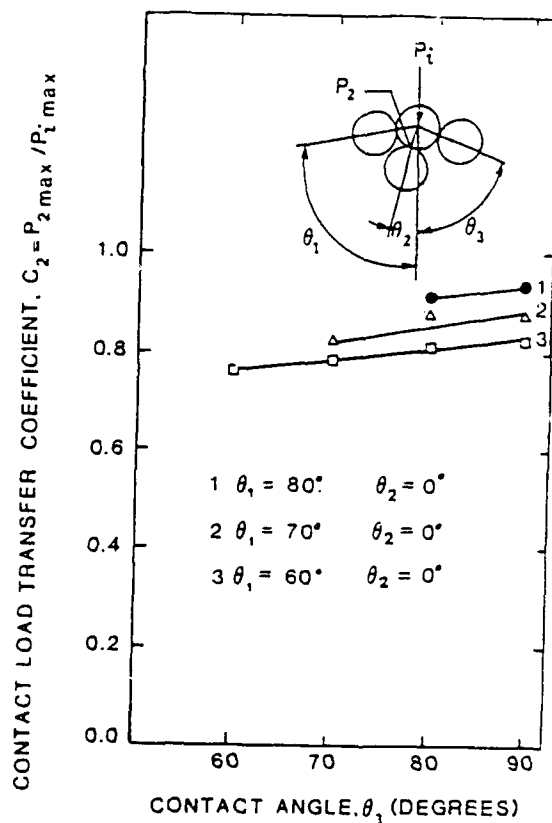Fig. 1.6 Contact load transfer coefficient C_1 as a function of
contact angles

Fig. 1.7 Contact load transfer coefficient C_2 as a function of
contact angles

25

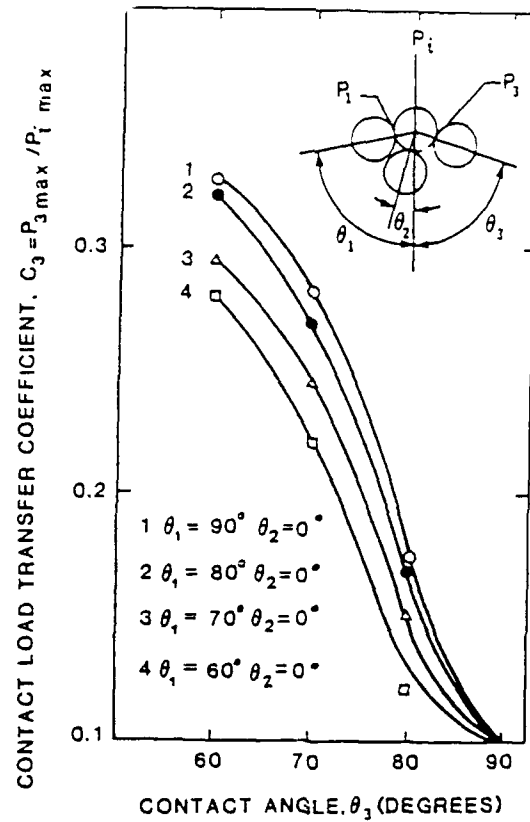Fig. 1.8 Contact load transfer coefficient C_3 as a function of contact angles
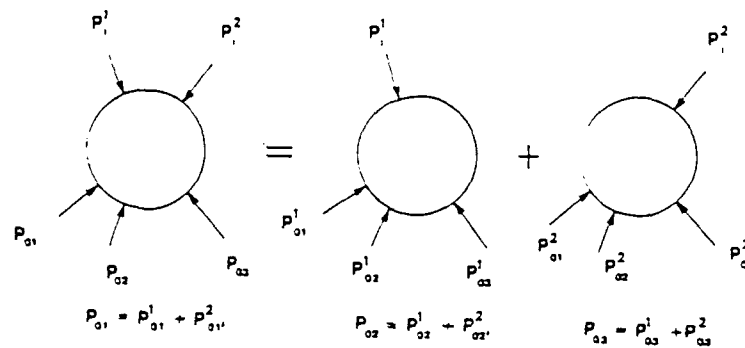
Fig. 1.9 Superposition model for two input loadings

26

Fig. 1.10 Comparison of the peak contact loads in a single chain arrangement for the geometry of Fig.1.1a (numerical data at bottom)

Fig. 1.11 Comparison of the peak contact loads in a HCP arrangement for the geometry of Fig.1.1b (numerical data at bottom)

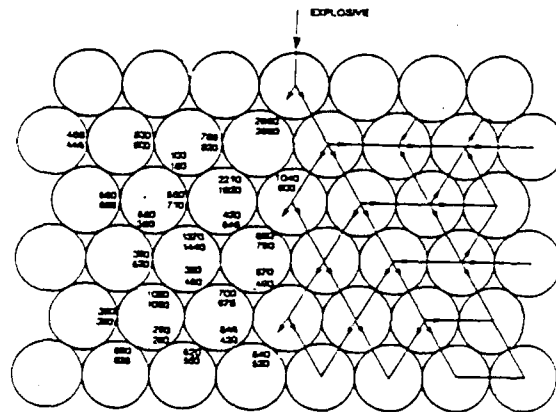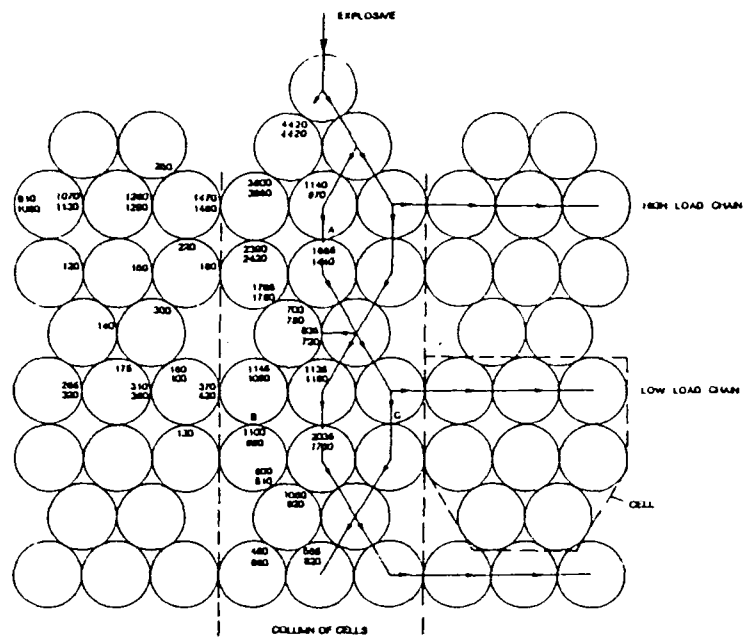Fig. 1.12 Comparison of the peak contact loads in a HHCP arrangement for
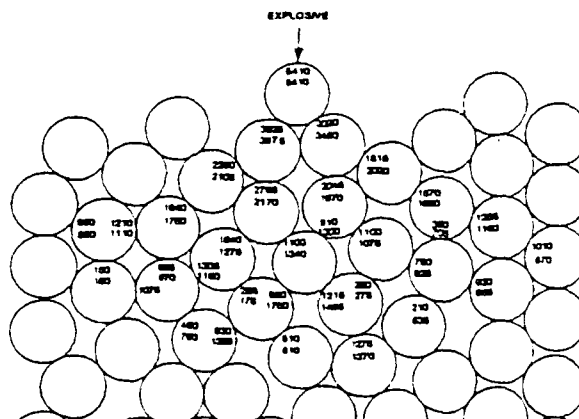the geometry of Fig.1.1c (numerical data at bottom)

Fig. 1.13 Comparison of the peak contact loads in an irregular arrangement
for the geometry of Fig.1.1d (numerical data at bottom).

CHAPTER 2

CONTACT LAW EFFECTS ON WAVE PROPAGATION IN PARTICULATE MATERIALS USING DISTINCT ELEMENT MODELING

2.1 INTRODUCTION

It has been well established (Oda et.al., 1982, Sadd et.al., 1989a, and Shukla et.al.,1988a) that load is transferred in a dry granular medium primarily through contact mechanisms between neighboring particles. Using such a discrete concept many authors, e.g., Digby (1981), Thornton and Barnes (1986), Patrakis and Dobry (1988), Patrakis, Dobry, and Ng (1988), Kishino (1988), Chang and Ma (1990), Ting and Corkum (1992), and Adely and Sadd (1992) have studied macroscopic quantities such as stress, strain, and effective elastic moduli from the microstructural standpoint for quasi-equilibrium cases. For the dynamic case, our previous studies (Shukla et.al., 1991, Zhu, et.al., 1991) have shown that the propagation of mechanical waves through such a medium occurs along a complex network of paths determined by the material's granular microstructure. Showing profound directional dependency in block-like materials, the recent numerical simulations carried by Walton et.al. (1991) also support this concept. The process of load transfer is determined by the particular contact interactions between the various grains in the media, and these interactions are primarily controlled by the particle's material properties and the local geometric arrangements of the particles. Previous research (Sadd, et.al., 1989a, Shukla, et.al., 1988a, 1991) has indicated that the wave speed will be primarily determined by the granule elasticity and mass density, while the wave amplitude will be most dependent on the geometry of the selected paths of propagation. Thus *local microstructure* or *fabric* plays a dominant role in the transmission of mechanical loadings through such materials.

Computer simulations employing *the distinct element method* as well as experiments using *dynamic photoelasticity* and *strain gages* have been conducted to investigate the effects of the local microstructure on wave propagation in granular media. Specific contact laws governing the interactions between granules are necessary for such computer simulations. The present study is concerned with the specific contact laws which govern the dynamic constitutive behavior. Results using linear, nonlinear and

nonlinear hysteretic normal contact laws with a nonlinear hysteretic tangential contact law are given. Computational and experimental studies have been conducted on specific aggregate assemblies composed of circular disks in order to simulate granular and particulate materials.

2.2 THE DISTINCT ELEMENT METHOD

A numerical scheme originally developed by Cundall and Strack (1979), called the *distinct element method* has been successfully used to simulate granular media by modeling the dynamic behavior of large assemblies of spheres, circular disks, and blocks (Thornton and Randall, 1988, Sadd, et.al., 1989a, Petrakis, et.al., 1988, Walton, 1991). The distinct element meth d is a simplified modeling concept which uses Newtonian rigid-body mechanics to model the translational and rotational motion of each disk in a model assembly. Particles are allowed to have overlapping contact, and contact forces are developed as a result of particular stiffness and/or damping characteristics. The technique establishes a discretized time stepping numerical routine, in which granule velocities and positions are obtained from numerical integration of the computed accelerations. It is assumed that during each time step, disturbances cannot propagate from any disk further than its immediate neighbors. Under these assumptions, the method becomes explicit, and therefore at any time increment the resultant forces (and thus the accelerations) on any disk are determined solely by its interactions with the disks it is in contact. For applications to wave propagation, the movements of the individual disks are a result of the propagation through the medium of disturbances originating at particular input loading points. Consequently, the wave speed and amplitude attenuation (intergranular contact force) will be functions of the physical properties of the discrete medium, i.e. the microstructure.

In order to describe the method, consider the case of two typical disks in contact as shown in Fig. 2.1. The position, velocity, acceleration, angular velocity, angular acceleration, radius, and mass of disk 1 are labeled as: r_1, v_1, a_1, ω_1, α_1, R_1, and m_1, with like notations for disk 2. The unit normal vector n and unit tangential vector t are defined as shown, and these establish the normal and tangential directions used for the contact analysis.

The normal component of relative contact velocity between the two disks is given

by

$$v_n = (v_1 - v_2) \cdot n \qquad (2.1)$$

while the tangential relative velocity is

$$v_t = (v_1 - v_2) \cdot t - (\omega_1 R_1 + \omega_2 R_2) . \qquad (2.2)$$

Using a finite difference scheme with constant properties over the time interval, the relative velocities may be integrated with respect to time to yield the incremental relative normal and tangential displacements, i.e.

$$\Delta\delta_n = v_n\Delta t = [(v_1 - v_2) \cdot n]\Delta t$$

$$\Delta\delta_t = v_t\Delta t = [(v_1 - v_2) \cdot t - (\omega_1 R_1 + \omega_2 R_2)]\Delta t . \qquad (2.3)$$

In a similar way, the absolute linear and angular velocities may be computed from the accelerations using the relations

$$\Delta v = a \, \Delta t$$

$$\Delta\omega = \alpha \, \Delta t \qquad (2.4)$$

Through allowable deformations, the disks in contact are permitted to overlap with one another such that the distance between their centers will become less than $(R_1 + R_2)$, and contact forces will therefore exist between them. A particular contact force-displacement law will then be necessary to calculate the forces on each disk in the assembly. In general the contact law between two granules can be written as two equations expressing the normal and tangential contact forces by

$$F_n = F_n(\delta_n, v_n, \delta_t, v_t)$$

$$F_t = F_t(\delta_n, v_n, \delta_t, v_t) . \qquad (2.5)$$

where δ_n and δ_t are the relative normal and tangential displacements between adjacent

31

disks in contact, and v_n and v_t are the relative normal and tangential velocities. The contact forces may also be history dependent. A Coulomb-type friction law is incorporated to deal with the tangential loading. This law is defined by

$$(F_t)_{max} = \mu F_n + c , \qquad (2.6)$$

where μ is the coefficient of friction and c is the cohesion between the two disks. If the magnitude of F_t found from equation $(2.5)_2$ is larger than $(F_t)_{max}$, then F_t is set equal to $(F_t)_{max}$.

Using Newton's second law of motion, the linear and angular accelerations of each disk at each time interval can be determined. For disk 1, such an application would give

$$\Sigma F_1 = m_1 a_1$$
$$\Sigma M_1 = I_1 \alpha_1, \qquad (2.7)$$

where ΣF_1 and ΣM_1 are the resultant force and moment on disk 1, and I_1 is the moment of inertia of the disk. Equations (2.7) can thus be solved for the accelerations a_1 and α_1 over each time increment. With the accelerations known, the velocities follow from application of equation (2.4) and the relative displacements can then be computed from equation (2.3). This leads to new values of the contact forces through relation (2.5) for the next time increment, and the cycle is repeated again for each disk (see flow chart in Fig. 2.2). In this manner, large assemblies of disks can be analyzed in a reasonable amount of computer time.

2.3 CONTACT LAW MODELS

It is obvious that the propagational characteristics depend on the process of load transfer between disks. Since the load transfer is governed by the contact mechanism of the disks, the characteristics will depend on the contact laws (2-5), and thus we wish to investigate the effects of using several different types of contact laws. Figure 2.3 illustrates the cases to be considered in this work

2.3.1 Normal Contact Law

For the static case the normal contact law can be determined by Hertz contact theory or from experiments. However, for the dynamic case in which the load is of short

duration, wave motion effects make it difficult to determine the contact law. In some of our previous work (Sadd, et.al., 1989a), a static normal contact law has been modified for use in dynamic cases. In general the normal contact law given by equation $(2.5)_1$ represents a variety of cases including both displacement and velocity dependent contact forces. Velocity dependent damping acting like dashpots will produce energy dissipation which is a needed ingredient to model real granular materials, and two forms of such damping have been introduced in (Sadd, et.al., 1989): a *local damping* proportional to the relative disk velocities, and a *global damping* proportional to the absolute velocities. Likewise, a *hysteretic* normal contact law depending only on the relative displacements will also produce energy dissipation. An appropriate contact constitutive law should have both the correct stiffness to be able to model the proper wave velocities and the correct dissipation mechanisms to accurately predict wave attenuation. Three specific cases shown in Fig. 2.3a,b,c will now be presented to demonstrate some of these basic features.

a. Linear Normal Contact Law

If the assumption is made that there is no deformation out of the contact area and plane strain conditions exist, then application of Hertz contact theory yields a static linear contact law between the forces and the relative displacement of two disks in contact. If it is further assumed that the dynamic contact stiffness is scalable from the static Hertz value, then the normal contact law reads

$$F_n = K_n \, \delta_n = \alpha \, K_n^{(s)} \, \delta_n \qquad (2.8)$$

where K_n is the dynamic stiffness, α is a stiffness ratio which is determined from experiments, and $K_n^{(s)}$ is the static contact stiffness from Hertz theory given by

$$K_n^{(s)} = \frac{\pi h E_1 E_2}{2(E_1 + E_2)} \qquad (2.9)$$

with h being the disk thickness, and E_1 and E_2 being the elastic moduli of the disks in contact. This particular contact law is shown in Fig. 2.3a.

Incorporating the distinct element method with this linear contact law required that some forms of local or global damping be included in the model. For dry granular materials the global damping can be neglected, and the local damping is taken to follow

a simple linear law (linear viscous dashpot) of the form $F_d = C_{tn}v_n$, where C_{tn} is called a local damping factor. In order to collect calibration data to determine the values of α and C_{tn}, photoelastic experiments were performed on a single straight chain of disks. Fig. 2.4 illustrates typical photoelastic isochromatic fringe patterns of the wave propagation at various instants of time for this simple configuration. Appropriate values for the normal stiffness and damping coefficients were thus determined to match the data from these calibration tests. In particular the normal contact stiffness value is primarily related to the wave speed, and this stiffness value was therefore determined by matching the model results with the velocity data (about 1010 m/s) from the experiments. In a similar fashion, the local damping constant is related to the wave attenuation, and thus it was found by matching the model results with amplitude attenuation data. The single straight chain consisted of 40 Homalite-100 circular disks with 25.4mm (1 inch) diameter and a 6.35mm (1/4 inch) thickness which were explosively loaded. To simulate the experiments, the theoretical nmodel input loading used a triangular time profile with a 60 μs duration and a peak value of 1000 N, and the time increment was taken as $\Delta t = 2\mu$s. Values of the stiffness and damping determined from the experiments along with the particle mass density were $K_n = 6.4 \times 10^6$ N/m, $C_{tn} = 32$ N s/m, and $\rho = 1.2 \times 10^3$ Kg/m^3.

Using these parameters, model predictions for the single straight chain are shown in Figs. 2.5 - 2.7. The time profiles of normalized contact load at every fourth contact point are shown in Fig. 2.5. It was observed that the linear stiffness law with linear velocity dependent damping gave wave speed and amplitude results which generally match with the experimental data (Sadd, et.al., 1989). However as illustrated in Fig. 2.5, this model produces unrealistic wave form dispersion. The period of the original 60 μs input wave profile was lengthened to more than 200 μs during the propagation over 40 disks, and this phenomena was not found in the experiments. With damping removed from the model the normalized contact load histories for every fourth contact point are shown in Fig. 2.6, and it can be seen that this model also produced attenuation. Further investigation showed that the attenuation for the case without damping is not due to any net energy loss but rather it indicates that the model overpredicts the dispersion, thus leading to a decrease in the peak contact forces. The potential, kinetic and total energies in the straight chain assembly are shown in Fig. 2.7 for this case. It is seen that the total

34

energy quickly becomes a constant value, and therefore the dispersion characteristics of the model are creating the peak amplitude attenuation. With the high dispersion associated with this model, the wave profile rapidly spreads producing an increasing wave length with propagation distance. This characteristic is not consistent with our experimental data, and thus indicates that a new model should be developed with a nonlinear contact law.

b. Nonlinear Contact Law

Based on the above observations, a nonlinear contact law was constructed in an effort to eliminate the highly dispersive characteristics of the previous linear model. According to Johnson (1985) the relative displacement between disks in contact cannot be determined by only considering the deformation near the contact point. Instead an elasticity solution that considers the shape, size, and the way in which the disk is supported is required. Johnson, using a superposition of Hertz theory, a uniform stress field, and a point-loaded disk problem, derived a nonlinear relationship between the contact force and the center-point displacement.

A simplified relation that appears to match with the approximate solution from Johnson, is of the form

$$F_n = \alpha_0 \delta_n^p \qquad (2.10)$$

where α_0 and p are model parameters dependent upon the material and geometry of the disk. Generally $p > 1$, thus providing a stiffness that increases with load, and this behavior is shown in Fig. 2.3b.

Distinct element results for a single straight chain using this nonlinear model are shown in Figs. 2.8 and 2.9. Fig. 2.8 shows the contact load history of every fourth contact point for the single straight chain without damping. The values of α_0 and p are chosen as 3×10^8 N/m$^{1.4}$ and 1.4 respectively, so as to yield a wave speed that matches with the experimental result. It is seen for this case that all contact loads, except the first one, have the same shape and the same peak value, i.e. no dispersion and no attenuation. The attenuation that exists at the very beginning of the chain is a result of the establishment of a stable wave motion from the input explosive source. Fig. 2.9

35

illustrates the attenuation behavior for the nonlinear case with linear velocity dependent damping. Including such damping clearly again produces excessive dispersion, and since we must have some form of damping in the model to correctly predict wave attenuation, this particular nonlinear law cannot accurately predict the resulting wave forms and thus must be modified.

c. Nonlinear Hysteretic Normal Contact Law

It is apparent from the previous case that the nonlinear stiffness law with velocity dependent damping will not correct the over-prediction of wave form dispersion. Furthermore the basic issue of velocity dependent damping would indicate that some form of viscous mechanism is present in the material. For dry granular media under study, there does not seem to be physical evidence of such a damping mechanism. Consequently, a different normal contact law is proposed which produces *deformation dependent damping* through a nonlinear hysteretic law accounting for different loading and unloading behaviors. The basic concept is illustrated in Fig. 2.3c, in which the unloading path lies below the loading curve and thus energy is lost during a cycle in proportion to the amount of deformation of each disk. For this case the velocity dependent damping (i.e. the dashpot) will be dropped from the model, and the normal contact law would read,

$$F_n = \begin{cases} F_{nL} = \alpha_L \delta_n^{p} \dots\dots\dots\dots\dots\dots\dots loading \\ F_{nU} = \alpha_U \delta_n^{p+q} \dots\dots\dots\dots\dots unloading,\ reunloading \\ F_{nrL} = \beta F_{nL} + (1-\beta)F_{nU} \dots\dots reloading \end{cases} \qquad (2.11)$$

If in the loading path the maximum value of the force is recorded as $F_{n\,max}$, then the reloading is defined as the state in which the load is increasing but its value is smaller than $F_{n,\,max}$. The reloading path will join the loading path at $F_{n\,max}$, and additional loading follows the origional loading path. The value of q is determined by

$$q = (A\ \delta_{n\,max}^{(i)})^2 \qquad (2.12)$$

where A is a constant to be determined and $\delta_{n\,max}^{(i)}$ is defined as the value of δ_n at contact point i when the normal contact force at the point has attained its maximum value. The value of β is given by

$$\beta = \frac{\delta_n^{(i)} - \delta_{n\,min}^{(i)}}{\delta_{n\,max}^{(i)} - \delta_{n\,min}^{(i)}} \qquad (2.13)$$

with $\delta_n^{(i)}$ is the current value of the relative normal displacement at contact point i, and $\delta_{n\,min}^{(i)}$ indicates its minimum value in the previous unloading or reunloading path. At the moment reloading begins, $\delta_n^{(i)} = \delta_{n\,min}^{(i)}$ and $\beta = 0$. The value of β increases with $\delta_n^{(i)}$, and it reaches a maximum value of 1 when $\delta_n^{(i)} = \delta_{n\,max}^{(i)}$ which indicates that new loading will begin. The values of α_L, p, and A are related to material and geometric properties of the disks, and will be determined from experimental calibration tests. The parameter α_U, however, is determined in order to make the unloading path initiate at the peak point of loading, see Fig. 2.3c.

Model results for the nonlinear hysteretic case consisted of simulations of the single straight chain. Again the parameters needed in the numerical model were determined from the experiments yielding: $p = 1.4$, $A = 8500$ m^{-1}, $\alpha_L = 3 \times 10^8$ N/m$^{1.4}$. With these parameters, the numerical predictions matched well with experimental data for the wave speed, wave attenuation, and the wave dispersion. These results will be discussed in section 2.4.

2.3.2 Tangential Contact Law

To simulate the wave motion in two dimensional assemblies, both a normal and a tangential contact law are required. The appropriate normal contact law was given by equation (2.11). The tangential contact law is considerably more complicated and thus more difficult to derive since the current value of the tangential contact force may depend on its history and the amplitude of the normal contact force. In addition there could be partial slip within the contact area. A tangential contact law proposed by Walton et.al. (1991) will be used here with some modifications. The basic concept embedded in this contact law is that the effective tangential contact stiffness decreases with an increase of the tangential force, and goes to zero when full sliding occurs. The tangential contact is thus written as,

$$F_t^{N+1} = F_t^N + K_t \Delta \delta_t^N \qquad (2.14)$$

37

where, F_t^N and $\Delta\delta_t^N$ are the tangential force and the relative tangential displacement increment at the N-th time step, and K_t is the tangential contact stiffness which is given by

$$K_t = \begin{cases} K_0 \left(1 - \dfrac{F_t - F_t^*}{\mu F_n - F_t^*}\right)^\gamma \quad\dots\dots\dots\dots\Delta\delta_t \geq 0 \\[3em] K_0 \left(1 - \dfrac{F_t^* - F_t}{\mu F_n + F_t^*}\right)^\gamma \quad\dots\dots\dots\dots\Delta\delta_t < 0 \end{cases} \qquad (2.15)$$

Here, K_0 and γ are constants to be determined, F_t is current tangential force, and F_t^*, which is initially set to zero, takes the value of F_t when the $\Delta\delta_t$ changes sign. If the normal force, F_n, changes during contact, the value of F_t^* will be scaled in proportion to the change in the normal force. Fig. 2.3d illustrates the relationship between F_t and δ_t when F_n is kept as a constant. In our numerical simulations, the values of K_0, γ, and μ are set to 5×10^5 N/m, 0.3, and 0.5 respectively, such that the numerical results match with the experimental data obtained in a two dimensional hexagonal close packing assembly shown in Fig. 2.12.

2.4 NUMERICAL RESULTS

2.4.1 One Dimensional Cases

As a calibration, once again the single straight chain was used in the numerical simulation, and a triangular time dependent impulse with a 60µs period was used to simulate the explosive loading in the experiments. Results from the distinct element model are shown in Figs. 2.10 and 2.11. Fig. 2.10 gives the profiles of contact loads of every fourth contact point versus time. The wave speed is approximately 990 m/s, the duration of contact load at each contact point is about 93µs, so the ratio of wavelength to disk diameter is around 3.6. The experimental results gave a wave speed of 1010 m/s and a ratio of wavelength to disk diameter of about 3.5. Fig. 2.11 compares the numerically predicted peak contact load versus distance with the data from the experiments. The numerical results match the experimental data quite well with difference less than 5%. Both the numerical model predictions and the experimental data show that the attenuation

38

is larger at the contact points near the point of input loading. Also some dispersion occurs near the explosive loading point, and this is probably due to the establishment of the propagating profile from the explosive time input. It appears that the wave motion signal needs to propagate a small distance in order to achieve a stable profile state.

2.4.2 Two Dimensional Cases

The distinct element method with the hysteretic normal contact law (2.11) and tangential contact law (2.15) was used to model wave propagation in several two dimensional granular assemblies. In order to compare with experimental results, the same disks and input loading were used as those in 'he one dimensional single straight chain case.

a. Hexagonal Close Packing (HCP) Assemblies

One of the assemblies studied is the hexagonal close packing geometry shown in Fig. 2.12. The disks in the close packed assembly have six contacts with neighboring disks. Given in Table 2.1 are the numerical predictions for the peak normal contact forces for cases both with and without tangential force modeling. As a comparison, the normal contact loads from the experiments are also given in the Table. It is apparent that including tangential contact interactions improves the results with a change of average relative error from 14.5% to 11.8%. The maximum F_t was recorded at the contact points (disks #13 : #12) and (disks #14 : #15). The same assembly with a void is shown in Fig. 2.13, but the position and the direction of input loading have been changed. The void was created by removing a disk from the assembly. Table 2.2 gives the distinct element analysis results for this case. It can be seen that including tangential forces in the model decreased the relative error of the normal contact loads especially around disks #28 and #29 where significant tangential forces would be expected. Another HCP assembly with three voids is shown in Fig. 2.14. Numerical predictions and comparisons are given in Table 2.3. Again the tangential contact model improved the comparisons with the experimental results especially at the contact points near the voids.

b. Irregular Assembly

An irregular assembly which was first used in the experiments is shown in Fig. 2.15. Due to the irregular packing geometry of the assembly, intergranular tangential loads will exist at many contact points and will play a more important role than in the other

assemblies previously presented. The comparison of numerical predictions with experimental results is given in Table 2.4. Without tangential contact forces the average relative error of peak normal contact forces is 20.7% which is larger than those in the HCP assemblies. Using the tangential contact force model, the error difference is reduced to 14.5%. The maximum tangential loading occurs at the contact point between disk #19 and #29, and its value is about two times that found in the HCP assembly previously discussed.

2.5 CONCLUSIONS

Three different normal contact laws have been incorporated into the distinct element numerical code used to simulate the dynamic behavior of granular materials. These contact laws provide the basic microstructural constitutive behavior that governs the way mechanical signals will propagate from particle to particle. The various laws must account for the proper stiffness and damping characteristics to accurately predict the wave speed and inter-granular wave attenuation/dispersion. The three cases included: simple linear stiffness/linear velocity dependent damping; nonlinear stiffness/linear velocity dependent damping; and nonlinear hysteretic behavior. Comparisons of the numerical predictions with each other and with experiments were made for a simple geometry of single disk chains of Homalite 100 material.

The linear contact law was simple to formulate, characterize and run, and it could provide reasonably accurate values for the wave speed and amplitude attenuation; however, it produces unreasonably high dispersion (wave profile spreading) than that found in the experiments. Incorporating a nonlinear stiffness contact law, did provide the means to reduce this excess dispersion; however, once velocity dependent damping was added to this model the dispersion again became unacceptably high. Failing to see any fundamental mechanism for velocity dependent damping for dry cohesionless granular materials, the final contact model incorporated a hysteretic stiffness law where loading and unloading contact responses were taken to be different. For this case the velocity dependent damping was removed and the hysteretic law provided the necessary damping to control and model the inter-granular wave amplitude behavior. The hysteretic model appears to provide the best match with the experimental data for both the wave speed and amplitude attenuation, and it predicts the proper dispersion characteristics observed in the

experiments.

A tangential contact law originally proposed by Walton et.al. (1991) was included with the nonlinear hysteretic normal contact law to predicte the wave propagation in two dimensional granular assemblies. It is found that these contact laws work well and the average relative errors between experimental data and predicted values were less than 15%.

Table 2.1 Numerical predictions of the normal contact loads
of the assembly shown in Fig. 2.12

| Contact Location | HCP Assembly (Input on Disk #5) | | | | |
| | Exp | Numerical Model with F_t | | Numerical Model without F_t | |
	Normalized F	Normalized F	Relative Error %	Normalized F	Relative Error %
5 : 13	1.203	1.357	12.8	1.301	8.1
13 : 21	1.000	1.000	0.0	1.000	0.0
13 : 22	0.470	0.387	17.6	0.359	23.6
12 : 13	0.346	0.360	4.0	0.413	19.4
11 : 12	0.240	0.257	7.1	0.309	28.8
10 : 11	0.206	0.195	5.4	0.242	17.5
20 : 21	0.385	0.265	31.1	0.306	20.5
19 : 20	0.253	0.207	18.2	0.260	2.8
22 : 30	0.403	0.383	5.0	0.341	15.4
21 : 29	0.620	0.740	19.4	0.780	25.8
29 : 38	0.176	0.178	1.3	0.209	18.8
30 : 39	0.258	0.272	5.4	0.275	6.6
30 : 38	0.316	0.370	16.8	0.322	1.9
29 : 37	0.489	0.553	13.1	0.617	26.2
37 : 36	0.172	0.140	18.6	0.183	6.4
37 : 45	0.403	0.417	3.6	0.495	22.8
37 : 46	0.131	0.124	5.4	0.161	22.9
38 : 46	0.281	0.350	24.5	0.303	7.8
38 : 47	0.247	0.199	19.3	0.221	10.5
39 : 47	0.244	0.276	12.9	0.270	10.7
46 : 54	0.307	0.327	6.4	0.283	7.8
Average Relative Error %		11.8		14.5	

42

Table 2.2 Numerical predictions of the normal contact loads
of the assembly shown in Fig. 2.13

HCP Assembly (One Void, Input on Disk #35)					
Contact Location	Exp	Numerical Model with F_t		Numerical Model without F_t	
	Normalized F	Normalized F	Relative Error	Normalized F	Relativ Error
35 : 36	1.000	1.000	0.0	1.000	0.0
27 : 28	0.126	0.110	12.4	0.082	34.9
28 : 29	0.268	0.277	3.5	0.207	22.7
29 : 30	0.190	0.214	12.6	0.162	14.7
30 : 31	0.140	0.164	17.3	0.131	6.4
20 : 21	0.126	0.174	37.8	0.172	36.5
35 : 27	0.436	0.422	3.1	0.425	2.5
27 : 19	0.300	0.311	3.7	0.329	9.7
19 : 11	0.252	0.239	5.1	0.269	6.7
36 : 28	0.422	0.424	0.5	0.471	11.6
28 : 20	0.356	0.373	4.7	0.443	24.4
20 : 12	0.316	0.325	2.7	0.402	27.2
29 : 21	0.147	0.063	57.2	0.055	62.6
Average Relative Error %		12.3		20.0	

43

Table 2.3 Numerical predictions of the normal contact loads
of the assembly shown in Fig. 2.14

Contact Location	HCP Assembly (3 Voids, Input on Disk #35)				
	Exp	Numerical Model with F_t		Numerical Model without F_t	
	Normalized F	Normalized F	Relative Error %	Normalized F	Relative Error %
35 : 36	1.000	1.000	0.0	1.000	0.0
27 : 28	0.103	0.110	7.2	0.082	20.3
28 : 29	0.268	0.277	3.5	0.207	22.8
29 : 30	0.190	0.213	11.9	0.162	14.7
30 : 31	0.197	0.180	8.7	0.141	28.4
31 : 32	0.155	0.141	9.3	0.119	23.2
20 : 21	0.127	0.174	36.7	0.172	35.4
21 : 22	0.134	0.156	16.2	0.150	11.9
23 : 24	0.101	0.132	30.8	0.125	23.8
12 : 13	0.120	0.119	1.0	0.141	17.5
13 : 14	0.134	0.112	16.5	0.124	7.5
14 : 15	0.155	0.108	30.4	0.113	27.1
35 : 27	0.437	0.422	3.3	0.425	2.7
27 : 19	0.300	0.311	3.7	0.329	9.7
19 : 11	0.254	0.240	5.9	0.269	5.9
36 : 28	0.423	0.424	0.2	0.471	11.3
28 : 20	0.359	0.373	3.8	0.443	23.4
20 : 12	0.310	0.325	4.7	0.402	29.7
29 : 21	0.148	0.063	57.5	0.060	59.5
Average Relative Error %		14.2		19.8	

Table 2.4 Numerical predictions of the normal contact loads
of the assembly shown in Fig. 2.15

Contact Location	Random Assembly (Input on Disk #1)				
	Exp	Numerical Model with F_t		Numerical Model without F_t	
	Normalized F	Normalized F	Relative Error %	Normalized F	Relative Error %
1 : 2	1.000	1.000	0.0	1.000	0.0
2 : 5	0.762	0.678	11.2	0.668	12.3
5 : 10	0.507	0.432	14.8	0.418	17.6
10 : 17	0.358	0.358	0.1	0.365	2.0
17 : 26	0.295	0.261	11.5	0.295	0.0
1 : 3	0.832	0.891	7.0	0.888	6.7
3 : 6	0.565	0.569	0.6	0.541	4.2
6 : 12	0.303	0.292	3.8	0.274	9.6
12 : 20	0.218	0.176	19.2	0.201	7.8
20 : 31	0.256	0.135	47.3	0.184	28.1
5 : 11	0.303	0.224	26.1	0.371	22.4
11 : 19	0.333	0.311	6.5	0.224	32.7
19 : 29	0.351	0.331	5.7	0.359	2.3
6 : 11	0.251	0.378	50.4	0.379	51.0
11 : 18	0.259	0.316	21.9	0.331	27.8
18 : 27	0.229	0.264	15.1	0.297	29.7
2 : 4	0.620	0.545	12.1	0.583	6.0
4 : 9	0.534	0.448	16.1	0.465	12.9
9 : 16	0.331	0.305	7.9	0.323	2.4
9 : 17	0.182	0.238	30.7	0.345	89.6
3 : 7	0.500	0.526	5.2	0.570	14.0
7 : 13	0.433	0.426	1.7	0.468	8.1
13 : 21	0.347	0.326	5.9	0.383	10.4
18 : 28	0.140	0.158	12.7	0.198	41.4
Average Relative Error %		13.2		18.3	

Distinct Element Method
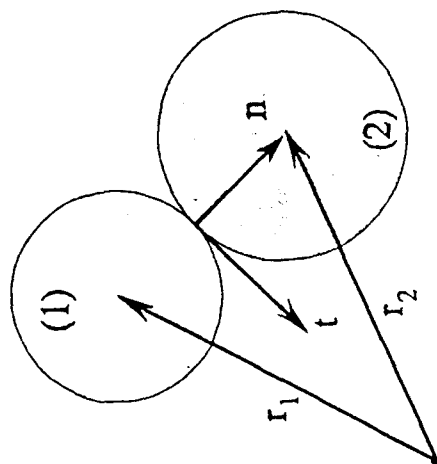
Fig. 2.2   Computer flowchart for the distinct element method

Fig. 2.1   Schematic of disk interaction

46

(a) Linear normal contact law   (b) Nonlinear normal contact law

(c) Nonlinear-hysteretic normal contact law   (d) Tangential contact law
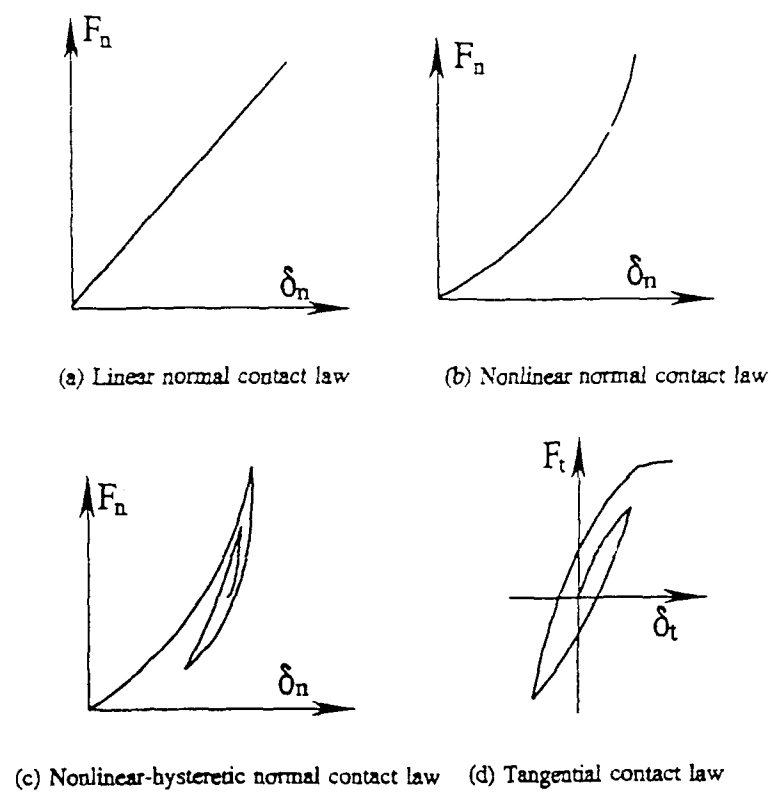
Fig. 2.3   Particle contact laws
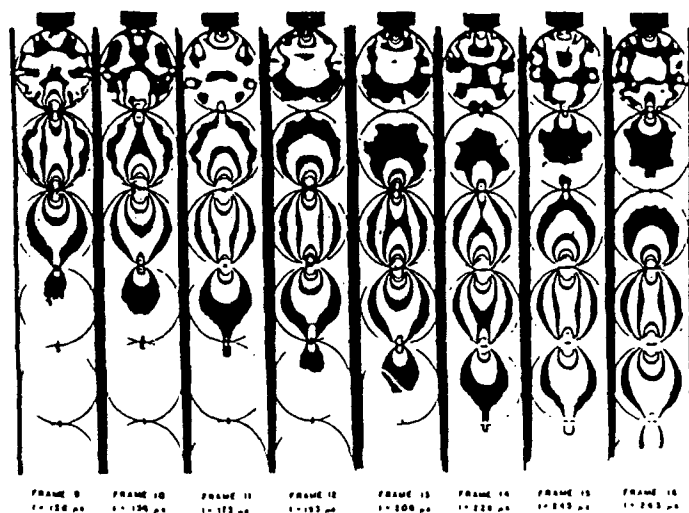
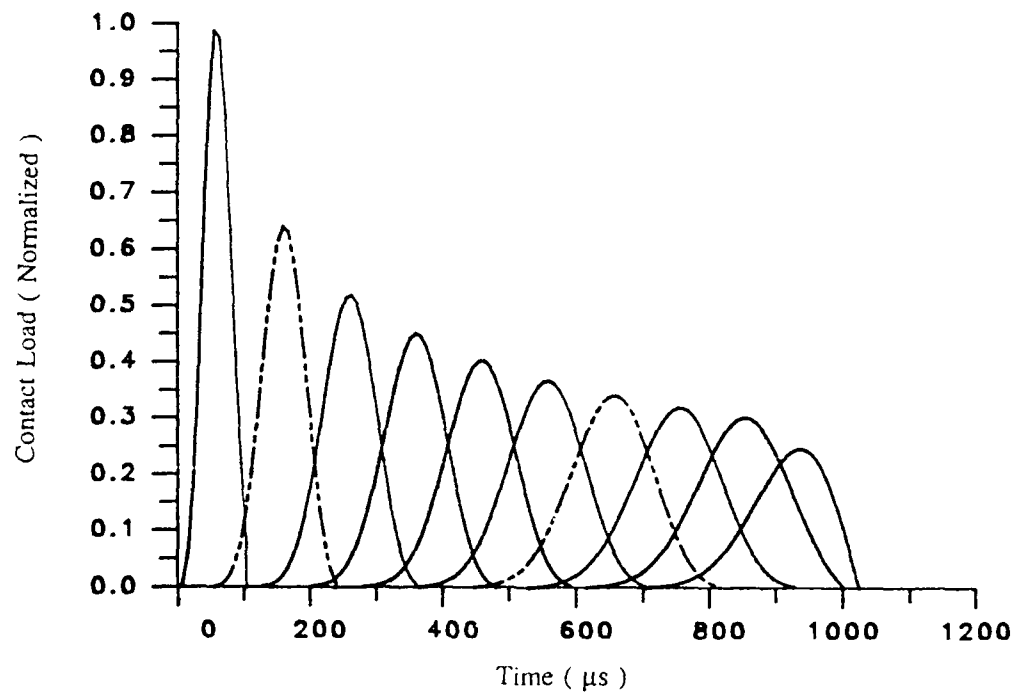Fig. 2.4   Typical isochromatic fringes obtained from a single chain experiment

47

Fig. 2.5   Contact load versus time in a single straight chain (linear normal contact law with velocity dependent damping)
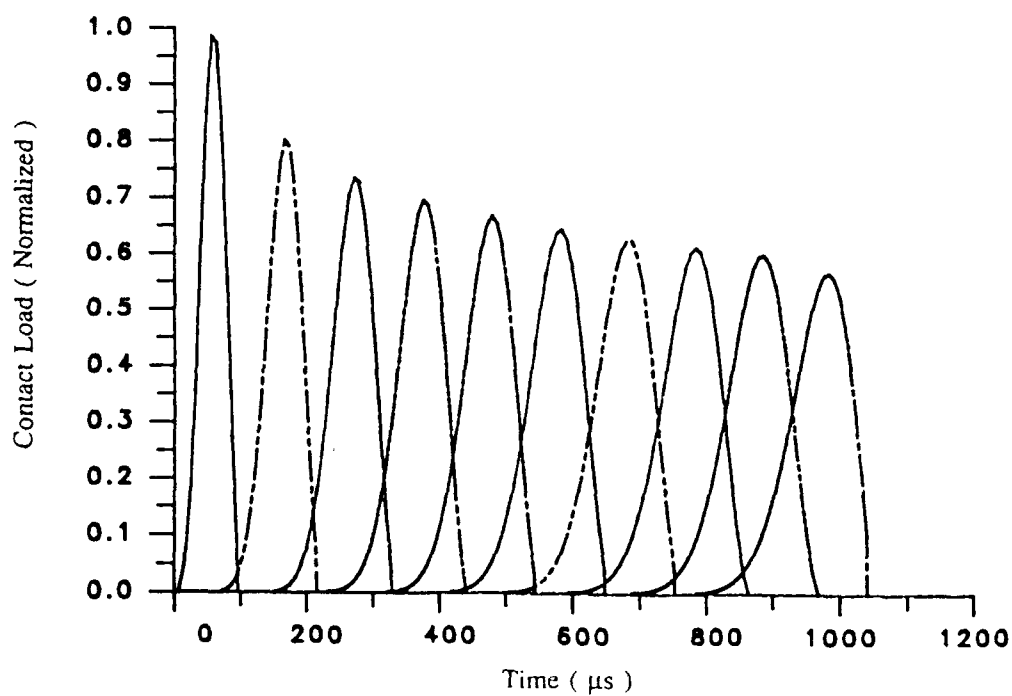
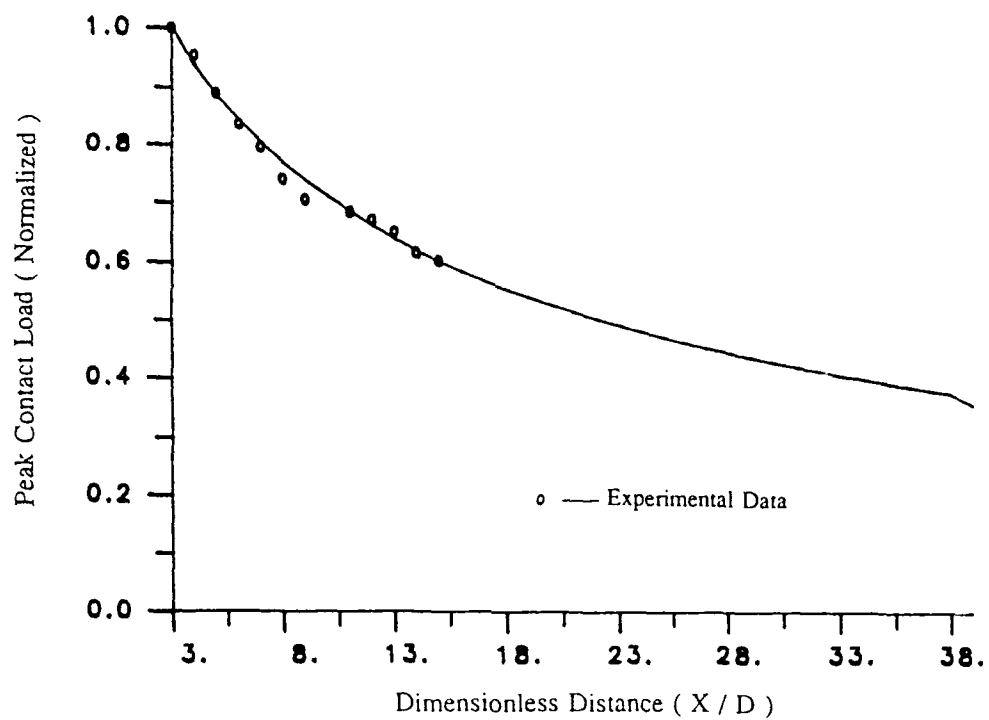Fig. 2.6   Contact load versus time in a single straight chain (linear normal contact law without damping)

48
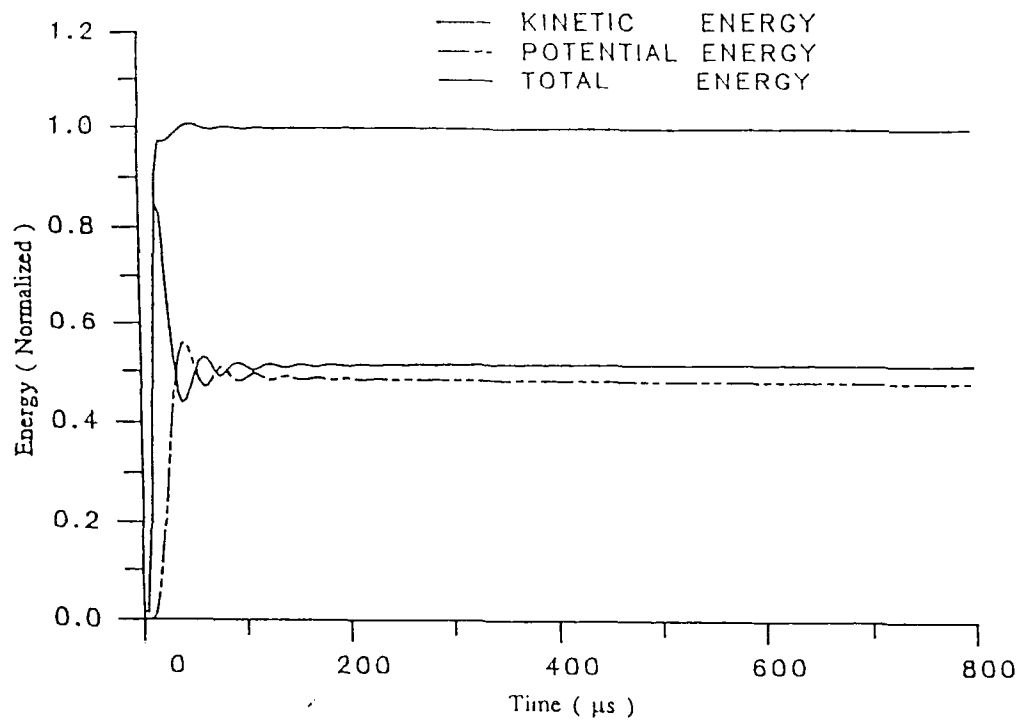
Fig. 2.7   Energies versus time in a single straight chain (linear normal contact law without damping)
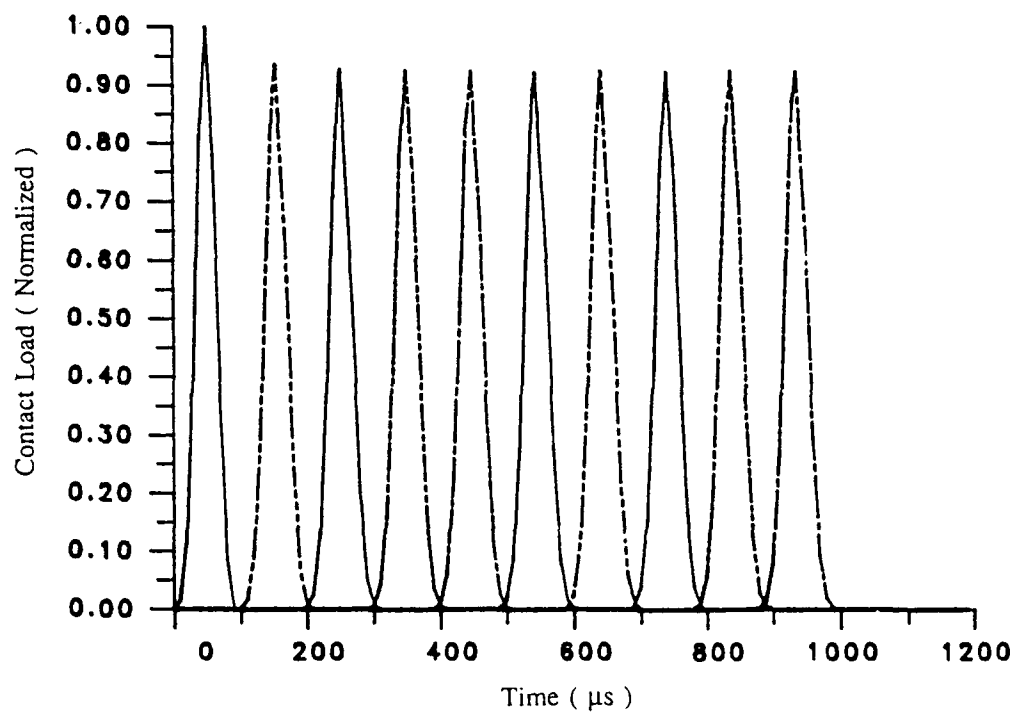
Fig. 2.8   Contact load versus time in a single straight chain (nonlinear normal contact law without damping)

49
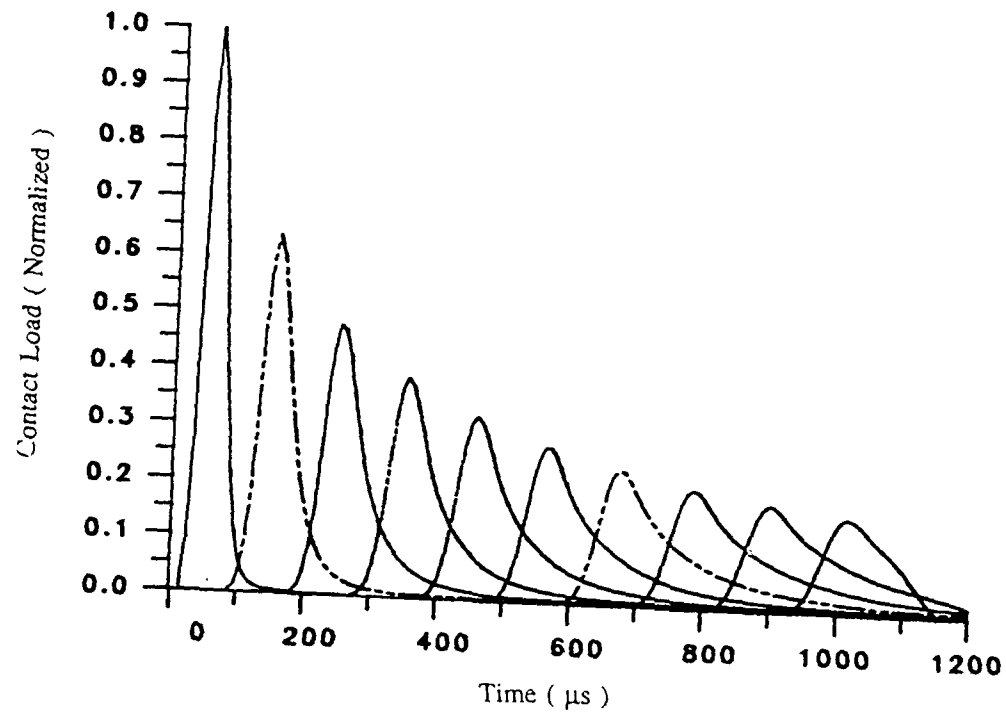
Fig. 2.9   Contact load versus time in a single straight chain (nonlinear normal contact law with velocity dependent damping)
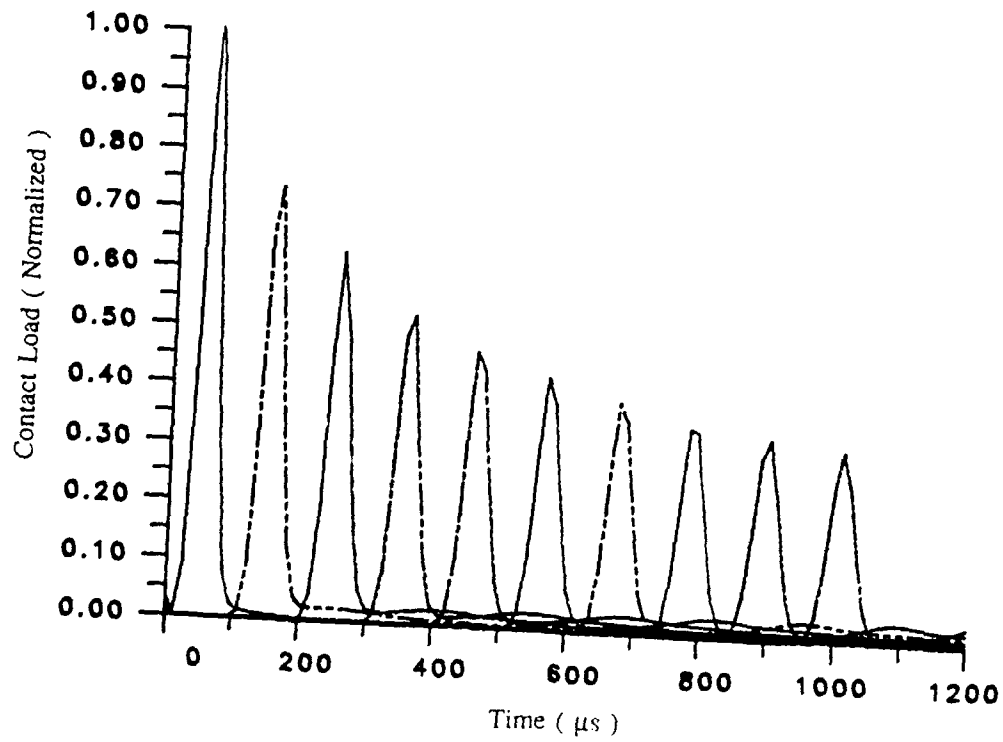
Fig. 2.10   Contact load versus time in a single straight chain (nonlinear-hysteretic normal contact law)

50

Fig. 2.11 Peak contact load versus the distance in a single straight chain (nonlinear-hysteretic normal contact law)
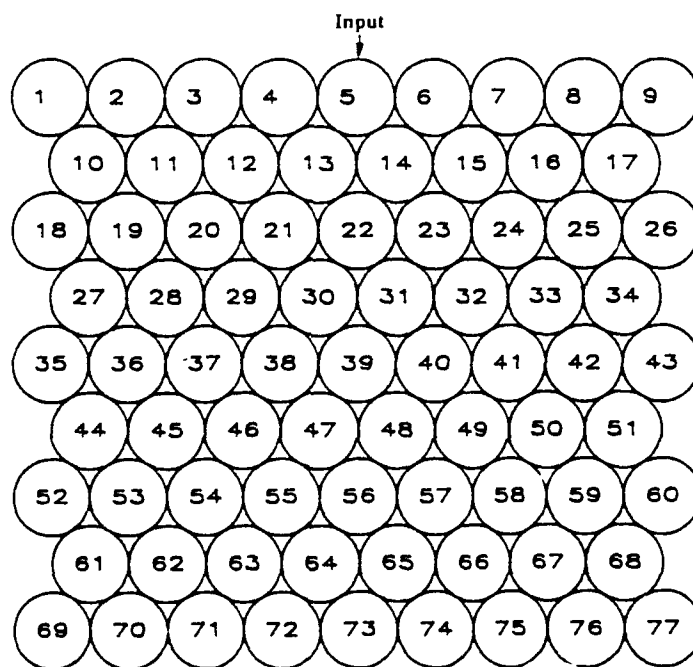
Fig. 2.12 A hexagonal close packing assembly
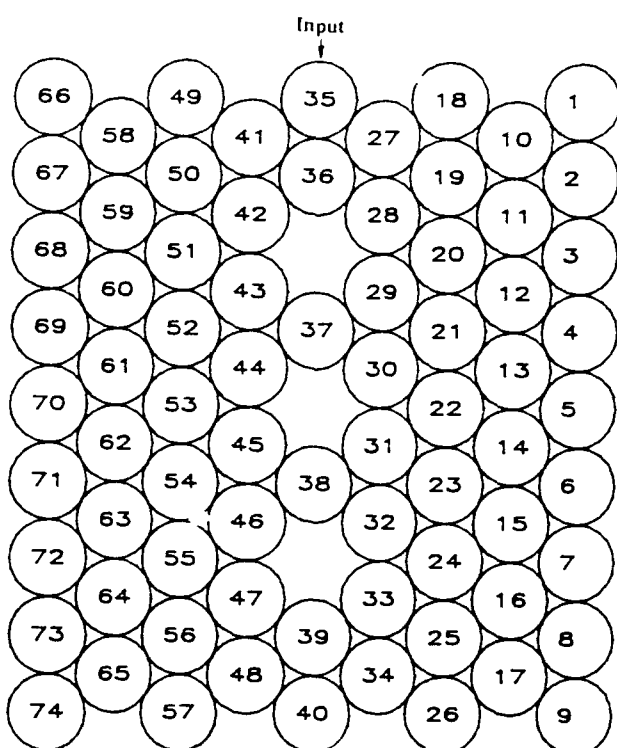
51
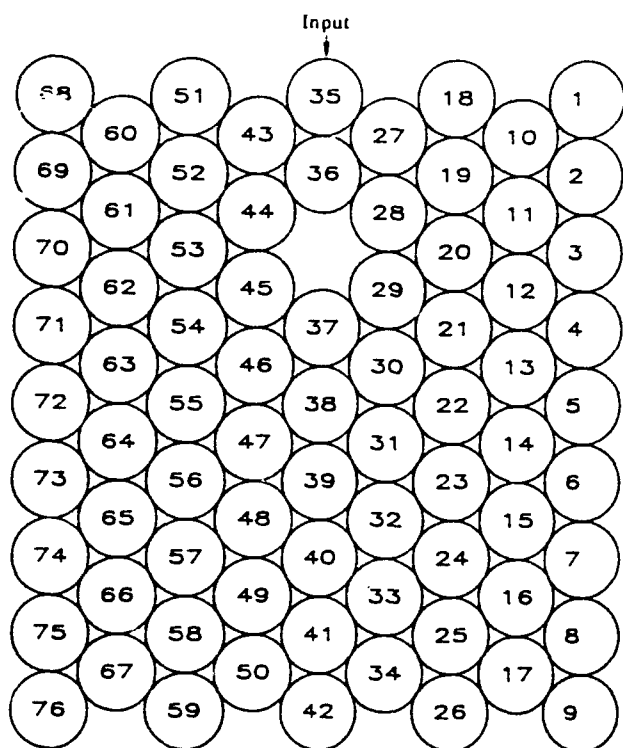
Fig. 2.13　A hexagonal close packing assembly with a void

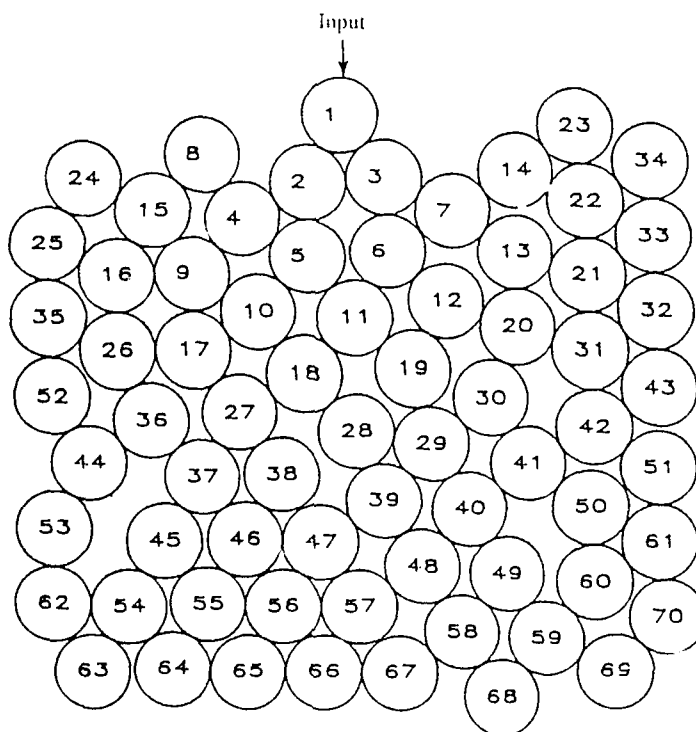Fig. 2.14　A hexagonal close packing assembly with three voids

Fig. 2.15　A random assembly

CHAPTER 3

APPLICATION OF STRAIN GAGES TO STUDY CONTACT LOADS
IN GRANULAR PARTICLES

3.1. INTRODUCTION

The study of contact load and wave propagation in granular materials is of importance in many areas of technology. These include powder metallurgy, earthquake engineering and soil mechanics etc.. The granular materials, such as sand, rock and clay, are often modeled as aggregate assemblies of disks or spheres interacting only through contact mechanisms. Wave propagation and load transfer in such materials are strongly dependent on their microstructures. An excellent review article by Deresiewicz (1958) presents both static and dynamic studies prior to 1958. Another more recent review article by Krizek (1971) presents the dynamic response of cohesionless granular soils.

The concept of modeling granular media as an array of elastic particles (eg. spheres or disks) lead to the initial attempts at predicting wave propagation through such media. Early work by Iida (1939), Takahashi and Sato (1949), Hughes and Cross (1951), Hughes and Kelly (1952), Gassmann (1951) and Brandt (1955) employed a normal granular contact force concept. This initial work investigated the propagation velocity as a function of confining pressure, particle size and aggregate geometry. It was discovered however, that the classical theory of contact due to only normal forces, does not in general accurately model real materials. With this in mind, Duffy and Mindlin (1957), proposed a theory for granular media which includes both normal and tangential contact loads. This theory produced a nonlinear and inelastic stress-strain relation. A considerable amount of work has been done to try to determine the elastic constants of particular granular assemblies, see for example, Hendron (1963), Petrakis and Dobry (1986,1988) and Walton (1987).

With regard to experimental work, the method of photoelasticty has been employed to study the behavior of granular materials. Photoelasticity was first used for granular media by Drescher and De Josseling De Jong (1972), while later work includes Derescher (1979) and Durelli and Wu (1983). This work was however only for the static behavior case. Dynamic analysis of granular media employing photoelasticity was first

reported by Rossmanith and Shukla (1982) and Shukla and Damania (1987). Later studies by Shukla et. al. (1988a,1988b) further investigated the use of dynamic photoelasticity using high speed photography to record wave propagation through various assemblies of birefringent disks.

In this paper, strain gages were employed to study contact loads, wave propagation and dynamic load transfer in granular media which was simulated using one and two dimensional assemblies of circular disks. The strain gages were placed on disks to obtain the two parameters namely, the half contact length b and friction factor β which control the stress field near the contact point. Using this data the normal and tangential contact loads were obtained by integrating the contact stresses along the contact length. By putting the strain gages at different locations in the aggregate assembly of circular disks the wave velocity and amplitude attenuation were also obtained. The static experiments were conducted first and the experimental results showed good agreement with similar results obtained from photoelasticity. Strain gages were then applied to dynamic contact problem and the results again compared with dynamic photoelasticity.

3.2 THEORETICAL ANALYSIS

The problem of contact of elastic bodies under normal loading was first solved by Hertz (1881). This problem was further studied by many researchers (Morton and Close, 1922, Thomas and Hoersch, 1930, Coker and Ahmed, 1921). The effect on the stresses due to the presence of a tangential load, however was not taken into consideration by investigators until 1939, when Lundberg (1939) developed a general theory of elastic contact between two semi-infinite bodies. Mindlin (1949) investigated the distribution of tangential load across the area of contact where one elastic body slides over the other. Smith and Liu (1953) derived the equations for the stresses σ_{zz}, σ_{xx}, σ_{yy}, and σ_{zx} at any point around the contact point. Shukla and Nigam (1985) used full field photoelastic data to evaluate the contact stresses and the contact area by utilizing the least square technique in conjunction with the Newton-Raphson method.

Fig.3.1 represents the cross section of a roller of elastic material that rests upon a flat surface of a solid elastic body. The roller is subjected to a distributed load of W Newtons per unit length, which presses it against the body over a long narrow area of contact whose width is $2b$. A lateral distributed load of f Newtons per unit length is also

54

applied to the body. Let β be defined as a friction factor such that $f=\beta W$. β will be the coefficient of friction if motion impends. The distribution of the normal and the tangential stresses will be assumed to be elliptical (Mindlin, 1949) as shown in Fig. 3.2. Smith and Liu (1953) gave the equations for the stresses σ_{zz}, σ_{xx} and σ_{zx} for points close to the contact. These equations are

$$\sigma_{zz} = -\frac{b}{\pi\Delta}\left(z(b\phi_1 - x\phi_2) + \beta z^2\phi_2\right) \tag{3.1}$$

$$\sigma_{xx} = -\frac{b}{\pi\Delta}\left[z\left(\frac{b^2+2z^2+2x^2}{b}\phi_1 - \frac{2\pi}{b} - 3x\pi_2\right) + \beta\left((2x^2-2b^2-3z^2)\phi_2\right.\right. \tag{3.2}$$

$$\left.\left. + \frac{2\pi x}{b} + 2(b^2-x^2-z^2)\frac{x}{b}\phi_2\right)\right]$$

$$\sigma_{zx} = -\frac{b}{\pi\Delta}\left[z^2\phi_2 + \beta\left((b^2+2x^2+2z^2)\times\frac{z}{b}\phi_1 - 2\pi\frac{z}{b} - 3xz\phi_2\right)\right] \tag{3.3}$$

where ϕ_1 and ϕ_2 are defined as

$$\phi_1 = \frac{\pi(M+N)}{MN\sqrt{2MN+2x^2+2z^2-2b^2}} \quad , \quad \phi_2 = \frac{\pi(M-N)}{MN\sqrt{2MN+2x^2+2z^2-2b^2}}$$

$$M = \sqrt{(b+x)^2+z^2} \quad , \qquad N = \sqrt{(b-x)^2+z^2}$$

$$\Delta = \frac{1}{A}\left(\frac{1-v_1^2}{E_1} + \frac{1-v_2^2}{E_2}\right)$$

$$A = \frac{1}{2}\left(\frac{1}{R_1} + \frac{1}{R_2}\right).$$

Subscripts 1 and 2 refer to the two bodies making the contact. R1 and R2 are radii of curvature at the point of contact. E is the modules of elasticity and v is the Poisson's

ratio. The two unknowns in the stress field equations are b and β. Other parameters depend on the geometry of the bodies, location coordinates and material properties. Therefore, two strain gages can be employed to find the two unknowns namely, half contact length b and friction factor β.

3.2.1 Frictionless Contact Problem

At some contact points within the assembly of disks, the tangential contact load is considerably less than the normal contact load (for example, in a single chain assembly of circular disks). Thus, the friction factor β in the Hertz contact stress equations can be considered to be zero. Then eqs. (3.1), (3.2) and (3.3) become

$$\sigma_{zz} = -\frac{bz}{\pi\Delta}(b\phi_1 - x\phi_2) \tag{3.4}$$

$$\sigma_{xx} = -\frac{bz}{\pi\Delta}\left(\frac{b^2 + 2z^2 + 2x^2}{b}\phi_1 - \frac{2\pi}{b} - 3x\pi_2\right) \tag{3.5}$$

$$\sigma_{zx} = -\frac{bz^2\phi_2}{\pi\Delta} \tag{3.6}$$

In the eqs. (3.4),(3.5) & (3.6), there is only one unknown, the half contact length b. From the stress-strain relation of a plane stress problem we have

$$\varepsilon_{zz} = \frac{1}{E}(\sigma_{zz} - \nu\,\sigma_{xx}) \tag{3.7}$$

In eq. (3.7) ε_{zz} is the strain value which can be obtained by using a strain gage located at any position of x and z.

When two circular discs with the same radius R and the same material are in contact, on the z axis, that is, x=0, the expressions for ϕ_1, ϕ_2, A, B and Δ can be simplified as below:

$$M = N = \sqrt{b^2 + z^2}$$

$$\phi_1 = \frac{\pi}{z\sqrt{b^2 + z^2}}, \qquad \phi_2 = 0$$

$$\Delta = \frac{2R(1 - \nu^2)}{E}$$

Therefore the stresses σ_{zz}, σ_{xx} and σ_{zx} will be further simplified as

$$\sigma_{zz} = -\frac{b^2}{\Delta\sqrt{b^2 + z^2}} \tag{3.8}$$

$$\sigma_{xx} = -\frac{b^2 + 2z^2}{\Delta\sqrt{b^2 + z^2}} + \frac{2z}{\Delta} \tag{3.9}$$

$$\sigma_{zx} = 0 \tag{3.10}$$

Substituting eq. (3.8) & (3.9) into eq. (3.7) results in the following expression

$$\varepsilon_{zz} = -\frac{1}{E}\left[\frac{(1 - \nu)b^2 - 2\nu z^2}{\Delta\sqrt{b^2 + z^2}} + \frac{2\nu z}{\Delta}\right] \tag{3.11}$$

In eq. (3.11) ε_{zz} is the strain value from the strain gage and the half contact length b on the right side of the equation is the only unknown. Thus, if the strain gage is placed at $x = 0$ and some distance z away from the contact point, then the half contact length b can be determined numerically as follows. Move the right side of eq (3.11) to the left we have a new function $f(b)$ as below

$$f(b) = \varepsilon_{zz} + \frac{1}{E}(\sigma_{zz} - \nu\sigma_{xx}) \tag{3.12}$$

For a given value of strain ε_{zz}, say, $\varepsilon_{zz} = -3000$ microstrain, $f(b)$ will be zero for some value of b. This b will be the correct half contact length correspondent to the given strain. To find this b we can plot $f(b)$ as a function of b starting from zero (since half contact length b cannot be negative), as shown in Fig. 3.3. It can be seen from Fig. 3.3 that b is

about 0.93 mm for ε_{zz} = -3000 microstrain.

3.2.2 Contact with Friction

When the tangential contact load is not negligible β has to be obtained to determine the stress field around the contact point. Thus, there are two unknowns b & β and two strain gages have to be used to solve them.

At first, an attempt was made to solve this problem using a two-element rectangular rosette. This two-element rectangular rosette can be placed at any location of x & z with an orientation angle θ (see Fig. 3.1). The stress-strain relations can be expressed as below:

$$\varepsilon'_{zz} = \frac{1}{E}\,(\sigma'_{zz} - \nu\sigma'_{xx}) \tag{3.13}$$

$$\varepsilon'_{xx} = \frac{1}{E}\,(\sigma'_{xx} - \nu\sigma'_{zz}) \tag{3.14}$$

where σ_{zz}' and σ_{xx}' are the transformed stresses (the corresponding coordinates shown in Fig. 3.1) and they can be written as

$$\sigma'_{zz} = \sigma_{xx}\sin^2\theta + \sigma_{zz}\cos^2\theta + 2\,\sigma_{zx}\sin\theta\cos\theta \tag{3.15}$$

$$\sigma'_{xx} = \sigma_{xx}\cos^2\theta + \sigma_{zz}\sin^2\theta - 2\sigma_{zx}\sin\theta\cos\theta \tag{3.16}$$

Where σ_{xx}, σ_{zz} and σ_{zx} are given in eqs. (3.1),(3.2) & (3.3). By substituting eqs. (3.15) & (3.16) into eqs. (3.13) & (3.14), one gets

$$
\begin{aligned}
\varepsilon'_{zz} = -\frac{b}{\pi E\Delta}\Bigg\{ & (\sin^2\theta - \nu\cos^2\theta)\Big[z(b\phi_1 - x\phi_2) + \beta z^2\phi_2\Big] \\
& + (\cos^2\theta - \nu\sin^2\theta)\Bigg[z\bigg(\frac{b^2+2z^2+2x^2}{b}\phi_1 - \frac{2\pi}{b} - 3x\phi_2\bigg) \\
& + \beta\bigg((2x^2 - 2b^2 - 3z^2)\phi_2 + \frac{2\pi x}{b} + 2(b^2 - x^2 - z^2)\frac{x}{b}\phi_1\bigg)\Bigg] \\
& + 2(1+\nu)\sin\theta\cos\theta\bigg[z^2\phi_2 + \beta\bigg((b^2+2x^2+2z^2)\frac{z}{b}\phi_1 - 2\pi\frac{z}{b} - 3xz\phi_2\bigg)\bigg]\Bigg\}
\end{aligned}
$$

$$\tag{3.17}$$

$$\varepsilon_{xx}' = -\frac{b}{\pi E \Delta} \left\{ (\cos^2\theta - \nu\sin^2\theta)\left[z(b\phi_1 - x\phi_2) + \beta z^2 \phi_2\right] \right.$$
$$+ (\sin^2\theta - \nu\cos^2\theta)\left[z\left(\frac{b^2 + 2z^2 + 2x^2}{b}\phi_1 - \frac{2\pi}{b} - 3x\phi_2\right)\right.$$
$$\left. + \beta\left((2x^2 - 2b^2 - 3z^2)\phi_2 + \frac{2\pi x}{b} + 2(b^2 - x^2 - z^2)\frac{x}{b}\phi_1\right)\right]$$
$$\left. -2(1+\nu)\sin\theta\cos\theta\left[z^2\phi_2 + \beta\left((b^2 + 2x^2 + 2z^2)\frac{z}{b}\phi_1 - 2\pi\frac{z}{b} - 3xz\phi_2\right)\right]\right\}$$

$$(3.18)$$

It can be clearly seen that b & β are coupled in the nonlinear system of eqs. (3.17) & (3.18). The correct solutions of b & β are quite dependent on the accuracy of the two strains ε_{zz}' & ε_{xx}' at the same time. If a two-element rectangular rosette is placed at x=0 the strain values of ε_{zz}' & ε_{xx}' are not very sensitive to β. Various other placements of the rosettes did not yield satisfactory results and therefore, after initial tries the two-element rectangular rosette was dropped as an option.

Careful observation of eqs. (3.1) and (3.2) shows that when x is zero, the stresses σ_{zz} and σ_{xx} are independent of β since ϕ_2 will also be zero. Thus, the half contact length b found from eq (3.11) is independent of β. Therefore, for the friction problem, one of the two strain gages can still be placed at the location described in the frictionless problem to find b. Once b is known, β will be the only unknown and can be simply solved using eq. (3.17). In eq. (3.17), ε_{zz}' is the strain value from the second strain gage which is placed at the location of coordinates x & z away from the contact with an orientation angle θ (refer to Fig. 3.1 & 3.4).

3.3 EXPERIMENTAL PROCEDURE AND RESULTS

The applicability of the theoretical equations developed in the previous section for the experimental determination of half contact length, b, and friction factor, β, was next verified. The experiments involved measurements of strains using strain gages at points in the vicinity of the contact of two circular disks. The half contact length, b, and friction factor β, were then obtained from the measured strains through eqs. (3.11) and (3.17). The experimentally obtained values of b and β using strain gages were compared with the values obtained through photoelasticity technique developed by Shukla and Nigam (1985).

The disk material used in the present investigation was a birefringent brittle polyester material, Homalite-100, whose mechanical and optical properties are well characterized. The elastic constants and the experimental model geometry are shown in Fig. 3.4. The disk diameter was 65-mm and its thickness was 12.7-mm. The strain gages used in the experiments were 0.4-mm long and 0.4-mm wide and were manufactured by Micromeasurement Inc., U.S.A. The location (vertical position, z, horizontal position, x and orientation angle, θ) of the strain gages were decided after a careful consideration of the strain field around the contact so that the error in strain measurement is minimized.

3.3.1 Selection of Strain Gage Positions (x & z)

Fig. 3.5 shows the strain ε_{zz} as a function of the normal distance z from the contact for various values of half contact length b. It can be seen that steep gradients in the strain exist near the contact point. As the distance normal to the contact point increases the strain gradients reduce and the strain profiles become almost flat after z=4 mm. Thus it is important that the strain gage be placed beyond z=4 mm so as to minimize the average error due to strain gradient. On the other hand, Hertz contact stress equations are valid for a distance approximately not more than $8b$ from the contact point. Typical half contact length was about 0.6 mm - 1 mm. Thus to meet the above constraints the strain gage must be placed at a distance between 4 mm to 8 mm from the contact point. In this investigation z=5 mm was chosen for the first strain gage placement.

In order to find the friction factor β the second strain gage has to be placed at a position where the strain should be sensitive to the value of the friction factor β. Fig. 3.6 shows the strain distribution of ε_{zz} along z=5 mm cross section for various values of β and b=1 mm. It is found that the strain ε_{zz} becomes sensitive to β after x=4 mm. Thus the location of the second strain gage was chosen to be z = 5-mm and x = 5-mm.

3.3.2 Selection of Strain Gage Orientation (θ)

It has been shown previously in eq. (3.11) that the strain ε_{zz} from the first strain gage with orientation angle $\theta = 0°$ is only related to the half contact length b. Thus the two unknowns b and β in Hertz contact stress equations are uncoupled. To take the advantage of this the orientation angle θ for the first strain gage was chosen to be $\theta = 0°$.

The strain ε_{zz}' from the second strain gage is plotted as a function of orientation

angle in Fig. 3.7. This Fig. shows that the second strain gage should be oriented at 45° to obtain maximum sensitivity with regard to friction factor β. For a 0.1 difference of the value of friction factor, the variation of strain can be as high as 180 microstrain ($b = 1$ mm). Thus the orientation angle for the second strain gage was chosen to be $\theta = 45°$.

3.3.3 Effect of Strain Gage Size

Since the strain gage has a finite size it averages the strain over its grid area. Therefore the measured strain will be different from the value of the center of the gage. This average error may be defined as $(\varepsilon_c - \varepsilon_{av})/\varepsilon_c$ where ε_c is the strain at the center of the gage grid and ε_{av} is the average strain over the entire grid area. ε_{av} was obtained by taking average of strains calculated at 121 points uniformly spread (11 X 11) over the entire gage grid area. Fig. 3.8 shows the average error for different gage lengths but a fixed aspect ratio of L/W = 1. The figure shows that if the gage length L is less than .5 mm the average error will be smaller than 1%. Thus the strain gage EA-06-015CK-120 with L = W = 0.4 mm was used in this study.

Thus, all the details about the location and orientation of the strain gages were finalized and are as follows:

	First strain gage	Second strain gage
Vertical position,	z = 5 mm	z = 5 mm
Horizontal position,	x = 0 mm	x = 5 mm
Gage orientation,	$\theta = 0°$	$\theta = 45°$
Gage length,	L = 0.4 mm	L = 0.4 mm
Gage width,	W = 0.4 mm	W = 0.4 mm

Theses value of different parameters were used for the actual measurements.

3.3.4 Strain Measurements and Determination of Half Contact Length & Friction Factor

3.3.4.1 Static Loadings

The experimental model shown in Fig. 3.4 was used for the measurement of strains and for the determination of half contact length and friction factor for static loadings. Two strain gages were mounted near the contact point at the locations and orientations given above. The disk (shown in Fig. 3.4) was loaded in the Instron machine. The strains from the two strain gages were recorded while photoelasticity technique was

61

employed simultaneously for comparison. The half contact length and friction factor were then determined using eq. (3.11) & (3.17). The values of half contact length and friction factor obtained from both the strain gages and photoelasticity for different loads are shown in Fig. 3.9. It was found that the values from the strain gages agree very well with the result from photoelasticity.

3.3.4.2 Dynamic Loadings

Dynamic loading was achieved by detonating a small mount of explosive on top of the experimental model. Since the wavelength of the loading pulse is much larger than the disk size there is quasi-static loading around the contact zone during the wave propagation event (Shukla and Damania, 1987). Thus, the static Hertz contact theory still can be used for the dynamic case. The dynamic strain recordings shown in Fig. 3.10 were substituted into eq. (3.11) & (3.17) to find the half contact length and friction factor. Fig. 3.11 shows the half contact length b increase and decrease with the passage of the wave while the friction factor keeping a constant around 0.25. The experiment with same geometrical arrangement and loading condition was repeated utilizing dynamic photoelasticity and high speed photography. Four out of twenty pictures are shown in Fig. 3.12 and the experimental results are plotted in Fig. 3.11.

3.3.5 Application of Strain Gage Method to Wave Propagation in Granular Media

Several strain gages were mounted at different locations in a single chain model consisting of 100 Homalite-100 disks with one inch (25.4 mm) diameter and 1/4 inch (6.35 mm) thickness as shown in Fig. 3.13. The typical dynamic contact strain profiles as obtained from strain gages are shown in Fig. 3.14. From these strain profiles the wave velocity, wave length and wave amplitude attenuation can be found as follows.

3.3.5.1 Wave Velocity

From the recorded strain profile data, wave velocity was calculated using the equation below

$$V = \frac{L}{t} \tag{3.19}$$

where V is wave velocity, L is the distance between any two strain gages and t is the travelling time of the wave from strain gage 1 to strain gage 2. The wave velocity also

can be found by plotting the wave front as a function of time from all the strain gage data as shown in Fig. 3.15. The slope in Fig. 3.15 gives the wave velocity which is about 987 m/s for thi.. experiment. This wave velocity is almost same as the one obtained by Shukla Damania (1987) using dynamic photoelasticity and high speed photography.

3.3.5.2 Wave length

The wave length λ can be obtained from the equation

$$\lambda = V T \tag{3.20}$$

where T is the wave duration which is the width of the strain profile. It was found that the wave length λ is about 100 mm which again compares well with dynamic photoelasticity results.

3.3.5.3 Wave Amplitude Attenuation

As mentioned before, the dynamic contact load can be obtained from the strain gage data. This load was obtained and is plotted as a function of propagational distance in Fig. 3.16. Due to the internal losses within the granule, energy spent in closing the contact and some frictional and reflection effects, the peak contact load decreases continuously as the wave propagates through the model. For a normalized propagational distance of X/D = 50 (X is the propagational distance and D is the disk diameter), this load drop is around 50%.

3.4. SUMMARY

A simple experimental procedure is developed to study static and dynamic contact loadings in granular assemblies. Theoretical equations for the strain field in the vicinity of the contact point between two disks are critically evaluated to obtain the optimum orientation and location of the strain gages to find the half contact length b and friction factor β. The comparison of experimental results from strain gage and photoelasticity is quite good for static loading as well as dynamic loading. Application of this strain gage method to wave propagation in granular media also shows good agreement between the results from strain gage technique and dynamic photoelasticity. The high speed photography systems are generally limited to few discrete points and field of view whereas the strain gage technique has no limit in time and space. Thus, the strain gage technique has a tremendous potential for appl·~ation in the area of wave propagation in

granular media, especially for those cases where the wavelength of the loading pulse is long and in cases where the granular assembly size is large.
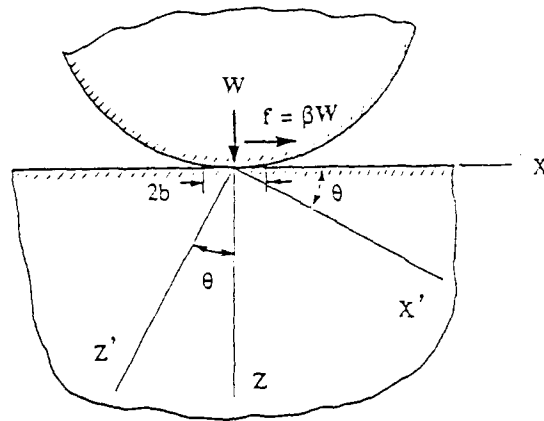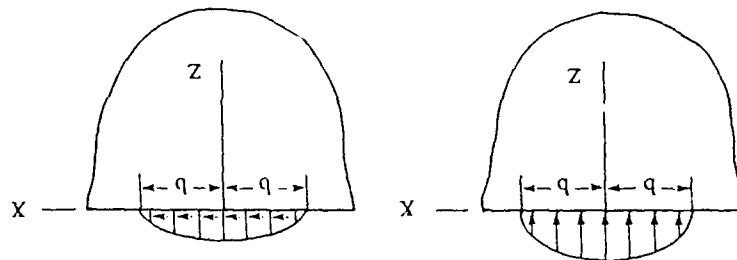
Fig. 3.1 A roller resting upon a flat surface

Fig. 3.2 Elliptical distribution of the normal and tangential stresses
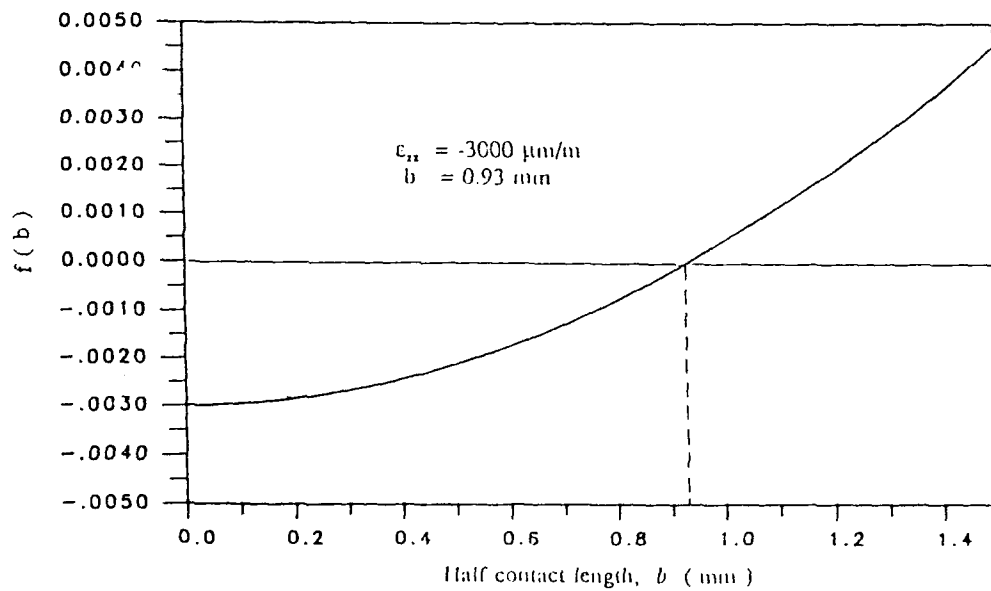

ε_{zz} = -3000 μm/m
b   = 0.93 mm

Fig. 3.3 Numerical search of half contact length b for a given
value of ε_{zz}

Disc diameter: D=65 mm
Disc thickness: h=12.7 mm
Disc material: Homalite 100
Material properties: E=3860 MPa
ν=0.35
f_σ=25.5 KN/m

■ strain gage

120°

D = 65 mm

5 mm
5 mm

P
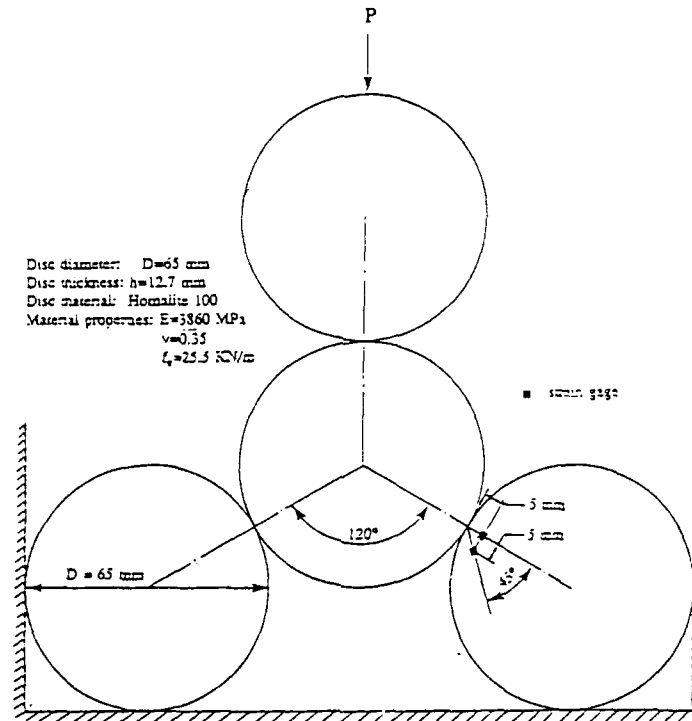
Fig. 3.4 Experimental model geometry
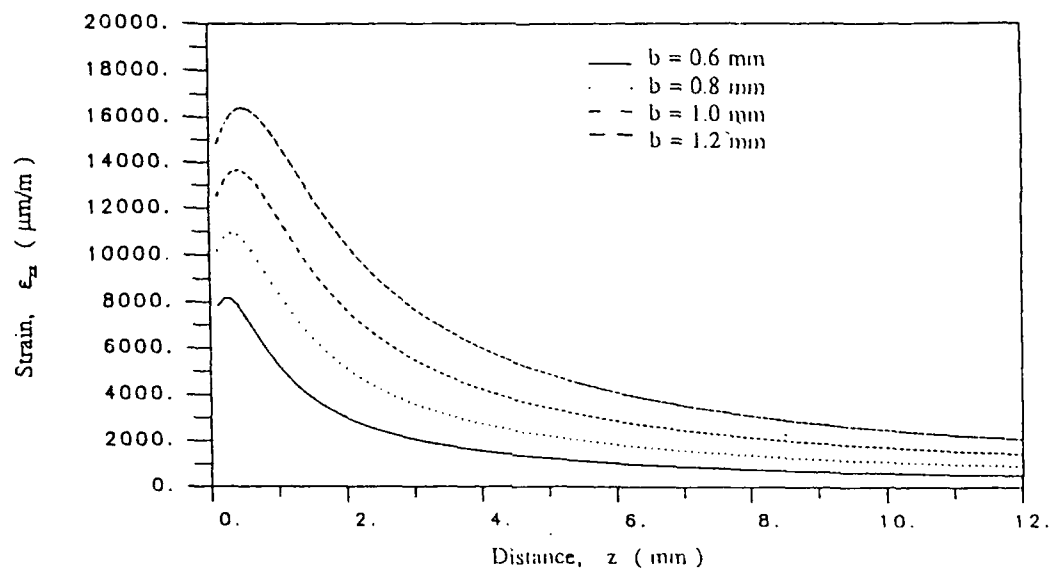
Fig. 3.5 Strains along the normal to the contact

66
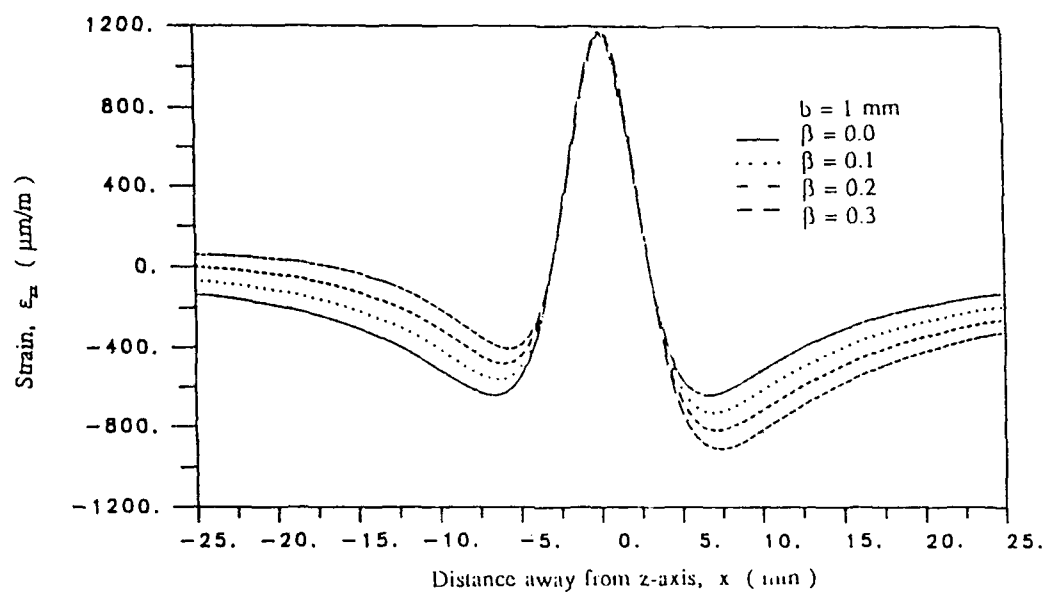
Fig. 3.6 Strain distribution along z=5 mm crosssection
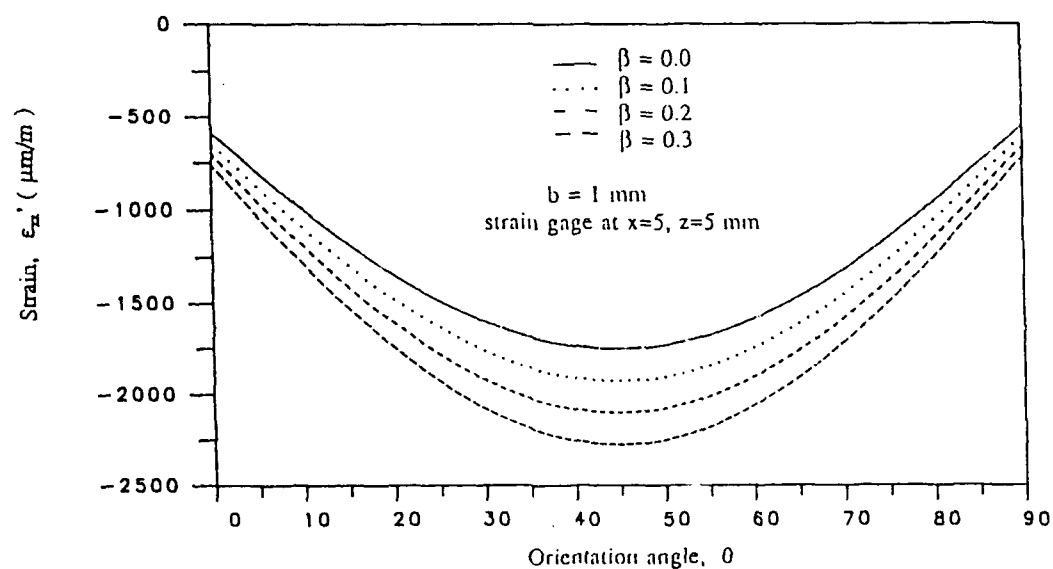
Fig. 3.7 Strains for various orientation angles

67
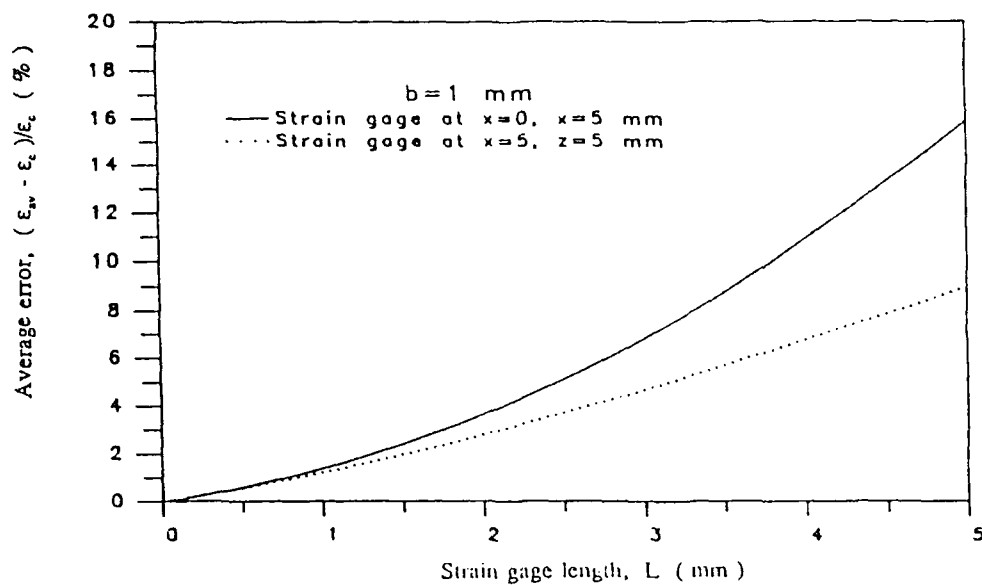
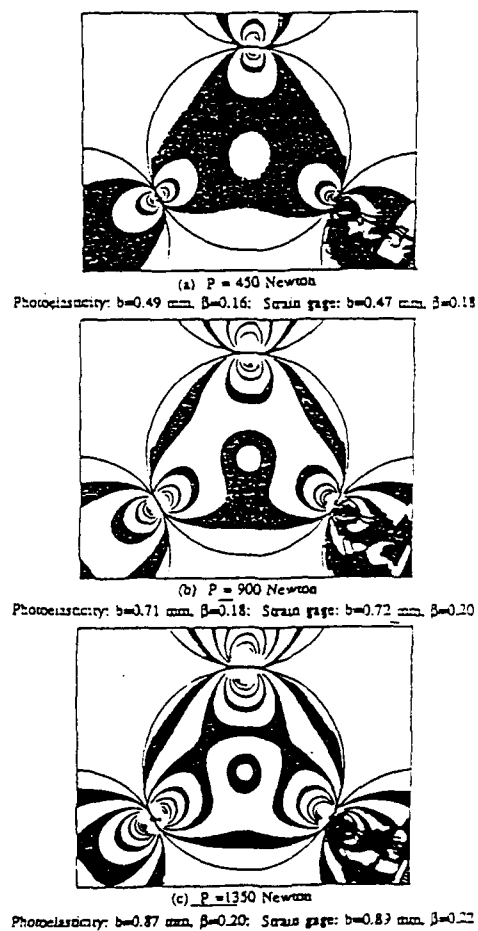Fig. 3.8 Average error as a function
of strain gage length

(a) P = 450 Newton
Photoelasticity: b=0.49 mm, β=0.16: Strain gage: b=0.47 mm, β=0.18

(b) P = 900 Newton
Photoelasticity: b=0.71 mm, β=0.18: Strain gage: b=0.72 mm, β=0.20

(c) P = 1350 Newton
Photoelasticity: b=0.87 mm, β=0.20: Strain gage: b=0.83 mm, β=0.22

Fig. 3.9 Comparison of experimental results from strain gages
and photoelasticity

68
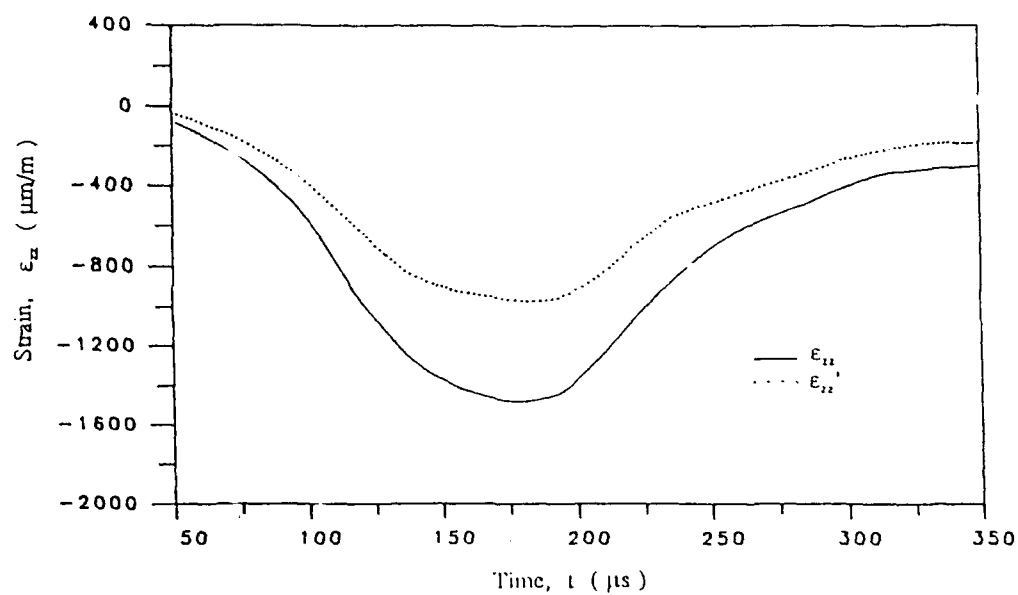
Fig. 3.10 Dynamic strain profiles
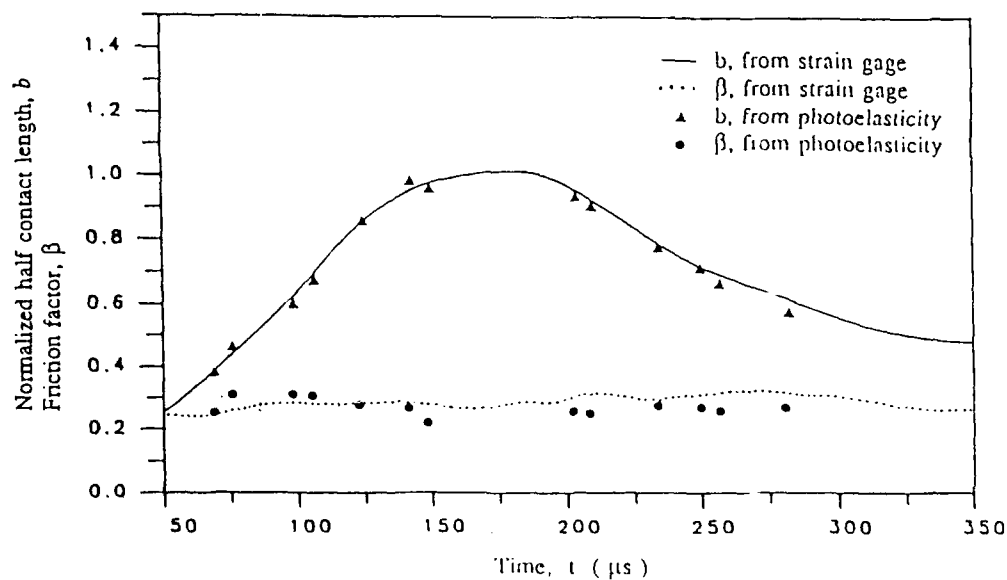
Fig. 3.11 Half contact length b and friction factor β as a
function of time

69

Frame 4, t = 58 μs

Frame 6, t = 92 μs

Frame 9, t = 134 μs
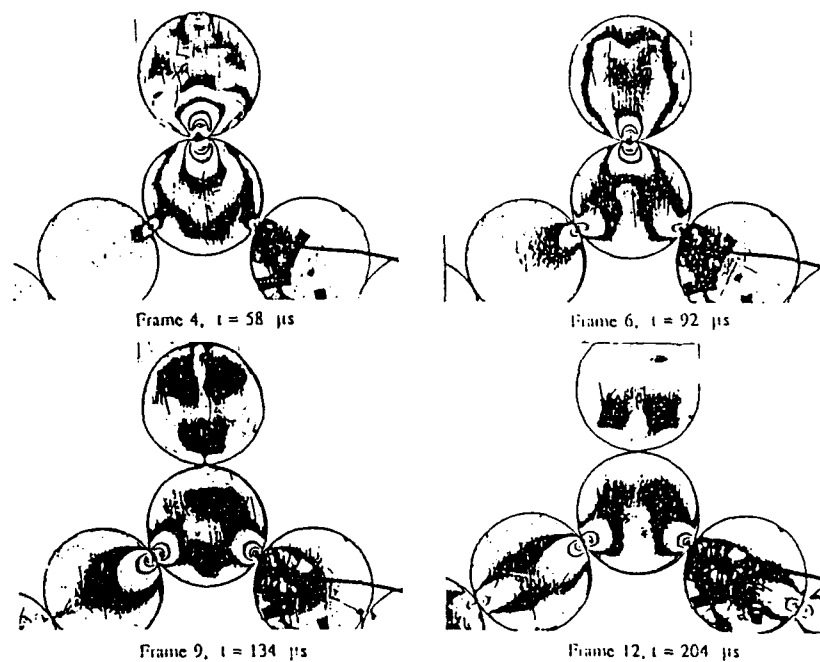
Frame 12, t = 204 μs

Fig. 3.12 Dynamic isochromatic fringe patterns in a mixed mode
contact problem

CHAPTER 4

EFFECTS OF PARTICLE SIZE AND LOADING AMPLITUDE
ON WAVE VELOCITY

Experiments were conducted to study the velocity with which mechanical signals propagate in a granular media. In particular, the dependence of this velocity on the size of the granules as well as the wave amplitude was investigated. A numerical study was also conducted to compare with the experimental results.

4.1 INTRODUCTION

This study primarily deals with the effects of particle size and the amount of explosive, on the stress wave velocity. Both the strain gage technique and dynamic photoelasticity were employed to obtain the wave velocity and its wavelength in a one-dimensional, relatively large-sized granular medium. The granular medium was simulated with a single chain of circular disks fabricated from Aluminum and Homalite 100, respectively. Different size disks, with diameters ranging from 6.4 mm to 76.2 mm (refer Table 4.1) and thickness 6.4 mm, were used in this investigation. The wave velocity obtained by both methods was found initially to increase with the increase of the disk diameter and then gradually approached a constant value. The wavelength monotonically increased with the increase of disk diameter.

4.2 EXPERIMENTAL PROCEDURE

Two groups of experiments were conducted using the strain gage technique and dynamic photoelasticity. For the strain gage experiments, the circular disks were fabricated from both Aluminum and Homalite 100 with disk diameters ranging from 6.4 mm to 76.2 mm. For the dynamic photoelasticity experiments, the disks were fabricated from Homalite 100 with diameters ranging from 6.4 mm to 71.1 mm. These disks were arranged in a single chain assembly as shown in Fig. 4.1. The assembly was loaded by exploding a small charge of explosive (LEAD AZIDE). The explosive was contained in a specially designed charge holder which was placed on top of the assembly. The stress wave generated by this loading was monitored either by strain gages or dynamic photoelasticity.

71

4.3 EFFECT OF PARTICLE SIZE ON WAVE VELOCITY

In this part of study, the disk diameter varied from 6.4 mm to 76.2 mm. However, the explosive amount was kept constant (10 mg Lead Azide) for all experiments.

4.3.1 Strain-Gage Technique

Two types of strain gages were used for this investigation. Strain gage CEA-06032UW-120 was used for larger size disks (25.4 mm diameter or above) and strain gage MA-06-008CL-120 was used for disks under 25.4 mm diameter. In each experiment two strain gages were bonded respectively on the center of two different Aluminum disks as shown in Fig. 4.1. The distance between the two strain gages was kept at 3 disk diameters in all the experiments. The first strain gage disk was located at least 4 disks away from the explosive so that the wave form was fully developed before reaching the gages. The strain gages were connected through an Ectron Model R513-5SG-16 dynamic amplifier to a Nicolet Digital Oscilloscope. A typical strain profile obtained in one of the experiments is shown in Fig. 4.2.

From the recorded experimental data, wave velocity was calculated using the equation below

$$V = \frac{L}{t} \tag{4.1}$$

where V is wave velocity, L is the distance between the two strain gages and t is the travelling time of the wave from strain gage 1 to strain gage 2. The wavelength λ was then obtained from the equation

$$\lambda = V \, T \tag{4.2}$$

where T is the wave duration (see Fig. 4.2).

The results obtained from the strain gage experiments are shown in Table 4.1. These results indicate that the wave velocity increased by almost 46% as the diameter was increased from 6.4 mm to 12.7 mm. Further increase in the disk diameter did not seem to affect the wave velocity. The variation of wave velocity as a function of disk diameter is shown in Fig. 4.3. The wavelength of the loading pulse showed a monotonic increase with the disk diameter as shown in Fig. 4.4. The reason for this is that in larger disks, reflected waves have to travel longer distances before coming back to the contact point.

72

This keeps the contact loaded for more time and as such produces larger wavelengths. It is interesting to note that the ratio of wavelength to disk diameter almost stays constant when the diameter is varied from 19 mm to 76.2 mm. This, in our opinion, is the reason why the wave velocity does not show a change for different disk diameters in this range.

4.3.2 Dynamic Photoelasticity

A multiple-spark-gap camera was used for dynamic photoelastic experiments. The one dimensional disk assembly was put in the optical bench of this camera. The camera was triggered at some prescribed delay after igniting the explosive and provided 20 photoelastic images at discrete times during the dynamic event. A typical sequence of 8 images for a single chain assembly of Homalite 100 disks with 25.4 mm diameter is shown in Fig. 4.5. These discrete images of the wave propagation phenomenon were enlarged using a Beseler enlarger. The wave front was digitized using the Hicomscan digitizer interfaced with an IBM personal computer. Thus the wave propagation distance as a function of time was obtained and a typical plot is shown in Fig. 4.6. The slope of this plot gave the wave velocity. The wavelength λ can be measured directly from the photographs of the wave propagation process shown in Fig. 4.5.

A series of experiments were conducted using dynamic photoelasticity and the experimental results are listed in Table 4.2. The wave velocity as a function of disk size is plotted in Fig. 4.3. It was found from Fig. 4.3 that the wave velocity for 6.4 mm disk is about 570 m/s while the ratio λ/D is around 11. When the disk diameter was increased to 9.5 mm, the wave velocity increased to 950 m/s. With the further increase of disk diameter, the wave velocity only increased slightly and approached a constant velocity of about 1100 m/s. The wavelength on the other hand monotonically increased with the disk diameter as shown in Fig. 4.4. Again like the aluminum disk experiments, it is interesting to note that velocity seems to be controlled by the ratio of λ/D in Homalite 100 disk experiments also.

The advantage of using dynamic photoelasticity is that the wave propagation process can be completely seen in the whole field. The photographs obtained from the experiments, showed that when the stress wave propagated inside the disk its wave front normally took the shape of the disk. Even in large size disks (71.1 mm), the body P and S-waves and the surface Rayleigh wave were not observed (except in the disks very close

73

to the explosion). The wave propagation in a granular medium is governed by contact mechanisms and the wave velocity is found to be much smaller than the dilatational wave or shear wave velocity.

4.4 EFFECT OF LOADING AMPLITUDE ON WAVE VELOCITY

A series of experiments were conducted using strain gage technique to study the effect of loading amplitude on wave velocity. The experimental setup is shown in Fig. 4.7. The disks were made of Homalite 100 with one inch diameter and four CEA-0632UW-120 strain gage were placed at four different disks as shown in Fig. 4.7. To obtain different loading amplitude various amount of explosive (Lead Azide) were used namely, 5, 10, 20, 30, 40, 50, 100 mg respectively.

Typical dynamic strain profiles obtained during the experiments are shown in Fig. 4.8. Since the strain gages were placed near the contact equation (4.4) was used to find the half contact length b. The contact load P was then calculated using the equation below given by Boresi (1978)

$$P = \frac{\pi \ h \ b^2}{2 \ \Delta} \tag{4.3}$$

Table 4.3 and Fig. 4.9 show the time of peak contact load occurring with different values of loading amplitude. It was found that with the increase of the peak load the stress wave took less time travelling from the explosion source to strain gage location. From the strain gage data the wave velocity were computed using a least square method and are listed in Table 4.4. The wave velocity in Fig. 4.10 shows about 14% increase from 940 m/s to 1070 m/s as the peak contact load increased from about 1000 to 5000 newton. Any attempt to increase peak contact load further by using more explosive resulted in the damage of disks and the strain gages.

The increase in wave velocity found from the experimental results can be explained as follows. Firstly, the larger contact load produced larger contact area and this made it easier for the wave to propagate from one particle to another one. Secondly, Homalite 100 is a strain rate sensitive material and the greater wave amplitude with the same wave duration resulted in a larger effective elastic modulus and correspondingly higher velocity.

74

4.5 NUMERICAL INVESTIGATION OF THE EFFECT OF PARTICLE SIZE ON WAVE MOTION

The distinct element method with a nonlinear-hysteretic contact law was also used to study the effect of granular size on wave motion. The input loading used was a triangular time dependent form with a duration of 20μs, and the parameters needed for calculation are given in Table 4.5 and 4.6. The numerical results of λ/D and the wave speed V are shown in Tables 4.5 and 4.6, and it is observed that the wavelength increases with the diameter of the disk. When the disk diameter $D \leq 25.4$ mm, the ratio of wavelength to disk diameter, λ/D, decreases with D; however, it remains almost a constant after $D > 25.4$mm. The distinct element results are compared with the experimental data in Fig. 4.11. Reasonably good agreement was found between theory and experiments for the prediction of the wave speed in single disk chains composed of different sized disks.

It is interesting to note that the values of a and b do not change with the ratio λ/D, and thus λ/D does not affect the hysteresis directly, though it will influence n and the ratio $\delta^{(i)}{}_r$. When λ/D decreases the value of n that represents the nonlinearity increases, and a similar behavior is noted for the parameter α_L. With the distinct element method, the wave motion is determined by the input loading, contact stiffness which is a function of n and α_L, and the mass of disk. Thus it is felt that when the ratio λ/D is subject to change both the particle geometric characteristics and the mass of the particle will have influence on the wave motion, but when λ/D is a constant the wave motion predictions will be influenced primarily by the inertia characteristics.

4.6 CONCLUSIONS

The results obtained using the experimental techniques of strain gages and dynamic photoelasticity, along with the numerical predictions from the distinct element method show that

(1) The wave velocity in granular medium initially increases with an increase of disk diameter and then approaches a constant velocity with further increases of disk size. This constant velocity is around 40%-50% of the wave velocity in a solid bar of the same material. Similar results were obtained by Iida (1939) who showed that wave velocity in granular materials was much lower than the wave velocity in bulk material.

(2) The wavelength increases monotonically with the disk diameter.

75

(3) The velocity with which dynamic signals can propagate in granular media is dependent on the ratio of wavelength to disk diameter λ/D. For larger ratios of λ/D, there are more contact points under one wave pulse, resulting in reduced stiffness of the disk chain. Therefore, as λ/D increases the wave velocity drops as shown in Fig. 4.11. Clearly as the diameter becomes very large, λ/D will approach zero and the wave velocity will reach the body wave velocity.

(4) The wave velocity increases slightly (about 14 %) with the loading amplitude.

(5) The distinct element numerical results matched well the experimental findings and specific model stiffness variations as a function of λ/D were determined.

Table 4.1 Results from Single-Chain Strain Gage Experiments
with Varying Disk Diameter (Aluminum)

Disk Diameter D(mm)	Wave Velocity V(m/s)	Wave Length λ(mm)	λ/D
6.4	1410	63	9.9
12.7	2060	74	5.8
19.0	2285	85	4.5
25.4	2275	102	4.0
31.8	2095	126	4.0
38.1	2220	159	4.2
44.8	2050	174	4.0
50.8	1970	203	4.0
57.2	2040	212	3.7
63.5	2005	263	4.1
76.2	1940	291	3.8

The wave velocity in a solid Aluminum bar is about 5090 m/s.

Table 4.2 Results from Single-Chain Photoelasticity Experiments
with Varying Disk Diameter (Homalite 100)

Disk Diameter D(mm)	Wave Velocity V(m/s)	Wave Length λ(mm)	λ/D
6.4	570	70	11.0
9.5	950	67	7.0
12.7	995	80	6.3
25.4	1070	91	3.6
31.8	1150	96	3.0
38.1*	1240	102	2.7
50.8*	1350	114	2.3
71.1	1130	227	3.2

* Results from reference |8| (different type of explosive used).
# The wave velocity in a solid Homalite 100 bar is about 2100 m/s.

Table 4.3 Distance from explosion vs. arrival time

Input peak load P (Newton)	time of peak contact load			
	d=132 mm	d=157.4 mm	d=182.8 mm	d=208.2 mm
960	t=165 μs	t=191 μs	t=221 μs	t=245 μs
1870	t=153 μs	t=178 μs	t=206 μs	t=233 μs
2500	t=150 μs	t=175 μs	t=200 μs	t=225 μs
3840	t=139 μs	t=164 μs	t=188 μs	t=213 μs
4430	t=140 μs	t=163 μs	t='88 μs	t=213 μs
4900	t=140 μs	t=164 μs	t=188 μs	t=211 μs
5440	t=138 μs	t=162 μs	t=186 μs	t=209 μs

* P is the peak contact load obtained from strain gage 1.

Table 4.4   Wave velocity due to various loading amplitude

Input peak load P (Newton)	Wave velocity V_1	V_2
960	939 m/s	800 m/s
1870	947 m/s	863 m/s
2500	1004 m/s	874 m/s
3840	1032 m/s	950 m/s
4430	1040 m/s	943 m/s
4900	1072 m/s	943 m/s
5440	1072 m/s	957 m/s

* V_1 obtained from four strain gages.

V_2 obtained by dividing the distance of the first strain gage   to explosive by the arrival time of peak contact load.

** P is the peak contact load obtained from strain gage 1.

Table 4.5 Parameters used for Homalite-100 and numerical results

D(mm)	α_L	n	a	b	λ/D	v(m/s)
6.35	2.8×10^6	1.03	0.5	0.05	7.5	577
9.525	1.5×10^7	1.1	0.5	0.05	6.0	953
12.7	3×10^7	1.15	0.5	0.05	5.4	1016
25.4	6×10^8	1.4	0.5	0.05	3.6	1080
31.8	7×10^8	1.4	0.5	0.05	3.0	1100
71.12	1×10^9	1.4	0.5	0.05	3.0	1129

Table 4.6 Parameters used for Aluminum disks and numerical results

D(mm)	α_L	n	a	b	λ/D	v(m/s)
6.35	4×10^7	1.03	0.6	0.02	7.1	1420
12.7	6×10^8	1.2	0.6	0.02	4.7	2020
19	5.5×10^9	1.35	0.6	0.02	4.0	2260
25.4	1×10^{10}	1.4	0.6	0.02	3.8	2180
44.8	1×10^{10}	1.4	0.6	0.02	3.9	2036
50.8	1×10^{10}	1.4	0.6	0.02	3.8	1992
76.2	1.1×10^{10}	1.4	0.6	0.02	3.8	1917
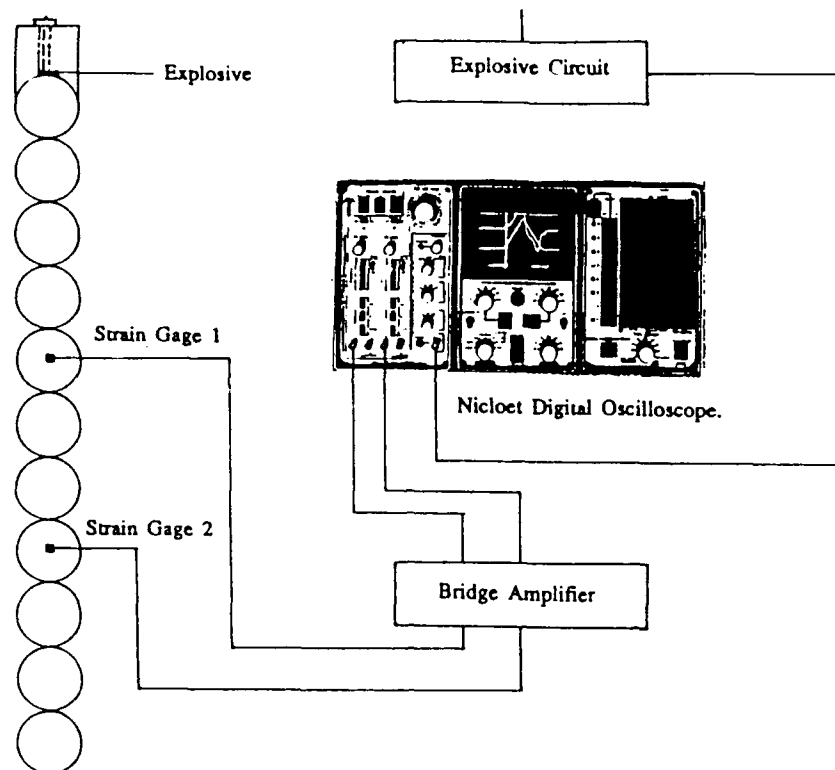
Fig. 4.1 Strain gage experimental setup for a single chain of Aluminum disks
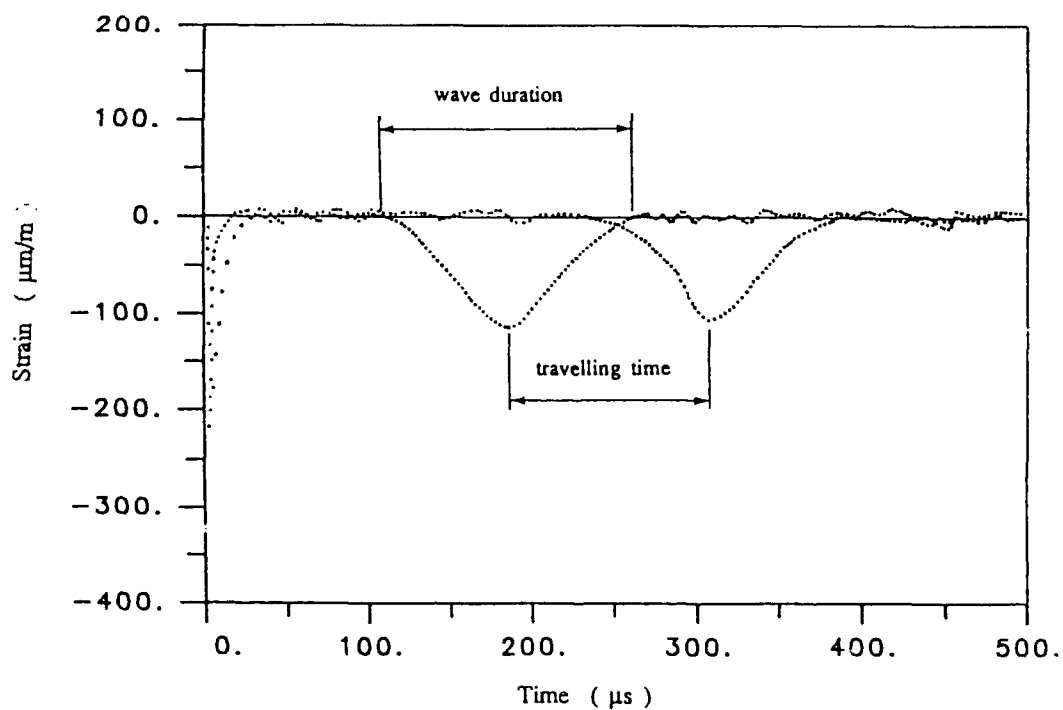
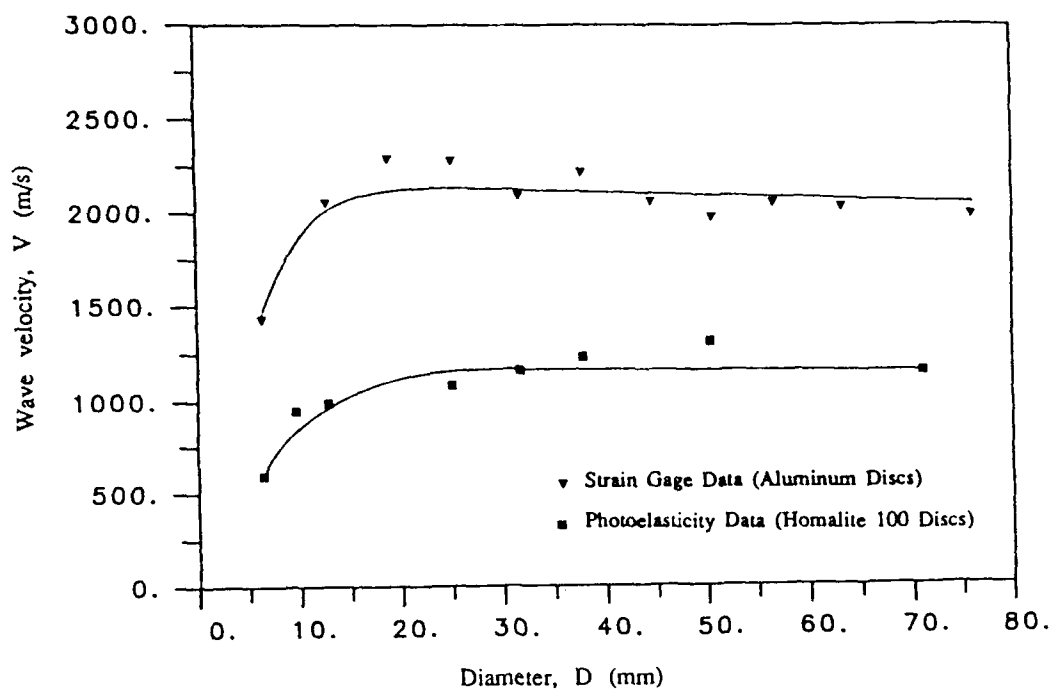Fig. 4.2 Variation of strain with time at two different aluminum discs (disc
diameter D=76.2 mm)

79
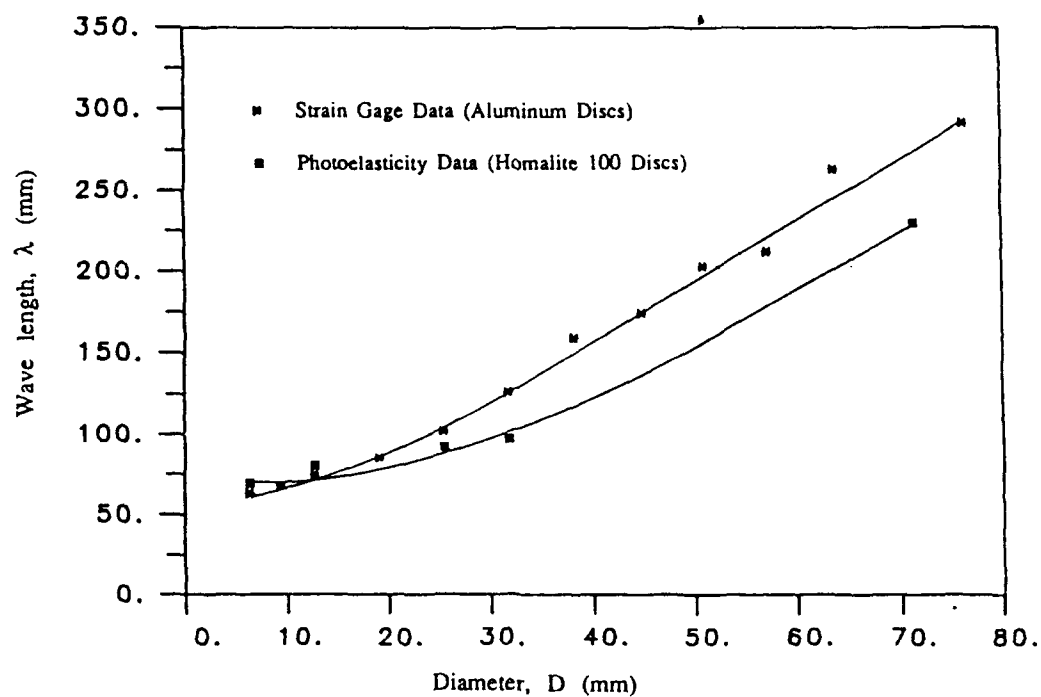
Fig. 4.3 Wave velocity V as a function of disc diameter D

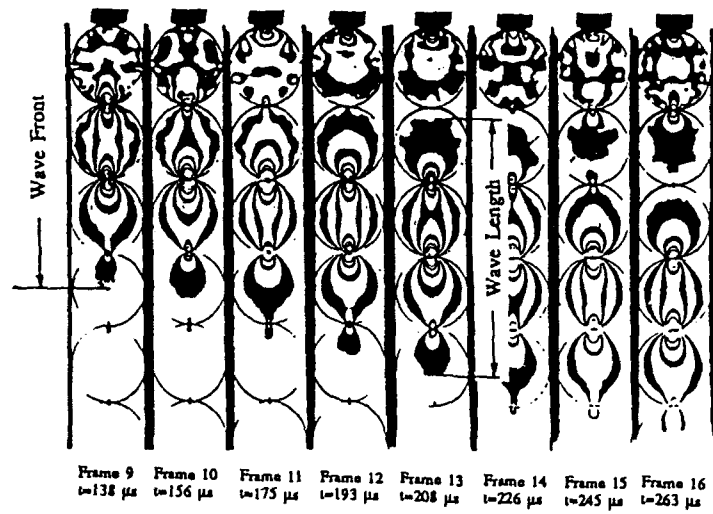Fig. 4.4 Wave length λ as a function of disc diameter D

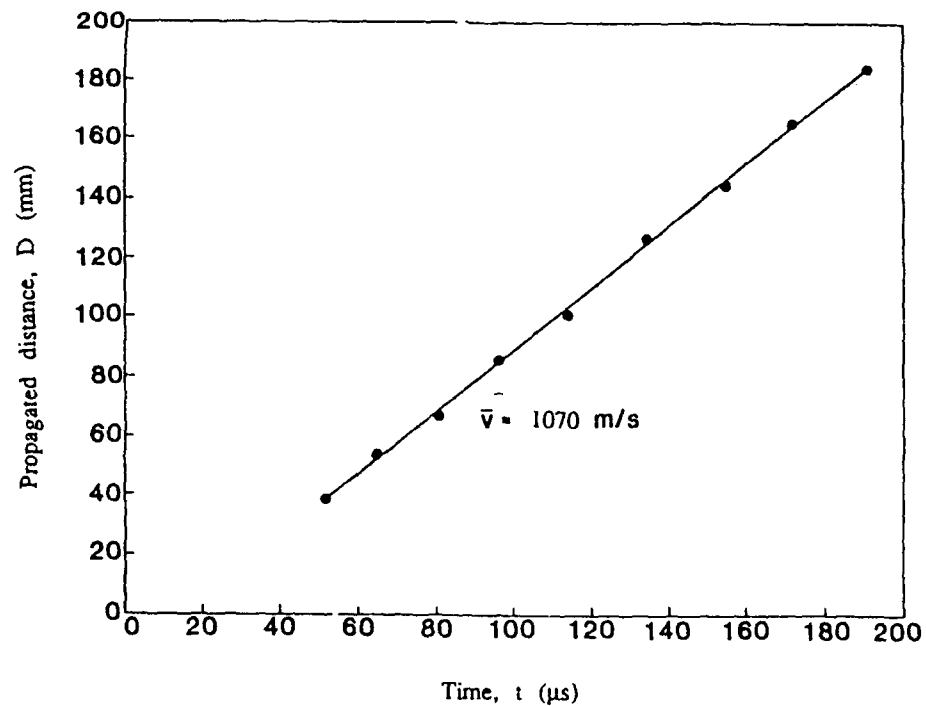Fig. 4.5 Isochromatic fringes obtained in a single chain experiment of Homalite 100 discs

Fig. 4.6 Wavefront position as a function of time for a single chain experiment of Homalite 100 discs (disc diameter D=25.4 mm)

81
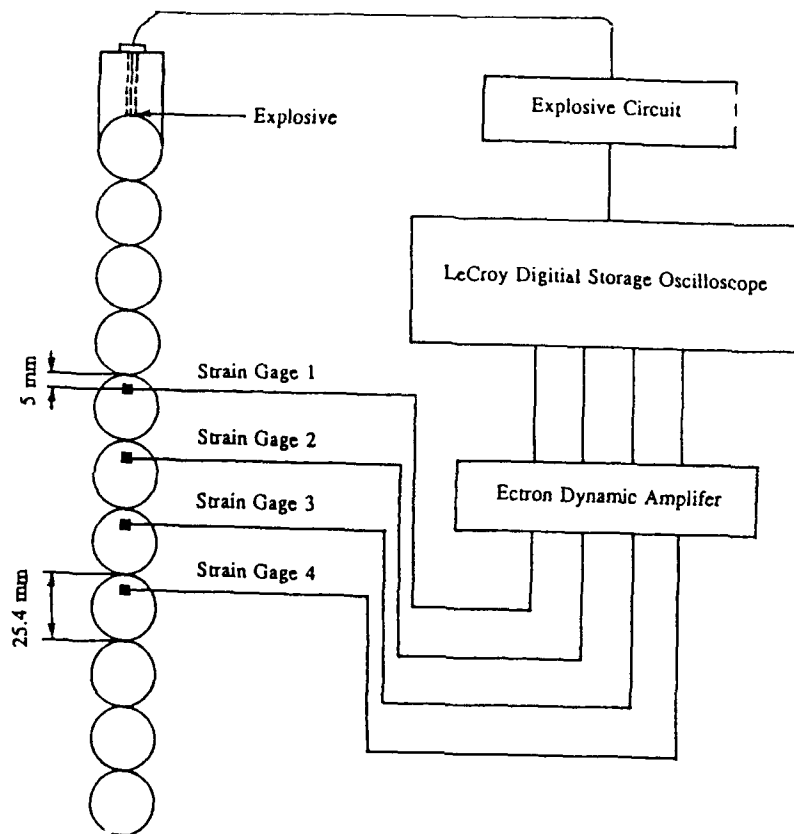
Fig. 4.7 Strain gage experimental setup for a single chain Homalite 100 discs
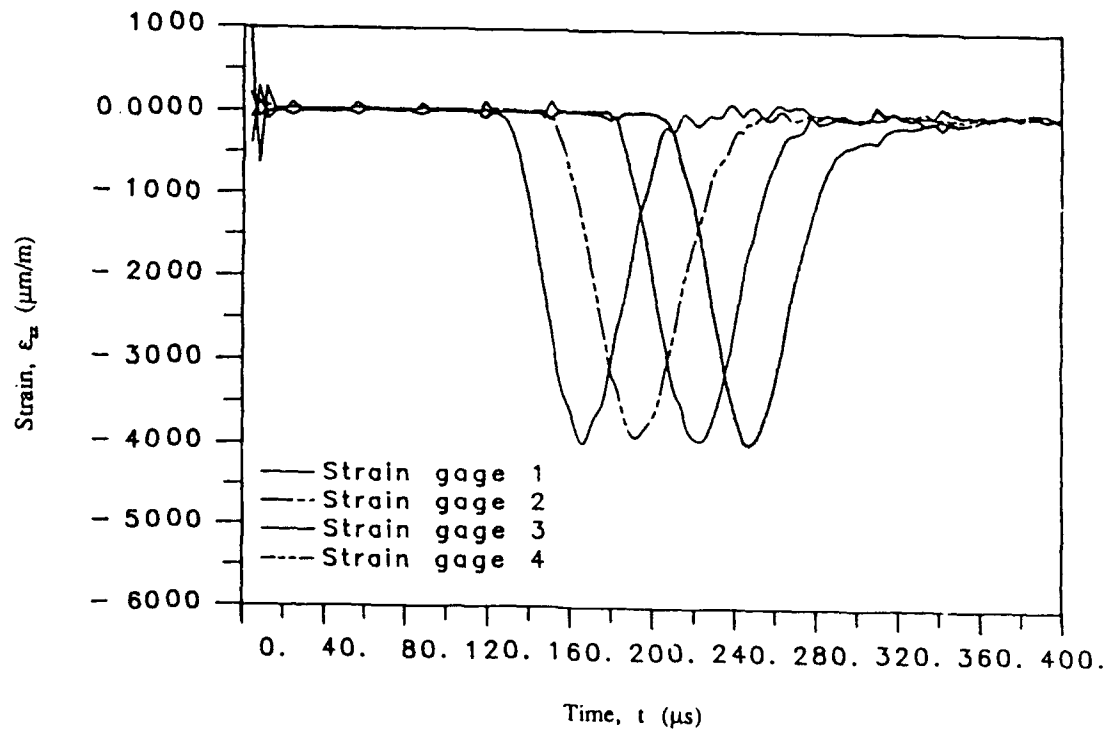
Fig. 4.8 Dynamic strain profiles
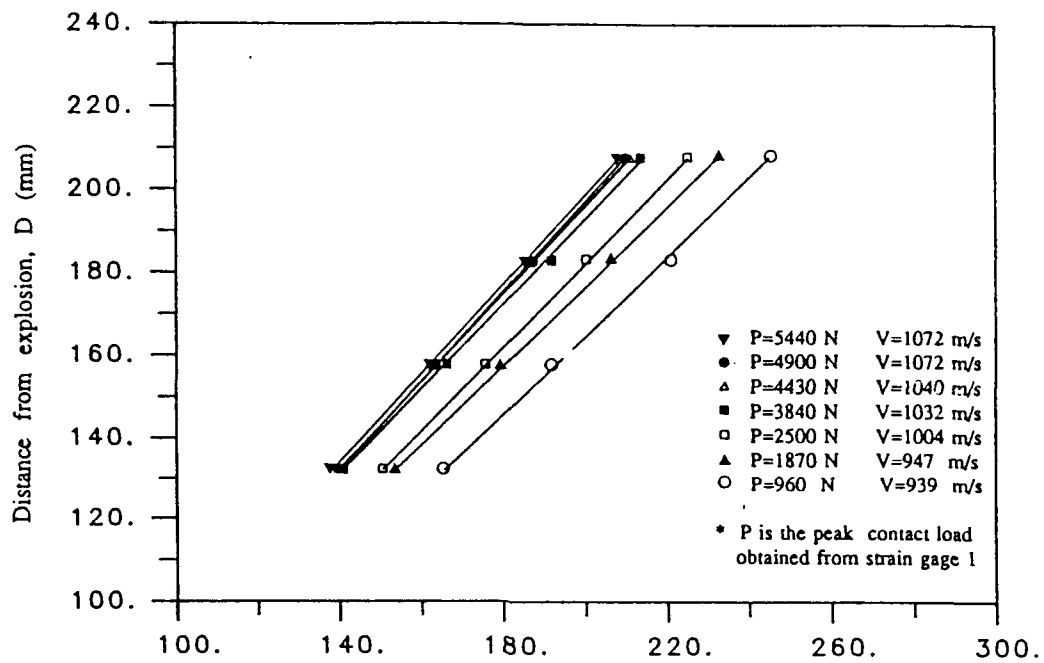
Fig. 4.9 Wavelocation due to various loading amplitudes
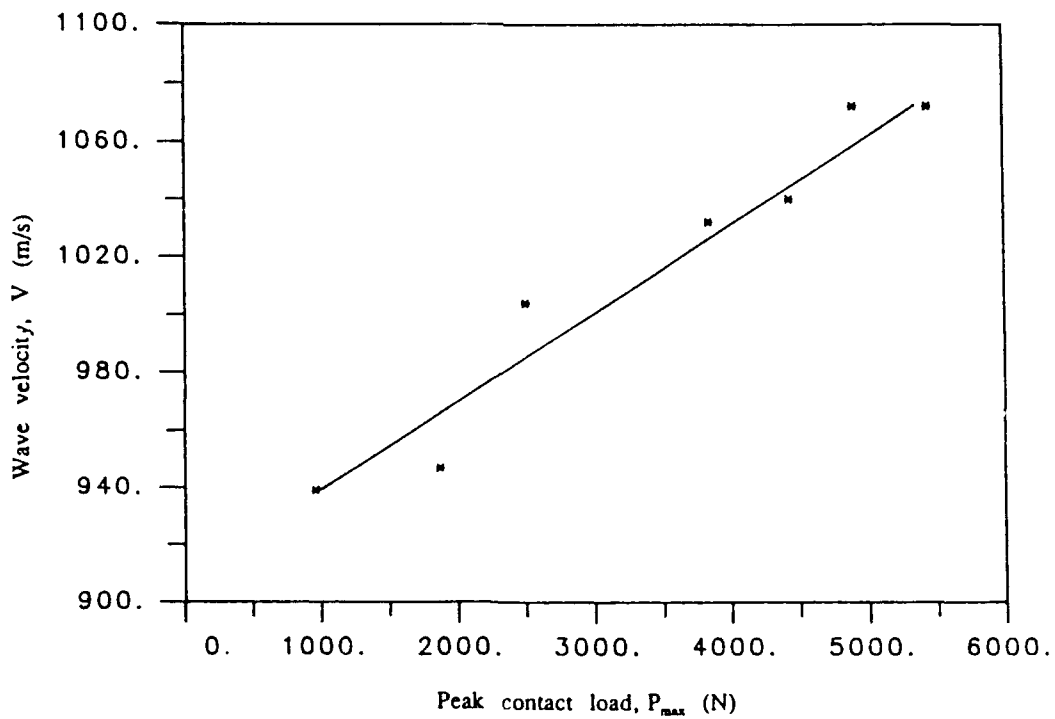
Fig. 4.10 Wave velocity as a function of loading amplitude

83
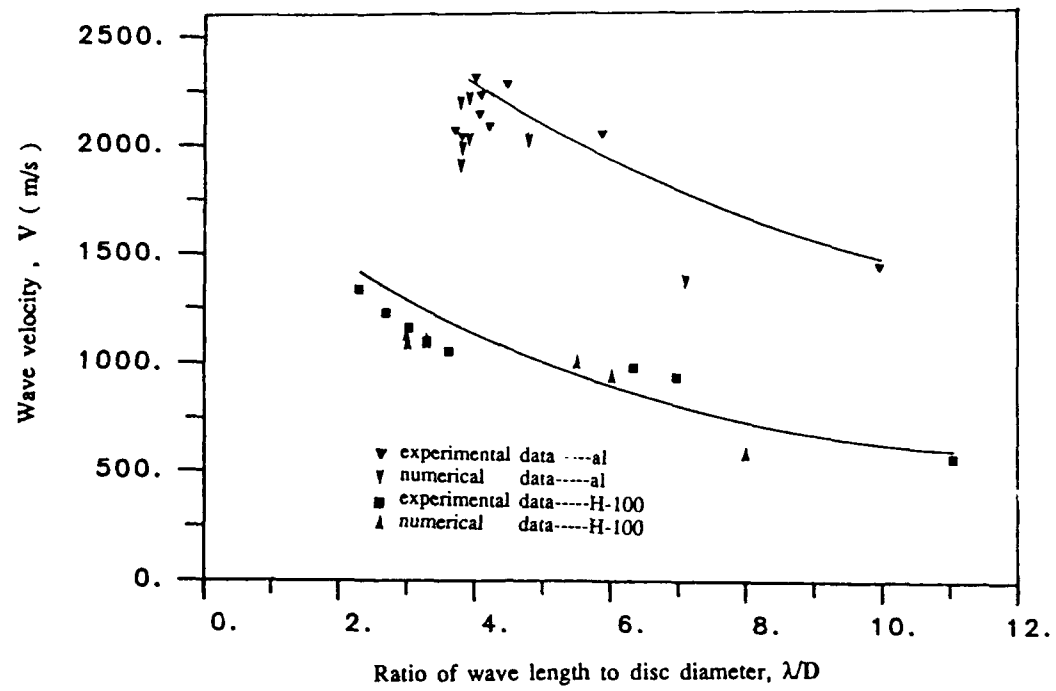
Fig. 4.11 Wave velocity V as a function of λ/D

84

CHAPTER 5

INFLUENCE OF LOADING PULSE DURATION ON DYNAMIC LOAD TRANSFER IN A SIMULATED GRANULAR MEDIUM

An experimental and numerical investigation was conducted to study the dynamic response of granular media when subjected to impact loadings with different wave lengths. The granular media was simulated by an assembly of circular disks arranged in a long straight single chain. The dynamic loading was produced by impacting a projectile from a gas gun onto one end of the granular assembly. It was found from the experiments that an input wave with a short period (about 90 μs) will propagate in this granular media with a steady amplitude attenuation. However, the long wave (period about 650 μs to 900 μs) will propagate through this granular media with first an increase of amplitude (up to 40% higher than the input) which is then followed by a decrease of amplitude. In addition, oscillation behavior was found within the main wave pulse indicating significant dispersion of the input signal. Thus there exists a fundamental change in the local propagational behavior of waves in granular media for waves with different wave length.

5.1 INTRODUCTION

The study of wave propagation in granular materials is important to many branches of science and engineering including geomechanics and powder metallurgy. Dynamic loads may occur due to earthquake motion, underground explosions, and construction operations. The ability to predict the behavior of structures and foundations necessitates the understanding of wave motion in granular media such as sand, rock, and clay. In addition, granular powders are of great importance to the forming of many solid materials which are frequently sintered by either static or dynamic compression of powders. Such sintering processes are associated with load transfer and flow of granules. Granular materials, having spatial discontinuities in their mass density, are modeled here as an array of elastic particles interacting only through contact mechanics, and wave propagation in them is strongly dependent on their microstructures. A sizeable amount of work has been done to study wave propagation in granular materials from a microstructural standpoint. Some of the earliest work is due to Ida (1939) who used a simple lumped mass-spring system. Contemporary work has proposed new modeling

approaches such as the *fabric tensor theory* (Nemat-Nasser and Mehrabadi, 1983), the *distributed body theory* (Goodman and Cowin 1972), and the *distinct element method* (Cundall, et.al., 1979) in order to predict the behavior of granular media.

Experimental techniques, such as the method of photoelasticity, have been employed to study the dynamic response of granular materials under explosive loading (Rosmanith and Shukla, 1982, and Shukla and Damania, 1987). Later studies by Shukla et.al.(1988b) using high speed photography further investigated the effects of defects, granular size, and branch angle on wave propagation caused by explosive loading in granular materials. Combining experimental techniques with numerical interpolation and the superposition principle, Zhu et.al (1989) used an experimental-numerical hybrid technique to predict the contact forces between granules in various assemblies.

The distinct element method is a computational scheme, which uses Newtonian rigid-body dynamics on each particle to simulate the wave motion in granular media. The intergranule contact mechanics are represented by assuming the granules to have a particular stiffness and damping. In this way an explicit numerical scheme is developed, and the wave motion in a large aggregate assemblies of granules can be simulated. This method has been applied by various authors (Sadd, et.al., 1989b, 1991 and Trent, 1989).

Using experimental techniques and the distinct element method, the effects of wavelength (or equivalently loading period) on the wave propagation in granular media are discussed in this paper. In the experiments, the model assembly consisted of a long straight single chain of circular discs. The simple one-dimensional assembly was chosen in order to eliminate the effect of variable direction load paths on the current wave length study. The impact loadings were produced with a projectile from a gas gun, as shown in Fig.5.1. High speed strain gage instrumentation was used to record the dynamic strain profiles caused by impact loadings. Hertz contact theory was used to convert the strain profiles into contact load profiles. In the computational study, the distinct element method was used to investigate the wave motion in the same assembly used in the experiments. Based on previous work, a nonlinear hysteretic contact law is used in the modeling. Results obtained from both experiment and computation indicate that the granular media acts like a nonlinear wave guide, propagating mechanical signals with significant dispersive characteristics. In one dimensional granular media, the dispersive phenomenon

depends on the relation of the wavelength to the particle size. For long wavelengths, wave propagational behavior shows significant differences from that for short wavelengths.

5.2 EXPERIMENTAL PROCEDURE AND RESULTS

The experimental method used in this study utilized electrical resistance strain gages to record the dynamic strain profiles as the stress wave passes through the granules. The experimental arrangement is shown in Fig. 5.1. The one dimensional granular media consists of 100 circular disks fabricated from Homalite 100 with 25.4 mm diameter and 6.35 mm thickness. The strain gages were bonded on the disks about 5 mm away from the contact point. Around the contact point Hertz contact equations are valid (Shukla, 1987). Since there is negligible friction, the stress field equations can be expressed as below

$$\sigma_{zz} = -\frac{bz}{\pi\beta}(b\phi_1 - x\phi_2) \ , \qquad \sigma_{zx} = -\frac{bz^2\phi_2}{\pi\beta} \qquad (5.1)$$

$$\sigma_{xx} = -\frac{bz}{\pi\beta}\left(\frac{b^2+2z^2+2x^2}{b}\phi_1 - \frac{2\pi}{b} - 3x\pi\phi_2\right) \qquad (5.2)$$

where ϕ_1, ϕ_2 and β are defined as

$$\phi_1 = \frac{\pi(M+Q)}{MQ\sqrt{2MQ+2x^2+2z^2-2b^2}} \ , \qquad \phi_2 = \frac{\pi(M-Q)}{MQ\sqrt{2MQ+2x^2+2z^2-2b^2}}$$

$$\beta = \frac{2R(1-v^2)}{E} \ , \qquad M = \sqrt{(b+x)^2+z^2} \ , \qquad Q = \sqrt{(b-x)^2+z^2}$$

where R is the radius of the disk, v is Poisson's ratio, and E is the elastic modulus. For a plane stress problem, we have

$$\varepsilon_{zz} = \frac{1}{E}(\sigma_{zz} - v\sigma_{xx}) \qquad (5.3)$$

If the strain gage is placed along the z-axis, that is, $x = 0$, the expressions for ϕ_1, ϕ_2 and β can be simplified and finally Eq.(5.3) can be written as

87

$$\varepsilon_{zz} = -\frac{1}{2R(1-v^2)} \left[\frac{(1-v)b^2 - 2vz^2}{\sqrt{b^2+z^2}} + 2vz \right] \qquad (5.4)$$

In Eq.(5.4) ε_{zz} is the strain value from the strain gage and the half contact length b on the right side of the equation is the only unknown. Thus, if the strain gage is placed at $x = 0$ and some known distance z away from the contact point, then the half contact length b can be obtained numerically. Once b is found the stress field can be determined and then the contact load can be obtained by numerically integrating the contact stresses along the contact length. In this study the strain gages were bonded on the disks 5 mm away from the contact points.

Short input loading

A series of experiments were conducted using the gas gun by placing an aluminum cap in front of the aluminum bar as shown in Fig. 5.1. The first strain gage was bonded on the first disk and the other three strain gages were put at various positions. Fig.5.2 shows the strain gage output due to impact loading from one of the experiments. The wave velocity was found to be around 987 m/s. The input loading pulse at disk 1 (shown in Fig. 5.2) has a duration of about 90 μs. It was found that the wave amplitude (peak inter-granular contact force) decreased steadily with propagational distance (see Fig.5.6). The wave shape remains similar with propagational distance indicating small geometrical dispersion. These results are very similar to those found by Shukla and Damania (1987) with explosive loadings.

Long input loading

To obtain a longer wavelength, a rubber type material PSM4 with 6.4 mm thickness was directly placed before the Homalite 100 disk chain before the impact from the gun. The duration of input loading was about 650 μs as shown in Fig. 5.3 (strain gage output at disk 1). The wave velocity was found to be around 950 m/s. Different from the short duration impact loadings, the wave amplitude was found to first increase and then decrease as shown in Fig. 5.6. In addition, the individual granules (disks) contribute to a ringing behavior, producing oscillations within the main wave pulse (see Fig. 5.3). By carefully observing the time interval between the oscillation peaks in given pulse it was found that this time interval increases with propagational distance. The first three time

88

intervals between peaks in one pulse were averaged and plotted in Fig. 5.4. It can be clearly seen from Fig. 5.4 that the time interval increases from 63 μs at disk 7 to 102 μs at disk 100. From this tendency of time interval increase it was found that this long period input wave tries to separate into many short waves with a time duration of around 100 μs. After the wave separation the amplitude then seems to decrease steadily. The phenomenon of increase in wave amplitude for this long duration loading can be explained by the tendency of the input wave separation. During the process of the wave separation, the leading portion of the wave gathers more energy which results in the increase of amplitude. The separated short waves seem to have a specific wave length which gives the ratio of wave length to disk diameter of about 4. This specific ratio was also found by Xu and Shukla (1990) for disks of 25 mm diameter or larger. These results imply for this material that there exists a specific ratio of wave length to disk diameter for which the wave propagation in the single chain is stable.

Additional experiments were conducted with long period impact loadings. Fig. 5.5 shows the typical strain gage output for 200 μs input wave duration. Wave separation phenomenon similar to that shown in Fig. 5.3 were also found in these experiments. For this case the wave amplitude remains almost constant for the entire propagational distance. The peak contact loads as a function of propagational distance are plotted in Fig. 5.6. From Fig. 5.6, the transition behavior of wave amplitude with the increase of wave length can be clearly seen. With the increase of input wave length to 900 μs, the maximum wave amplitude increases up to about 1.5 times the input wave amplitude. This amplitude transition phenomenon can be explained by the fact that the longer duration waves carry more energy than shorter duration waves. Thus, when the main wave separates to many short waves the leading short wave can have shorter duration and higher wave amplitude.

5.3 NUMERICAL RESULTS

The distinct element method was used to theoretically investigate the effects of wavelength on the wave propagation in the one-dimensional granular assembly used in the experiments. This numerical method models the behavior of granular assemblies through Newtonian rigid-body mechanics. The interaction between granules is determined by a particular interaction or contact law and a damping relation. The interaction forces

are related to relative displacements and velocities of the granules in contact, and the granules (disks) are allowed to overlap each other to represent contact deformation. In addition, the distinct element technique discretizes the time period during which the wave propagates into a series of time intervals. Each interval is chosen so small that during a single time step disturbances can not propagate from any disk further than its immediate neighbors, thus the granule accelerations and velocities can be considered as constants during a given step. Using a simple forward difference formula the increments of relative normal and tangential displacements can be written as

$$\Delta\delta_n = v_n\Delta t = [(v_1 - v_2)\cdot n]\Delta t$$

$$\Delta\delta_t = v_t\Delta t = [(v_1 - v_2)\cdot t - (\omega_1 R_1 + \omega_2 R_2)]\Delta t$$

(5.5)

where v_1, ω_1, and R_1 are the velocity, angular velocity, and radius of disk 1, with like notation for disk 2. The terms n and t designate normal and tangential contact unit vectors respectively, and they are shown in Fig.5.7 for disk 1. δ_n and v_n denote the relative normal displacement and velocity between adjacent disks in contact whereas δ_t and v_t are the relative tangential values. The interaction law between adjacent disks can be written as

$$F_n = F_n(\delta_n, v_n), \qquad F_t = F_t(\delta_t, v_t, \delta_n, v_n)$$

(5.6)

where F_n is the normal contact force, and F_t the tangential contact force. Using Newton's law, the acceleration for each particle is determined by the relation

$$a = \Sigma F / m.$$

(5.7)

Once the acceleration is known, the velocity follows by using the simple difference equation

$$v = a\Delta t$$

(5.8)

Equation (5.5) may be used to determine the disk displacements, and then new contact forces may be determined for the next time step using relations (5.6). In this way, the distinct element method develops an explicit numerical scheme which can be used to study the dynamic behavior of large assemblies of granules.

Previous studies have considered various forms for the contact law (Sadd et.al, 1991, 1992b). A nonlinear-hysteretic contact law was found to be more appropriate than other attempted laws in that using this law the predicted wave amplitude, wave shape, and wave velocity agreed best with experimental results. Therefore a nonlinear-hysteretic contact law is adopted in this work, and is expressed as

$$
F_n = \begin{cases}
F_{nL} = \alpha_L \delta_n^p & \text{................................} loading \\
F_{nU} = \alpha_U \delta_n^{p+q} & \text{................................} unloading,\ reunloading \\
F_{nrL} = \eta F_{nL} + (1-\eta)F_{nU} & \text{................} reloading
\end{cases}
\tag{5.9}
$$

and is shown in Fig. 5.8. Here loading indicates that the force reaches its maximum value in its history and is still increasing, and reloading is defined as the state in which the load is increasing but its value is smaller than its maximum value. The value of q is determined by

$$
q = (A\ \delta_{n\ max}^{(i)})^2
\tag{5.10}
$$

where $\delta_{n\ max}^{(i)}$ is defined as the value of δ_n at contact point i when the normal contact force at the point has attained its maximum value and A is a constant to be determined. The value of η is given by

$$
\eta = \frac{\delta_n^{(i)} - \delta_{n\ min}^{(i)}}{\delta_{n\ max}^{(i)} - \delta_{n\ min}^{(i)}}
\tag{5.11}
$$

with $\delta_n^{(i)}$ is the current value of relative normal displacement at contact point i, and $\delta_{n\ min}^{(i)}$ indicates its minimum value in the previous unloading or reunloading path. At the moment reloading begins, $\delta_n^{(i)} = \delta_{n\ min}^{(i)}$ and $\eta = 0$. The value of η increases with $\delta_n^{(i)}$, and it reaches maximum value of 1 when $\delta_n^{(i)} = \delta_{n\ max}^{(i)}$ which indicates that new loading will begin.

The value of α_L and A are related to material and geometric properties of the disks

91

and period of input loading, and p is a parameter of the disk geometry. The parameter α_U, however, is determined in order to make the unloading path initiate at the peak point of loading as shown in Fig. 5.8. The chosen numerical values of α_L, A, and p are given in Figs.5.9, 5.10, and 5.11. The experimental impact input loading was digitized as the input loading for numerical simulation.

The numerical results from the numerical model are shown in Figs. 5.4, 5.9, 5.10, 5.11, and 5.12. Fig. 5.9 shows the contact load histories at three different points for a short period loading (90 μs). The wave amplitude decreased monotonically with the distance that wave propagated. The wave dispersion is small which matches with the experimental results shown in Fig 5.2. The dynamic responses of the granular assembly to long period loadings show significant differences from the results in Fig 5.9. In Fig. 5.10 three contact load profiles at different contact points are given for the case of a 650 μs input. Like the experimental results, within a wave profile a ringing phenomenon is observed, and wave separation can be observed in the 2nd and 3rd wave profiles. The amplitudes of the ringing oscillations decrease with propagational distance whereas the time intervals of the oscillations increase. The average values of the first three time intervals of each wave profile are compared with experimental results in Fig. 5.4. Similar ringing behavior can also be observed for the cases with 200 μs (see Fig. 5.11) and 900 μs period input loadings. The normalized peak contact loads of the 90, 200, 650, and 900 μs input are presented in Fig. 5.12. From this figure it is found that, in contrast to the short input loading case (90μs), the peak contact loads here are not always smaller than the value of the input loading. Instead of decreasing monotonically the peak contact loads first increase with propagational distance, and then they begin to decrease steadily. For 650 μs input case the maximum contact load is about 1.56 times of the maximum input loading.

5.4 DISCUSSION

It is apparent from our studies that for wave inputs with periods greater than approximately 200 μs, the original smooth input signal will suffer severe dispersion as it propagates along the granular chain. In essence, the chain acts as a nonlinear wave guide, and thus the input signal will undergo significant changes in shape. The increase in amplitude and the resultant ringing behavior shown in Figs. 5.3, 5.5, 5.10, and 5.11

92

indicate that the wave energy is being rearranged within the profile due to the microstructure of the chain. In order to attempt to analyze this phenomenon, we consider the behavior of the N-disk system from the viewpoint of a standard modal analysis. In the following discussion the subscript n has been dropped for conciseness.

Using $\delta_{i,i+1}$ to denote the deformation between the i-th and $(i+1)$-th disks, R the radius of the disks, and u_i and u_{i+1} the absolute displacements of the i-th and $(i+1)$-th disks, then $\delta_{i,i+1} = 2R - (u_{i+1} - u_i)$. For a system of N disks in contact, according to Newton's law, we have

$$m\ddot{\delta}_{i,i+1} = F_{i-1,i} - 2F_{i,i+1} + F_{i+1,i+2} \tag{5.12}$$

where m is the disk mass, and $F_{i,i+1}$ the contact force between disks i and $(i+1)$ which equals $K\delta_{i,i+1}$. The stiffness K follows from Eq. (5.9) to be

$$K = 1.4\alpha^{1/1.4} F^{0.4/1.4} \tag{5.13}$$

Eq. (5.12) can be linearized as

$$\ddot{\delta}_{i,i+1} = \frac{K_0}{m} (\delta_{i-1,i} - 2\delta_{i,i+1} + \delta_{i+1,i+2}) \tag{5.14}$$

by using $K_0 = 1.4\alpha^{1/1.4} F^{0.4/1.4}_{average}$, where $F_{average}$ is a constant, and represents the average value of F. For N disks in contact, we thus have the system

$$\ddot{\Delta} + \frac{K_0}{m} A \, \Delta = 0 \tag{5.15}$$

where $\Delta = (\delta_{1,2}, \delta_{2,3}, \delta_{3,4}, ..., \delta_{N-1,N})^T$, and A is a tridiagonal matrix given by

$$A = \begin{bmatrix} 2 & -1 & & & & & \\ -1 & 2 & -1 & & & & \\ & & \cdot & \cdot & \cdot & & \\ & & & \cdot & \cdot & \cdot & \\ & & & & \cdot & \cdot & \cdot \\ & & & & -1 & 2 & -1 \\ & & & & & -1 & 2 \end{bmatrix}$$

The associated eigenvalue problem of relation (5.15) reads as

$$(\mathbf{A} - \lambda\mathbf{I}) \mathbf{X} = 0 \qquad (5.16)$$

There are $N-1$ eigenvalues of Eq.(5.16), which give the contact resonance frequencies ω_i ($i = 1, ..., N-1$), where

$$\omega_i^2 = \lambda_i K_0/m \qquad (5.17)$$

The normal mode $\mathbf{X}_i$ related to ω_i is the solution of Eq.(5.16) with $\lambda = \lambda_i$. The response of the system will be the superposition of the $N-1$ modes:

$$\Delta = \sum_{i=1}^{N-1} C_i X_i$$

Initially when the wave propagates along the chain, at the beginning, there are only two disks in contact, and thus there is only one natural frequency $\omega^2 = 2K_0/m$. At later times the number of the disks in contact increases until it reaches a certain number (about 28 for 650 μs input loading). Thus all the eigenvalues for the system from $N = 1$ to $N = 28$ were calculated. After a careful check, it was determined that all systems with even numbers of disks in contact have the eigenvalue, $\lambda = 2$. No other eigenvalue has such a property. In Fig. 5.13 the normal modes corresponding to $\lambda = 2$ are presented for systems with an even number (2k) disks in contact. In the figure dots stand for the amplitude of deformation between disks. The dot above the centerline means that two disks approach each other (deformation increases), and therefore the contact load is large. The dot below the line represents that two disks tend to separate (deformation decreases), and contact load is small. It is clear from Fig. 5.13 that the mode for k = 2 is a part of the mode for k = 3, and the mode for k = 3 is a part of the mode for k = 4 and so on. Hence once the mode related to $\lambda = 2$ is stimulated when $N = 2k$, it will be retained when $N = 2(k+1)$, and with k increasing this mode will gradually predominate over the other modes. So the approximate resonant frequency of the system will be $\omega^2 = 2K_0/m$.

Consider now the period of the resonance, τ. With $\alpha = 1.7 \times 10^8$ N/m$^{1.4}$ and $F_{average}$ = 1000 N, $\lambda = 2$ gives $\tau = 100.0$ μs. If $F_{average} = 500$ N, then $\tau = 107.8$ μs. These values

are close to the experimental results. The mode for k = 3 is a complete repeatable structure for the higher modes shown in Fig. 5.13, and it was found out that the distance between the two points with large contact load is four disks. Therefore when the resonances of the system corresponds to $\lambda = 2$, the wavelength will be of four disk diameters, which also agrees with experimental results.

It should be point out that the previous analysis has been carried out after the linearization of Eq.(5.12). The actual system, however, has nonlinear hard springs. According to nonlinear vibration theory, higher amplitudes are associated with higher resonance frequencies, which can be observed in Figs. 5.3 and 5.10.

5.5 CONCLUSION

Experimental and numerical results indicate that the granular media acts as a *nonlinear wave guide*, propagating mechanical signals with significant dispersive characteristics. For one-dimensional granular chains, the dispersive behavior depends on the relationship of the wave length to the particle size and material. For very short duration input loadings (90 μs), the wave amplitude decreases steadily with propagational distance. However, for longer duration loading, the amplitude is found to first increase and then decrease. Moreover, for loading durations of several hundred microseconds or more, individual granules (disks) contribute to a *ringing behavior*, producing oscillations within the main wave pulse. This oscillation was found to persist, thus separating the single input wave into many waves with shorter durations. Hence there exists a fundamental change in the local propagational behavior of waves in granular media for waves of varying wavelength. The ringing is found to be associated with the contact resonance. It should be noted that the observed dispersion behavior is also a function of the particle size (disk diameter).
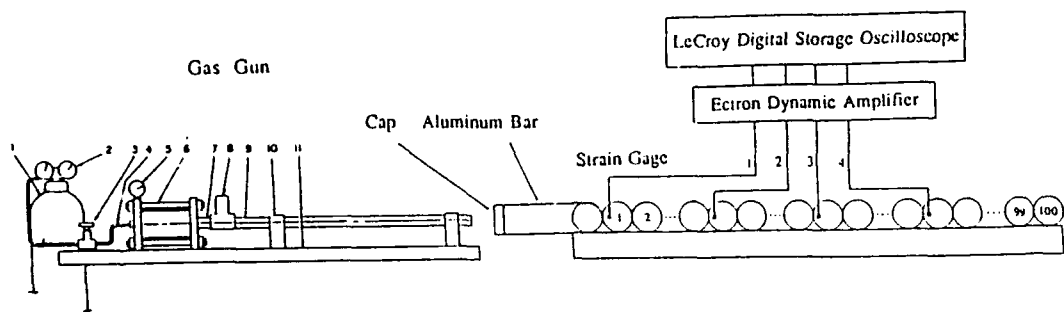
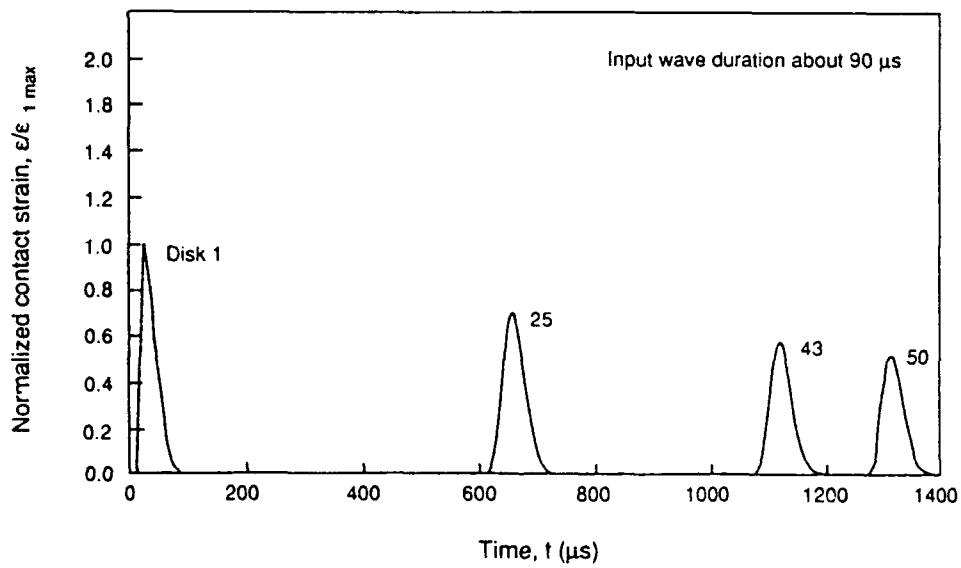Fig.5.1 Experimental setup of impact loadings

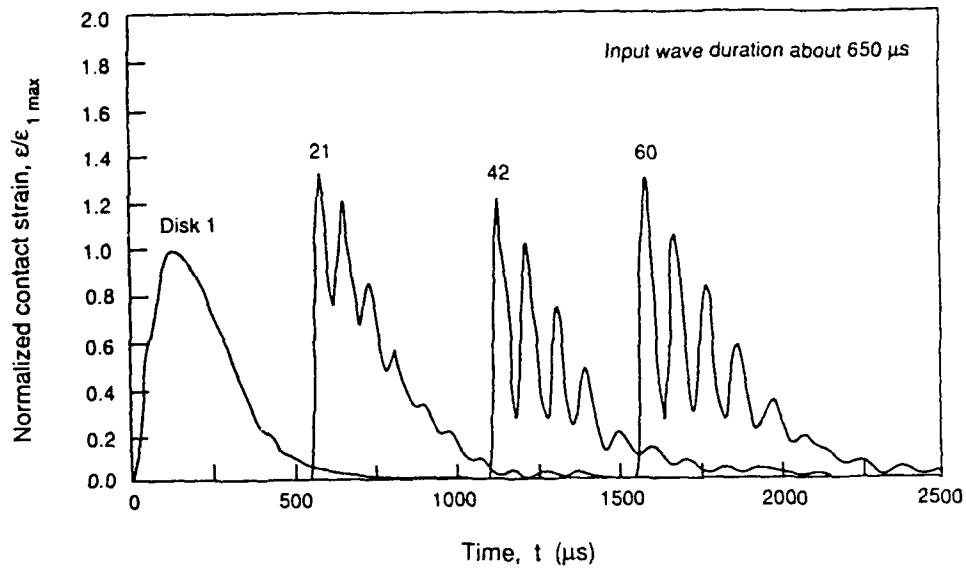Fig.5.2 Normalized strain gage output in a 1-D chain of Homalite-100 discs

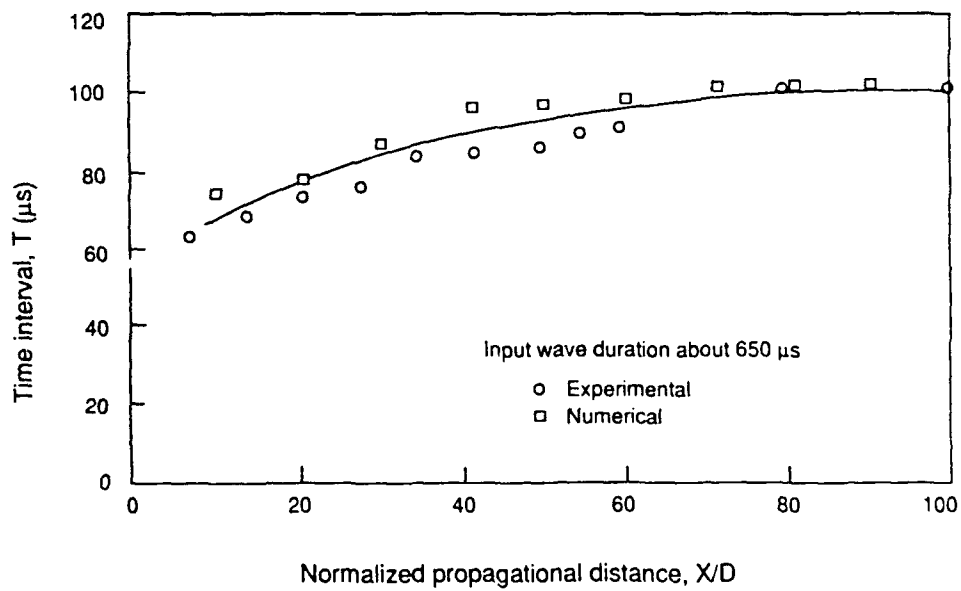Fig.5.3 Normalized strain gage output in a 1-D chain of Homalite-100 discs

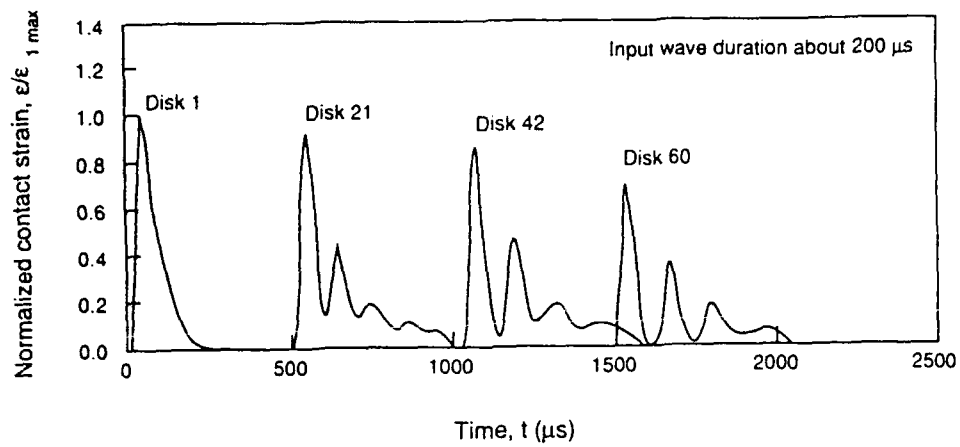Fig.5.4 Time interval between peaks in one pulse for various locations

97

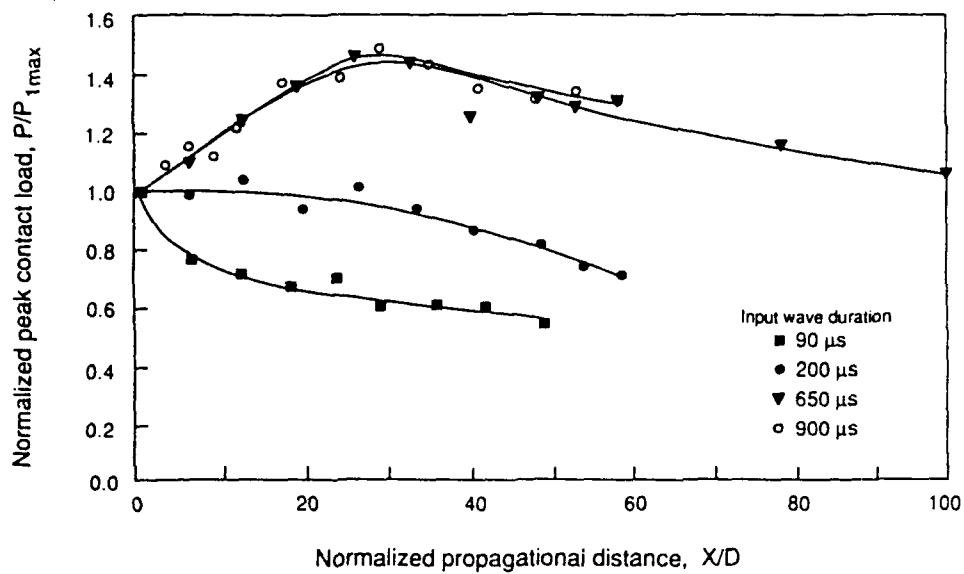Fig.5.5 Normalized strain gage output in a 1-D chain of Homalite-100 discs

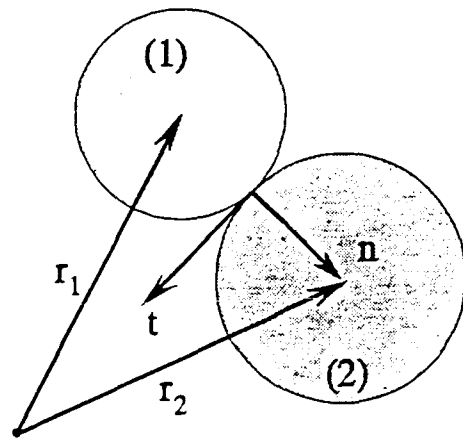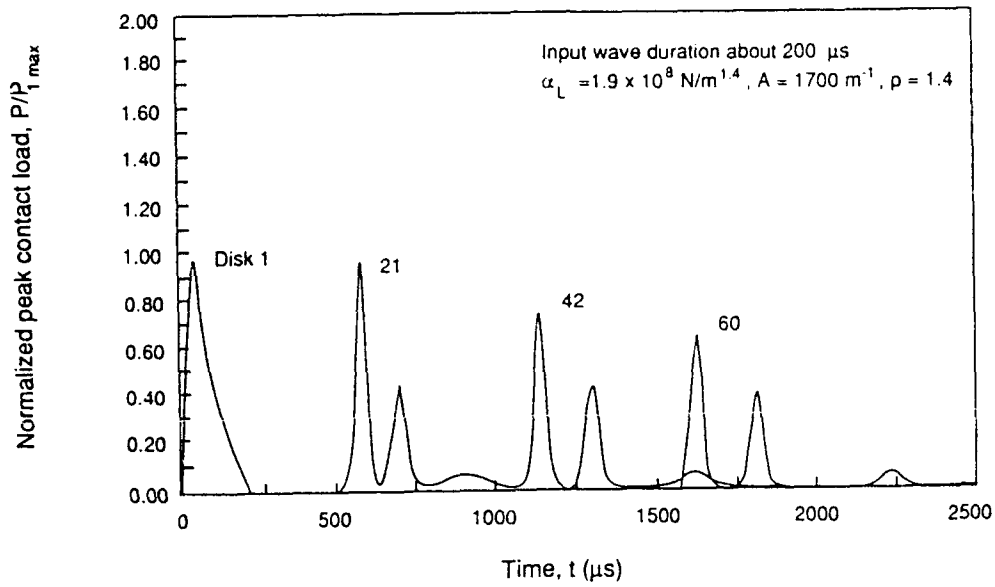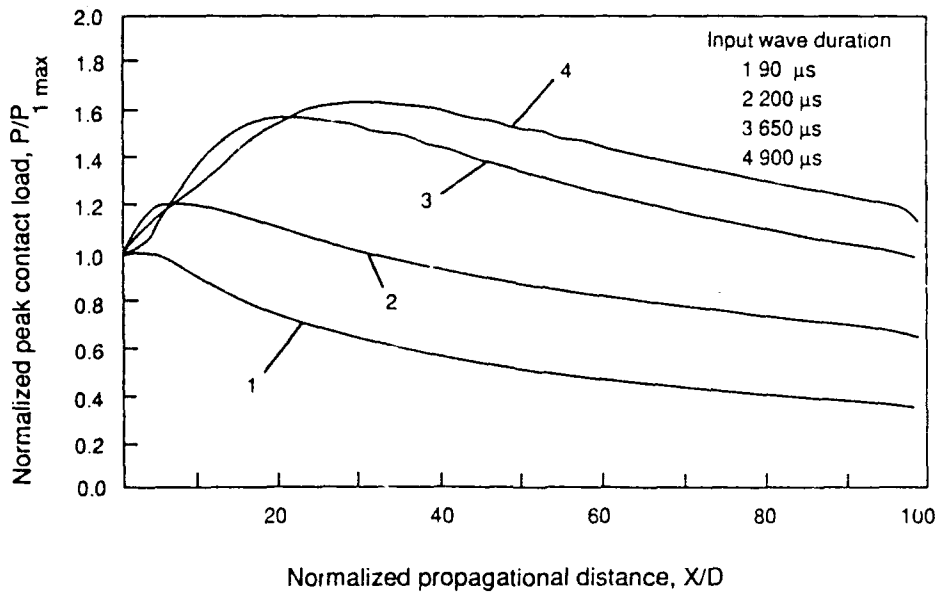Fig.5.6 Normalized peak contact loads as a function of propagational distance for different input wave durations

98

Fig.5.7 Schematic of disk interaction
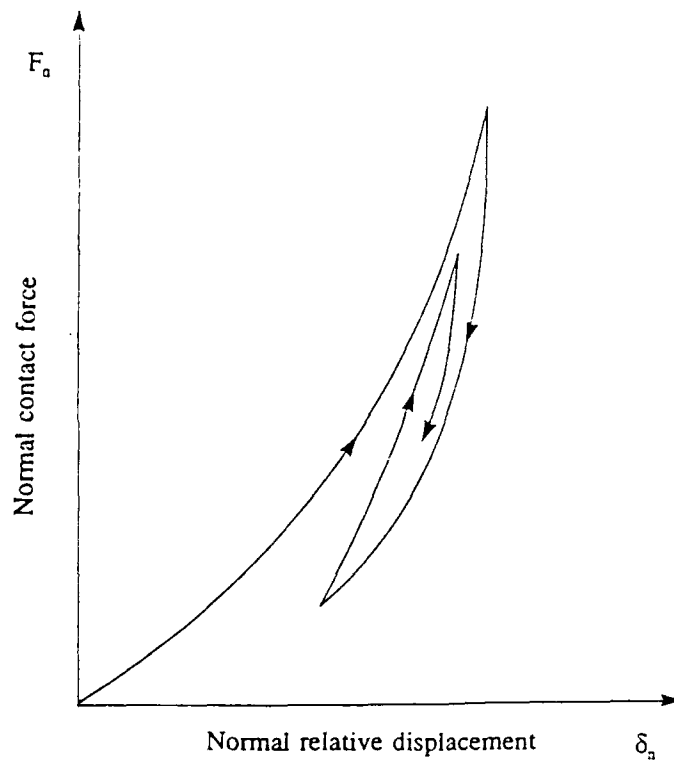
Fig.5.8 Schematic of normal contact law

Fig.5.9 (top chart)

Normalized peak contact load, $P/P_{1\,max}$

2.00
1.80
1.60
1.40
1.20
1.00
0.80
0.60
0.40
0.20
0.00

Input wave duration about 90 μs
$\alpha_L = 2.6 \times 10^8$ N/m$^{1.4}$, A = 4000 m^{-1} , p = 1.4

Disk 1

25

43

50

0   200   400   600   800   1000   1200   1400

Time, t (μs)
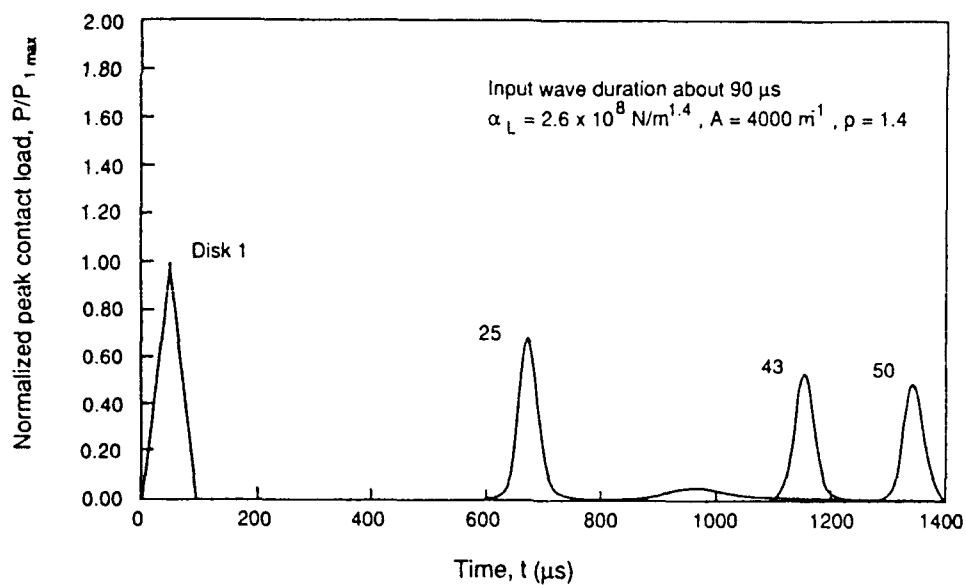
Fig.5.9 Normalized contact loads in a 1-D chain of Homalite-100 discs (numerical)

Fig.5.10 (bottom chart)

Normalized peak contact load, $P/P_{1\,max}$

2.00
1.80
1.60
1.40
1.20
1.00
0.80
0.60
0.40
0.20
0.00

Input wave duration about 650 μs
$\alpha_L = 1.7 \times 10^8$ N/m$^{1.4}$, A = 1700 m^{-1} , p = 1.4

Disk 1

21

42

60

0   500   1000   1500   2000   2500

Time, t (μs)
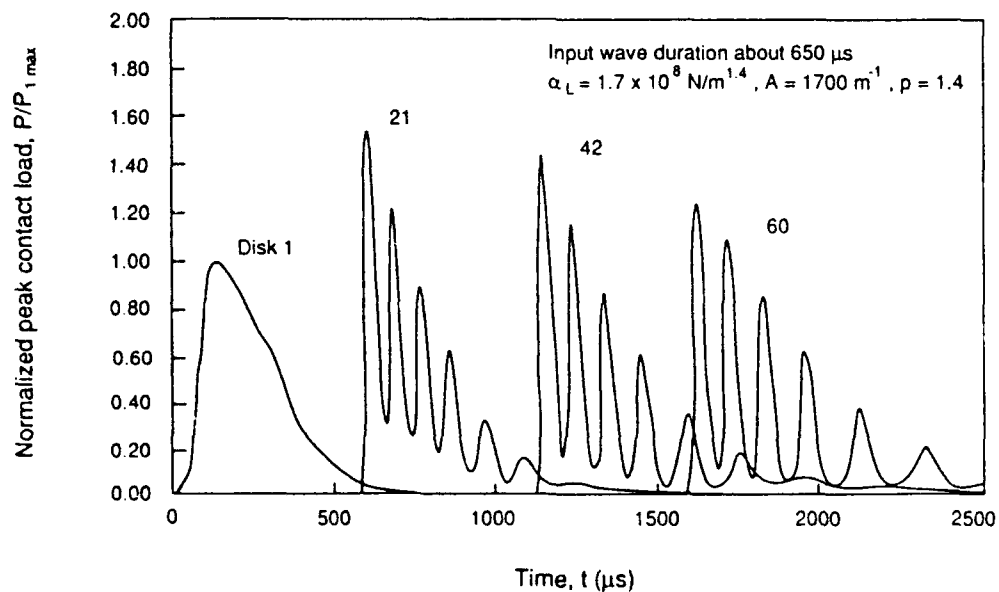
Fig.5.10 Normalized contact loads in a 1-D chain of Homalite-100 discs (numerical)

Fig.5.11 Normalized contact loads in a 1-D chain of Homalite-100 discs (numerical)

Fig.5.12 Normalized peak contact loads as a function of propagational distance for different input wave durations (numerical)
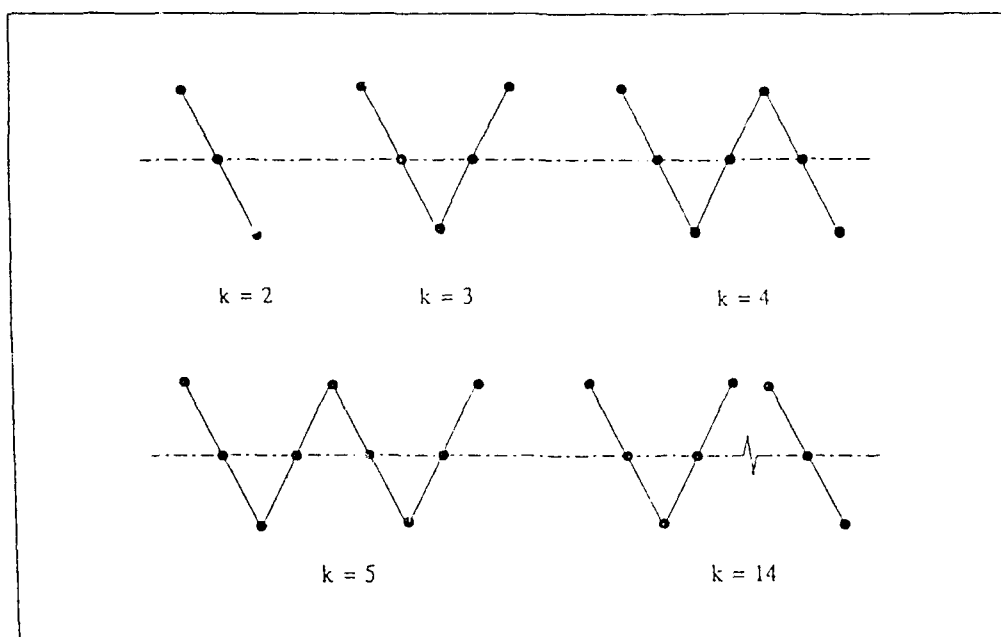
101

Fig..5.13 Normal modes corresponding to $\lambda = 2$ for systems with 2k disks(relative motion)

CHAPTER 6

ROLE OF PARTICLE SHAPE AND CONTACT PROFILE ON THE DYNAMIC RESPONSE OF PARTICULATE MATERIALS

Experimental and numerical studies have been conducted to investigate the effect of particle shape and particle surface roughness on inter-granular load transfer, velocity and wavelength of a stress wave transmitted through granular media subjected to explosive loading. Dynamic photoelasticity was used as the experimental technique to study stress wave propagation through granular media simulated by assemblies of elliptical and circular particles with varying surface roughness. Numerical studies employed a computational scheme based upon the distinct element method. Results indicate that the shape of the particle affects both the velocity of the transmitted stress wave pulse and the load transfer characteristics. The wavelength shows no appreciable dependency on the particle shape. Particle surface roughness seems to affect the load transfer characteristics and the wave length, and to a limited extent, the wave velocity.

6.1 INTRODUCTION

This experimental and numerical study attempts to investigate the influence of particle shape and particle surface roughness on the dynamic response of granular materials. Using granular media simulated by circular disks with smooth surfaces (Rossmanith and Shukla, 1982, Shukla and Nigam, 1985, Shukla and Rossmanith, 1986, Shukla and Damania, 1987, Sadd, et.al., 1989a, Xu and Shukla, 1990), experimental and numerical techniques have been previously used to study the load-transfer, wave velocity and wave dispersion characteristics for various loading parameters and packing geometries, However, modelling a granular media using such particles has the following limitations:

(1). Particles in actual granular media are not necessarily circular.

(2). In general a granular medium can have more or less number of contacts per particle than those for circular disks.

(3). For non-circular particles the contact normal vectors may not pass through the centers of the particles in contact.

(4). Real life particles may or may not have smooth contact surfaces.

103

In this study, particle shape was controlled by using elliptical particles of different shapes and sizes. The ellipse was chosen since it provides a simple scheme to introduce particles with an oblong shape, and a circular particle can be treated as a special case of an ellipse with an aspect ratio of one. For surface roughness studies circular disks with varying surface roughnesses were used to simulate the granular media.

6.2 EXPERIMENTAL PROCEDURE AND ANALYSIS

The experimental setup comprised of various assemblies of Homalite-100 particles which were loaded by exploding a small amount (10-15 mg) of Lead Azide in a specially designed charge holder. Figure 6.1 shows one such single chain setup used for simulating one dimensional granular media using elliptical particles. A Cranz-Schardin multiple spark-gap camera was used to capture 20 separate photoelastic images of the dynamic process, at predetermined timings. A typical sequence of 5 photographs for one of the single chain setups is shown in figure 6.2. These images capture the wave propagation process at discrete time frames and can be used to provide data for determining contact loads, wavelength and velocity for the transmitted stress wave pulse. Dynamic photoelasticity was chosen as the experimental technique as it provides full field information and enables one to see the shape of the stress wave front, as it propagates down the granular assembly.

The elliptical particles were routed out of Homalite 100, a photoelastic material. The template used for routing was machined out of aluminum using a CNC milling machine. The routing was carefully monitored so as to avoid producing any heat related residual stresses in the material.

To separate the effect of particle shape and particle size the single chain experiments were designed so that the number of contacts per unit length remained constant while the aspect ratio was being varied. Thus, while varying the aspect ratio of the elliptical particles within a set of comparative experiments, the axis length along the direction of wave propagation was kept constant and the other axis length was varied. See figure 6.3 for a definition of the particle width, length and aspect ratio.

Rough particles were fabricated from 1" (25.4 mm) diameter Homalite-100 disks by roughing the surface with a band saw. The disks were later heat treated to remove any residual stresses. Root mean square value of the edge variation of the disk from a mean

104

value was taken as a measure of the surface roughness (Johnson, 1985). Moreover, the thickness being small, this value of roughness was assumed to be uniform across the thickness. Replication of the same roughness on several disks was achieved by using the same band saw blade.

The photoelastic images were enlarged using a Besseler enlarger and data was collected with a Hicomscan digitizer linked to an IBM PC-AT. Contact load calculation at a particular contact and time was done by assuming a local Hertz contact stress field and applying the multi-point, non-linear least square method developed by Shukla and Nigam (1985). Data of the wave propagation distance as a function of time was used to obtain the stress wave velocity. The average velocity was calculated using a linear least-square fit through the experimental data points. The wavelength λ of the stress wave pulse can be measured directly from the photographs of the wave propagation process as shown in figure 6.2. It can also be calculated using the duration of contact at any given contact point and the average velocity of the stress wave.

6.3 NUMERICAL MODELLING

The distinct element method was used to model stress wave propagation in granular materials. This method, originally proposed by Cundall and Strack (1979) for the static case, has been applied to dynamic load transfer processes in granular materials by various authors (Sadd, et.al., 1989, Walton, et.al., 1991, Trent, 1989). The distinct element method uses Newtonian rigid-body mechanics to determine the motion of each particle in the granular medium. The interaction between particles is governed by a particular interaction or contact law, and this law plays a dominant role in overall material behavior. The interaction forces are related to relative displacements and velocities of the particles in contact, and the particles are allowed to overlap with each other to represent contact deformation. Also, the time period is discretized into a series of time intervals. The velocity and displacement of each particle can be obtained from its acceleration using a finite difference scheme. The time step is chosen to be small enough so that in a single time step disturbances cannot propagate any further than the immediate neighbors of the particle in question. Thus the particle accelerations, velocities, and displacements can be determined explicitly during a given time step. Referring to figure 6.4, using a simple forward difference formula the increments of relative normal and tangential displacements

can be written in terms of velocities as

$$\Delta\delta_n = v_n\Delta t = [(v_1 + \omega_1 \times R_1 - v_2 - \omega_2 \times R_2)\cdot n]\Delta t$$

$$\Delta\delta_t = v_t\Delta t = [(v_1 - v_2 + \omega_1 \times R_1 - \omega_2 \times R_2)\cdot t]\Delta t \tag{6.1}$$

where v_1, ω_1, and R_1 are the velocity, angular velocity, and the distance between the mass center and the contact point of particle 1, with like notation for particle 2. The vectors n and t designate normal and tangential contact unit vectors, δ_n and v_n denote the relative normal displacement and velocity between the adjacent particles, and δ_t and v_t are the relative tangential values.

Generally the interaction contact law between adjacent particles can be written as

$$F_n = F_n(\delta_n, v_n), \qquad F_t = F_t(\delta_t, v_t, \delta_n, v_n) \tag{6.2}$$

where F_n and F_t are the normal and tangential contact forces. Using Newton's law, the acceleration a and the angular acceleration α for each particle are determined by the relation

$$a = F / m, \qquad \alpha = M / I \tag{6.3}$$

where F and M are the resultant force and moment on the particle, m is the mass of the particle, and I is the moment of inertia of the particle. Once the accelerations are known, the velocities follow by using the simple difference equation

$$\Delta v = a\Delta t \qquad \Delta\omega = \alpha\Delta t \tag{6.4}$$

Equation (6.1) may be used to determine the particle displacements, and then new contact forces may be determined for the next time step using equation (6.2). In this way, the distinct element method develops an explicit time-stepping numerical scheme which can be used to study the dynamic behavior of large assemblies of particles. Figure 6.5 illustrates a typical computer flowchart of the distinct element numerical routines.

It is obvious that the wave propagation is directly related to the process of load transfer between particles. Thus the contact law which governs the load transfer is

106

important, and studies of various contact laws have been conducted (Sadd, et.al., 1992). These studies have shown that a nonlinear-hysteretic contact law as shown in figure 6.6 provided the best comparisons with experimental data for granular materials simulated by assemblies of circular disks. Therefore this contact law is used here, and it is expressed as

$$F_n = \begin{cases} F_{nL} = \alpha_L \delta_n^p \dots\dots\dots\dots\dots\dots\dots loading \\ F_{nU} = \alpha_U \delta_n^{p+q} \dots\dots\dots\dots\dots\dots unloading,\ reunloading \\ F_{nrL} = \beta F_{nL} + (1-\beta)F_{nU}\ \dots\dots\dots reloading \end{cases} \tag{6.5}$$

If in the loading path the maximum value of the force is recorded as $F_{n\,max}$, then reloading is defined as the state in which the load is increasing but its value is smaller than $F_{n\,max}$. The reloading path will join the loading path at $F_{n\,max}$, and additional loading follows the original loading path. The value of q is determined by the relation

$$q = (A\ \delta_{n\,max}^{(i)})^2 \tag{6.6}$$

where A is a constant to be determined and $\delta_{n\,max}^{(i)}$ is defined as the value of δ_n at contact point i when the normal contact force at the point has attained its maximum value. The value of β is given by

$$\beta = \frac{\delta_n^{(i)} - \delta_{n\,min}^{(i)}}{\delta_{n\,max}^{(i)} - \delta_{n\,min}^{(i)}} \tag{6.7}$$

where $\delta_n^{(i)}$ is the current value of the relative normal displacement at contact point i, and $\delta_{n\,min}^{(i)}$ indicates its minimum value in the previous unloading or reunloading path. At the moment reloading begins, $\delta_n^{(i)} = \delta_{n\,min}^{(i)}$ and $\beta = 0$. The value of β increases with $\delta_n^{(i)}$, and reaches a maximum value of 1 when $\delta_n^{(i)} = \delta_{n\,max}^{(i)}$ which indicates that new loading will begin. The values of α_L, p, and A are related to material and geometric properties of the disks, and are determined from experimental calibration tests. The parameter α_U, however, is selected to make the unloading path initiate at the peak point of loading, see figure 6.6.

The distinct element method with the nonlinear-hysteretic contact law has been

used to simulate the wave propagation along a single straight chain of elliptical particles. A triangular time dependent impulse with 1000 N maximum load and 60 μs period was used to simulate the explosive loadings used in experiments. The time step was chosen as 2 μs, and the parameters used for various cases are given in Table 6.1.

6.4 RESULTS AND DISCUSSION

6.4.1 Effect of Particle Shape.

Four different single chain setups were used, with contacts at 25.4 mm intervals. For the four chains the width of the elliptical particles was increased from 12.7 mm to 38.1 mm while the length was kept constant at 25.4 mm. Thus, single chain granular assemblies were constructed with varying particle shapes but a constant contact interval. Figure 6.7 shows the plot of distance propagated by the wavefront as a function of time for the single chain of 12.5 x 25.4 mm ellipses. The average velocity obtained from the slope of this plot is also shown. Average wave velocities obtained from the four different single chain setups are listed in Table 6.2. As the particle width was decreased from 38.1 mm to 12.7 mm the wave velocity was seen to increase from 950 m/s to 1250 m/s. The wave speeds predicted by the distinct element method are listed in Table 6.1, and the numerical values agreed with experimental data to within 5%.

Increasing the particle width increases the radius of curvature at the contact point which influences the contact stiffness. If the radius of curvature at the contact point is increased while keeping the contact interval constant the contact stiffness increases, which would imply a higher wave velocity. The increase in contact stiffness as the particle width is increased was also reflected by the increase in the α_1 parameter, as given in Table 6.1. However, as the width of the particle increases, the particle mass per unit length also increases and this tends to reduce the wave speed. An approximate equation for the speed of a stress wave propagating in one dimensional granular media is given by Takahashi and Sato (1949).

$$V = d \sqrt{\frac{K}{m}} \tag{6.8}$$

where d is the distance between the centers of two particles in contact, K is the contact stiffness, and m is the mass of the particle. For the cases studied, the distance d was kept

constant at 25.4 mm, and the mass was given as,

$$m = \pi \rho a b h \qquad (6.9)$$

where a and b are the half major and minor axes of the elliptical particle, h is the thickness, and ρ is the density. From the nonlinear contact law, neglecting damping, the stiffness can be expressed as a function of the contact force F and the parameter α_L,

$$K = 1.4 \alpha_L^{1/1.4} F^{0.4/1.4} \qquad (6.10)$$

The stiffness reaches its maximum value of K_{max} when the contact force is maximum at F_{max}. Assuming a linear variation of force F with time, and the same peak contact force F_{max} at every contact point, the average stiffness of each contact point is given as,

$$K_0 = 0.5 \alpha_L^{1/1.4} F_{max}^{0.4/1.4} \qquad (6.11)$$

The ratios of K_0/m for the different particles are listed in Table 6.1. The peak contact force between particles 3 and 4 has been taken as F_{max}. It is seen that K_0/m decreases as the particle width is increased, which emphasizes the predominance of the particle mass over the contact stiffness in influencing the wave speed.

Table 6.2 lists the wavelength, λ, of the transmitted stress wave pulse as it traveled down the single chain assembly. The wavelength showed no appreciable change as the particle aspect ratio was changed. Earlier experiments done with circular disks (Xu and Shukla, 1990) have shown that changing the length of the particles changes the velocity and the λ/D ratio, where D is the contact interval (i.e., the particle length). In this set of experiments the λ/D ratio remained constant, as expected, as the particle width rather than the particle length was being changed.

Photographs obtained from the experiments also showed how the stress wavefront took the shape of the particle, as shown in figure 6.8. Figure 6.9 shows the change in the fringe width with the fringe length of the wavefront fringe contour as the stress wave propagates down any given particle. Near the contact area the fringe width and the fringe

length were nearly equal for all the different particles and the fringes were circular. This conforms with the Hertz contact theory which predicts circular fringes (Shukla and Nigam, 1985). Further down the particle the free boundary effects become prominent and the particle shape influences the shape of the wavefront fringe contour, as seen in figure 6.8. Wave propagation through a granular media occurs by contact mechanisms which result in load transfer from particle to particle. Within a particle, however, the wave propagation process is through a reflection mechanism, and each particle acts as a wave guide. The stress wavefront observed is a resultant of the various reflection of the stress wave from the free boundaries of the granular particle. For a wider particle the time taken by the stress wave to reach the sides and reflect back would be more than for a narrower particle, leading to a broader wavefront and a lower wave velocity.

Data from the various single chain assemblies was used to determine the normal contact loads at different contact points. Figure 6.10 shows the typical normal contact load variation for a single chain assembly. The contact loads, F, were normalized with respect to the peak contact load occurring between particles 4 and 5, viz. $F_{4.5\,max}$, particle numbers being counted from the top down. This contact was chosen for normalization because at this point the wave had travelled through four particles, i.e. one wavelength, and thus had stabilized. This normalization allows for easy comparison between different experiments (Shukla and Damania, 1987). The normalized contact loads for the 25.4 mm (1") diameter circular disk chain were available from earlier experiments done using circular disks (Shukla and Damania, 1987).

Normalized contact load plots provide information about load or wave attenuation as the stress wave travels from contact to contact. They also provide information about the duration of contact which can be used along with the wave velocity to give the wavelength of the transmitted stress wave pulse. Figure 6.11 gives the contact load attenuation plots for the various elliptical particles as the stress wave traveled down the single chain assembly. Again, the peak contact loads, F_{max}, were normalized to allow direct comparison. As shown the load attenuation increased with the width of the elliptical particles. For a wider particle the stress wave had to travel through more material for the same distance of propagation. This resulted in increased material dispersion for particles with greater width, as seen in figure 6.11. Values for peak contact load attenuation, as

obtained from the experiments, are also listed in Table 6.2. The numerical distinct element predictions are also shown in figure 6.11, and these numerical results generally agreed with the experimental data to within 5%. It should be noted that the distinct element model requires that different values of the model parameters α_t and A be used for each of the different particle shapes. This is related to the fact that the contact mechanics behavior of each of these cases will change due to the surface radius of curvature, and the internal wave propagation paths within the particle. Wider particles also produce longer internal wave propagation paths within the particle, and this leads to an increase in the attenuation characteristics of the particle. This agrees with the increasing values of the A parameter in Table 6.1 since this parameter is related to the hysteresis associated with the contact law.

6.4.2 Effect of Particle Surface Roughness.

Experiments were conducted to study stress wave propagation through single chain assemblies of circular Homalite 100 disks of roughness 0.01 mm and 0.022 mm. Prior to the dynamic experiments, static loading experiments were done to test the applicability of the Hertz contact laws and to determine a validity zone for the governing equations. Figure 6.12 shows two rough disks under compressive loading. From the static experiments, it was found that the Hertz contact laws were valid for 2b<r<8b, where 'r' is the radial distance from the contact point and 'b' is the half contact width. During dynamic wave propagation in disks, the wavelength of the loading pulse is several times the disk diameter, hence the loading is essentially quasi-static (Rossmanith, 1982). Therefore, all the experimental data for analysis was collected from this zone.

Figure 6.13 shows the plots of distance propagated by the wave front as a function of time for single chain assemblies of circular particles of roughness R_a = 0.01 mm and R_a = 0.022 mm. The average velocities obtained for the two cases of roughness were 1020 m/s and 950 m/s, the velocity decreasing as the roughness was increased. Due to the brittle nature of the rough edges, crushing of material at the contact zone occurred as the wave passed which was also corroborated by the debris obtained at the contact zone. This resulted in a decrease in stiffness at the contact. Moreover, as the roughness is increased more free boundary is created, which results in increased scattering of the wave at the free surfaces of the particle. Hence the wave suffers more reflections within the particle

and the group wave velocity decreases. This accounts for the decrease in average wave velocity as the particle surface roughness is increased.

Figure 6.14 shows a plot of the normalized contact loads as a function of time. The dotted lines on the curves show the extrapolation that has been done based on the position of the wave as determined from the photographs. The peak contact load did not show an attenuation as was the case with the smooth disks. The contact stiffness of the rough edges was different for different contacts and this resulted in the absence of any continuous attenuation in the value of the peak contact load as was seen in figure 6.10. Crushing of the rough edges as the wave passed through the contact caused a change in the loading rate as seen in contact load behavior in figure 6.14. Actual photoelastic peak loading of the contacts 3-4 and 4-5 is shown in figure 6.15 where it is seen that although there is some local disturbance due to surface roughness, the photoelastic fringes are very clear and the results can be stated with confidence.

For rough particles, the wavelength showed a decrease of 20% as compared to the results obtained from smooth disks and no variation in wavelength occurred as the wave passed through the chain of particles; e.g, the wavelength as seen from the first loading curve(1-2) is 80 mm. Minor variations in the wavelength as the wave passed through a contact can be attributed to the fact that the waveform had to change as it encountered a disk of different contact roughness.

6.5 CONCLUSION

These experimental and numerical results of wave propagation in particulate materials have shown the following:

(1). Wave velocity showed a strong dependence on the particle shape. The velocity increased from 950 m/s to 1250 m/s as the particle width was decreased from 38.1 mm to 12.7 mm, while holding the particle length at 25.4 mm. This change in the stress wave velocity can be attributed to a change in the particle mass per unit length in the direction of wave propagation. As the particle width is varied, the internal wave reflection mechanisms influence the travel time of the wave within a particle. This influence was also seen in the wavefront shape. The wavefront took the shape of the particle as the stress wave traveled through it. The experimental results were well corroborated by numerical distinct element modelling.

(2). The wavelength of the stress wave pulse showed no appreciable change as the particle shape was varied, as long as the contact interval was kept constant.

(3). Both experimental and numerical studies showed that the peak contact load attenuation increased as the particle width was increased. This was due to the longer internal wave propagation paths within the wider particles, which resulted in an increase in the particle attenuation characteristics.

(4). The wave velocity decreased as the particle surface roughness was increased. This was due to waves being scattered and reflected more number of times inside the disk because of the increase in free boundary due to surface roughness.

(5). With rough particles, the peak contact loads did not show an attenuation as was the case with smooth disks. Moreover, the loading curves were not very smooth. This can be attributed to the difference in contact stiffness between different rough contacts and also to the crushing of the rough edges as the wave passed through the contact zone.

Further experiments are currently being conducted to study the effect of contact stiffness and contact profile on dynamic load transfer in granular media. This is necessary to reach a better understanding of the influence of the particle shape on load transfer characteristics, wave velocity and wavelength. Experiments are also being conducted to study two-dimensional assemblies of elliptical particles, and random assemblies of particles of different size and shape as shown in figures 6.16 and 6.17. Surface roughness definitely affects dynamic wave propagation in a significant manner. Further experiments with higher roughness are being currently done to develop conclusive relations between roughness and the various parameters which govern wave propagation.

Table 6.1 Numerical modeling parameters and results for single chain
assemblies of various elliptical particles.

Particle Size	A (m^{-1})	p	α_L $(10^8\ N/m^{1.4})$	F_{max} (N)	$K_0\ /\ m$ $(10^8\ s^2)$	Wave Speed (m/s)
25.4 x 12.7 mm	1900	1.4	1.7	891.5	1.91	1221
25.4 x 19.05 mm	4100	1.4	2.3	812.8	1.54	1095
25.4 mm dia.	6500	1.4	3.2	785.5	1.45	1058
25.4 x 38.1 mm	11000	1.4	5.1	739.2	1.32	992

Table 6.2 Experimental results for the dynamic loading of single chain
assemblies of various elliptical particles.

Particle Size	Average Wave Speed	Wavelength	Radius of Curvature at the point of contact	Peak Contact Load Attenuation*
25.4 x 12.7 mm	1250 m/s	101 mm	3.2 mm	5.3 %
25.4 x 19.05 mm	1140 m/s	103 mm	7.1 mm	10.5 %
25.4 mm dia.	1070 m/s	102 mm	12.7 mm	13.0 %
25.4 x 38.1 mm	950 m/s	104 mm	28.6 mm	18.1 %

* This is the drop in the peak contact load as the stress wave travels across four contact
points, from contact 3-4 to contact 7-8.
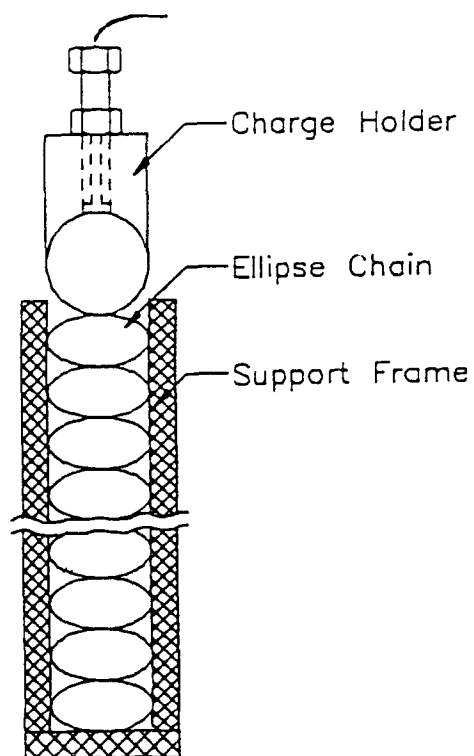
Fig.6.1   Single chain assembly of elliptical particles

| Frame 7 | Frame 9 | Frame 10 | Frame 11 | Frame 16 |
| 101.5 µs | 125.5 µs | 135.0 µs | 160.0 µs | 187.0 µs |
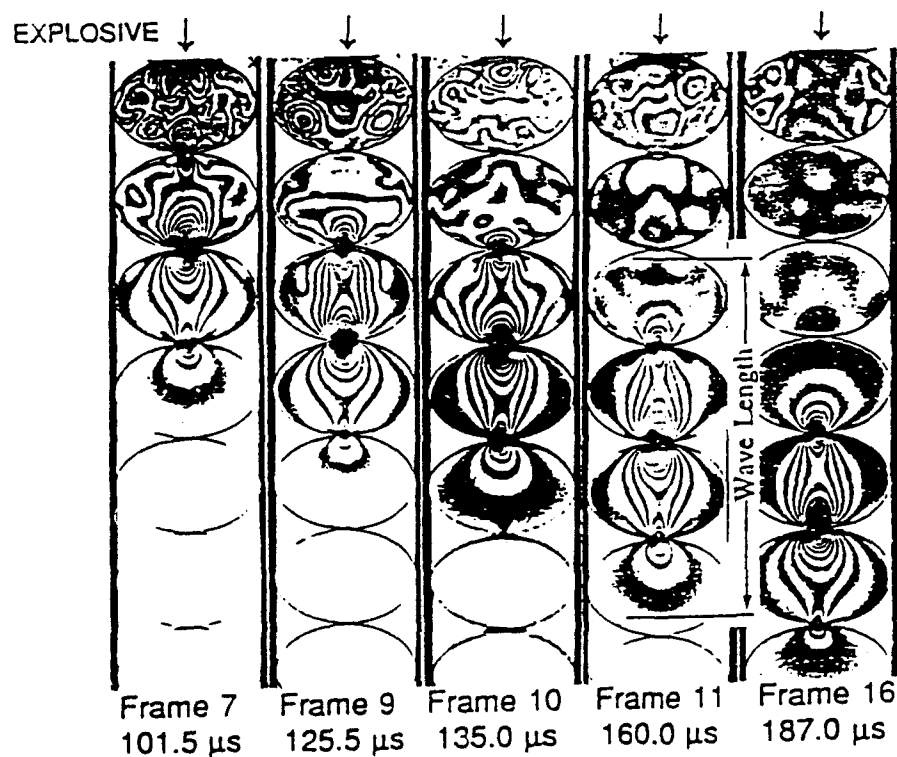
Fig.6.2   Isochromatic fringes obtained for the 25.4 x 38.1 mm ellipses single chain
assembly

115

Aspect Ratio = $\dfrac{\text{Particle Length}}{\text{Particle Width}}$
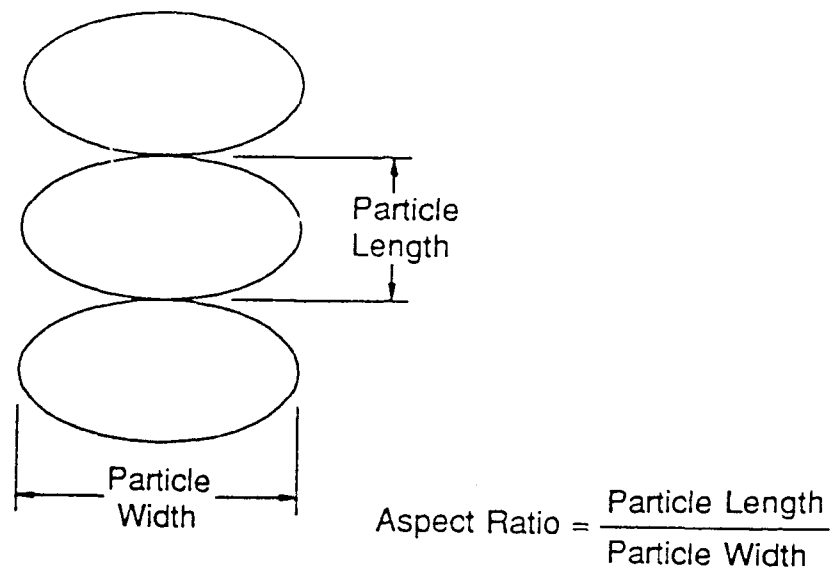
Fig.6.3 Definition of the particle aspect ratio
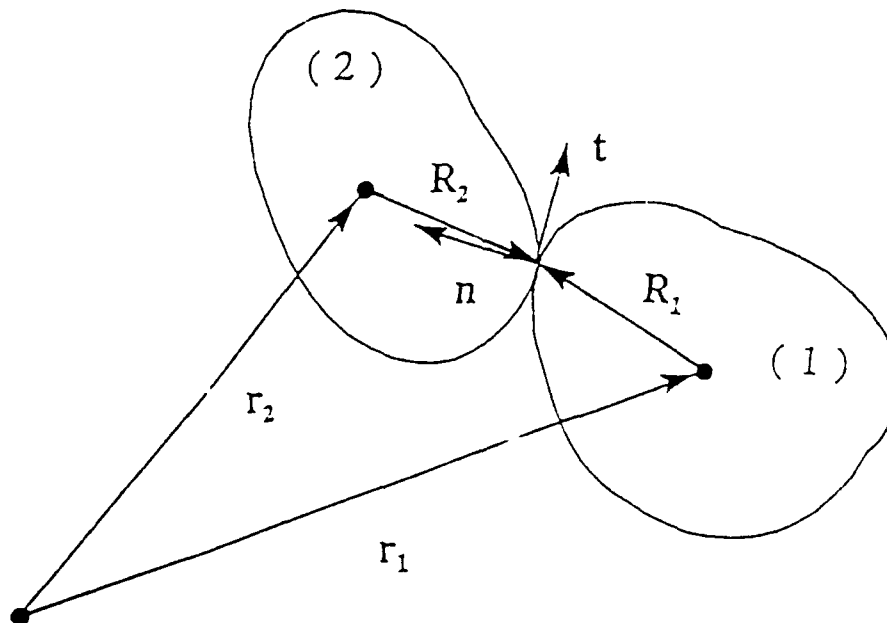
Fig.6.4 Schematic of inter-particle interaction

116
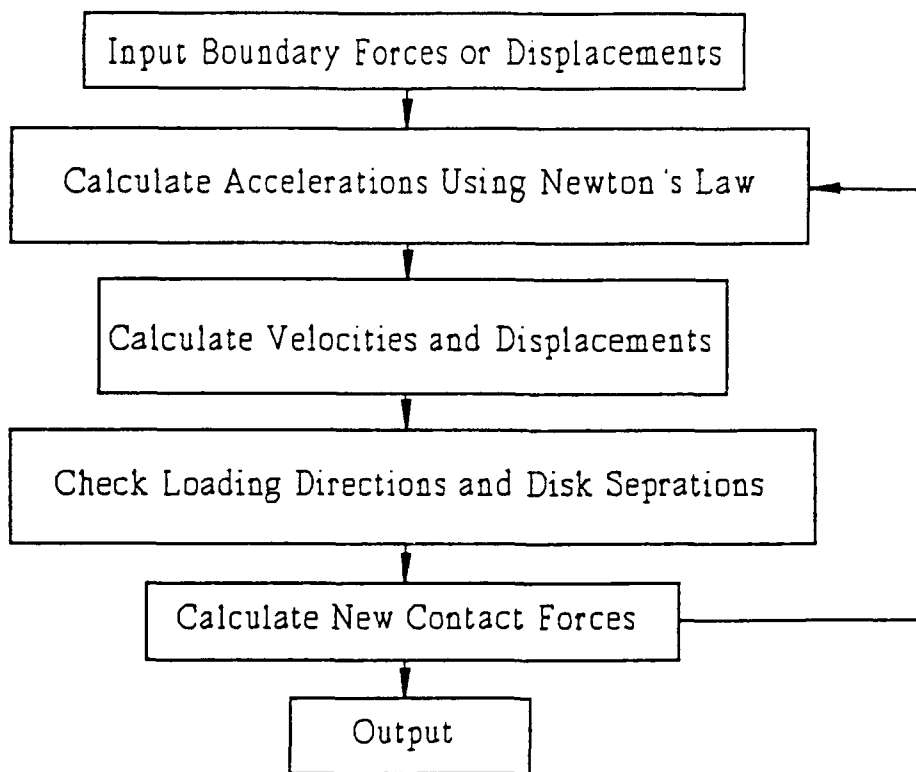
Fig.6.5 Flowchart for the distinct element method
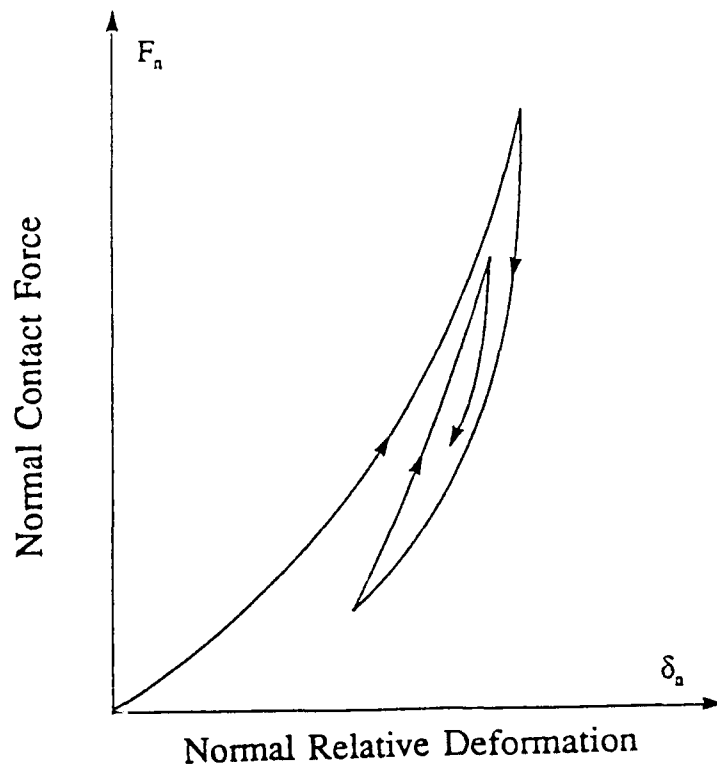
Fig.6.6 Schematic of the non-linear-hysteretic normal contact law
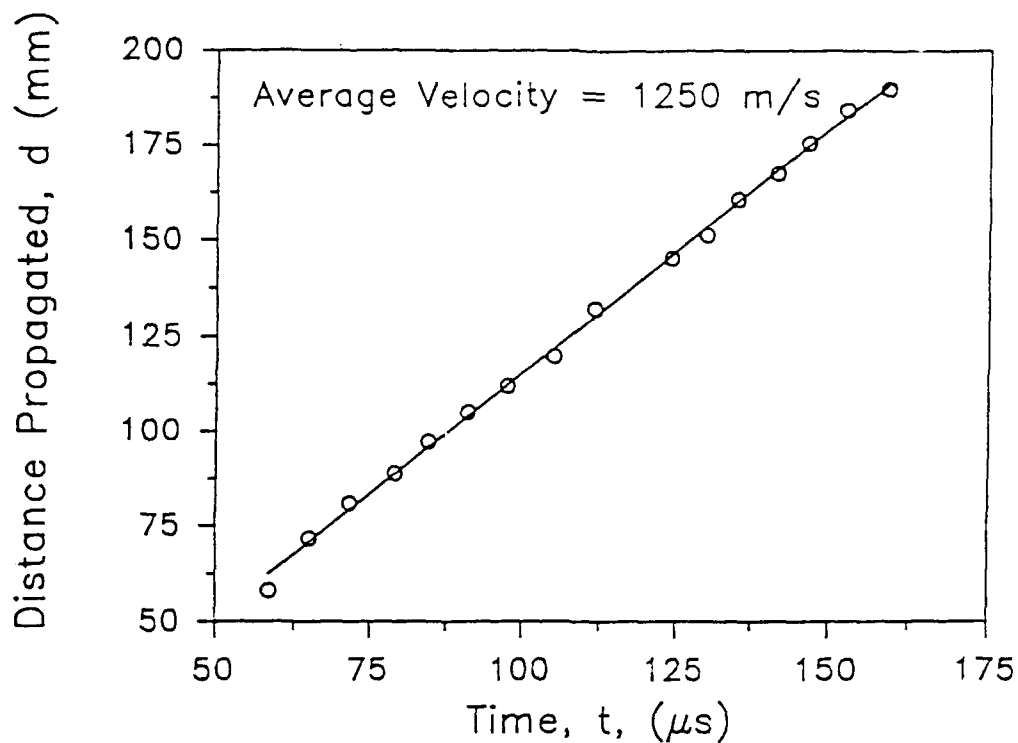
Fig.6.7 Distance propagated by the wavefront as a function of time for the 25.4 x 12.7
mm ellipse chain

25.4 x 12.7 mm Ellipse   25.4 x 19.05 mm Ellipse

25.4 mm diameter Disk   25.4 x 38.1 mm Ellipse
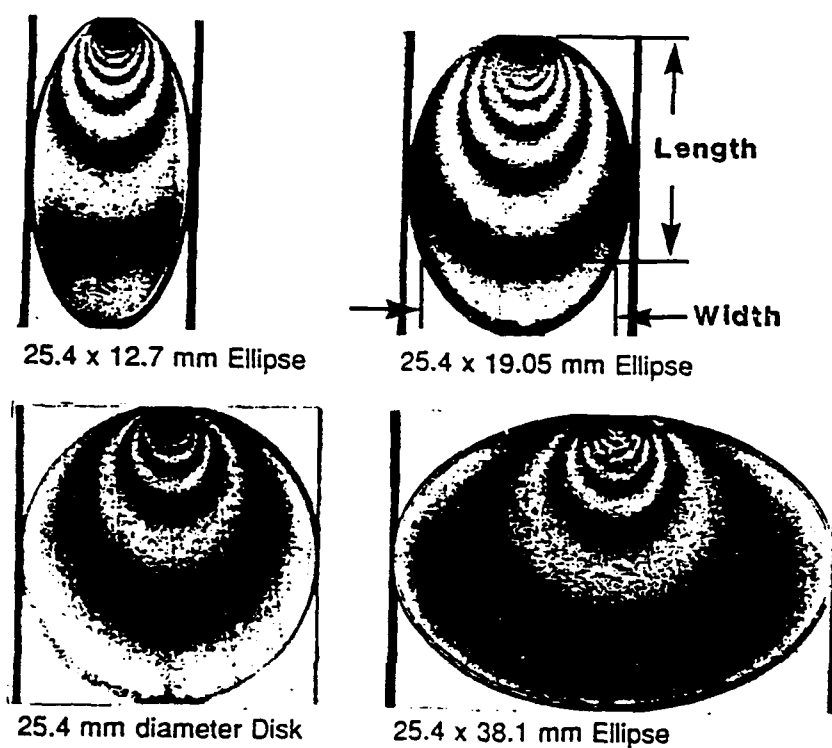
Fig.6.8 Wavefront fringe contour chapes for different particles

118
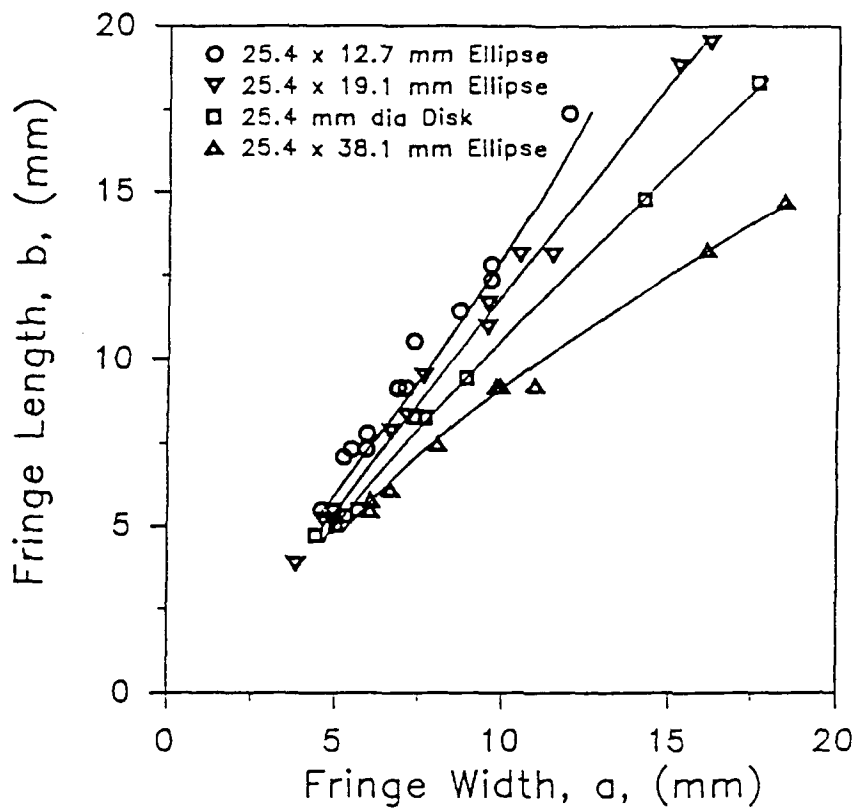
Fig.6.9 Change in the fringe length with the fringe width
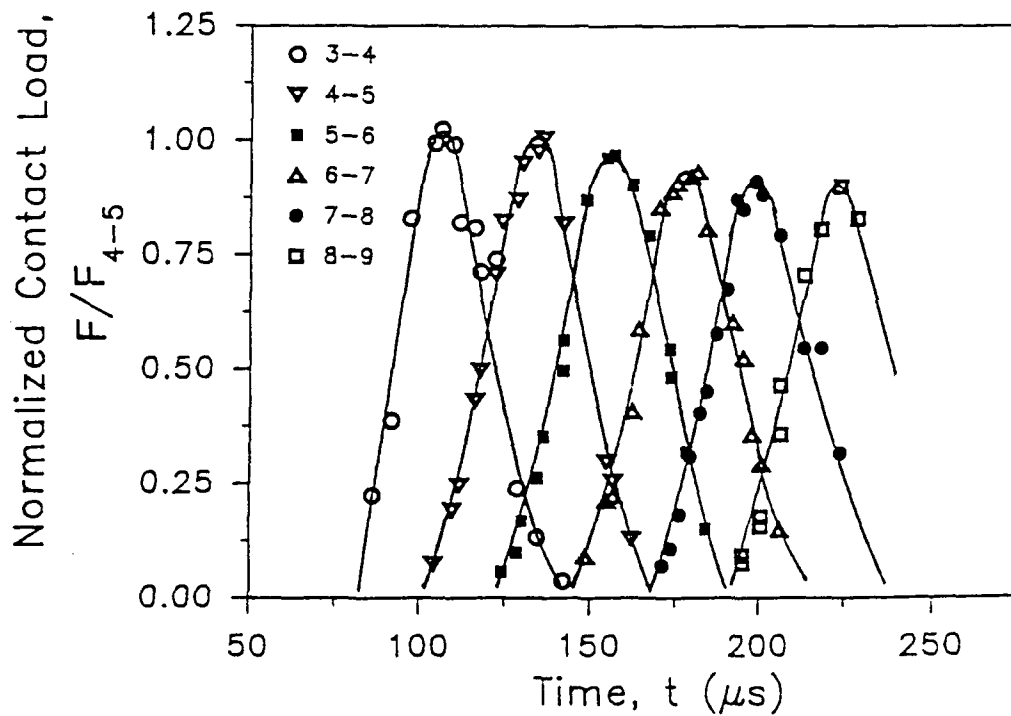
Fig.6.10 Normalized contact load contours for the 25.4 x 19.1 mm single chain ellipse
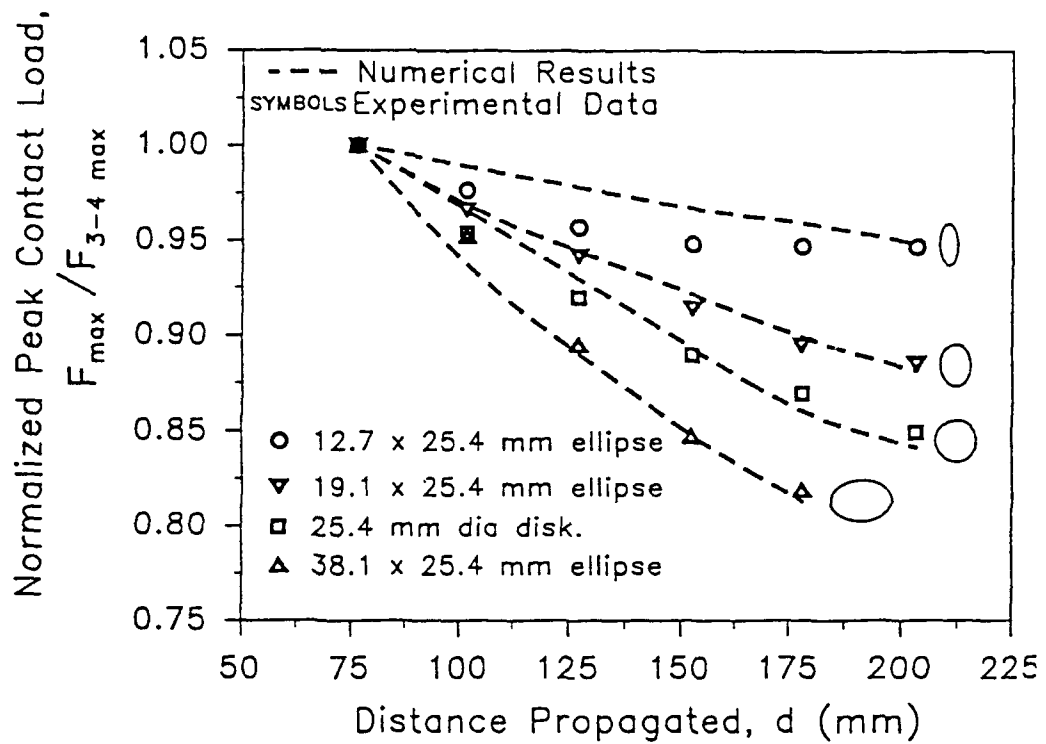
Fig.6.11 Attenuation of the normalized peak contact load with distance propagated down the single chain
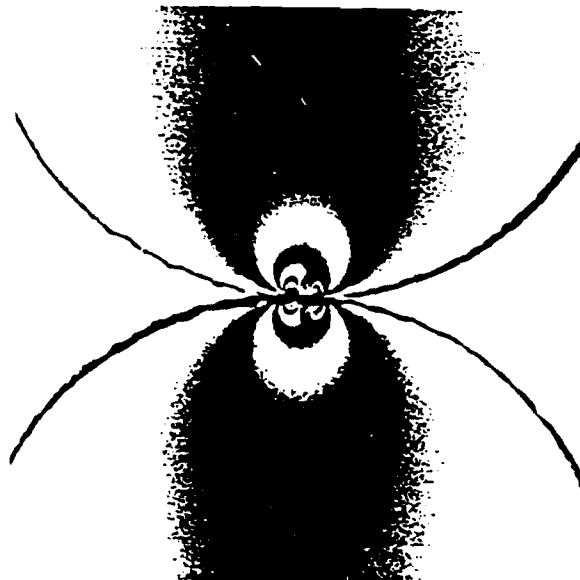
Fig.6.12 Photograph showing a multiple point contact between two rough particles
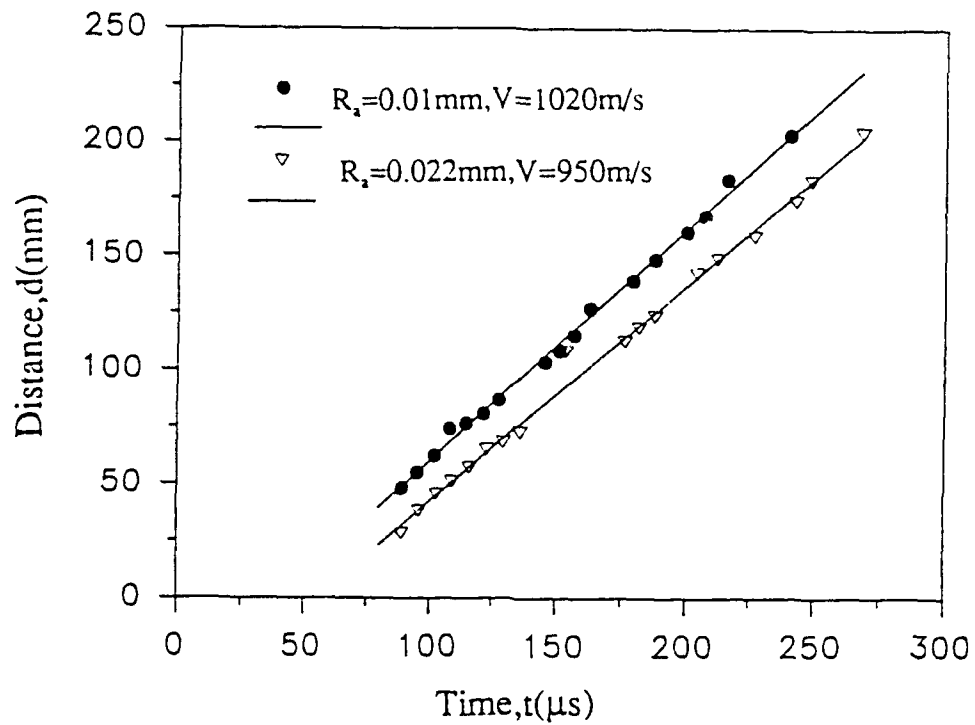
Fig.6.13 Plot of distance versus time for 1" diameter Homalite 100 disks of roughness, $R_a=0.01$ mm and $R_a=0.022$ mm
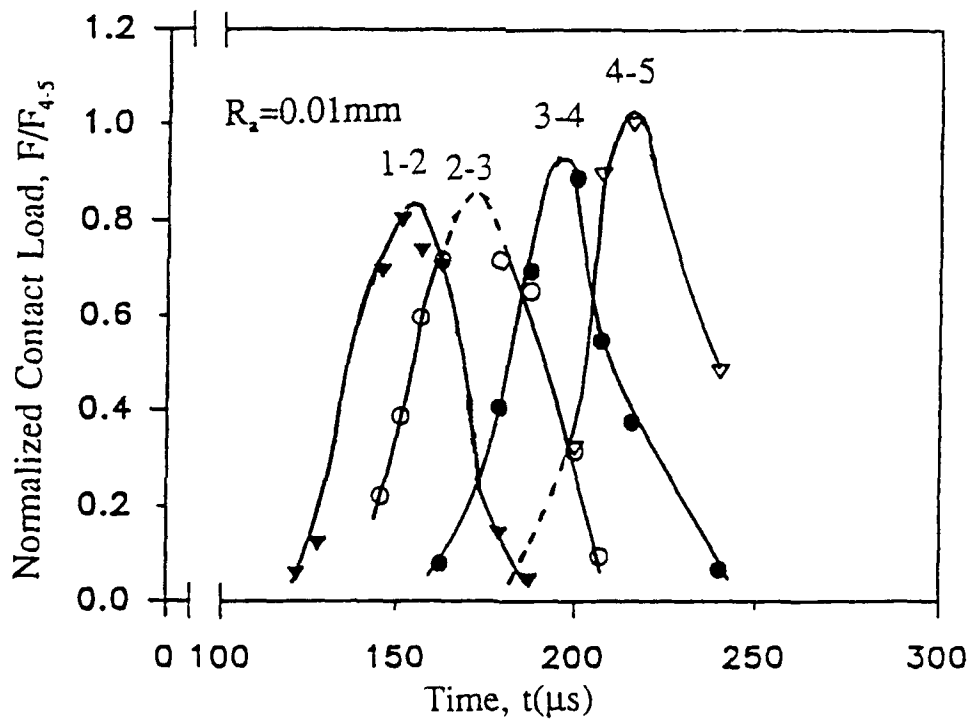
Fig.6.14 Plot of normalized contact load versus time for 1" diameter Homalite 100 disks of roughness, $R_a=0.01$mm

121

Explosive

3-4 →

4-5 →

Frame 17   Frame 19
200μs   215.5μs
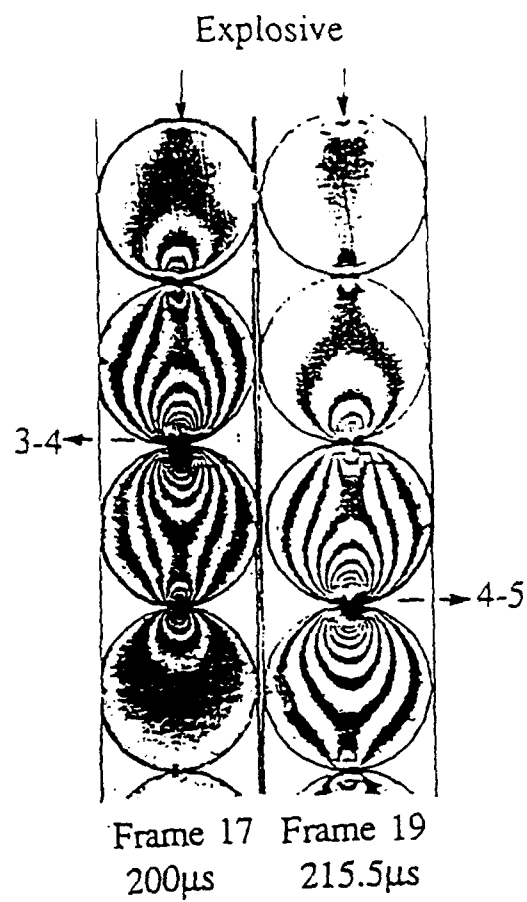
Fig.6.15 Loading of rough contacts 3-4 and 4-5 as seen from the photoelastic fringes

☆ EXPLOSION

FRAME 20
t=165μs
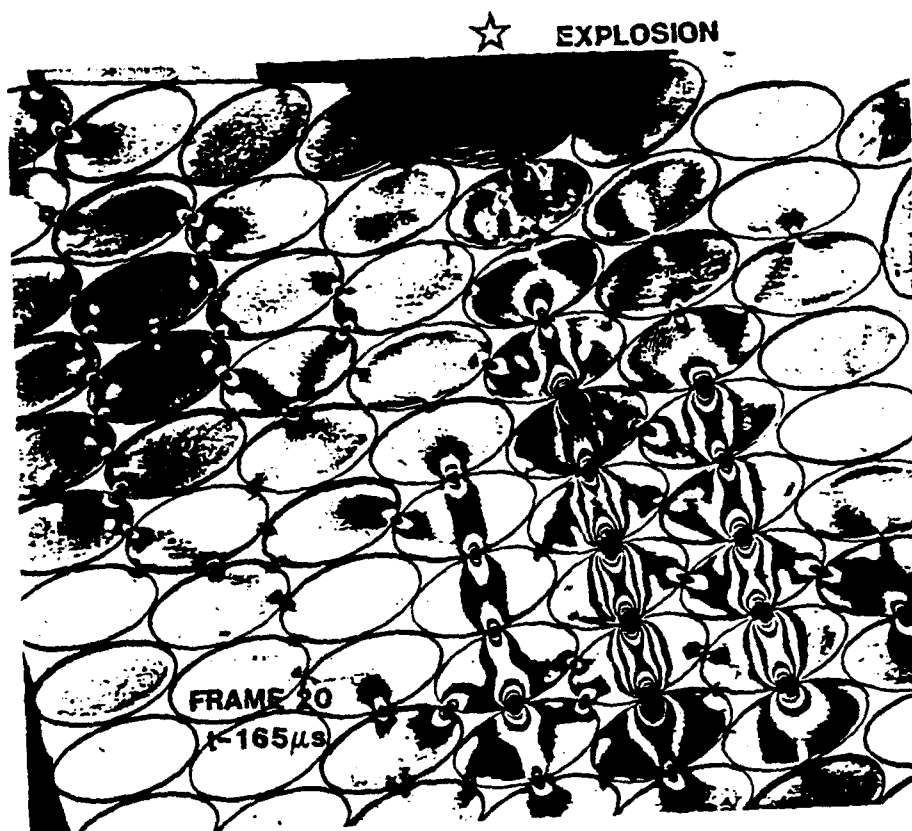
Fig.6.16 Typical photoelastic fringes for a two dimensional assembly of ellipses

122

Explosive
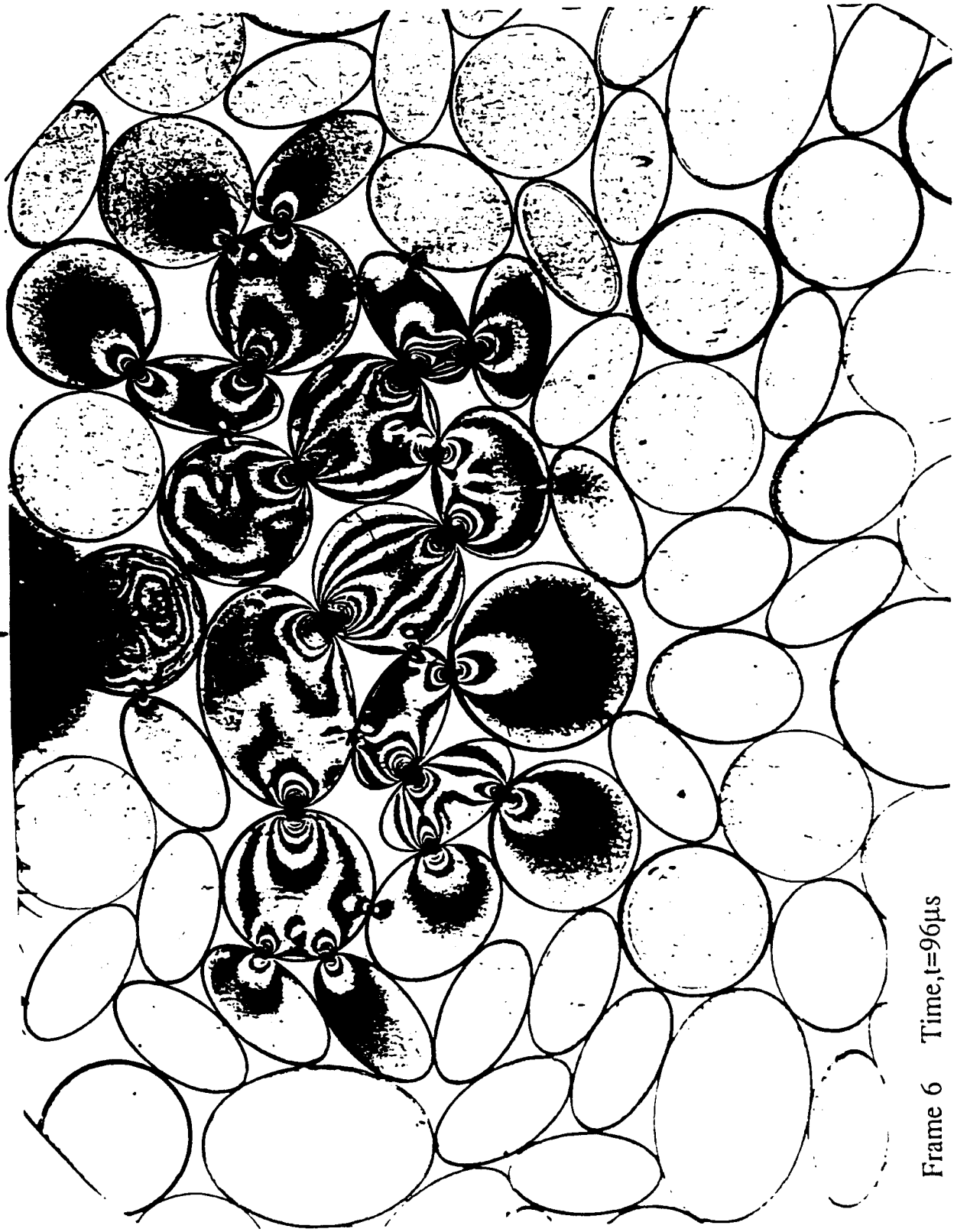
Frame 6   Time,t=96μs

Fig.6.17   Wave propagation in a 2-dimensional array of random shape Homalite 100 particles

CHAPTER 7

THE EFFECT OF PRELOADING

7.1 INTRODUCTION

It has been recognized that the stress history has a profound influence on the cyclic behavior of granular materials. The reason is that a preloading introduces changes in the initial fabric and provides the material with the memory of the stress history. In connection with geophysics the effect of initial stress on the oscillations of gravitating spheres has been considered by Love (1927) for the case of an incompressible material under hydrostatic pressure. He also points out that the compressibility must introduce an important effect of buoyancy. By an extension of Love's method Macelwane and Sohon (1936) have established equations for oscillations of a compressible gravitation sphere. Birch (1938) has applied Murnaghan's (1937) theory of finite strain and shows that the hydrostatic pressure without initial pressure gradient has no effect on the law of wave propagation. Biot (1940) showed that when there is an initial pressure gradient there is a coupling between rotational and compression waves. This coupling is due to a buoyancy effect. This effect is small for usual earthquake waves, but becomes predominant if we consider tidal waves or the modes of oscillation of the earth.

Due to the difficulties in carrying out experiments to investigate directly the effect of prestress on wave propagation phenomenon, researchers instead studied the effect of prestress on the strength or shear modulus of granular materials.

The mechanism underlying the observed strengthening effects in the cyclic behavior of precompressed sand was investigated by Ishihara and Okada (1978) by the use of the triaxial shear test apparatus. The effect of prestress on the liquefaction resistance of sand was conducted by Finn, Bransby and Pickering (1970). They showed an increased resistance to liquefaction occurred when small shear strains (below the level of phase transformation) were applied on the sand sample prior to the cyclic loading test. Whereas, preshearing involving large shear strains (above the level of phase transformation) tended to cause the sand to liquefy easily. Similar strengthening effect due to the small preshearing was also noted by Lee and Albaisa (1974) in their study of cyclic strength

124

of dense sands through the use of the cycle triaxial test device. The effect of small preshearing bears its practical significance in determining cyclic strength of sand deposits subject to a series of small earthquakes occurring over a period of years. Through a shaking table test, Seed, Mori and Chan (1979) showed that the sand subject to a preshearing could sustain several times more cycles than the sand could do in its initial condition without preshearing. Taki and Kitago (1974) also observed an increase in static modulus of a loose dry sand which had undergone several hundred cycles of small-amplitude vibratory stresses. Ishihara (1978) conducted cyclistatic triaxial test to study the possible preshearing effects on the cyclic behavior of saturated sand. He found that small preshearing developed less pore water pressure and shear stress in both sides of triaxial compression and extension. Large preshearing made the material stiffer on one side of triaxial loading, compression or extension, but softer on the other side. The increased resistance to liquefaction or increased stiffness in static loading due to small preshearing is expected to result from the hardening phenomenon which generally occurs in granular materials due to plastic yielding. Chen, Ishibashi and Jenkins (1988) performed torsional experiments on a hollow cylindrical sample consisting of glass spheres with two different diameters to investigate preshearing effects on stress-strain response and dynamic shear modulus. They found that the stress-strain response is stiffer when the material is sheared in the direction of preshearing, softer when sheared perpendicular to it and little changed when sheared in directions 45° to it. The dynamic shear modulus is sensitive to the preshearing. There is little reduction in the modulus when the material is sheared in the direction of preshearing and greater reduction when sheared perpendicular to it.

An experimental investigation of the effect of preloading on wave propagation behavior in granular materials was conducted. A range of ratios of the biaxial compression was used in this study. Investigation was also conducted on the effect of the loading magnitude when the loading ratio was a constant.

7.2 GENERAL THEORY UNDER INITIAL LOADING

The behavior of stress waves in soil cannot be only accounted for by elastic anisotropy or a change in elastic coefficients and the existence of stress introduces an essentially new aspect in the nature of the wave propagation. The velocity of propagation depends on the stress and it is possible to obtain reflection in a medium which has

uniform elastic properties but contains discontinuities of initial stress.

Consider a state of initial stress such that a principal direction is always parallel with the z axis, while the small additional strains are assumed to constitute a state of plane strain in the xy plane. The initial stress is defined by the components S_{11}, S_{22} and S_{12} referred to rectangular axes x, y. They satisfy the equilibrium conditions

$$\frac{\partial S_{11}}{\partial x} + \frac{\partial S_{12}}{\partial y} + \rho(x,y)X(x,y) = 0$$

$$\frac{\partial S_{12}}{\partial x} + \frac{\partial S_{22}}{\partial y} + \rho(x,y)Y(x,y) = 0$$

(7.1)

where ρ is the specific mass and X, Y the components of the body force per unit mass. An elastic element of coordinates x, y acquires the coordinates $\xi=x+u$, $\eta=y+v$ after deformation and rotates through an angle

$$\omega = \frac{1}{2}(\partial v/\partial x - \partial u/\partial y)$$

(7.2)

The stress components after deformation referred to directions which rotate with the material are

$$\sigma_{11} = S_{11} + s_{11}$$

$$\sigma_{22} = S_{22} + s_{22}$$

(7.3)

$$\sigma_{12} = S_{12} + s_{12}$$

The components s_{11}, s_{22} and s_{12} of the stress increment depend only on the strain. This stress may be referred to the original x, y directions and the components then become in first approximation

126

$$\sigma_{xx} = s_{11} - S_{11}$$

$$\sigma_{yy} = s_{22} + S_{22} \qquad (7.4)$$

$$\sigma_{xy} = s_{12} + (S_{11} - S_{22})\omega$$

These are the stresses at the point ξ, η along the x and y directions.

These components satisfy the dynamical equilibrium relations

$$\partial\sigma_{xx}/\partial\xi + \partial\sigma_{xy}/\partial\eta + \mu(\xi,\eta)X(\xi,\eta) = \mu(\xi,\eta)\partial^2 u/\partial t^2$$

$$\qquad (7.5)$$

$$\partial\sigma_{xy}/\partial\xi + \partial\sigma_{yy}/\partial\eta + \mu(\xi,\eta)Y(\xi,\eta) = \mu(\xi,\eta)\partial^2 v/\partial t^2$$

where $\mu(\xi, \eta)$ is the specific mass after deformation.

Now we can express these equations in terms of the independent variable x, y by using transformations of the type

$$\frac{\partial\sigma_{xx}}{\partial\xi} = \frac{\partial\sigma_{xx}}{\partial x}\frac{\partial x}{\partial\xi} + \frac{\partial\sigma_{xx}}{\partial y}\frac{\partial y}{\partial\xi}, \qquad etc. \qquad (7.6)$$

The partial derivatives of x, y with respect to ξ, η are in first approximation

$$\frac{\partial x}{\partial\xi} = \frac{1}{D}\left(1 + \frac{\partial v}{\partial y}\right) \qquad \frac{\partial x}{\partial\eta} = -\frac{1}{D}\frac{\partial u}{\partial y}$$

$$\qquad (7.7)$$

$$\frac{\partial y}{\partial\xi} = -\frac{1}{D}\frac{\partial v}{\partial x}, \qquad \frac{\partial y}{\partial\eta} = \frac{1}{D}\left(1 + \frac{\partial u}{\partial x}\right)$$

where D is the Jacobian

$$D = \frac{d(\xi,\eta)}{d(x,y)} = \begin{vmatrix} 1 + \dfrac{\partial u}{\partial x} & \dfrac{\partial u}{\partial y} \\[2ex] \dfrac{\partial v}{\partial x} & 1 + \dfrac{\partial v}{\partial y} \end{vmatrix} \qquad (7.8)$$

Using these relations and the property

127

$$\rho(x,y) = D\ \mu(\xi,\eta)$$

expressing the conservation of mass Eqs.7.5 become

$$\frac{\partial \sigma_{xx}}{\partial x} + \frac{\partial \sigma_{xy}}{\partial y} + e_{yy}\frac{\partial \sigma_{xx}}{\partial x} + e_{xx}\frac{\partial \sigma_{xy}}{\partial y} - (e_{xy}-\omega)\frac{\partial \sigma_{xx}}{\partial x}$$

$$-(e_{xy}+\omega)\frac{\partial \sigma_{xx}}{\partial y} + \rho X(\xi,\eta) = \rho \frac{\partial^2 u}{\partial t^2}$$

(7.9)

$$\frac{\partial \sigma_{xy}}{\partial x} + \frac{\partial \sigma_{yy}}{\partial y} + e_{yy}\frac{\partial \sigma_{xy}}{\partial x} + e_{xx}\frac{\partial \sigma_{yy}}{\partial y} - (e_{xy}-\omega)$$

$$-(e_{xy}+\omega)\frac{\partial \sigma_{xy}}{\partial y} + \rho Y(\xi,\eta) = \rho \frac{\partial^2 v}{\partial t^2}$$

in which $e_{xx}=\partial u/\partial x$, $e_{yy}=\partial v/\partial y$, $e_{xy}=\frac{1}{2}(\partial v/\partial x+\partial u/\partial y)$ are the strain components. We now substitute the values eq.7.4 for σ_{xx}, σ_{yy} and σ_{xy} and drop terms of higher order than the first; the above equations become

$$\frac{\partial s_{11}}{\partial x} + \frac{\partial s_{12}}{\partial y} + \rho u\frac{\partial X}{\partial x} + \rho v\frac{\partial X}{\partial y} + \rho \omega Y - 2S_{12}\frac{\partial \omega}{\partial x} + (S_{11}-S_{22})\frac{\partial \omega}{\partial y}$$

$$+e_{yy}\frac{\partial S_{11}}{\partial x} + e_{xx}\frac{\partial S_{12}}{\partial y} - e_{xy}\left(\frac{\partial S_{11}}{\partial y} + \frac{\partial S_{12}}{\partial x}\right) = \rho \frac{\partial^2 u}{\partial t^2}$$

(7.10)

$$\frac{\partial s_{12}}{\partial x} + \frac{\partial s_{22}}{\partial y} + \rho u\frac{\partial Y}{\partial x} + \rho v\frac{\partial Y}{\partial y} + \rho \omega X + (S_{11}-S_{22})\frac{\partial \omega}{\partial x} + 2S_{12}\frac{\partial \omega}{\partial y}$$

$$e_{yy}\frac{\partial S_{12}}{\partial x} + e_{xx}\frac{\partial S_{22}}{\partial y} - e_{xy}\left(\frac{\partial S_{12}}{\partial y} + \frac{\partial S_{22}}{\partial x}\right) = \rho \frac{\partial^2 v}{\partial t^2}$$

In order to obtain these equations account must be taken of the initial equilibrium conditions eq.7.1 and identities

128

$$\partial e_{xx}/\partial y = (\partial/\partial x)(e_{xy}-\omega)$$

$$\partial e_{yy}/\partial x = (\partial/\partial y)(e_{xy}+\omega)$$

(7.11)

The stress increments s_{11}, s_{22} and s_{11} depend only on the strain. They may be taken as linear functions of the strain components

$$s_{11}=B_{11}e_{xx}+B_{12}e_{yy}+B_{13}e_{xy}$$

$$s_{22}=B_{21}e_{xx}+B_{22}e_{yy}+B_{23}e_{xy}$$

(7.12)

$$s_{12}=B_{31}e_{xx}+B_{32}e_{yy}+B_{33}e_{xy}$$

Assuming the existence of a potential energy function of the strain it is possible to prove that the elastic coefficients must satisfy the relations

$$B_{12}+S_{12}=B_{21}+S_{22}$$

$$B_{13}-S_{12}=B_{31}+\tfrac{1}{2}S_{12}$$

(7.13)

$$B_{23}-S_{12}=B_{32}+\tfrac{1}{2}S_{12}$$

It is only in case of initial.hydrostatic pressure ($S_{11}=S_{22}$, $S_{12}=0$) that the elastic coefficients will be symmetric ($B_{ij}=B_{ji}$).

The boundary conditions along an element dx, dy of the boundary contour are found to be

$$(s_{11}-S_{12}\omega)dy-(s_{12}-S_{22}\omega)dx=dF_x$$

(7.14)

$$(s_{12}+S_{11}\omega)dy-(s_{22}+S_{12}\omega)dx=dF_y$$

where dF_x, dF_y are the projection of the force acting on the boundary element dx, dy.

We consider a simple case of a hydrostatic pressure with uniform pressure gradient. This approximates the state of stress in a soil material near the surface of the earth. Where under the action of gravity the influence of creep has been acting a sufficiently long time so that the stress condition at every point has become isotropic.

Taking the y axis positive downward we have

X=0, Y=g.

where g is the acceleration of gravity. Also $S_{11}=S_{22}$ and $S_{12}=0$. We assume the specific mass to be uniform (ρ=constant). With these equations eqs.7.10 become

$$\frac{\partial s_{11}}{\partial x} + \frac{\partial s_{12}}{\partial y} + \rho g \frac{\partial v}{\partial x} = \rho \frac{\partial^2 u}{\partial t^2}$$

$$(7.15)$$

$$\frac{\partial s_{12}}{\partial x} + \frac{\partial s_{22}}{\partial y} - \rho g \frac{\partial u}{\partial x} = \rho \frac{\partial^2 v}{\partial t^2}$$

These equations are different from the classic ones for an initially unstressed medium. The additional terms are due to the existence of a pressure gradient. In order to investigate the behavior of tne waves for those case, let us assume the stress-strain relations to be Hooke's law for an isotropic medium

$s_{11} = \lambda e + 2G e_{xx}$

$s_{22} = \lambda e + 2G e_{yy}$ $\qquad (7.16)$

$s_{12} = 2G e_{xy}$

By substitution in Eq. (7.15) we find

$$G\nabla^2 u + (G + \lambda)\frac{\partial e}{\partial x} + \rho g \frac{\partial v}{\partial x} = \rho \frac{\partial^2 u}{\partial t^2}$$

$$(7.17)$$

$$G\nabla^2 v + (G + \lambda)\frac{\partial e}{\partial y} - \rho g \frac{\partial u}{\partial x} = \rho \frac{\partial^2 v}{\partial t^2}$$

We derive the following equations for the dilatational e and rotation ω by the usual method

$$(2G + \lambda)\nabla e^2 + 2\rho g \frac{\partial \omega}{\partial x} = \rho \frac{\partial^2 e}{\partial t^2}$$

$$(7.18)$$

$$G\nabla^2 \omega - 2\rho g \frac{\partial e}{\partial x} = \rho \frac{\partial^2 \omega}{\partial t^2}$$

These equations show the existence of coupling between longitudinal and transversal waves. This coupling is due to an initial pressure gradient. The physical meaning of this coupling is as follows. Consider a dilatational plane wave propagation in

130

the horizontal direction. At a point where the material is compressed it is denser and therefore has a negative buoyancy, while in the region of positive dilation the buoyancy is positive. The dilatational wave is therefore associated with a periodic distribution of vertical buoyancy force which generates a transverse wave. Conversely a transverse wave propagating in the horizontal direction produces a dilatational wave. In this case a portion of the material which is horizontal in the initial state undergoes a rotation and the initial pressure gradient acquires a horizontal component of alternating sign which causes a dilatational wave. It has been shown that the effect increases with the wave-length.

7.3 EXPERIMENTAL PROCEDURE

In last section, it has been shown that even in an isotropic material there is a coupling between longitudinal and transversal waves due to the initial pressure gradient. In a granular material, even under uniform initial contact loads, there is an inherent stress gradient inside the particle. This then leads to an inevitable coupling between longitudinal and transversal waves. This kind of coupling as well as particle reflection effects result in an extremely complicated wave phenomena in a granular material under preloading. Experiments were conducted on BCC models under biaxial preloading, as shown in Fig. 7.1. Attention was concentrated on the investigation of the effect of preload ratio and amplitude on wave velocity and wave attenuation. Dynamic photoelasticity along with high speed photography were used in this study to record the dynamic event. The granular media was simulated by Homalite-100 discs which were so arranged as to simulate a body centered cubic packing granules. A specially designed loading fixture, as shown in Fig. 7.1, was used to obtained the biaxial preloading. The loading fixture consists of a cylinder driven by a hydraulic pump, a block which is mounted at the end of the cylinder, a three block movable frame and a fixed frame used to support the cylinder and the movable frame. When the cylinder moves down, the block on the cylinder loads the model from the top. The model then passes force to the bottom block of the movable frame. The bottom block then pulls the two side blocks inward through the links connecting them. Therefore the model inside the fixture is loaded biaxially. The maximum preload is limited by the capacity of the pump. The preload ratio is varied by using different spacers between the model and the movable frame. A 11 rows by 11 columns disc assembly was used to simulate the BCC granular media. Dynamic loading was

achieved by firing a small amount of 50 mg PETN in a specially made charge holder as also shown in Fig.7.1. The charge holder was placed near one corner of the disc assembly to avoid the reflection effect on the particles of interests. In the following discussion, x is defined as the direction of wave propagation, while y is the direction perpendicular to the wave propagation.

7.4 RESULTS AND DISCUSSION

Dynamic photoelasticity has the advantage of providing a view of the whole stress field during wave propagation in a granular assembly under preloading. First, the assembly was loaded statically. A picture of the static fringes was taken for the determination of the biaxial preloads. Four typical pictures of dynamic fringes obtained for an experiment with the preload ratio being $P_x/P_y=1.5$ are shown in Fig.7.2. Wave propagation in a granular assembly under preloading can be seen clearly in these pictures. The wave propagation phenomena in biaxial preloaded granular media shows the similar dependence of the angle made by the normals of contacting granules on wave propagation to that of zero preload condition. When the contact angle is equal or larger than $90°$, no mechanical signal can pass through that contact. The disturbance of the preloading fringes gives the position of the wave front as well as the average wave velocity. While the dynamic fringes recorded by the high speed camera along with the static preloading fringes give the wave attenuation. Wave velocity as a function of preload which is in the direction of wave propagation for the ratio of P_x/P_y equal to 4 is shown in Fig.7.3. The velocity as a function of preload which is in the direction perpendicular to the propagation for the ratio of P_x/P_y equal to 0.25 is shown in Fig.7.4. It can be seen from these figures that the wave velocity increases with the increase of preload for both ratios. When the preload is less than 60 % of the dynamic load, the velocity increases at an increased rate for both preload ratios. It increases at a lower rate afterwards. Part of this is due to the closing up of the pore space thus forcing individual particle into better contact. The maximum preload used in this investigation is 4500 N, which is 90% of the peak dynamic load. Under this maximum preload, the maximum wave velocity for the preload ratio of 0.25 is 1380 m/s, which is about 28% higher than that of zero preload. The wave velocity for the ratio of 4 is less than that of 0.25. The average velocity difference between these two preload ratio is less than 5 %. One reason for this is because the particles used are

isotropic, preload in either direction will have the same effect on the material density of particles in a BCC assembly. As the preload had little effect on either the fabric of the BCC assembly or the wave travel path, the wave velocity is almost independent of the preload ratio. The small difference of the average wave velocity between these preload ratios suggests that the wave velocity is dependent of the average preload. The wave velocity plotted as a function of the average preload is shown in Fig. 7.5. The velocity increases as the average preload increases.

The wave attenuation for the wave travelling from the disc after the one adjacent to the explosive plotted as a function of preload for these two ratios is shown in Figs.7.6 and 7.7. For zero preload, the wave attenuation for the same distance of travel is 18 %. This attenuation was increased by about 60 % as the preload increases to 4500 N for the preload ratio of 4. The wave attenuation for larger preload ratio is less than that of smaller preload ratio. This is because the initial contact length in the direction of wave propagation for the ratio of 4 is larger than that for the ratio of 0.25. The larger contact length leads to less reflection and less dispersion at the contacts. Thus results in lower wave attenuation. However, the energy from the explosive tends to pass through both chains in contact with the charge holder in the same amount. The final contact length difference at the corresponding points is negligible. Thus the maximum difference of average wave attenuation between these two ratios is about 10%.

The fluctuation and scattering of experimental data was largely due to the friction effect which results in a certain amount of variation in the initial preload at different contact, therefore leads to different initial contact length.

7.5 SUMMARY

The results of this investigation reveal that preload amplitude has effect on both velocity and attenuation of stress waves in a BCC granular model. However, the preload ratio has less effect on wave velocity than on wave attenuation. Due to the limited capacity of the biaxial preloading fixture, the maximum preload obtained in this investigation could not be larger than the dynamic loading used. It was noted in this investigation that the peak dynamic load generated by the same amount of explosive was a constant for different preload amplitude. This means the increment of the dynamic load decreased as the preloads increased, as shown in Fig.7.8.
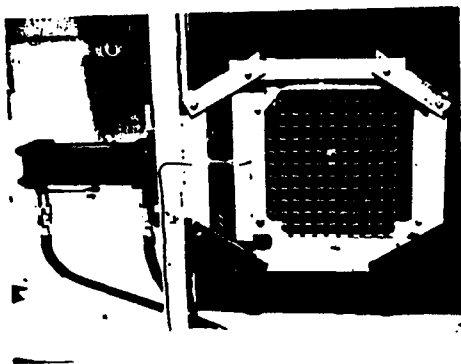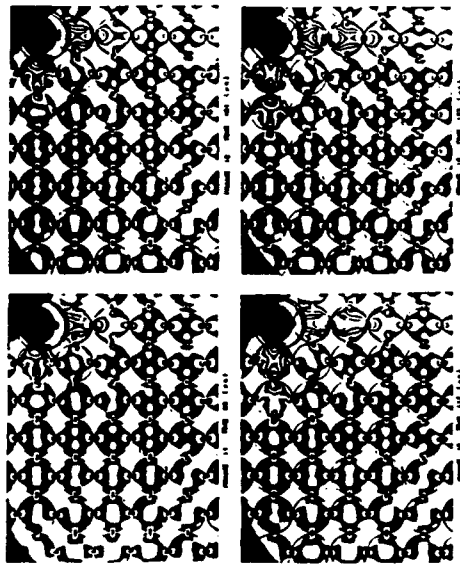
Fig. 7.2 Typical pictures showing dynamic isochromatic fringes

Fig. 7.4 Wave velocity (V_x) vs. preload (P_x/P_y = 0.25)
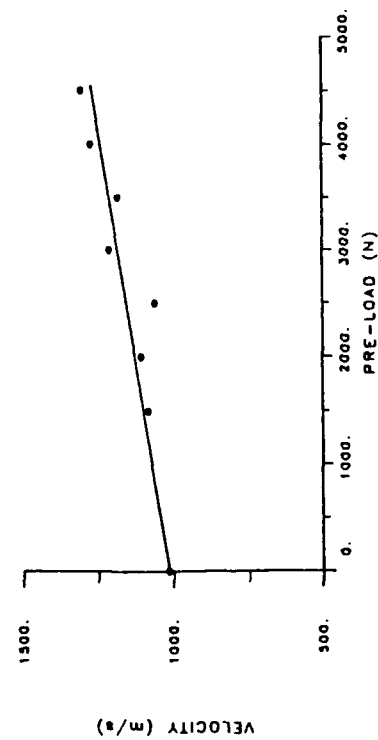

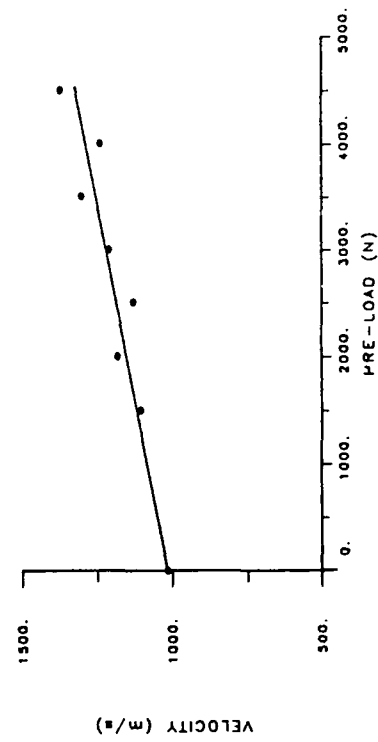Fig. 7.1 Biaxial preloading fixture
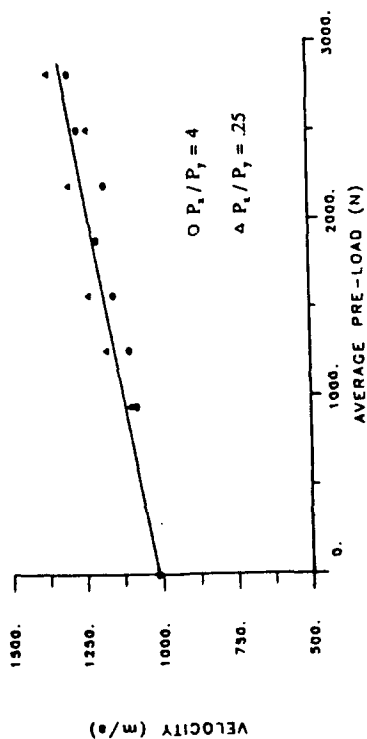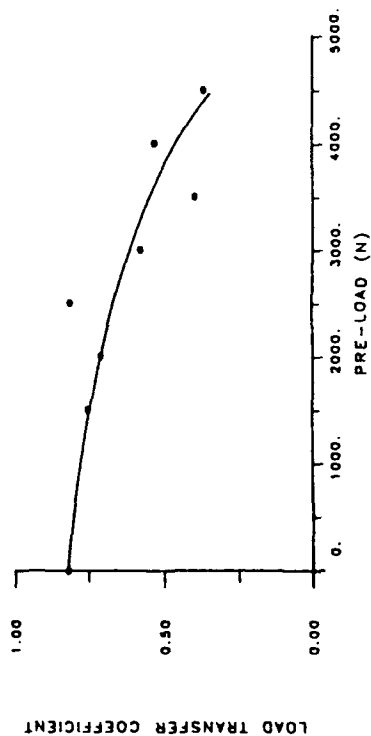

Fig. 7.3 Wave velocity (V_x) vs. preload (P_x/P_y = 4)

134

Fig. 7.6 Wave attenuation vs. preload ($P_x/P_y = 4$)

Fig. 7.8 Peak dynamic contact load vs. preload

Fig. 7.5 Wave velocity (V_x) vs. average preload ($P_x/P_y = 4$)

Fig. 7.7 Wave attenuation vs. preload ($P_x/P_y = 0.25$)

135

CHAPTER 8

MODELING WAVE PROPAGATION IN GRANULAR MEDIA
USING ELASTIC NETWORKS

8.1 INTRODUCTION

Geological materials such as sand, gravel and rock are composed of large numbers of individual particles packed in complex spatial arrangements. Such materials are commonly referred to as *granular media,* and the load transfer is primarily conducted through contact interactions between adjacent particles. The static and dynamic response of these types of materials has been studied for many years by members of the soil mechanics and geophysical community. An understanding of the dynamic behavior of such materials is important in many geophysical applications involving seismic and blast loading phenomena, and active interest also exists in applications to dynamic compaction of powders in pharmaceutical and metallurgical processes.

Early attempts at modeling granular media behavior used continuum mechanics, e.g elasticity, plasticity or viscoelasticity. However, it was gradually realized that the complex microstructural nature of these materials requires that a microstructural model be used to more accurately predict the mechanical behavior. Granular media has been commonly described as a collection of distinct particles which can displace from one another with some degree of independence and which interact basically only through contact mechanisms. Because of this constituency, these materials establish discrete paths along which major load transfer occurs; see for example the work of Oda, Konishi and Nemat-Nasser (1982). The local microstructure or *fabric,* i.e. the local geometrical arrangement of particles, plays a dominant role in establishing this discrete load transfer phenomena. With regard to the propagation of dynamic loadings, it is found that the discrete nature of the media creates a structured waveguide network of selective paths for the waves to propagate along. The propagational characteristics of wave speed, amplitude attenuation, and dispersion are thus related to the local fabric and the established wave paths.

Early attempts at modeling granular media involved simulations with arrays of elastic disks or spheres. Studies of the dynamic response of granular media using a

microstructural approach began with the work of Iida (1939) on simple lumped mass-spring systems. Later, classic studies by Duffy and Mindlin (1957) investigated the contact mechanics effects on the dynamic load transfer. More recently, there has been a large volume of micromechanics research applied to a variety of complex materials. *Fabric tensor theories* have been developed by Nemmat-Nasser, et.al., (1982, 1984), and Oda, et.al., (1982) to investigate the microstructural constitutive behavior of granular media. A special continuum mechanics theory called the *distributed body theory was* developed by Goodman and Cowin (1972) for materials with discontinuous fields, and this model was applied to wave propagation in geological materials by Sadd and Hossain (1988). Numerical simulations of wave propagation in these materials was carried out by Sadd,et.al.(1989b), Bathurst and Rothenburg (1989), and Thornton and Randall (1988) using the *distinct element method* first formulated by Cundall et.al' (1979). Extensive experimental studies using methods of dynamic photomechanics and strain gages have been conducted on these problems by Shukla and Nigam (1985), Shukla et.al.(1988a), and Shukla and Damania (1987).

Based on the fact that granular materials transmit loads only through nearest neighbor contact, this mechanism may be modeled as a simple load carrying link between adjacent mass centers. Through the application of this concept, a load carrying network can be established for various particle packing geometries, see Figure 8.1. Such network theories have been employed in static theories for granular media by Trollope and Burman (1980), Bagster and Kirk (1985), Bideau et.al. (1986) and Thornton and Barnes (1986). In related work, Burt and Dougill (1977) used a simple planar pin-jointed truss network to simulate the stress-strain behavior of heterogeneous materials which exhibit progressive failure and strain softening behavior.

Following along these similar lines, Boardman (1990) developed a dynamic finite element model for wave propagation studies based upon the elastic network representation. In his work, each link in the network was taken as a one-dimensional dynamic bar element with lumped mass at the end nodal points. The material was chosen to be cohesionless, thus requiring that no element be capable of transmitting tensile loadings. This produced a nonlinear finite element model which was solved using an iterative scheme. The present study is a generalization of Boardman's work to include

137

both normal and tangential contact loadings through the development of a new one-dimensional dynamic element. The element possesses both normal and tangential stiffness and damping coefficients whose numerical values were obtained from dynamic photoelastic experiments. Comparisons of the proposed numerical model with experimental results are given.

8.2 THE FINITE ELEMENT MODEL

As previously mentioned, a granular media is composed of a large number of independent particles in contact with each other as shown in Figure 8.1a. For the case of dry cohesionless media, neighboring particles transmit normal and tangential loads only through contact mechanisms. This type of load transfer process can be modeled by replacing each contact interaction with a tensionless load carrying link with prescribed load transmission characteristics. Applying this process for all contacts in an aggregate assembly, a network of links is established as illustrated in Figure 8.1b. For the case of homogeneous circular particles as shown in Figure 8.1, all links connect the mass centers of the particles to each other.

The load transfer characteristics of the links in such established networks are modeled using the finite element method whereby each link is represented by a one-dimensional finite element similar to bar or beam elements. The *shape* or *interpolation function* concept normally used in finite element formulation is not used for this case because of the contact mechanics processes that occur at points within the element. Thus the generation of the element stiffness matrix is accomplished through a direct stiffness method rather than using a variational scheme.

The generic element, shown in Figure 8.2, is taken to be a two-noded element connecting the particle centers. The kinematics of each granule is determined through specification of the two in-plane displacements and the rotation about the mass center. Thus, the interaction between two disks is characterized by the generalized element displacement vector $\{u_1,v_1,\theta_1,u_2,v_2,\theta_2\}^T$. The corresponding generalized forces would include the horizontal and vertical nodal forces and a nodal moment. Therefore the static element equation can be written as

138

$$[K^{(e)}] \begin{Bmatrix} u_1 \\ v_1 \\ \theta_1 \\ u_2 \\ v_2 \\ \theta_2 \end{Bmatrix} = \begin{Bmatrix} F_{x_1} \\ F_{y_1} \\ M_1 \\ F_{x_2} \\ F_{y_2} \\ M_2 \end{Bmatrix} \tag{8.1}$$

The elements of the stiffness matrix $K_{ij}^{(e)}$, represent the ith-force corresponding to a unit j^{th}-displacement. For example, in order to calculate $K_{11}^{(e)}$ an element displacement vector of the form $\{1,0,0,0,0,0\}^T$ is applied to the element model. Through the normal contact, equilibrium produces the force system shown in Figure 8.3a, and this results in an element force vector of the form $\{K_n,0,0,-K_n,0,0\}^T$, where K_n is regarded as the *normal stiffness* between the two generic disks. It should be pointed out that for the static case, this value could be determined from Hertz contact theory. Thus $K_{11}^{(e)} = -K_{14}^{(e)} = K_n$.

Next consider the case of a displacement vector of the form $\{0,0,1,0,0,0\}^T$. At the contact point, there is a *relative tangential displacement* $\Delta v = \theta_1 r_1$, and the *tangential contact force* may be written as $F_t = K_t r_1$, where K_t is the *tangential stiffness coefficient*. In order to maintain equilibrium, each disk must have forces and moments as shown in Figure 8.3b. For this case the force vector thus becomes $\{0,K_t r_1,K_t r_1^2,0,-K_t r_1,-K_t r_1 r_2\}^T$, and thus $K_{13}^{(e)}=0$, $K_{23}^{(e)}=K_t r_1$, $K_{33}^{(e)}=K_t r_1^2$, $K_{43}^{(e)}=0$, $K_{53}^{(e)}=-K_t r_1$, $K_{63}^{(e)}=K_t r_1 r_2$. The various other stiffness elements are computed in an analogous fashion yielding

$$[K^{(e)}] = \begin{bmatrix} K_n & 0 & 0 & -K_n & 0 & 0 \\ . & K_t & K_t r_1 & 0 & -K_t & K_t r_2 \\ . & . & K_t r_1^2 & 0 & -K_t r_1 & K_t r_1 r_2 \\ . & . & . & K_n & 0 & 0 \\ . & . & . & . & K_t & -K_t r_2 \\ . & . & . & . & . & K_t r_2^2 \end{bmatrix} \tag{8.2}$$

Because real granular materials exhibit damping, the finite element model should

contain this feature. This is easily incorporated through a velocity dependent dashpot at the element level, and by employing similar methods as outlined for the stiffness matrix, a *damping element matrix* $[C^{(e)}]$, can be determined. The inertia modeling will assume that the disk mass is concentrated at the disk center(i.e. at each node) and thus the mass matrix $[M^{(e)}]$ will be diagonal. Therefore, the complete model is given by the usual element equation

$$[M^{(e)}]\{\ddot{u}\} + [C^{(e)}]\{\dot{u}\} + [K^{(e)}]\{u\} = \{P^{(e)}\} \tag{8.3}$$

The discrete nature of cohesionless granular media causes the load transfer between particles to behave discontinuously in that if any two adjacent disks displace such that the relative distance between their centers becomes greater than the sum of their respective radii, the contact forces must vanish. Therefore, the contact model can only transmit compressive forces and thus the actual stiffness and damping matrices for any typical element connecting the ith and j^{th} disks must be multiplied by the function $H((r_i+r_j)-\ell_{ij})$, where $H(.)$ is the Heaviside step function operator and ℓ_{ij} is the computed distance between the disk centers. This situation causes the numerical routine to become non-linear, and requires a load incrementation procedure along with an iteration solution scheme based on the Newton-Raphson method. Thus during the load incrementation process all elements are continually checked for compression-only behavior resulting in some elements being turned off while others possibly being turned back on. Finally, the time integration of equation (8.3) was accomplished using a direct integration method based on the Newmark scheme.

8.3 DETERMINATION OF MODEL PARAMETERS

In order to apply the developed finite element model to specific problems of wave propagation in granular media, the mass, stiffness and damping matrices must be determined for the media under study. Since the inertia modeling employed the lumped mass concept, the elements of the diagonal mass matrix are completely determined by the density and size of the individual particles. The stiffness and damping matrices are however, not as easily calculated. As mentioned previously, for the static case the normal and tangential contact stiffnesses K_n and K_t may be estimated from Hertz or more general contact theories. However, for the dynamic case the contact mechanics problem becomes

quite difficult to solve. It is for this case that experimental results were used to help in the determination of particular parameters.

The specific experiments involved the use of dynamic photoelasticity to photographically collect information on the wave propagation in transparent model assemblies of granular materials. Details on the experimental techniques can be found in previous papers (Shukla and Nigam 1985, Shukla et.al.1988, and Shukla and Damania 1987) and will not be repeated here. The photographic data collected at various instants of time provides sufficient information to determine the wave speed and the amplitude (intergranular contact force) behavior for specific granular assemblies which have been subjected to explosive loading.

In order to determine the normal contact stiffness and damping parameters, experiments were conducted on a single straight chain of equal sized disks of radius 12.7mm and thickness 6.35mm. The disk material was Homalite-100 which has a mass density of 1.2×10^3 kg/m^3. Typical photoelastic data in the form of isochromatic fringe patterns is shown in Figure 8.4 which illustrates a time sequence of the dynamic event. Through a trial-and-error process, finite element predictions were calculated until satisfactory agreement was reached with the experimental data. Thus by matching both the wave speed and the amplitude attenuation, the normal stiffness and damping parameters were determined as $K_n = 7.04 \times 10^6$ N/m and $C_n = 35$ Ns/m.

The tangential stiffness and damping coefficients were determined from a simple branch type of assembly shown in Figure 8.5. For this geometry, there exists tangential contact forces between particles in the assembly. Again fitting the numerical predictions with the experimental data determined the values $K_t = 10^6$ N/m and $C_t = 10$ Ns/m.

8.4 MODEL RESULTS

The developed elastic network, finite element model will now be used to simulate the propagation of dynamic signals through specific assemblies of model granular materials. For all of the cases under study, the input loading was taken to be a triangular time pulse of 60μs duration. It was felt that this type of input would reasonably simulate the explosive loadings used in the experiments. The time stepping scheme used an increment $\Delta t = 1\mu$s. Comparisons of the numerical predictions are made with existing photoelastic experimental data.

8.4.1 Single Chain Assembly

The first example investigated was the straight single chain assembly previously shown in Figure 8.4. For this case the wave speed predicted from the model was 1071 m/s which matched quite well with the experimental value of 1080 m/s. In regard to the wave amplitude as measured by the intergranular contact load, comparisons were made for the maximum contact load between disks. These peak values were then normalized with respect to the input loading to provide a consistent and convenient comparison technique. Results of these peak contact load values for this assembly are shown in Figure 8.6 with the upper number specifying the normal loading, the lower number giving the tangential component, and the values in parentheses corresponding to the experimental results of the normal component. Since the single chain is a symmetric assembly, there will be no tangential contact loadings developed irregardless of the values of the tangential stiffness and damping. Of course, numerical results for this case matched experimental values quite well since this assembly was the one used to calibrate the numerical model parameters.

8.4.2 Branch Assembly

The second assembly that was studied was the simple chain branch geometry shown previously in Figure 8.5. The two branch angles θ_1 and θ_2 control how much wave motion will be transferred into and along each branch. Figure 8.7 shows results of the contact force ratio P_3/P_2 for both the normal and tangential components for the case of $\theta_1 = \theta_2 = 30°$. The numerical predictions compare reasonably well with the experimental results. Various other cases with different branch angles have been computed, and some of these results are shown in Table 8.1. It is seen from this Table that the normal peak contact loading in a given branch generally decreases as the branch angle increases.

8.4.3 Hexagonal Close Packing

Another assembly which was studied was the hexagonal close packing as shown in Figure 8.8. For this case the disks are in their closest packing situation with six contacts per disk. Waves will move in several different paths determined by the assembly structure and the input location and direction. For the loading shown in the Figure 8., numerical values along a main transfer path and a secondary path are shown. Again, numerical results for both the normal and tangential peak loadings are shown and experimental

normal loading values are also given for comparison. It is observed that for this case very little tangential loading occurs. Figure 8.9 illustrates a second hexagonal assembly that was studied in which the loading direction has been changed. Again very little tangential loadings are present for this case. The effect of removing a disk to create a void in this geometric fabric is shown in Figure 8.10. Results for this void case appear to cause an increase in the local tangential forces around the void. Finally Figure 8.11 illustrates the case of replacing a disk with another of higher density and stiffness to create a heterogeneous inclusion. The inclusion was modeled by a disk of steel material with properties $K_n = 1.58 \times 10^7$ N/m , $C_n = 78.72$ N s/m , $\rho = 7.8 \times 10^3$ Kg/m^3. The inclusion, like the void, causes local wave scattering; however, it appears that the inclusion produces less local tangential loadings than the void case.

8.4.4 Random Assembly

The final assembly which was studied was a randomly arranged system of equal sized disks as shown in Figure 8.12. The irregular packing geometry produces a quite varied wave propagational system, and creates tangential loadings at most of the intergranular contacts. The comparisons of the numerical predictions with the experimental data for the normal components are not quite as good as found in the other assemblies. This may be a result of the significant amount of tangential loading present, and could imply that a more sophisticated tangential stiffness law may be needed.

8.5 CONCLUSIONS

A microstructural wave propagation model has been presented for cohesionless granular materials in which the dynamic load transfer between adjacent particles is simulated through a special finite element. The particulate media is thus modeled by an elastic network which accounts for the contact interactions and local microstructure. Both the displacement and rotation of the particles are taken into account, and this leads to a scheme to calculate both normal and tangential intergranular contact forces. Necessary model stiffness and damping parameters were determined from experimental photoelastic data from simple single chain and branch geometries. Several different types of two-dimensional assemblies were then studied using the proposed numerical routine, and comparisons with existing experimental data were made. Numerical predictions were generally within 10-20% of most of the experimental data.

The current stage of the model employing linear stiffness and damping properties gave reasonable results. However, it appears from both the experimental correlations and general insight to the nature of the dynamic contact phenomena between particles, that a more sophisticated nonlinear contact law would provide a more accurate model of the physics. Such nonlinear contact laws have been used with success in our distinct element modeling and future directions of this type of modeling could include such a nonlinear finite element along with a more generalized tangential force response.

The present finite element method of analysis can be compared with our other numerical technique employing the distinct element method (Sadd,et.al.1989a). Comparisons of the results of the two methods with experimental data indicated that each numerical technique provided about the same level of correlation. It was generally found that the finite element scheme was more computationally efficient, solving the same problem on the same hardware in a shorter CPU time. However, the distinct element model allows for general (finite) particle motions; whereas the current finite element approach is limited to small deformations, thus precluding significant particle or fabric rearrangement.

Table 8.1. Peak Contact Force Ratio for Branch Model

θ_1	θ_2	θ_1 Side		θ_2 Side	
		Normal	Tangential	Normal	Tangential
$30°$	$30°$	.554	-.054	.554	.054
$30°$	$45°$	.631	-.062	.486	.082
$30°$	$60°$	.694	-.078	.399	.106

144
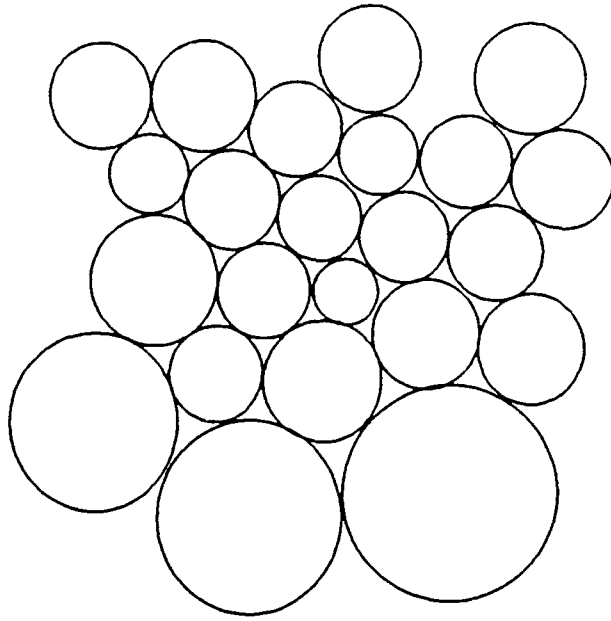
(a) Simulated Granular Media
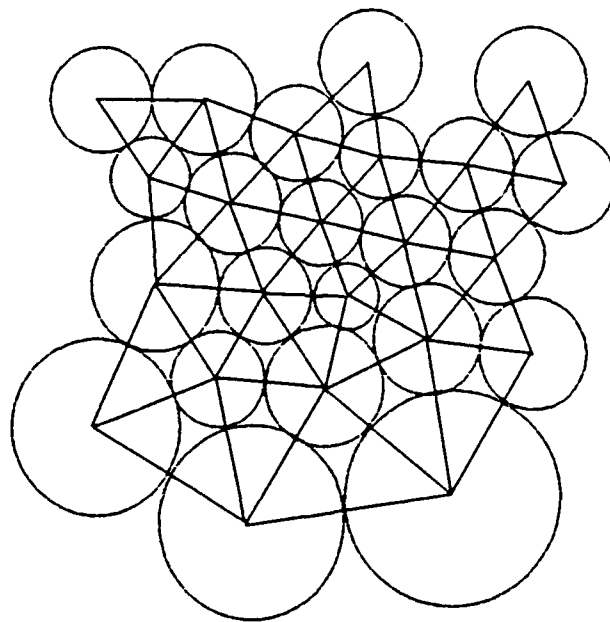
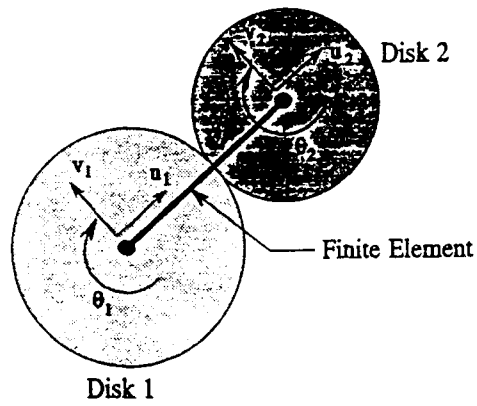(b) Equivalent Elastic Network

Fig. 8.1 Elastic network modeling concept
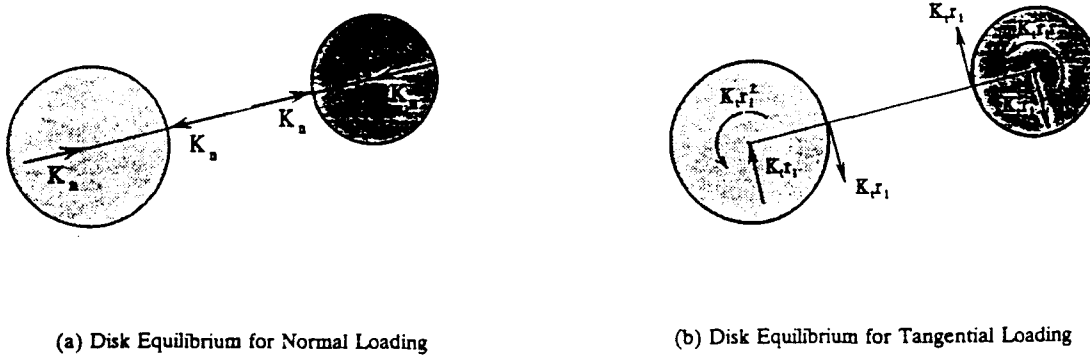
145

Fig. 8.2 Basic element of the elastic network

(a) Disk Equilibrium for Normal Loading

(b) Disk Equilibrium for Tangential Loading

Fig. 8.3 Disk equilibrium

146

Fig. 8.4 Isochromatic fringes obtained in a
single chain granular arrangement
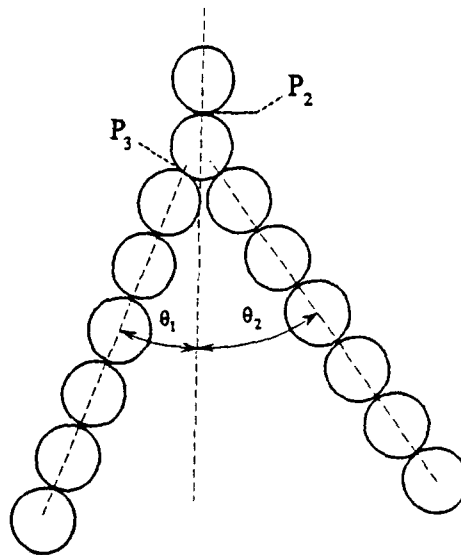
Fig. 8.5 Simple branch assembly
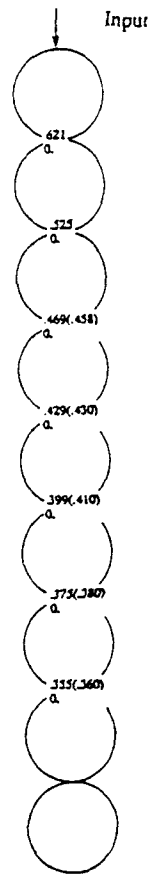
147

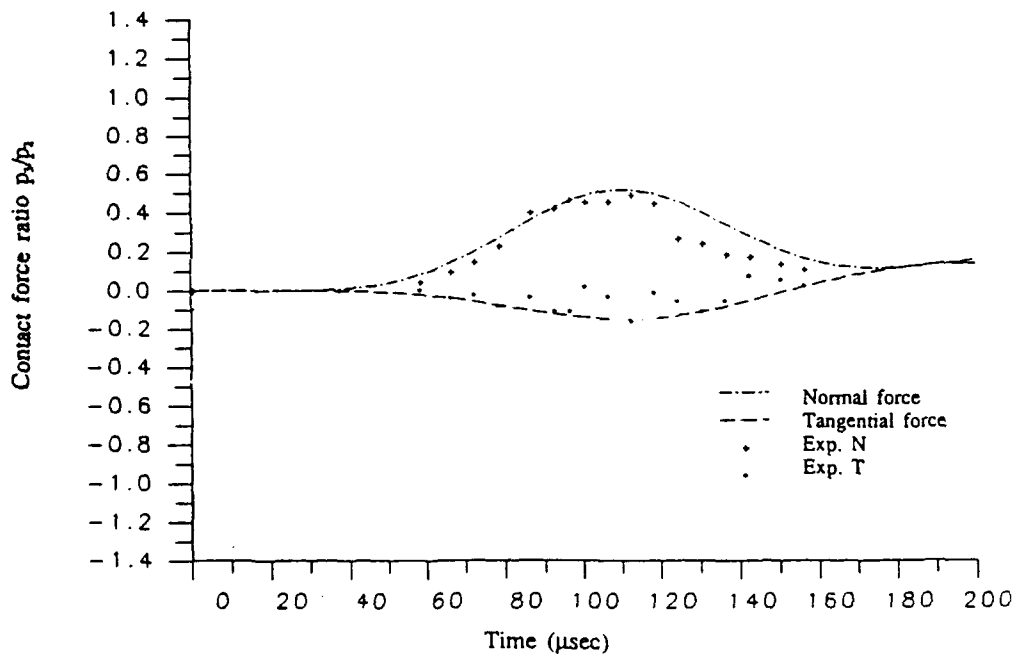Fig. 8.6 Results and comparison of normalized peak
contact loading in the single chain assembly

Fig. 8.7 Normalized and tangential contact force ratios
for the simple branch assembly

148
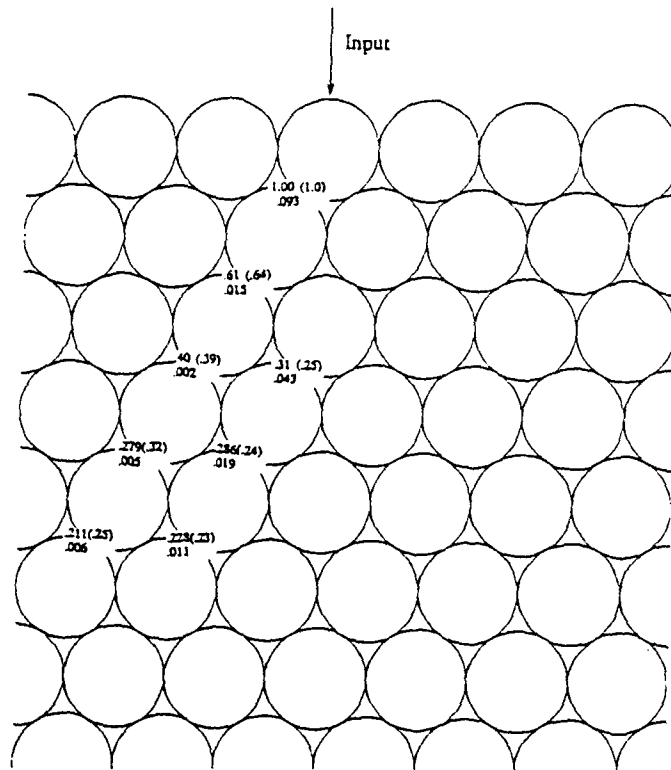
Fig. 8.8 Results and comparison for the HCP assembly
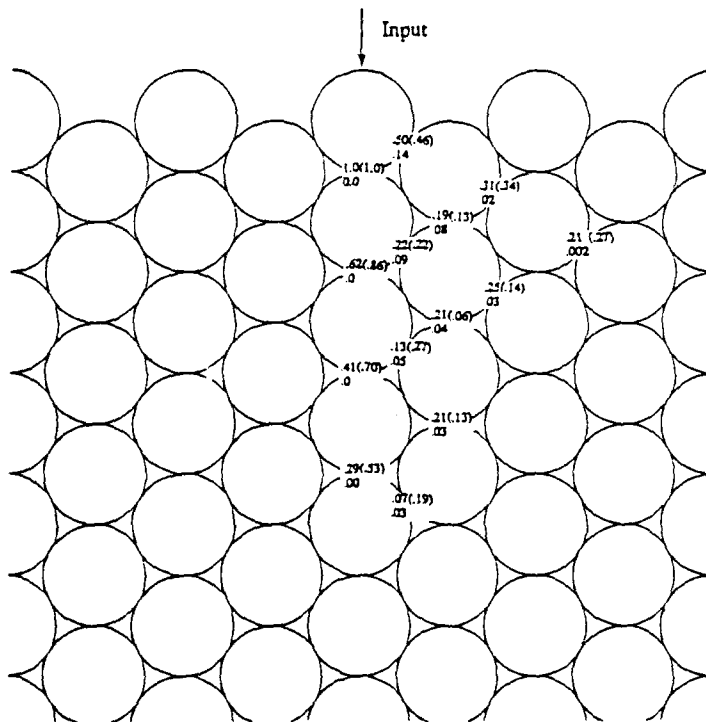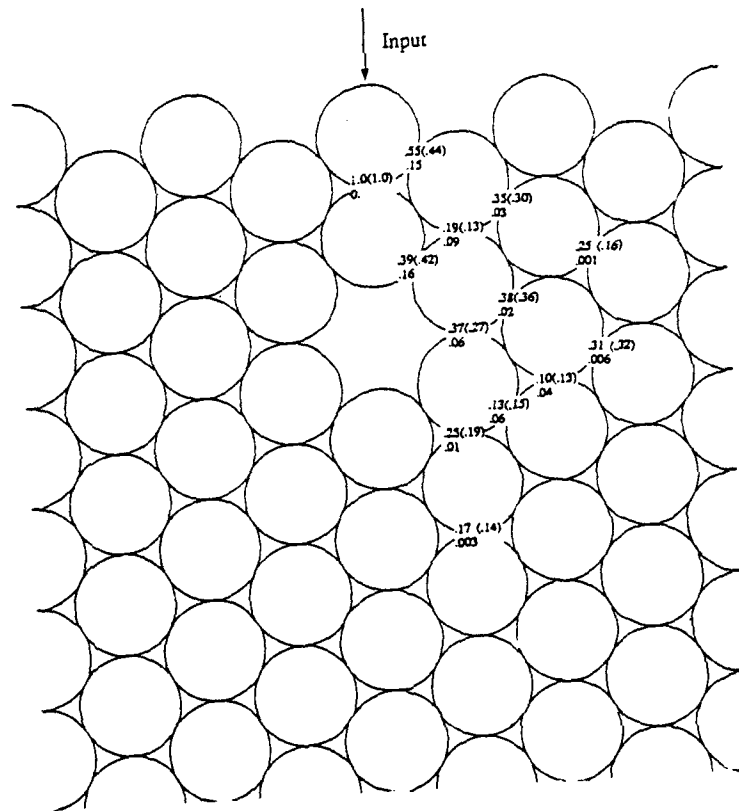

Fig. 8.9 Results and comparison for a second HCP assembly

149

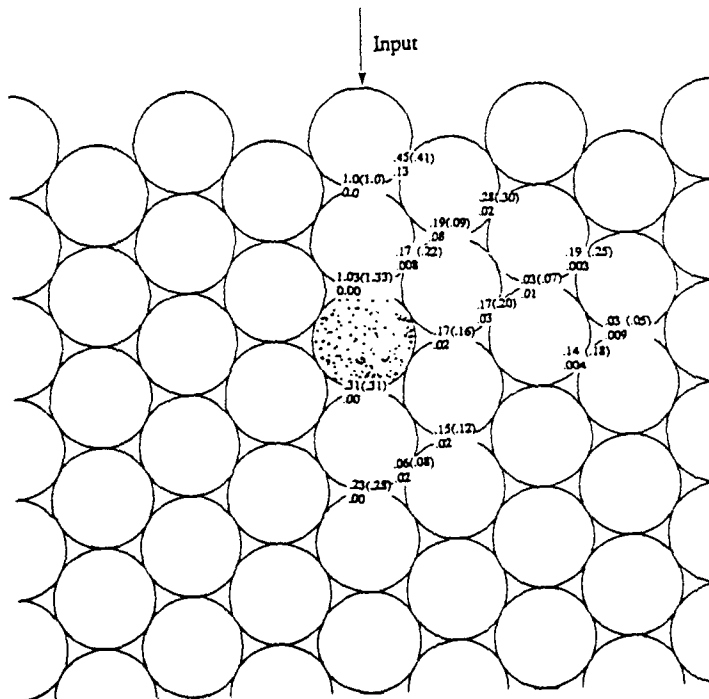Fig. 8.10 Results and comparisons for a HCP assembly contained a void

Fig. 8.11 Results and comparison for a HCP assembly contain
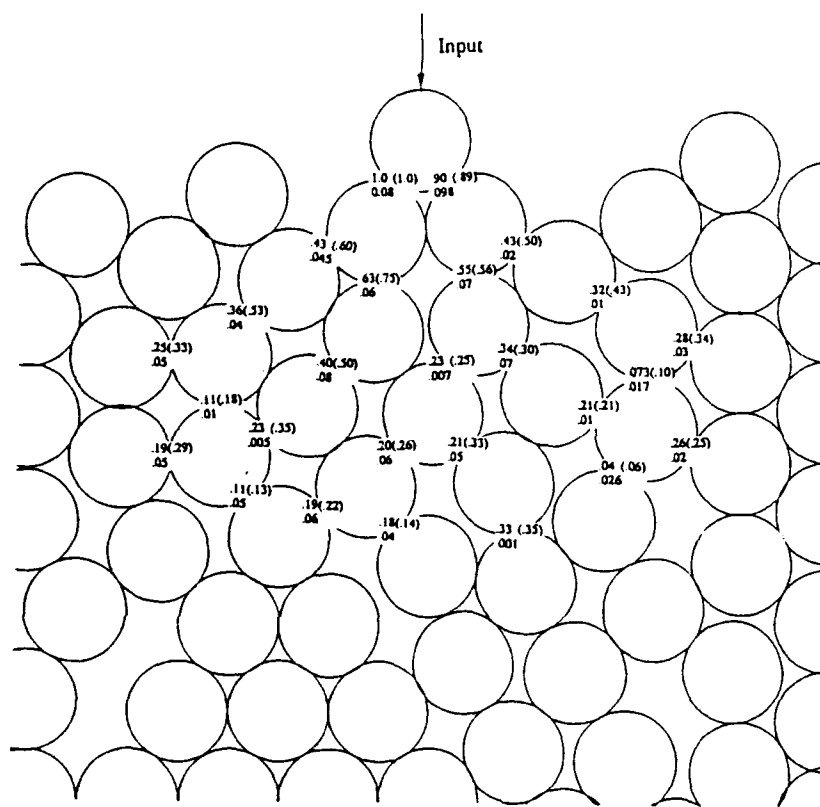an inclusion of different material properties

Fig. 8.12 Results and comparisons for a random assembly

151

CHAPTER 9

DYNAMIC GRANULAR INTERACTIONS USING
BOUNDARY AND FINITE ELEMENT METHODS

9.1 INTRODUCTION

Wave propagation in granular materials occurs by means of dynamic signal transfer through each of the granular contact points in the material. Our past modeling schemes to simulate this type of wave motion have employed the distinct element method (Sadd et.al., 1989a, 1989b, 1991a) and the elastic network method (Shukla and Sadd, 1990, Sadd et.al., 1992). Both of these models require specific contact load transfer relations which provide the load-displacement characteristic of the granular contact. Our past work has used experimental data to provide estimates of these stiffness parameters. In this section we provide a review of our efforts to use boundary element methods (BEM) and finite element methods (FEM) to determine these basic dynamic granular interactions for general elastic granules.

The dynamic interaction of two or more elastic granules in contact can be classified as a nonlinear initial/boundary value problem of elastodynamics. Such problems are normally attacked using methods of finite or boundary elements. The finite element scheme is based on an interior discretization concept whereby the entire domain is divided into elements, and the solution is obtained at all interior nodal or Guass points. The boundary element method however, only discretizes the boundaries of the domain under study. The resulting solution determines unknown boundary values of displacement and/or traction. It would therefore seem that this method would be quite appropriate for the granular contact problem in that one could investigate the dynamic load transfer from granule to granule by only analyzing the granule boundaries. The boundary element method would thus involve fewer unknowns by avoiding the calculation of the solution of the stress field within each granule.

The basis of the boundary element method lies with development of the integral formulation of the general elastodynamic equations. Integral formulations have a long history and can be traced back to the work of G.Green in 1828. Elastodynamic applications of the boundary element method were originally conducted by (Cruse and Rizzo, 1968, Cruse,1968) by incorporating the Laplace transform scheme. Direct time

152

dependent BEM methods have been developed and utilized by (Cole, et.al., 1978) and (Manolis, 1983 and Manolis and Beskos, 1988), and (Brebbia, 1985) provides a comprehensive review of these BEM applications.

This chapter will present analyses using both boundary and finite element methods to calculate the basic interaction mechanics between two or more granules in contact. A dynamic input will be applied to one of the granules, and the transient load transfer through the contact point(s) will be computed. Of specific interest will be the wave transfer speed and attenuation through the disk-contact system. The photoelastic and strain gage experiments have shown that the wave velocity in an assembly of disks is less than that in the disk material itself. For a material of Homalite 100, the P-wave velocity is approximately 2000 m/s, whereas in an assembly of disks of Homalite 100, the wave velocity has been measured as 1080 m/s. The effect of the granule shape and assembly geometry will also be presented. Comparison of the numerical results will be made with existing experimental data.

9.2 BOUNDARY ELEMENT METHOD FORMULATION

The basis for the integral equation formulation in elastodynamics is the dynamic extension of Betti's reciprocal theorem. This theorem is derived from virtual work considerations and essentially relates two different dynamic states for the same elastic body. The obvious choice for one of two elastodynamic states is the unknown solution that is to be found, while the second state is normally chosen to be an appropriate Green's function.

Using this procedure the resulting integral statement can be developed

$$C_{ij}(\xi)u_i(\xi,t) = \int_S \int_0^t \left(G_{ij}(x,t-\tau;\xi)t_j(x,\tau) - F_{ij}(x,t-\tau;\xi)u_j(x,\tau)\right)d\tau\,dS(x) \qquad (9.1)$$

where ξ is the source point and x is the receiver point, G_{ij} and F_{ij} are Green's function tensors, and u_i and t_i are the displacement and traction on the boundaries. The coefficient C_{ij} is specified by

$$C_{ij}(\xi) = \begin{cases} 0 & \text{for } \xi \, \epsilon \, V_c \\ \delta_{ij} & \text{for } \xi \, \epsilon \, V \\ 0.5\delta_{ij} & \text{for } \xi \, \epsilon \, S \end{cases} \qquad (9.2)$$

where V_c is complement set of $V+S$.

153

Methods of solving the basic integral equation (9.1) have included direct time domain approaches, and the use of Laplace and Fourier transformation. Our initial research investigated the use of both time domain and Laplace transform domain techniques. Better success was achieved using the Laplace transform method, and this technique was then used for our detailed studies on granular interactions. The Laplace transform is defined in the standard form as

$$\bar{f}(x,s) = \int_0^\infty f(x,t)e^{-st}dt \tag{9.3}$$

where s is the Laplace parameter. In the Laplace domain equation (9.1) becomes

$$C_{ij}(\xi)\bar{u}_i(\xi,s) = \int_S \left(\bar{G}_{ij}(x;\xi,s)\bar{t}_j(x,s) - \bar{F}_{ij}(x;\xi,s)\bar{u}_j(x,s) \right) dS(x) \tag{9.4}$$

Comparing equation (9.1) with equation (9.4) it can be seen that in the Laplace domain the equation involves only the integration over space. The problem thus becomes static-like for a fixed value of parameter s. The unknown boundary values of u_i and t_i in equation (9.4) can be solved by using standard methods from boundary element theory by dividing the boundary into a known group of boundary elements thereby reducing the problem into a set of algebraic equations. The unknown displacements and tractions u_i, t_i, are related to the corresponding nodal values using appropriate interpolation functions. The element employed in this calculation is a three node type using quadratic interpolation. Equation (9.4) is thus discretized into an algebraic system

$$[K]\{u\} + [G]\{t\} = 0 \tag{9.5}$$

where $\{u\},\{t\}$ are the displacement and traction matrices, and $[K]$ and $[G]$ are coefficient matrices. The number of the variables in the equation (9.5) is 4n (2n displacements and 2n tractions) where n is the number of nodes. In order to solve equation (9.5), the boundary conditions have to be set. In general for non-contacting boundaries either the displacement or the traction is known for each node. However in the contact zone both the displacements and tractions are unknown, and some additional conditions have to be used. We assume that the contact is a no-slip type. The no-slip contact condition requires that the displacements and tractions be continuous across the contact zone. A general

154

contact model is shown in Fig.9.1. This model includes three particles which are denoted as domains Ω_1, Ω_2 and Ω_3, and boundary segments $\Gamma^{(1)}$ and $\Gamma^{(2)}$ represent two contact zones between the particles. The analysis procedure starts by first establishing boundary equations for each domain. The displacements and tractions are then separated into two parts. One is related to the contact zone and the other is related to the remaining segments of the boundary. Thus the coefficient matrices [K] and [G] also follow a corresponding decomposition. For domain Ω_1 the algebraic BEM system would read

$$
\begin{bmatrix} K_1^{11} & K_1^{1(1)} \\ K_1^{(1)1} & K_1^{(1)(1)} \end{bmatrix} \begin{Bmatrix} u_1 \\ u_1^{(1)} \end{Bmatrix} = \begin{bmatrix} G_1^{11} & G_1^{1(1)} \\ G_1^{(1)1} & G_1^{(1)(1)} \end{bmatrix} \begin{Bmatrix} t_1 \\ t_1^{(1)} \end{Bmatrix} \tag{9.6}
$$

where u_1 is the displacement on the non-contact boundary of domain Ω_1 and $u_1^{(1)}$ is the displacement on contact boundary $\Gamma^{(1)}$ of domain Ω_1, and t_1 and $t_1^{(1)}$ are the corresponding tractions. For domain Ω_2 the system would be

$$
\begin{bmatrix} K_2^{(1)(1)} & K_2^{(1)2} & K_2^{(1)(2)} \\ K_2^{2(1)} & K_2^{22} & K_2^{2(2)} \\ K_2^{(2)(1)} & K_2^{(2)2} & K_2^{(2)(2)} \end{bmatrix} \begin{Bmatrix} u_2^{(1)} \\ u_2 \\ u_2^{(2)} \end{Bmatrix} = \begin{bmatrix} G_2^{(1)(1)} & G_2^{(1)2} & G_2^{(1)(2)} \\ G_2^{2(1)} & G_2^{22} & G_2^{2(2)} \\ G_2^{(2)(1)} & G_2^{(2)2} & G_2^{(2)(2)} \end{bmatrix} \begin{Bmatrix} t_2^{(1)} \\ t_2 \\ t_2^{(2)} \end{Bmatrix} \tag{9.7}
$$

where u_2, $u_2^{(1)}$, $u_2^{(2)}$ and t_2, $t_2^{(1)}$, $t_2^{(2)}$ follow similar definitions as before. Similarly the equation for domain Ω_3 can be obtained in a similar manner.

On boundary $\Gamma^{(1)}$ we have

$$
\begin{aligned} u_1^{(1)} &= u_2^{(1)} \\ t_1^{(1)} &= -t_2^{(1)}, \end{aligned} \tag{9.8}
$$

and a similar relationship exists on boundary $\Gamma^{(2)}$. Using the contact conditions, the boundary element equations for each domain can be combined into the single system

$$
\begin{bmatrix}
K_1^{11} & K_1^{1(2)} & 0 & 0 & 0 & G_1^{1(2)} & 0 \\
K_1^{(1)1} & K_1^{(1)(1)} & 0 & 0 & 0 & G_1^{(1)(1)} & 0 \\
0 & K_2^{(1)(1)} & K_2^{(1)2} & K_2^{(1)(2)} & 0 & -G_2^{(1)(1)} & G_2^{(1)(2)} \\
0 & K_2^{2(1)} & K_2^{22} & K_2^{(2)(2)} & 0 & -G_2^{2(1)} & G_2^{2(2)} \\
0 & K_2^{(2)(1)} & K_2^{(2)2} & K_2^{(2)(2)} & 0 & -G_2^{(2)(1)} & G_2^{(2)(2)} \\
0 & 0 & 0 & K_3^{(2)(2)} & K_3^{(2)3} & 0 & -G_3^{(2)(2)} \\
0 & 0 & 0 & K_3^{3(2)} & K_3^{33} & 0 & -G_3^{3(2)}
\end{bmatrix}
\begin{Bmatrix}
u_1 \\ u_1^{(1)} \\ u_2 \\ u_2^{(2)} \\ u_3 \\ t_1^{(1)} \\ t_2^{(2)}
\end{Bmatrix}
=
\begin{bmatrix}
G_1^{11} & 0 & 0 \\
G_1^{(1)1} & 0 & 0 \\
0 & G_2^{(1)2} & 0 \\
0 & G_2^{22} & 0 \\
0 & G_2^{(2)2} & 0 \\
0 & 0 & G_3^{(2)3} \\
0 & 0 & G_3^{33}
\end{bmatrix}
\begin{Bmatrix}
t_1 \\ t_2 \\ t_3
\end{Bmatrix}
\qquad (9.9)
$$

At this stage, the solution of (9.9) for the displacements and tractions yields values in the Laplace transform domain and these have to be inverted to the time domain. The standard analytic inverse Laplace transformation formula

$$
f(x,t) = \frac{1}{2\pi i} \int_{\beta - i\infty}^{\beta + i\infty} \bar{f}(x,s) e^{st} ds \qquad (9.10)
$$

can not be used in this case because of the complexity of u_i and t_i. Thus a numerical method using *Dubner and Abate's method* (Durbin, 1974) was incorporated to invert the results.

9.3 NUMERICAL RESULTS OF BOUNDARY ELEMENT METHOD

The preceding boundary element theory will now be applied to several granular contact problems of interest to the research program.

9.3.1. Circular Disk Contact Models

The first application of our BEM analysis was made on a two disk contact model shown in Fig.9.2. The boundary of each disk was discretized into 16 elements with 32 nodes. Contact was modeled by forcing the conditions in relation (9.8) at a single nodal point as shown. Two different simulations were considered. In the first case, the bottom of the disk was fixed, while the second test the bottom was free. For both simulations the input load was applied at the top of the disk on node 1. The time history of the input loading was a triangular profile with duration of 60 microseconds. The amplitude of the input loading was chosen as unity. Other parameters taken to model the material and size used in the experiments where

Diameter of the disk = 0.0254 m. (1.0 in)
Young's modulus E = 4.82x10^9 N/m^2.
Poisson ratio v = 0.35. (9.11)
Mass density ρ = 1.2x10^3 kg/m^3

Shown in Fig.9.3 is a typical numerical profile illustrating the comparison of the input profile with the contact force profile between the two disks. The wave speed was calculated in terms of the formula

$$c = L/\Delta t \qquad (9.12)$$

where L is the distance between the input and contact points, i.e. the diameter of the disk, Δt is the time interval between the peaks of the input and contact profiles. It was found that the wave speed of case one was 1004 m/s, while that of case two was 1168 m/s. The experimentally determined wave speed was measured as 1080 m/s, and thus, the velocity of test one was less than that of the experiment and while the value of test two was larger. The reason for this difference in the results is of course the boundary condition. In reality the boundary condition is neither fixed, nor free but is a compliant condition being somewhere in between these two idealized conditions.

Because the boundary condition at the bottom of the second disk plays a significant role in the load transfer process a three disk model shown in Fig.9.4 was constructed. This model will then more accurately simulate the conditions which exist in a large granular assembly. The wave transfer profile for the model is shown in Fig.9.5. For this case the wave velocity was calculated as 1080 m/s, and this value was consistent with the experimental results.

In our previous research using the elastic network method (Sadd et.al., 1992) a required dynamic stiffness coefficient k_n was determined by matching numerical results with experiment data. In that work it was found that k_n=7.04x10^6 N/m. The stiffness coefficient k_n can also be obtained through calculation. Using Hertz contact-stress theory, it has been proposed by (Mei, 1989) that

$$k_n = \alpha(\pi h E/4) \qquad (9.13)$$

157

where $\alpha = c^2/(E/\rho)$ is a dynamic modification factor. Now according to our BEM analysis using the computed wave speed, $\alpha = 0.29$, and thus, $k_n = 6.96 \times 10^6$ N/m, which agrees quite closely with the experimentally determined value.

The wave attenuation is a measure of the reduction of the peak load transfer through a granular system. Using Fig.9.3 and Fig.9.5 this reduction relative to the triangular unit input can easily be determined. The attenuation for the three disk case was found to be 0.875. The average measured attenuation of single chain disk assemblies was found to be 0.935, thus the numerical result is slightly less than that from the experiments.

9.3.2. Elliptical Disk Models

In order to investigate the effect of granular shape on the dynamic load transfer process, additional numerical simulations were conducted on two groups of elliptical disks as shown in Fig.9.6. These two sets of disk assemblies have the same particle height being equal to 1 inch. The results of these numerical runs are shown in Table 9.1 along with the previous circular disk case of $a = b = 1.0$ in. The profiles of the contact forces are shown in Fig.9.7 and 9.8.

The numerical results show that the wave velocity in these model granular materials depends on the shape of the particles. The wave velocity is clearly dependent on the ratio a/b of the particle, and the velocity increases with a decrease of the ratio a/b. Within an individual disk, wave propagation is quite complicated and a given wave profile is the result of many waves that are reflected from the disk boundaries. Also some waves will actually be confined to move on the boundary surface of the particle. The wave is a synthesis of all of the direct and reflected waves propagating through many different paths within a disk. As shown in Fig.9.6, the waves starts from the input source point, and then propagates along many different paths to the output or contact point. For the case shown in Fig.9.6 (a) ,the waves travel slightly longer paths than in the case of Fig.9.6 (b), thus accounting for the change in the wave speed. Table 9.2 compares the computational results with the experimental values. The comparisons show consistent trends with a reasonable match in the wave speeds.

9.4 FINITE ELEMENT METHOD CALCULATION

A second numerical modeling technique which was used for this dynamic contact

simulation was the finite element method. Using a standard two-dimensional plane stress model for an elastic continuum with damping, the finite element scheme produces an algebraic system model of the form

$$[M]\{\ddot{u}\} + [C]\{\dot{u}\} + [K]\{u\} = \{F\} \qquad (9.14)$$

where $[M],[C]$ and $[K]$ are the mass, damping and stiffness matrices respectively, and $\{F\}$ is external loading matrix. In this study a quadrilateral four node element, and a triangular three node element have been employed. A consistent mass model was used to create the mass matrix. At present, the damping matrix is ignored. A standard Newmark integration scheme was employed to solve equation (9.14). The finite element method requires that a two-dimensional mesh be generated, and a computer code was developed to generate the mesh automatically. The FEM model is shown in Fig.9.9 for the case of a three disk model.

The input load and the material and geometry of the disks are the same as the previous BEM model. The total model includes 360 quadrilateral elements and 72 triangular elements, resulting in 433 total nodes. The time step used in the Newmark scheme was 1 microsecond. The time history of the contact load of node 13 is shown in Fig.9.10. Results from this FEM analysis indicated a wave speed of 1104 m/s while the normalized peak amplitude attenuation was 0.82.

9.5 CONCLUSION

The boundary element method and finite element method were used to analyzed the dynamic behavior of wave propagation in model granular systems. The numerical results showed similarity to the experimental data in that the wave velocity in the granular system is less than that in the particle material. Also consistent with the experimental data, was the fact that the wave velocities were found to be dependent on the shape of the particles in contact (see chapter 6 for the experimental studies). For elliptical disk models, the velocity decreases with an increase in the particle dimension perpendicular to the axis of propagation. The peak attenuation of the amplitude of the wave compared reasonably well with experimental data.

The stiffness coefficient k_n which is required in the distinct element and elastic

network calculations, can be evaluated by these boundary and finite element methods of analysis. Our preliminary numerically generated results for k_n matched closely with the previous values we have determined empirically.

Table 9.1 The Wave Speed and the Peak of the Amplitude of the Contact Force

		a=1.5" b=1.0"	a=1.0" b=1.0"	a=.75" b=1.0"
Two Disks (fixed)	Velocity (m/s)	806	1004	1250
	Peak Attenuation	.802	.880	.919
Two Disks (free)	Velocity (m/s)	915	1168	1411
	Peak Attenuation	.697	.831	.870
Three Disks (free)	Velocity (m/s)	891	1080	1300
	Peak Attenuation	.746	.857	.893

Table 9.2 The Comparison of Wave Speed with Experiment

	a=1.5" b=1.0"		a=1.0" b=1.0"		a=.75" b=1.0"	
	Num.	Exp.	Num.	Exp.	Num.	Exp.
Wave Velocity (m/s)	891	955	1080	1080	1300	1125
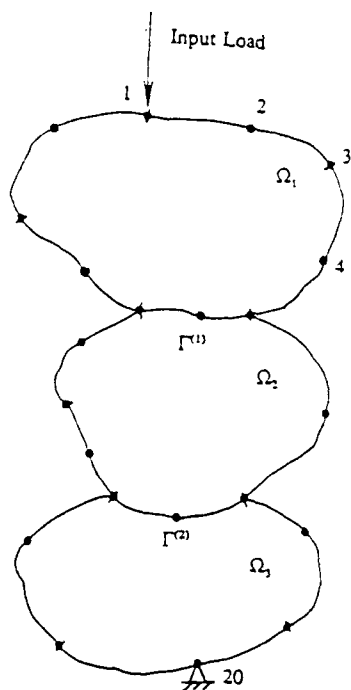
Fig. 9.1 A general contact scheme
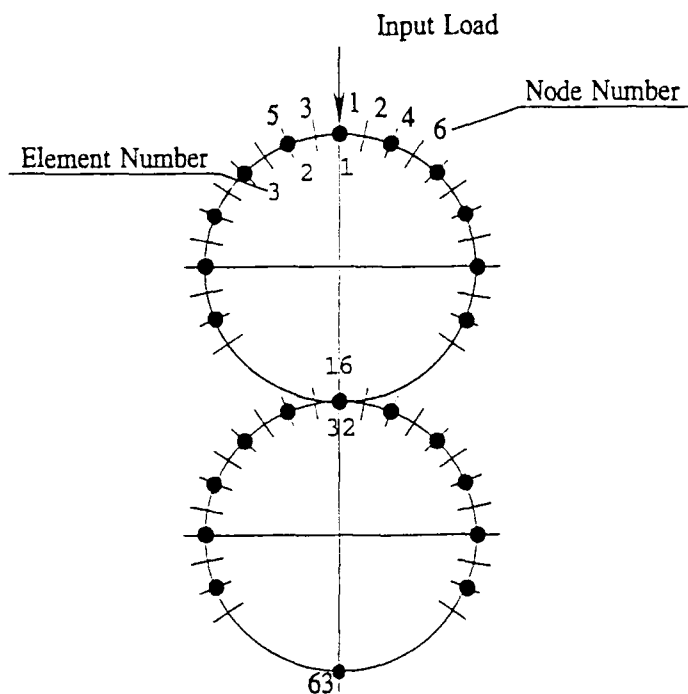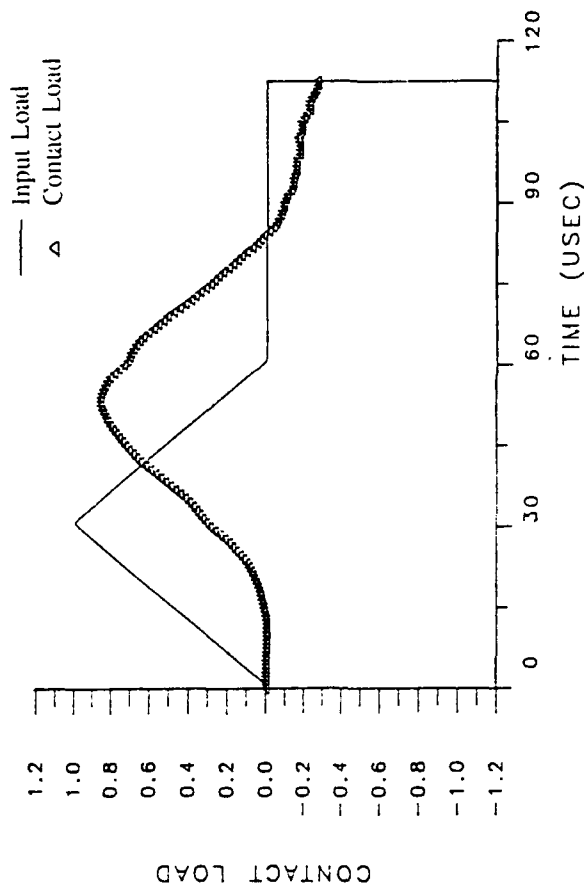

Fig. 9.2 Two disk model
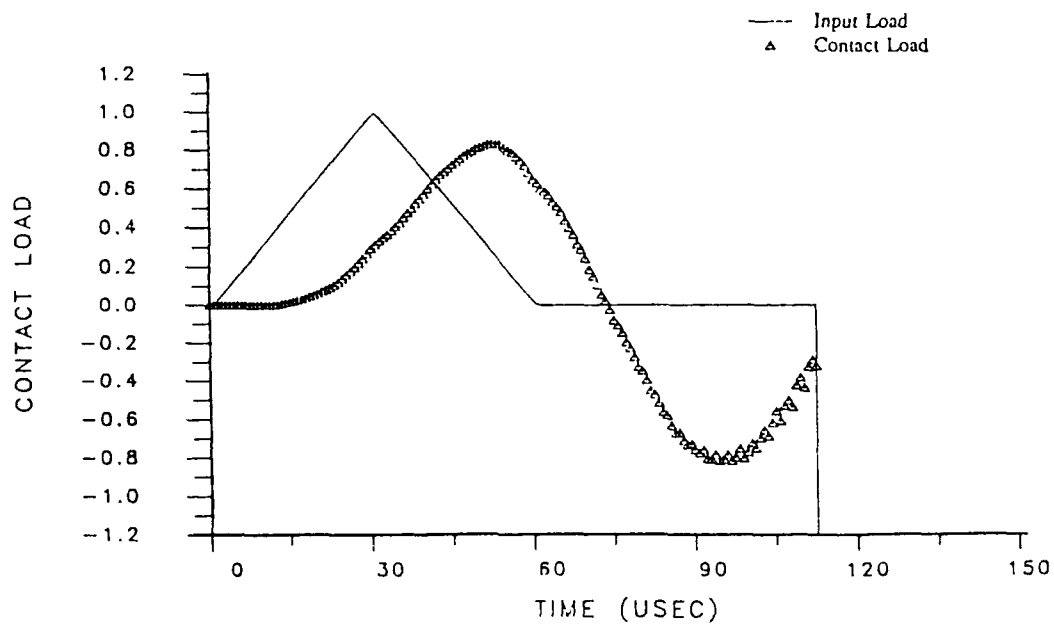
Fig. 9.3 Contact load in two disk model

161

Fig. 9.6   Elliptical disk model
            (a) a/b = 1.5 (b) a/b = 0.75

Fig. 9.5   Contact load in three disk model

Fig. 9.4   Boundary element model
            of three disks

162

Fig. 9.7 Contact load in elliptical model (a/b = 1.5)
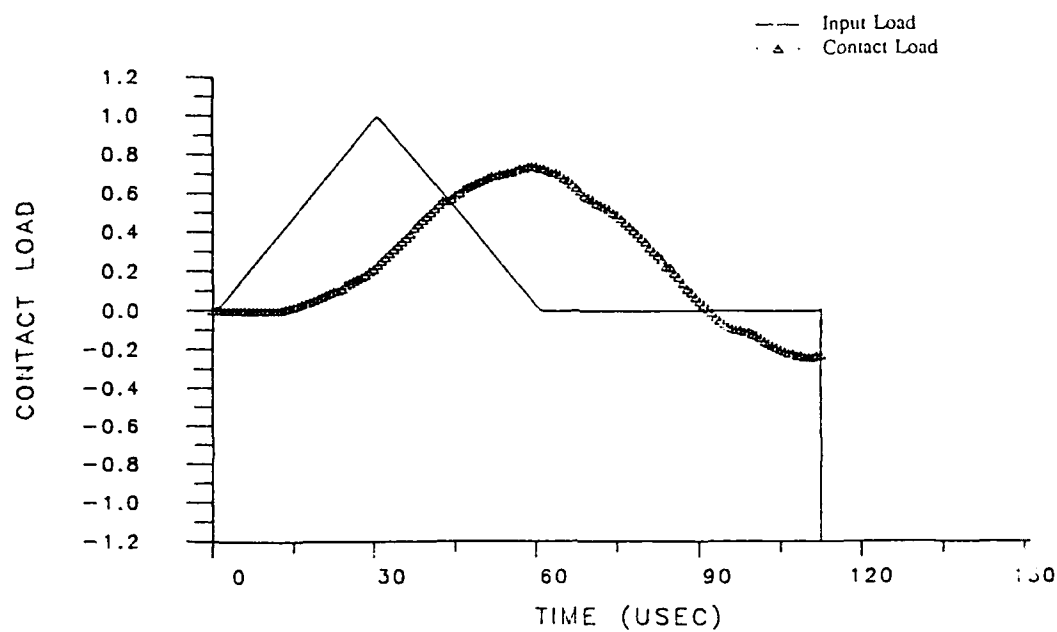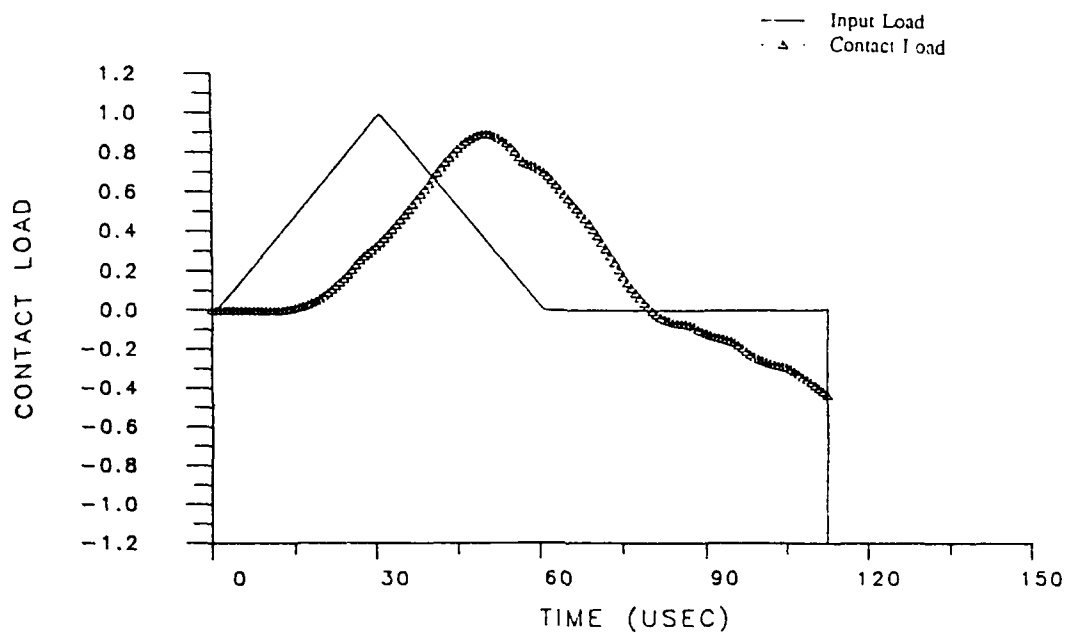

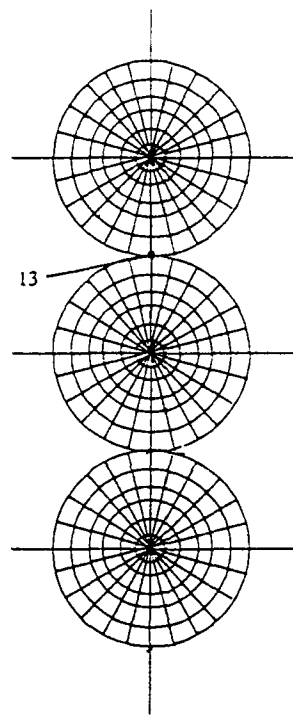Fig. 9.8 Contact load in elliptical model (a/b = 0.75)

163

Fig. 9.9   Mesh of finite element model
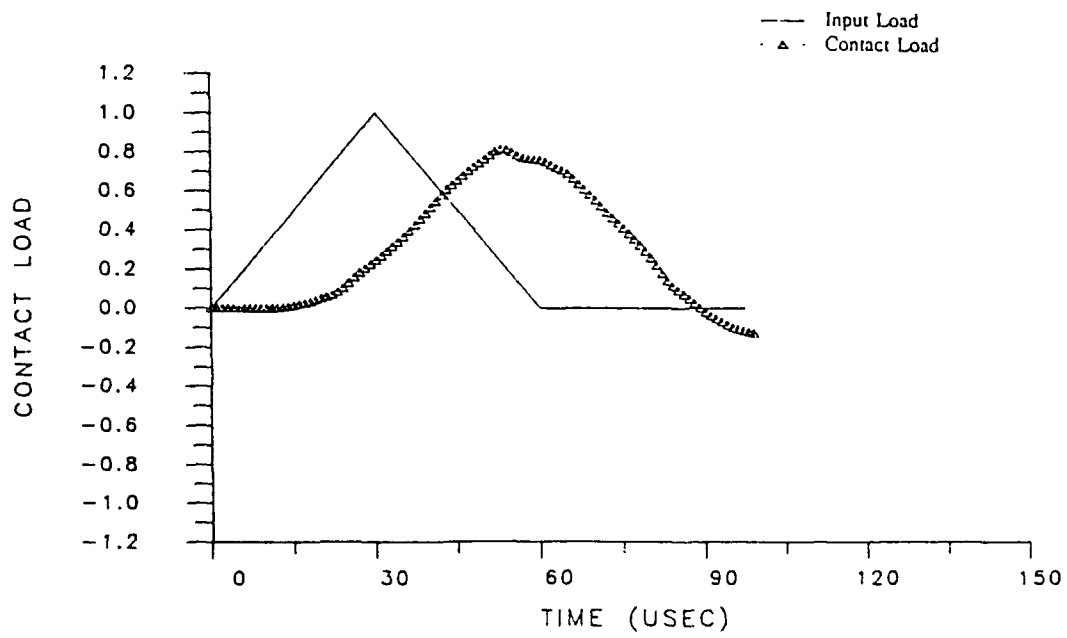

Fig. 9.10   Contact load in FEM model

164

CHAPTER 10

INFLUENCE OF LOCAL HETEROGENEITIES ON DYNAMIC
STRESS HISTORY IN GRANULAR ASSEMBLIES

An experimental study has been conducted to investigate the effects of local heterogeneities like inclusions and voids on the wave propagation phenomena in granular materials. Dynamic photoelasticity was used to study the effect of these defects on the local stress field as the stress wave passes by. The results indicate that both inclusions and voids produce local wave scattering through various reflection mechanisms. Inclusions increase the wave length and produce more local attenuation while voids can change the energy transfer paths.

10.1 INTRODUCTION

It is well known that actual granular media contains both voids and heterogeneous inclusions. At the boundary of these discontinuities, an incident wave will produce reflection waves of different modes. The increased complexity of the elastic-reflection phenomenon, due to mode conversion effects, yields scattering. This further complicates the wave propagation phenomena in an already complex microstructural material. In a real granular material, wave propagation phenomenon not only depends on the microstructure but also on the existence of voids and inclusions. There exist two possible modes of compressibility commonly observed in granular materials, i.e. compressibility of granules and compaction or distention of the void volume. Researchers have devoted much effort to the study of the scattering of elastic waves by granular media itself. Mason and Mcskimin (1947) measured the attenuation of elastic waves propagating through aluminum and magnesium rods. They constructed a simple first-order theory of scattering treating the granular materials as a distribution of small spheres. The scattering was calculated as the sum of the scattering of individual spheres. Papadakis (1961) developed this result to allow for variation in grain size. Hudson (1968) used the expression derived for the first-order displacements of scattered waves from a region where the elastic parameters vary smoothly to study the scattering of elastic waves by granular media. A statistical approach was made by Huntington (1950), using ray theory and by Knopoff and Hudson (1964), using full wave theory, for media whose properties vary smoothly with

position. Martin (1984) developed a stochastic theory for the wave propagation in a one dimensional model of a solid with a discrete random microstructure. Two Markov operators parameterized by the internal and macroscopic times were used in his formulation. Nunziato showed (1977) that the effects arising from the two different modes of compressibility and the dispersive effects resulting from the initial non-uniformity of the volume distribution function are coupled. In general, there are two distinct types of acceleration waves. If the effects of coupling are small, one wave propagates with a velocity close to that determined by the elasticity of the granules. While the second wave is associated predominately with the compaction process. However the reflection and scattering due to the random geometry of the particle boundary represents only a secondary effect as compared to that due to the inclusion and void of which the size is comparable to that of the particle in the granular media. Little work has been done on the study of the effect of inclusions and voids on the waves in granular materials, up to date. Few experimental studies of wave scattering and reflection because of inclusions and voids can be found in literature.

An experimental study has been conducted to study the dynamic response of granular materials with specific interest in investigating the local effects of inclusions and voids on the wave propagation. Local microstructure or fabric plays an important role in the way waves propagate in granular materials, and it has been found that porosity alone is not sufficient to characterize such dynamic behavior.

10.2 EXPERIMENTAL PROCEDURE

Experimental dynamic photomechanics has been applied to aggregate assemblies of circular disks in an effort to simulate the behavior of real granular materials. Inhomogeneous inclusions and specific voids were constructed within the granular medium, and the local wave propagation phenomena associated with wave scattering was determined. One dimensional (single chain) and two dimensional (hexagonal closed packing) granular materials, as shown in Fig. 10.1, were simulated by assemblies of 25.4 mm diameter, 6.3 mm thick disks of Homalite-100. The inclusions were created by replacing particular disks with ones of different material. While voids were created by removing disks from different locations. The experimental models were placed in the optical bench of the high speed multiple spark gap camera and dynamically loaded by

firing a small charge of explosive PETN which was contained in a specially designed charge holder. The camera was triggered at some prescribed delay time after igniting the explosive. Experimental results indicate the primary role which local microstructure plays in determining the wave propagation behavior. Much of the results can be related to a fabric vector called the branch vector which is drawn between adjacent disk mass centers. Both inclusions and voids produce local wave scattering through various reflection mechanisms, and the results seem to indicate that the inclusions produce more local attenuation.

10.3 RESULTS AND DISCUSSION

10.3.1 Wave Propagation in One Dimensional Models with an Inclusion

a. Wave Propagation in One Dimensional Models with a Steel Inclusion

The first experiment was conducted on a one dimensional chain granular assembly of Fig. 10.1a with a steel disk in it. Steel has much higher acoustic impedance than Homalite-100 disk does. A sequence of four photographs obtained during wave propagation in this model are shown in Fig. 10.2. The maximum contact loads obtained from these photoelastic data are shown in Fig. 10.3. In this model, each disk has two contact points. It can be seen from Fig. 10.2 that when wave reaches the steel disk, very high contact stresses were observed. The peak load at contact 3 is about 1.8 times the peak load at contact point 1. The wave transmitted by the steel inclusion propagated at an enlarged wave length about four times that of the input wave. Due to the existence of the harder inclusion, the peak contact load of the transmitted wave at contact point 4 was reduced to 50% of the input Load at point 1. In Fig. 10.2, it was found that the fringe pattern appeared, vanished and appeared again around the contact point 1 because of reflection at contact point 3. It reveals that large reflection wave generated by this inclusion propagated backward with the same wave length as the input wave. The peak reflection wave at point 1 was as high as 60 % of the input load to this point.

b. Wave Propagation in One Dimensional Models with a PSM4 Inclusion

When the rubber type material, PSM4 (with much lower acoustic impedance than Homalite-100) was used for the inclusion the wave propagation phenomenon was different from the previous one. The experimental photographs are shown in Fig. 10.4. The maximum contact loads obtained from these photoelastic data are shown in Fig. 10.5.

Very low contact load was found at the mismatch point. Since the reflection wave generated by this inclusion (from high impedance material to low impedance one) is in tension, it could not propagate through contacts. Therefore, no sizable reflection was found. The peak value of the transmitted wave at contact point 4 was only about 25% of the input. This was half of what was observed with the steel inclusion. The transmitted wave by this inclusion propagated with a wave length 3.6 times that of the original one.

By comparing the above two experiments it was found that both steel and PSM4 inclusions can largely change the local contact stresses and enlarge the transmitted wave length. Steel and PSM4 inclusions introduce large wave attenuation by different mechanisms. A steel inclusion acted as a reservoir, which made it difficult for waves to come out of it. While a soft inclusion acted as a dumper which made it difficult for waves to enter it. In addition, harder inclusion can generate a compressive reflection wave with the same wave length as the input while no reflection can be found with a softer inclusion.

10.3.2 Wave Propagation in Two Dimensional Models with Defects

For the purpose of comparison, two-dimensional experiments were conducted on a normal HCP model (with neither inclusion nor void), and HCP models with inclusions or voids. Fig. 10.6 shows a sequence of four photographs obtained during wave propagation in a normal HCP model. The normalized peak contact loads obtained from these photoelastic data are shown in Fig. 10.7. In this model, each disk has six contact points. There were neither orientation nor packing anisotropies. The wave front was of the same shape as a HCP microstructure. Disk L in Fig. 10.1b was named the loading disk on which the explosive loading took place. It can be seen that most of the energy was transferred through three chains, A, B and B', in contact with the loading disk, and two chains C and C', in contact with the disk just under the loading disk. Particular attention was paid to chains A and C as well as disk M to study the local effect of inclusions and voids. The contact load profiles for disk M plotted as a function of time are shown in Fig. 10.8. P_1 and P_2 are the two inputs to the disk M, while P_4 and P_5 are the outputs. These four contact loads were found to have almost the same duration. The average wave velocity in the vertical direction is 1070 m/s. The contact load attenuation in chain A for the wave travelling two disks from the one adjacent to the loading disk

was 30 %. It was 41 % in chain B for the wave travelling two disks from the one adjacent to the loading disk and 60 % in chain C for the wave travelling two disks from the disk after the one adjacent to the loading disk.

a. Wave Propagation in Two Dimensional Models with Inclusions

When a steel inclusion was placed in chain A for the HCP model, the wave front as shown in Fig. 10.9 was found to have the same shape as in media without inclusion shown in Fig. 10.6. Most of the energy was transferred through the vertical chain under the loading disk. The high impedance inclusion enabled the energy to be transferred into it at a faster speed. The peak load at contact point at which wave entered the steel inclusion was much higher than the input load. As in the single chain experiments, the high impedance inclusion acted as a wave reservoir. It made it very difficult for the energy to flow out to the low impedance material and increased the wave length considerably. The peak contact loads obtained from these photoelastic data, as shown in Fig. 10.7, also show tremendous effect of this inclusion on contact load attenuation in the vertical chain A. For this arrangement, it was 69 % for two disk diameter of travel while it was only 30 % for the normal HCP model. Wave propagation phenomenon in chains B and C was not effected by the existence of the inclusion. The wave attenuation was 39 % and 19 % respectively in chain B and C for two disk diameter of travel. The contact load profiles of disk M appeared similar to that in the normal HCP model. The inclusion seemed to have little effect on the wave velocity. It was found to be 1070 m/s in the vertical direction of this model.

Fig. 10.10 shows a sequence of four photographs obtained during wave propagation in a HCP model with three steel inclusions. Since inclusion did not change the energy transfer path, wave propagation phenomena in this model were similar to that in the HCP model with only one inclusion. However three inclusions introduced large wave attenuation and greatly increased the wave length in the vertical chain A. The average wave velocity in the vertical direction was 1050 m/s. The wave attenuations in chain B and C were almost the same as that in the model with one inclusion. Because of the considerably increased wave length, the wave attenuation in the vertical chain A could not be calculated form the photoelastic data obtained in this experiment.

169

b. Wave propagation in Two Dimensional Models with Voids

When the inclusion becomes very soft, it is expected to act as a void. Thus experimental investigation was also conducted on the HCP granular assemblies with voids in it.

Fig. 10.11 shows a sequence of four photographs obtained during wave propagation in a HCP model with a void in chain A. Around the void, each disk has five contact points. Orientation is anisotropic for the disks around the void. Disks away from the void still have six contact points. The shape of the wave front seems to be the same as in the former model. However, it can be seen in Fig. 10.11 that the energy transfer was seriously disturbed by the discontinuity in this assembly due to the void. The energy flow along the vertical chain A was completely blocked by this void. The stress wave had to change its propagation path when it reached the void. This results in large increase of contact loads in chain C as shown in Fig. 10.12. Most of the energy transfer occurred through chains B, B', C and C,' as shown in Fig. 10.1b, which were in contact with either the loading disk or the one right under the loading disk. Larger tangential contact forces were found in chain C and the chains beside the vertical chain A than what were in a normal HCP model. It can be clearly seen in Fig. 10.13 where the contact load profiles for disk M are plotted as a function of time. The void not only changed the energy flow pattern in this model but also made it very difficult for the energy flow to come back to the vertical chain under the void. After passing the void, wave propagation phenomena in the two vertical chains beside chain A were similar to what were in a single chain. Little energy was transferred to disks neighboring these two vertical chains. When the wave reached the void, wave velocity dropped suddenly as wave could not pass through an empty space. However, the average wave velocity in the vertical direction was not affected by this single void. It was found to be 1080 m/s. The wave attenuation in chain B was 41 %, while it was 24 % in chain C for two disk diameter of travel.

Fig. 10.14 shows a sequence of four photographs obtained during wave propagation in a HCP model with three voids. The wave propagation phenomena in this model was similar to what was in a HCP model with one void. Chains B, B', C and C' were still the main energy transfer path. It has been shown that a single void in chain A can block the energy flow in that chain completely. So the effect of three voids on the

vertical chain A was the same as that of one void. The average wave velocity in the vertical direction was 1070 m/s. Wave attenuation was 43 % in chain B , and it was 26 % in chain C, for two disk diameter of travel. These are almost the same as that in a HCP model with a single void.

10.4 SUMMARY

An experimental investigation has been conducted to study the dynamic response of granular assemblies with inclusions and voids. The results show that both inclusions and voids have little effect on the wave velocity in the experimental models. An inclusion has no sizeable effect on the wave propagation path. However, it can introduce large wave attenuation through reflection mechanism from the mismatch of material impedances. A void produces wave scattering through free-surface reflection from the empty volume. It can change the energy transfer path in a granular assembly.
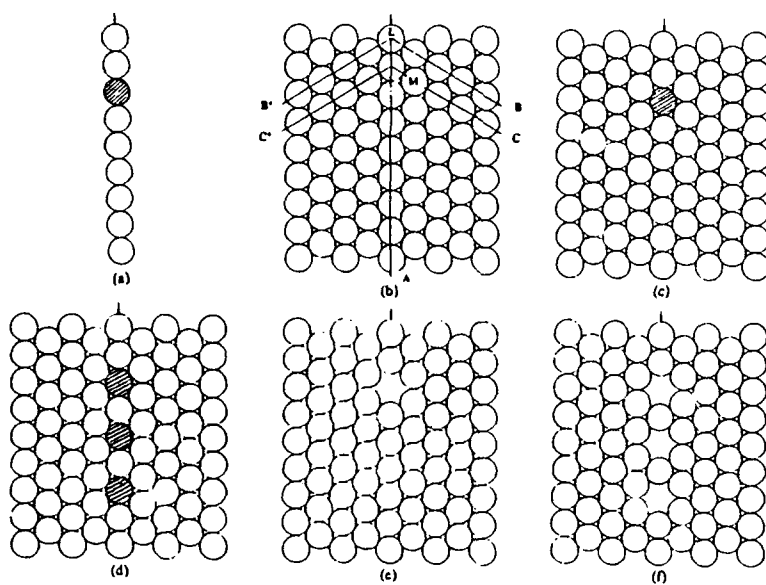
Fig. 10.1   Geometries of the models used in this study
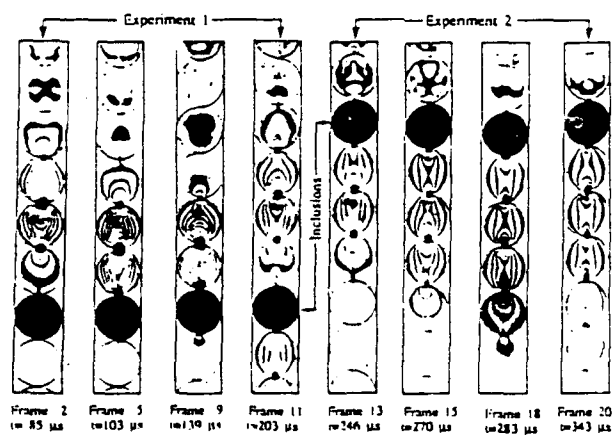
Fig. 10.2   Photoelastic fringe patterns of a single chain
with a steel inclusion

172
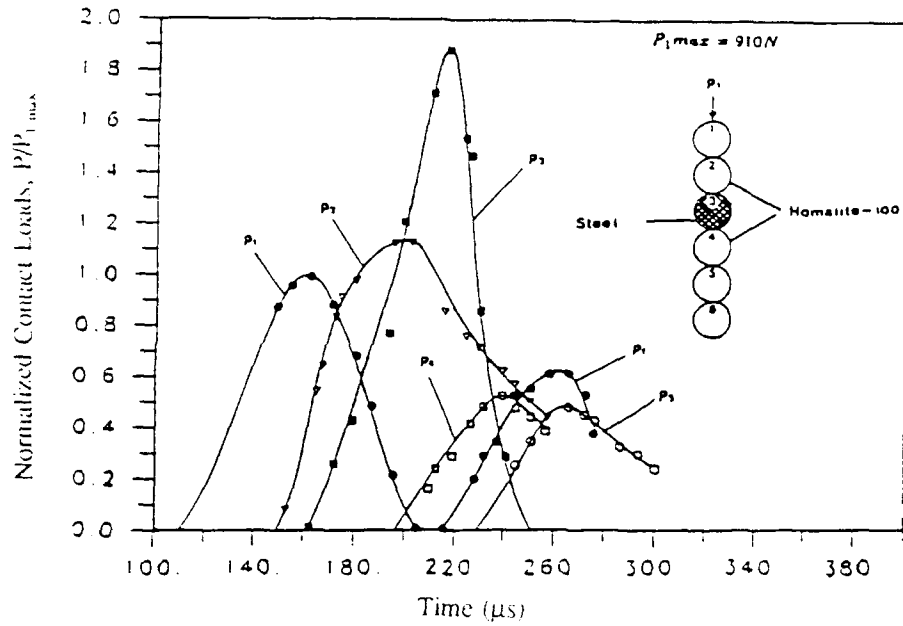
Fig. 10.3   Maximum contact loads obtained from the photoelastic data for a single chain model with a steel inclusion
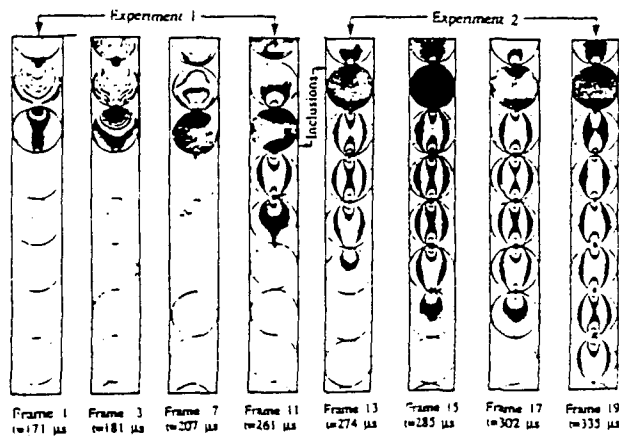

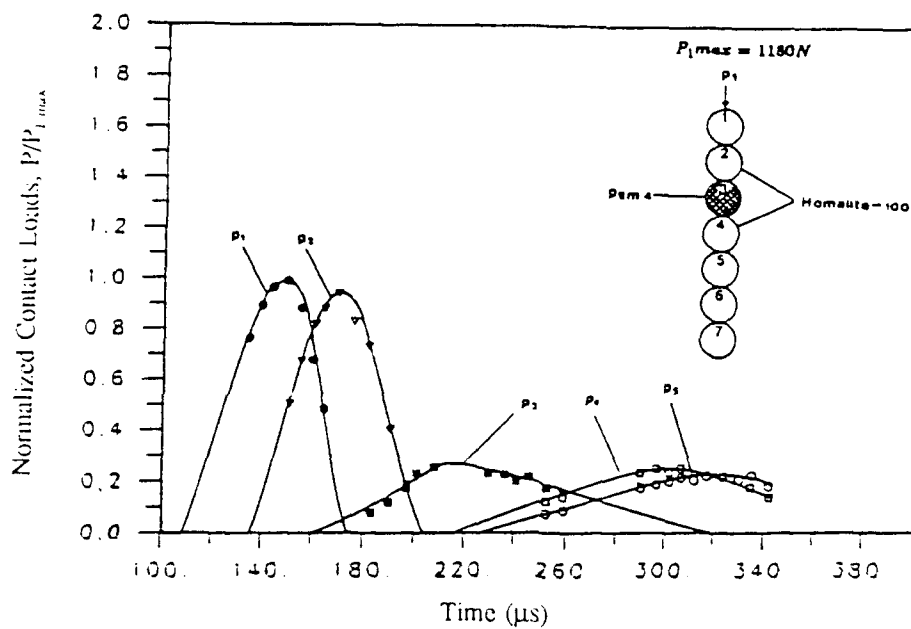Fig. 10.4   Photoelastic fringe patterns of a single chain with a PSM4 inclusion

173

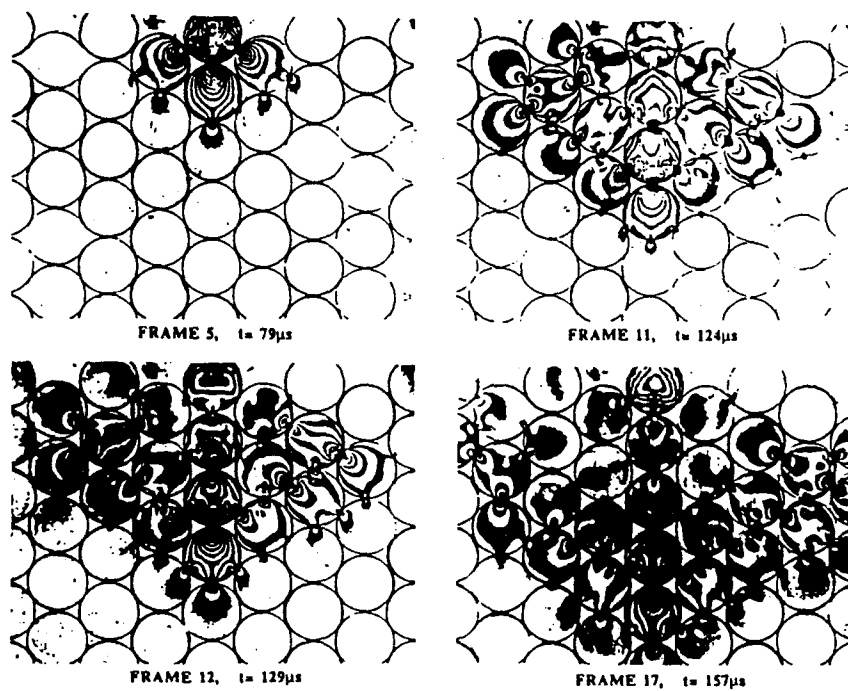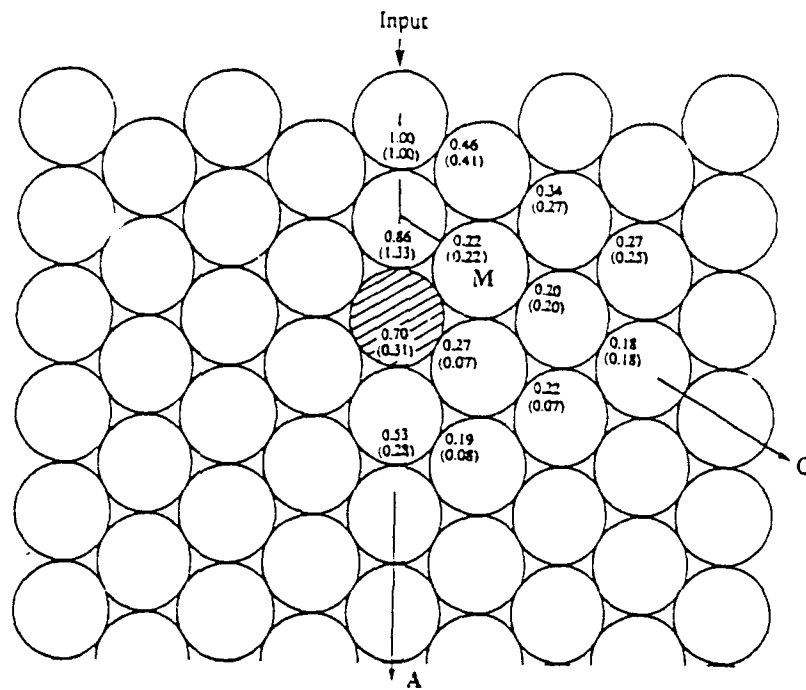Fig. 10.5 Maximum contact loads obtained from the photoelastic data for a single chain model with a PSM4 inclusion

Fig. 10.6 Photoelastic fringe patterns of a normal HCP model

174

* Top data for a normal HCP model and bottom data a for HCP model with one inclusion.

Fig. 10.7 Maximum contact loads obtained from the photoelastic data for a normal HCP model and a HCP model with an inclusion
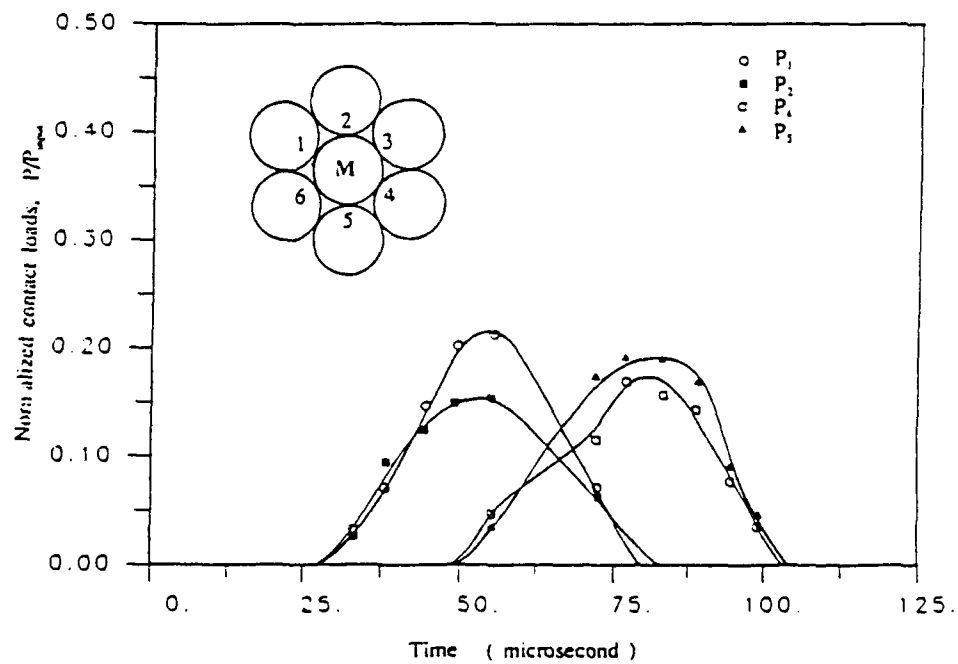

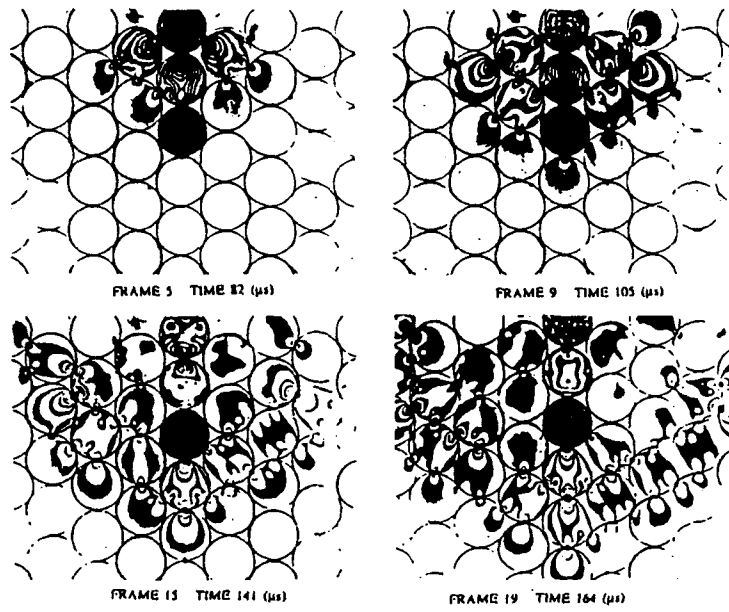Fig. 10.8 Contact load profiles of disk M in a normal HCP model

175

FRAME 5 TIME 82 (µs)   FRAME 9 TIME 105 (µs)

FRAME 15 TIME 141 (µs)   FRAME 19 TIME 164 (µs)

Fig. 10.9   Photoelastic fringe patterns of a HCP model with one inclusion

FRAME 2, t= 269 µs   FRAME 5, t= 286 µs

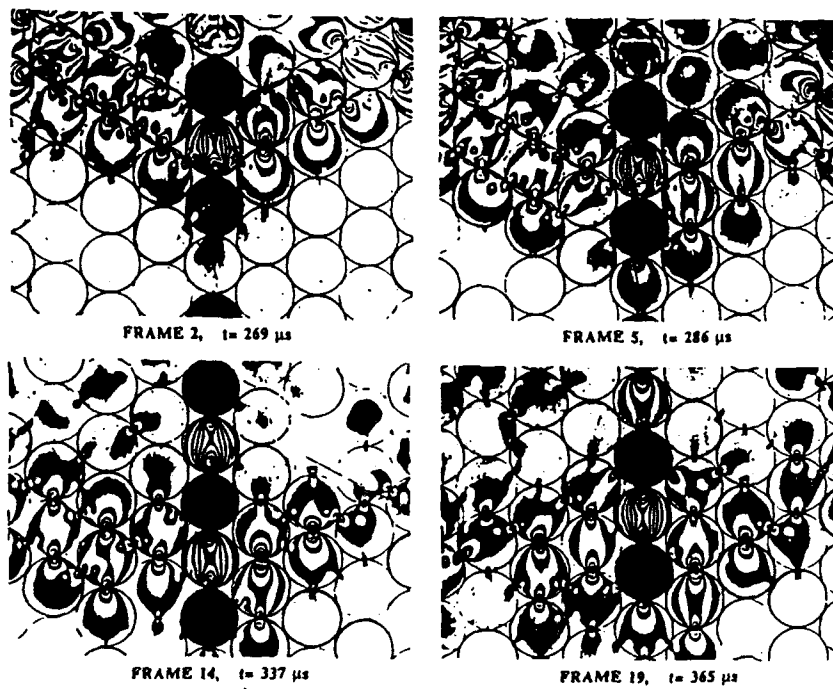FRAME 14, t= 337 µs   FRAME 19, t= 365 µs

Fig. 10.10   Photoelastic fringe patterns of a HCP model with three inclusions
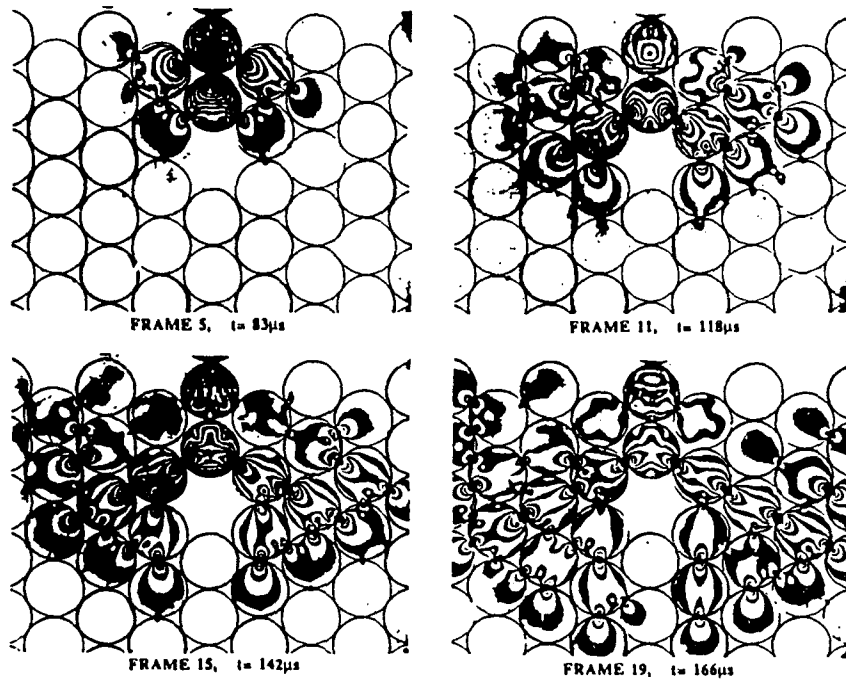
176

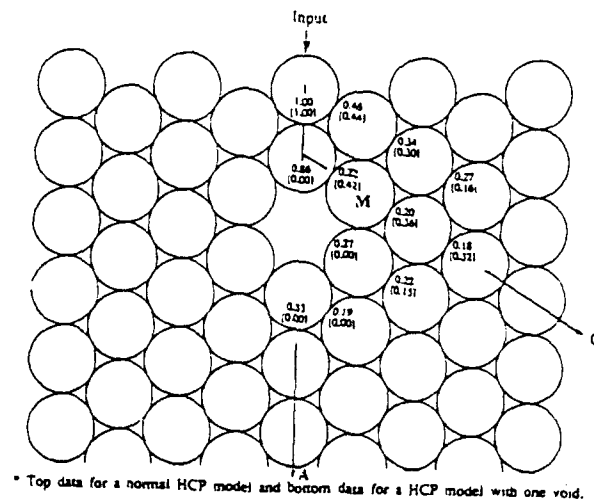Fig. 10.11   Photoelastic fringe patterns of a HCP model with one void

Fig. 10.12   Peak contact loads obtained from the photoelastic data
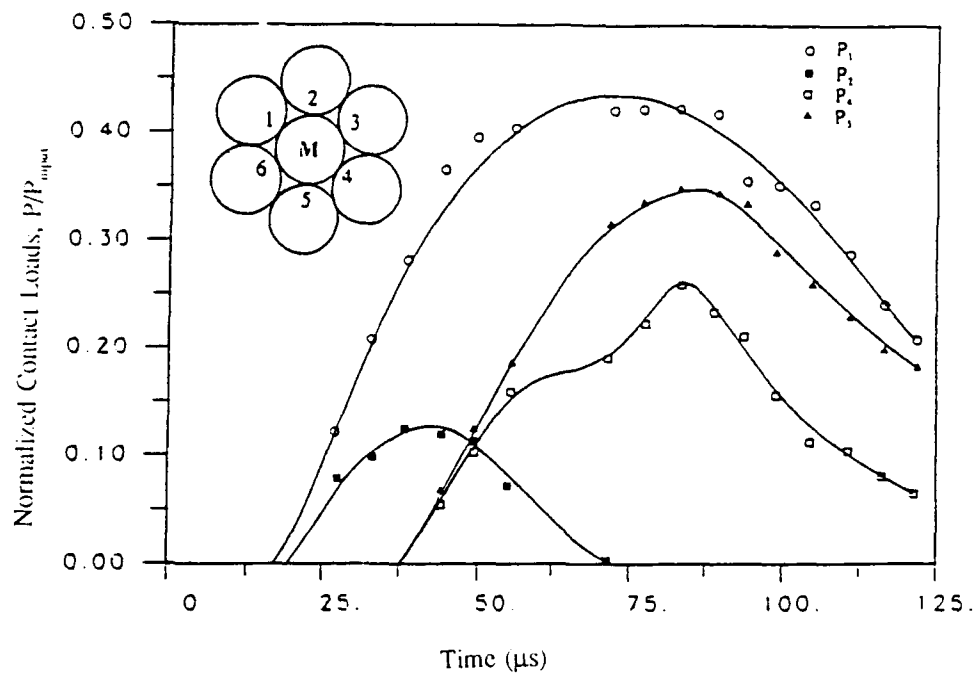for a normal HCP model and a HCP model with a void

177

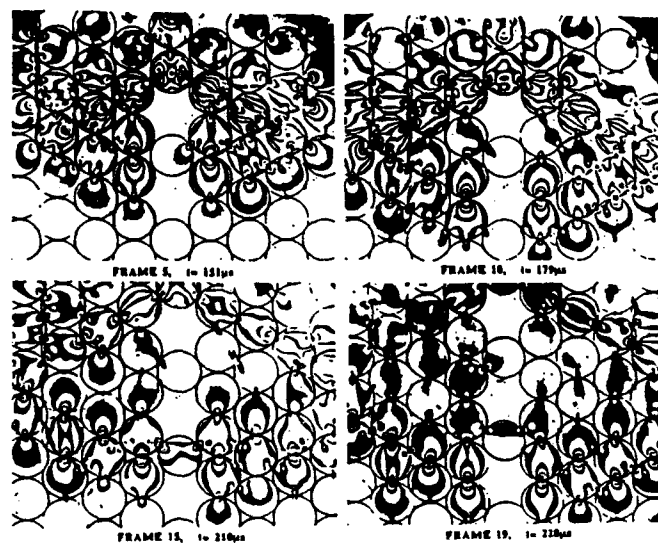Fig. 10.13   Contact load profiles of disk M in a normal HCP model

Fig. 10.14   Photoelastic fringe patterns of a HCP model with three voids

178

CHAPTER 11

EFFECTS OF CONTACT ANGLE AND MATERIAL PROPERTY ON WAVE PROPAGATION IN HETEROGENOUS GRANULAR MEDIA

An experimental investigation was conducted to study the effects of contact angle and material impedance on wave propagation and dynamic load transfer in two dimensional heterogenous granular media. The main attention was on how the stress wave propagates from one granule to its neighboring granules made of different materials. The inhomogeneous granular media were simulated by circular disks made of different photoelastic materials such as, Homalite 100, PSM1, PSM4, PSM9, CR39 and nonphotoelastic materials like steel and aluminum. The experimental method utilizes the combination of high speed photography and dynamic photoelasticity to visualize stress wave transmission and reflection in two dimensional chains of different materials. The photographs thus obtained were analyzed to get the normal and tangential contact loads at the contact points as a function of time. The results indicate that the load transfer is not only dependent on the angle between the vectors drawn from the mass centers of the contacting granules, but also dependent on the material impedance of the contacting granules. An empirical load transfer model is proposed to predict the peak contact loads in heterogenous chains. Predictions from this model are compared with the experimental data.

11.1 INTRODUCTION

Studies of the load transfer in granular media have been previously conducted by many researchers. (Drescher and De Josselin De Jong, 1972) simulated granular media by using assemblies of circular disks, and then studied the static load transfer through the assembly by means of photomechanics. (Rossmanith and Shukla, 1982) extended this idea to the dynamic case through the use of high speed photography. Additional dynamic work was also carried out by (Shukla and Damania, 1987), and (Shukla and Rossmanith, 1986). Most of this previous work focussed on the wave propagation phenomenon in general without going into details of relating specific microstructure to the associated wave motion. Granular media transmit mechanical loadings primarily through contact mechanisms between various grains. This is quite a complex process and depends

179

inherently on the microstructural packing arrangements of the media. Recent theoretical and experimental investigations (Nemat-Nasser and Mehrabadi, 1984 and Oda et.al., 1980) have related microstructure to macroscopic behavior. This work points to the singnificance of the local microstructure or fabric and that particular fabric vectors and tensors can be used to develop theories to predict the mechanical behavior of such materials. The concept of branch vectors in the direction of the contact normals have been proposed. Particularly, (Nemat-Nasser and Mehrabadi, 1984) addresses this issue for the case of dynamic load transfer by investigating the effects of the angle between branch vector on the wave propagation through granular aggregate assembly chains. Recently, (Shukla et al., 1988a) obtained experimentally the relation between the dynamic load transfer and the contact angle in two dimensional chain assembly of circular disks.

The dynamic load transfer problem will be much more complicated when granules make contact with different materials. Both transmission and reflection of the mechanical signal are involved and not much literature exists on the theoretical analysis. This study is thus focussed on both effects of contact angles and material impedance on wave propagation and dynamic load transfer in heterogenous granular media.

11.2 EXPERIMENTAL AND ANALYTICAL PROCEDURE

The experimental method used in this study was the combination of dynamic photoelasticity and high speed photography. The experimental model is shown in Fig. 11.1. The chain 1 (input chain) consists of Homalite 100 disks and chain 2 and 3 (output chains) consists of disks made of other materials such as steel (which has much higher Elastic Modulus E and Density ρ than Homalite 100), CR39 (which has similar material properties as Homalite 100) and PSM1 (which has much lower E and ρ than Homalite 100).

The experimental models were placed in the optical bench of a high speed Cranz-Schardin type camera. The camera was triggered at some prescribed delay time after igniting the explosive which is placed on the top of the model (see Fig. 11.1). This high speed photography system operated as a series of high intensity extremely short duration pulse of light and provides twenty photoelastic images at discrete times during the dynamic event.

The Hertz stress field equations along with the stress optic law were then used to

calculate the contact loads. All the dynamic contact loads between two different material disks were obtained by analyzing the Homalite-100 disk. The experimental results are discussed in the following section.

11.3 RESULTS AND DISCUSSIONS

A series of experiments were conducted with the experimental arrangements shown in Fig. 11.1. Both, the effects of the branch angles θ_1, θ_2 and material impedance on load transfer phenomenon were taken into account. The first group of experiments was conducted with $\theta_1=\theta_2=45°$. The left branch of disk chain was always of the same material as input chain, i.e, Homalite 100. The material on the right branch, however was varied from a very low impedance material, PSM4, to a very high impedance material, steel. Here the material impedance is defined as ρC, where ρ is the material density and C is the longitudinal wave velocity in the material. The typical dynamic isochromatic photographs obtained are shown in Fig. 11.2. The fringes are distributed symmetrically around the contacts in both chains, indicating predominantly normal loading. And there are no fringe patterns at contact points along the side supports meaning that all the energy is channelled along the disk chains. More intense fringe patterns at the contact point of the right branch implies that a larger contact load transfer occurred in the steel chain. This is also clearly shown in Fig. 11.3 where the contact loads as a function of time are plotted. From Fig. 11.3 it is found that the contact load P_{3max} is even larger than the input load P_{1max}. This can be explained by wave motion theory, the input stress of a bar can be even doubled if the end of the bar is fixed. Another extreme case was investigated in which rubber type material PSM4 was placed in the right branch chain, as shown in Fig. 11.4. The experimental results are shown in Fig. 11.5. This time, P_{3max} is highly reduced due to lower impedance of the material in that chain. On the other hand, comparing with the previous experiment, there is little difference in the contact load at the left branch, P_{2max}/P_{1max} are 0.59, 0.61 respectively.

Other materials such as PSM1, PSM9 and CR-39 were also used and the results are shown in Table 11.2. It is very surprising to find that even for the same branch angle ($\theta_1=\theta_2$) the output contact loads P_{2max} and P_{3max} are not equal and the ratio, P_{3max}/P_{1max}, varies largely if different materials are present. This result quantitatively shows how the mismatch of material impedance affects the dynamic load transfer locally at contacts in

181

heterogenous granular media.

From the above experimental results and discussions, it is felt that the dynamic load transfer is dependent on both the contact angle and the material impedance and there should be some relation between them. On the other hand, it would be very cumbersome to do thousands of experiments for different combinations of contact angles and material properties to obtain this relationship. Therefore, a load transfer model is proposed here by taking into account both the effects of contact angle and the material property.

11.4 LOAD TRANSFER MODEL

First, let us focus on the stress wave problem in a bar with discontinuous cross section made of different materials (Fig. 11.6). A disturbance at the left end of bar 1 will cause an elastic compressive pulse with intensity σ_I to propagate to the right. At the interface with bar 2, the wave will be partly transmitted and partly reflected. Call the transmitted wave amplitude σ_T and the reflected wave amplitude σ_R. Then, we have the expressions

$$\sigma_T = \frac{2\rho_2 C_2}{\rho_1 C_1 + \rho_2 C_2} \sigma_I \tag{11.1}$$

$$\sigma_R = \frac{\rho_2 C_2 - \rho_1 C_1}{\rho_1 C_1 + \rho_2 C_2} \sigma_I \tag{11.2}$$

where ρ is the material density and c the wave velocity in bar.

Now let us look at the wave propagation in one dimensional chain with different materials (Fig. 11.7). In this problem we try to predict P_2 by knowing P_1. Experimentally this has been done for the case of identical materials, Homalite-100. In general we have

$$P_2 = KP_1, \qquad \text{where} \quad K = 0.97 \text{ for } 1" \text{ disk} \tag{11.3}$$

If the disk chain consists of two kinds of materials, then equation (11.3) can be simply written as

$$P_2 = K \frac{2\rho_2 C_2}{\rho_1 C_1 + \rho_2 C_2} P_1 \qquad (11.4)$$

Since we are mainly investigating the transmitted wave, thus reflection is not considered here. Finally, if the angular dependence effect is also considered, we obtain the relationships between P_{2max}, P_{3max} and P_{1max} as

$$P_2 = f(\theta_1, \theta_2) \frac{2\rho_2 C_2}{\rho_1 C_1 + \rho_2 C_2} P_1 \qquad (11.5)$$

$$P_3 = f(\theta_2, \theta_1) \frac{2\rho_2 C_2}{\rho_1 C_1 + \rho_2 C_2} P_1 \qquad (11.6)$$

where the function f is plotted in Fig. 11.8 (Shukla et.al.,1988) and the factor K in equation (11.3) is included in $f(\theta_1, \theta_2)$ function. The equations (11.5) and (11.6) can be used to predict peak contact loads of P_2 and P_3 if P_{1max} is given. Fig. 11.9 shows the comparison of experimental results and theoretical prediction for $\theta_1 = \theta_2 = 45°$. It is seen that the load transfer model has a good agreement with the experimental results.

To verify the load transfer model more experiments were done for $\theta_1 = 45°$, $\theta_2 = 60°$ and $\theta_1 = 60°$, $\theta_2 = 45°$. Also, materials other than Homalite-100 were used. It is found from Table 11.2 that even for larger angles and different materials in both left and right branches, the predicted values match the experimental results well (maximum error is 14%).

11.5 CONCLUSIONS

The results indicate that:

(1) The dynamic load transfer from one disk to the neighboring disks not only depends on the branch angles and the inter-relationship between the two angles, but also depends on the relative material impedance of the two branches.

(2) For the same branch angles ($\theta_1 = \theta_2$) the higher contact load occurs in the branch where the larger material impedance exists.

(3)The load transfer model proposed can predict the peak contact loads very well. Good agreement was found between the proposed theoretical formulation and the experimental results. This model is a necessary first step for further study of wave

propagation in heterogenous granular media.

Table 11.1   Material Properties

Material	Elastic Modulus E(MPa) Static Dynamic		Poisson's Ration μ	Fringe Value $f_o(K_n/m)$	Mass Density ρ (Kg/m)	Wave Velocity V^{**}(m/s)
Homalite 100	3860	4800	0.35	23.6	1200	1050
PSM1	2480		0.38	7.0	1160	850
PSM4	3	125	0.46	0.18	1090	250
PSM9	3310		0.37		1170	930
CR-39	1900	3120*	0.42	15.4	1180	880
Steel	210000		0.29		7800	2000
Aluminum	70000		0.34		2700	2200

*   "Static & Dynamic Calibration of a Photo Model Material CR-39", by A.B.J. Clark, S.E.S.A Proceddings, Vol. XIV No. 1, 195-204

**   Wave Velocity in One Dimensional Chain of Circular Disks obtained by authors
Other data from "Experimental Stress Analysis", Dally, J. & Riley, W.

Table 11.2   Comparison of Experimental Results and Proposed Formula

Materials and Angles left branch	right branch	Experimetnal Results P_{2max}/P_{1max}	P_{3max}/P_{1max}	Prediction P_{2max}/P_{1max}	P_{3max}/P_{1max}	Error (%)	
Homalite 100 $\theta_2=45°$	PSM 1 $\theta_1=45°$	0.65	0.49	0.60	0.53	8.3	8.2
Homalite 100 $\theta_2=45°$	PSM9 $\theta_1=45°$	0.64	0.59	0.60	0.56	6.3	5.1
Homalite 100 $\theta_2=45°$	CR-39 $\theta_1=45°$	0.64	0.58	0.60	0.54	6.3	6.9
Homalite 100 $\theta_2=45°$	PSM4 $\theta_1=45°$	0.61	0.19	0.60	0.21	1.7	10.5
Homalite 100 $\theta_2=45°$	Steel $\theta_1=45°$	0.59	1.06	0.60	1.11	2.0	5.0
Homalite 100 $\theta_2=45°$	Aluminum $\theta_1=45°$	0.57	0.97	0.60	0.98	5.3	1.0
Homalite 100 $\theta_2=45°$	Steel $\partial_1=60°$	0.71	0.96	0.68	0.89	4.2	7.3
Homalite 100 $\theta_2=45°$	PSM4 $\theta_1=60°$	0.66	0.18	0.68	0.17	3.0	5.0
Homalite 100 $\theta_2=60°$	Steel $\theta_1=45°$	0.56	1.14	0.48	1.26	14.3	10.5
Homalite 100 $\theta_2=60°$	PSM4 $\theta_1=45°$	0.42	0.21	0.48	0.24	14.3	14.0

185
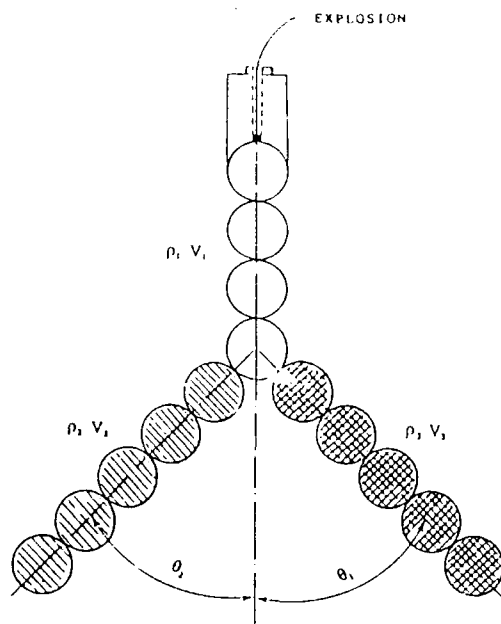
Fig. 11.1 Geometrical arrangement of experimental model

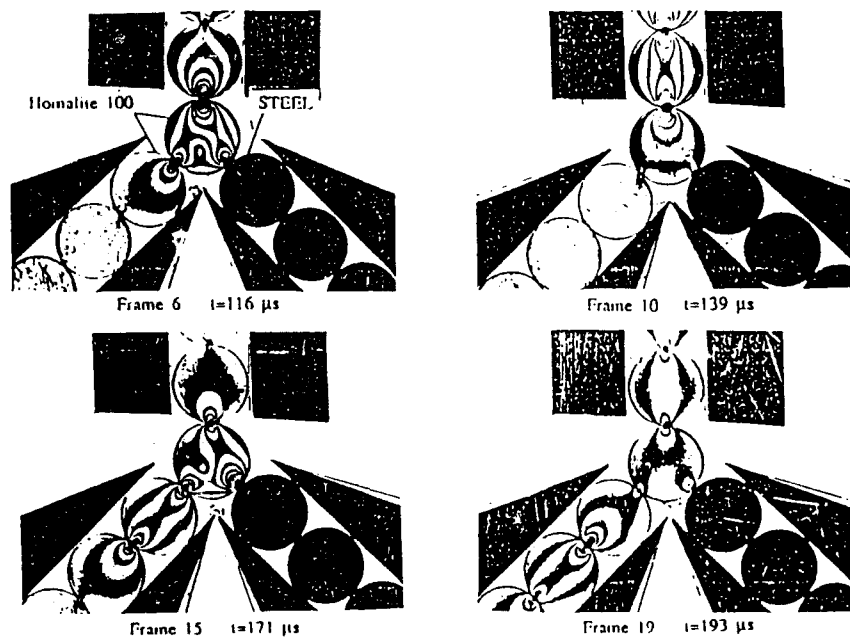Fig. 11.2 Typical isochromatic fringes obtained in a symmetric arrangement ($\theta_1 = \theta_2 = 45°$)
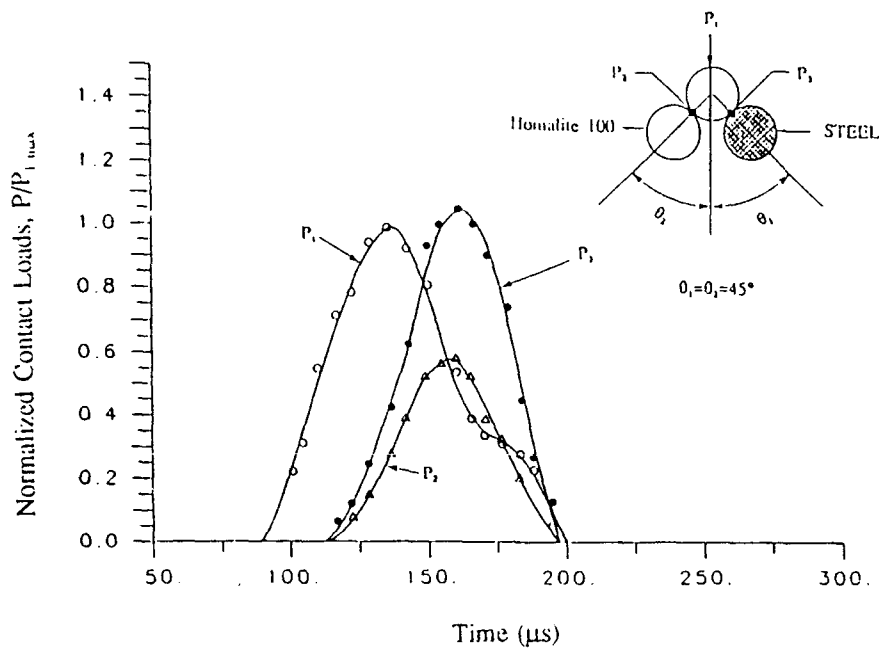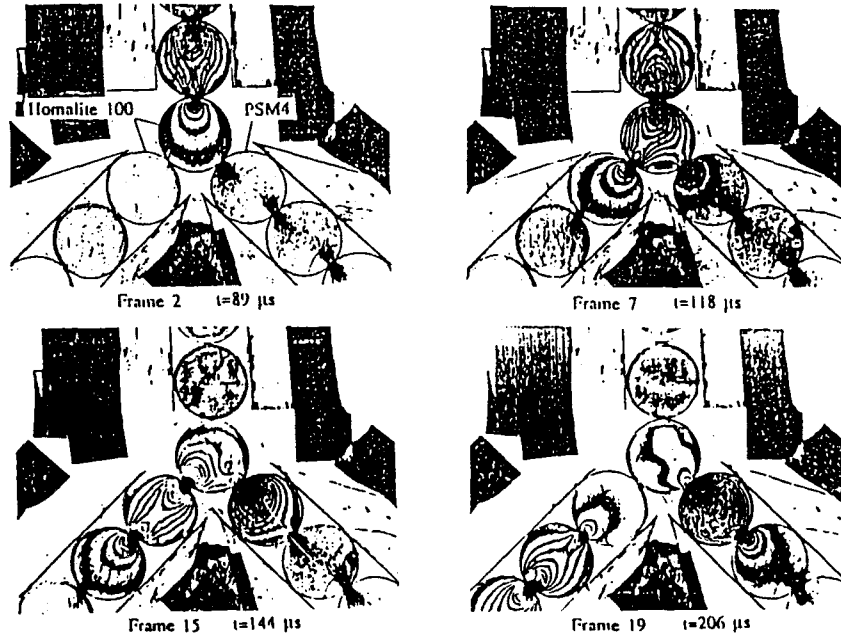
Fig. 11.3   Normalized contact loads as a function of time

Fig. 11.4   Typical isochromatic fringes obtained in a unsymmetric
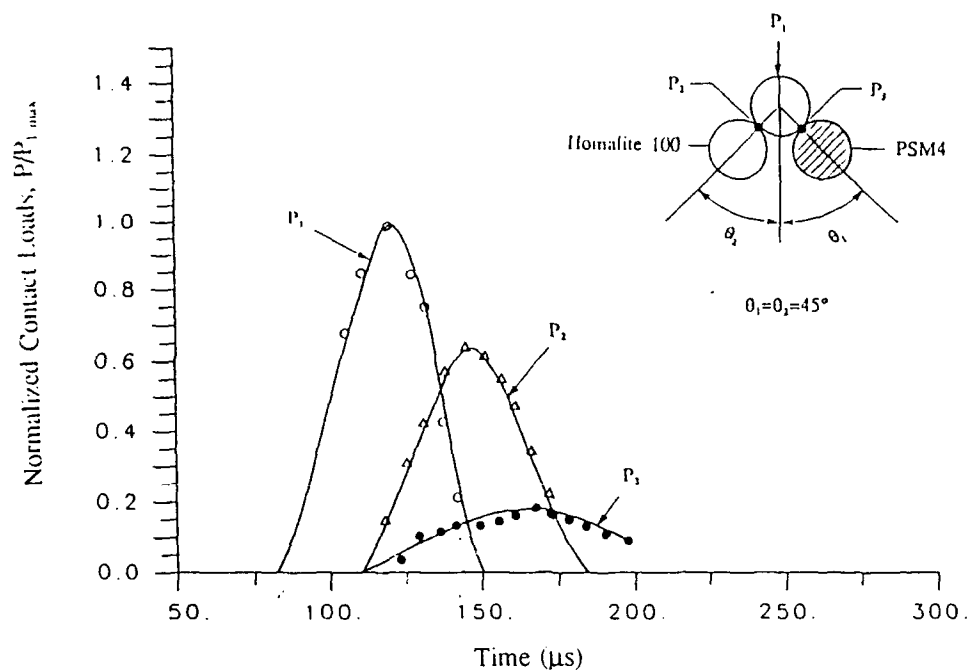arrangement ($\theta_1 = 45°$, $\theta_2 = 60°$)

187

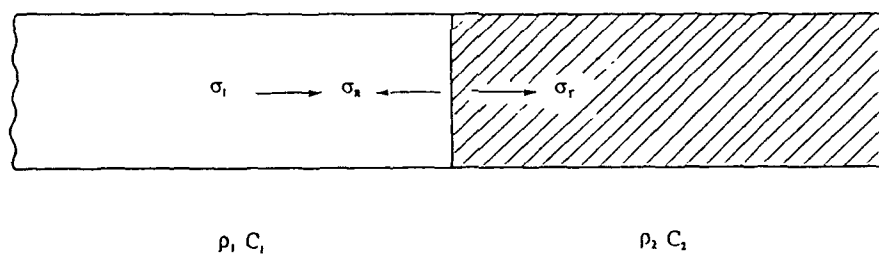Fig. 11.5 Normalized contact loads as a function of time

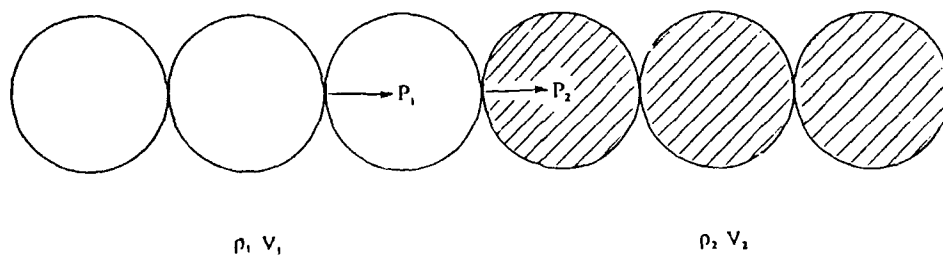Fig. 11.6 Wave reflection and transmission at changes in cross section

Fig. 11.7 Dynamic load transfer at material
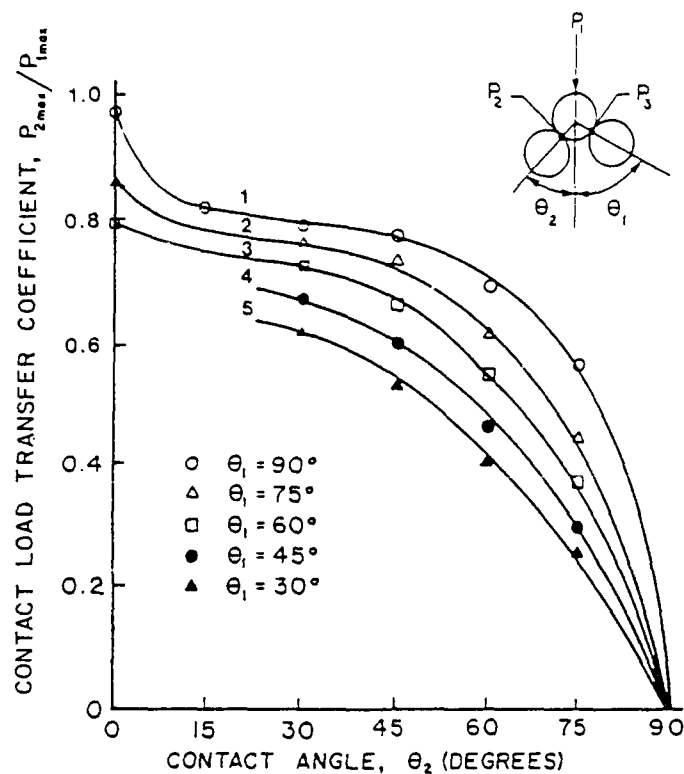impedance changes of disk chain

188

Fig. 11.8   Load transfer ~oefficients as a function of branch angles θ_2
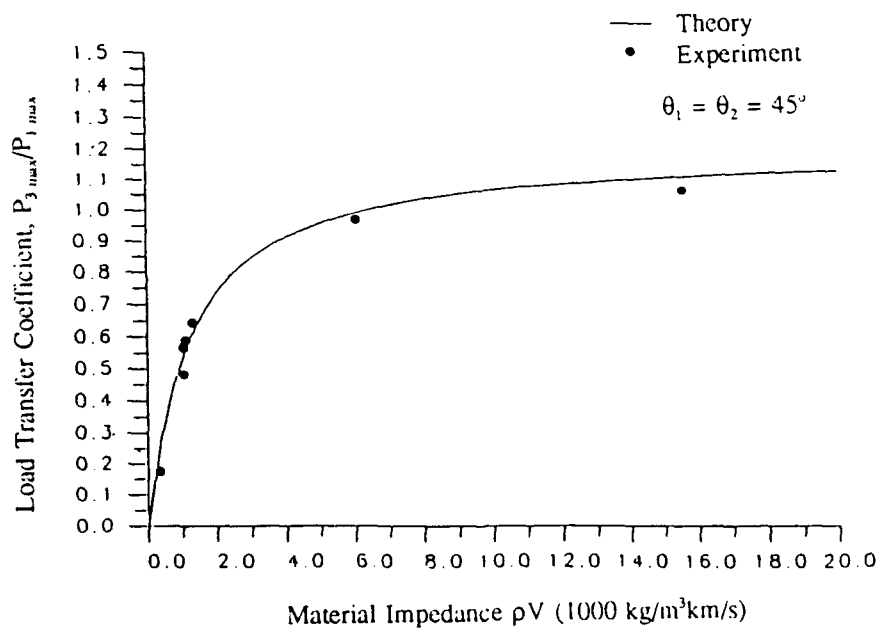for various values of θ_1

Fig. 11.9   Load transfer coefficient as a function of acoustic impedance
for given values of θ_1 and θ_2

189

CHAPTER 12

WAVE PROPAGATION AND DYNAMIC LOAD TRANSFER
IN LAYERED AND HETEROGENOUS GRANULAR MEDIA

12.1 INTRODUCTION

Dynamic load transfer due to explosive loading in layered and heterogenous granular assemblies was studied using dynamic photoelasticity. The heterogenous granular assemblies consisted of circular discs fabricated from photoelastic materials such as Homalite 100, PSM1, PSM4, PSM9, CR-39 and nonphotoelastic materials such as steel, rock and aluminum. The preliminary experimental results showed that the local microstructure controls the magnitude of load transferred in any given direction. The load transfer depends not only on the angle between the vectors drawn from the mass center of the contacting granules but also on the acoustic impedance of the contacting granules. The wave dispersion and scattering produced by the mismatch of acoustic impedance in the heterogenous assemblies resulted in much more peak contact load drop than that in a homogenous granular medium.

12.2   RESULTS AND DISCUSSIONS

12.2.1 Wave Propagation in Layered Granular Media

Fig. 12.1 shows an experiment conducted by replacing a layer of Homalite 100 discs with steel discs in a hexagonal closed packing. The average wave velocity through the steel layer in the vertical direction was found to be about 860 m/s which is 9.5% less than the average wave velocity 950 m/s in the assembly of Homalite 100 discs. The peak contact load attenuation in the main chain A or B was 73% for four disc diameter travel (see Fig. 12.2) which is slightly larger than 70% in a pure Homalite 100 discs assembly (Shukla and Damania, 1987). The contact loads before the steel disc layer were greatly increased and those after the layer were greatly decreased as for the one dimensional chain. The contact duration after the steel disc layer was also increased. It was also noticed that the steel disc layer created a large reflection wave which resulted in a large contact load (even greater than the transmitted contact load). Fig. 12.3 shows photoelastic photographs when PSM1 disc layer were used as the inhomogeneous layer. PSM1's acoustic impedance (ρV) is slightly less than that of Homalite 100. It was found that the

average wave velocity through the layer was around 840 m/s which is 11% less than the average velocity in a homogenous granular assembly of Homalite 100 discs. The peak contact load attenuation in the main chain was almost same as for the homogenous arrangement. Due to the very small difference in acoustic impedance of the two materials, Homalite 100 and PSM1, no reflection wave was noticed.

When a layer of rubber type disks made from PSM4 was placed in the HCP model as shown in Fig. 12.4 the wave propagated through this layer with a great reduction of amplitude and a large increase of wave length. Fig. 12.5 shows the comparison of peak contact loads along the main chain between the normal HCP model and HCP model with a PSM4 disk layer. The peak contact load attenuation in the main chains was as high as 90% with PSM4 disk layer. The average wave velocity in the vertical direction was also greatly decreased by this soft layer from about 1000 m/s of the normal HCP model to about 650 m/s. No sizable reflection wave was noticed from this inhomogeneous layer. This can be explained by that the reflection wave would be a tension wave which can not propagate via contact mechanism of granular materials.

Fig. 12.6 shows an experiment conducted by placing two different layers (one steel disk layer and one PSM4 disk layer) in HCP models. In Fig. 12.6 the PSM4 disk layer was placed on top of the steel disk layer. It was found that the wave amplitude attenuation in the main chains after these two layers was about 95%. When the steel disk layer was placed on top of the PSM4 disk layer the experimental results showed same wave attenuation after these two layers in the main chain. In addition, a large reflection wave was generated and it propagated back with same wave length as the input. However, there was no reflection wave when the PSM4 disk layer was placed first.

12.2.2 Wave Propagation in Heterogenous Granular Media

Fig. 12.7 shows a sequence of four photographs obtained during wave propagation in an heterogenous HCP model. The disk material distribution is shown in Fig. 12.8. It can be seen from Fig. 12.8 that this granular assembly consisted of different materials such as aluminum, rock, steel, PSM4 and Homalite 100. A steel disk and a PSM4 disk were placed in the two main energy transfer chains respectively. When wave reached the left main chain, higher contact load was obtained due to the existence of a steel disk. However, at the right main chain the contact load became very small due to the PSM4

191

disk.

Fig. 12.9 shows the wave propagation event in another type of heterogenous HCP model. In this HCP model, the energy transfer occurs at three disks under the input one (we call this a vertical HCP model, the HCP model mentioned at the above paragraph has two disks to transfer energy under the input disk and is simply called HCP). The maximum contact loads are shown in Fig. 12.10. In a normal vertical HCP model there are five main energy transfer paths. However, when PSM4 and steel disks are placed in the three main chains, as shown in Fig. 12.10, the peak contact load becomes less than 10% of the input for a four disk travel distance . If we look at the disk in the vertical chain under the input disk, then, due to the existence of PSM4 disks, the contact loads become only 13% of the input (for a normal vertical HCP model, it is 55% of the input). At the left and right branches, the peak contact loads are 33% and 31% of the input. For a normal vertical HCP model it was only 22% of the input. From these results, we see that because it is difficult for energy to transfer through a disk with much lower acoustic impedance, tne energy transfer path changes. This results in the increase of peak contact loads at the two branches mentioned above.

The last experiment conducted is shown in Fig. 12.11. The disks were randomly placed with randomly distributed disk materials. In this heterogenous model, one particle (disk) usually has three and four, or even two contacts with other particles (a HCP model has six contacts). When this model is explosively loaded at one point, instead of quasi-circular wave front observed in a homogenous HCP model, or quasi-triangular wave front observed in a vertical HCP model, the wave front in this case is irregular as shown in Fig. 12.11. The wave velocity in the vertical direction is reduced due to the zig-zag packing of particles. Fig. 12.13 shows the comparison of wave velocity in the vertical direction for different experimental models. It can be seen from Fig. 12.13 that wave velocity in the homogenous HCP model is higher than that in a random heterogenous model. Some of disks in this assembly were not loaded at all as shown in Fig. 12.11 and 12.12. On the other hand, some disks were loaded by reflection waves from the mismatch contacts.There is no main energy transfer path through the particle arrangement. However, the maximum contact loads can be traced through those disks with smaller contact angles and less difference in acoustic impedance.

12.3 CONCLUSIONS

The above preliminary experiments show that:

(1) When a wave propagates through a much harder layer in granular media, it will largely increase the contact load locally before the mismatch points and decrease the contact load after the layer. It will also generate a reflection wave with the same wave length. Also the contact duration after the harder layer can greatly increase.

(2) When a wave propagates through a much softer layer in granular media, it will result in decrease of the contact loads before and after the layer. The wave length will be increased greatly and no sizable reflection will be found. When the difference in the acoustic impedance of constituents in heterogenous granular media is small, the dynamic load transfer phenomena is similar to that in a homogenous model.

(3) The main energy transfer path in an heterogenous granular media varies according to the microstructural arrangement and acoustic impedance of disk materials. However, this path can be found through lines connecting the disks with less acoustic impedance change and smaller contact angles.
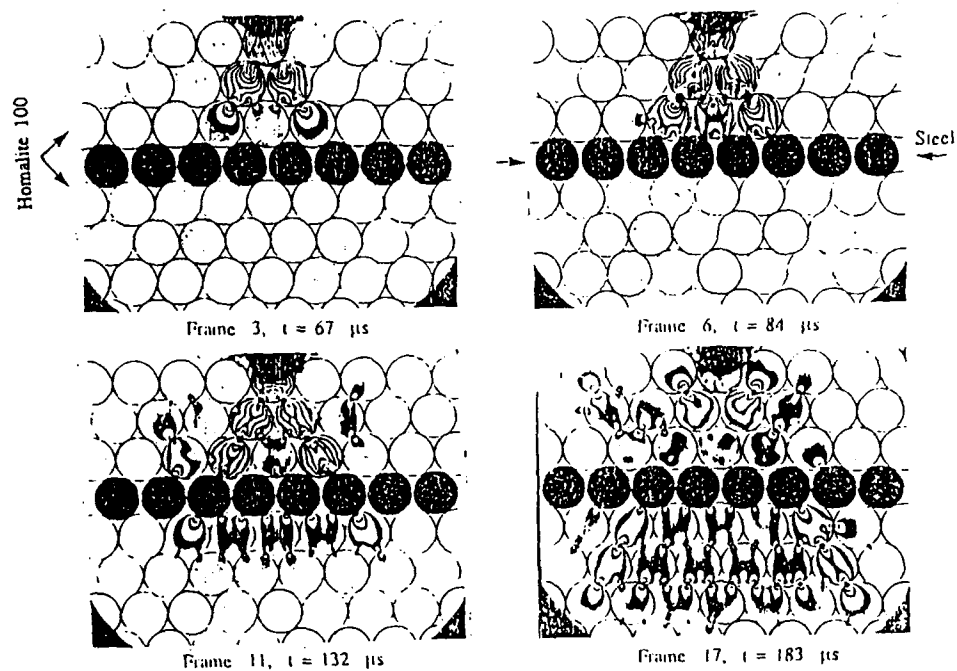
Fig. 12.1 Photoelastic fringe patterns of a HCP model with a layer of steel disks
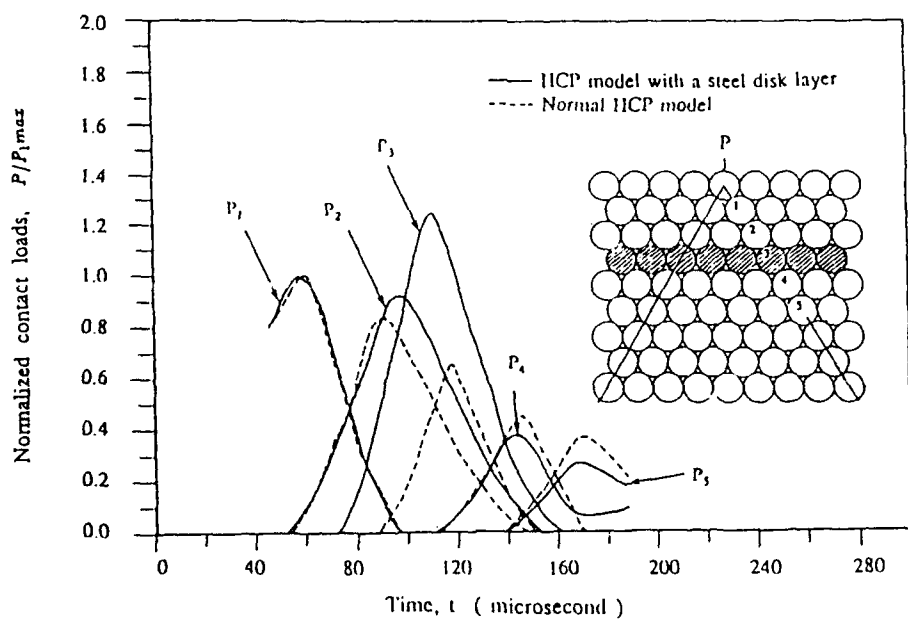

Fig. 12.2 Comparison of peak contact loads along the main chain between the normal HCP model and HCP model with a steel disk layer
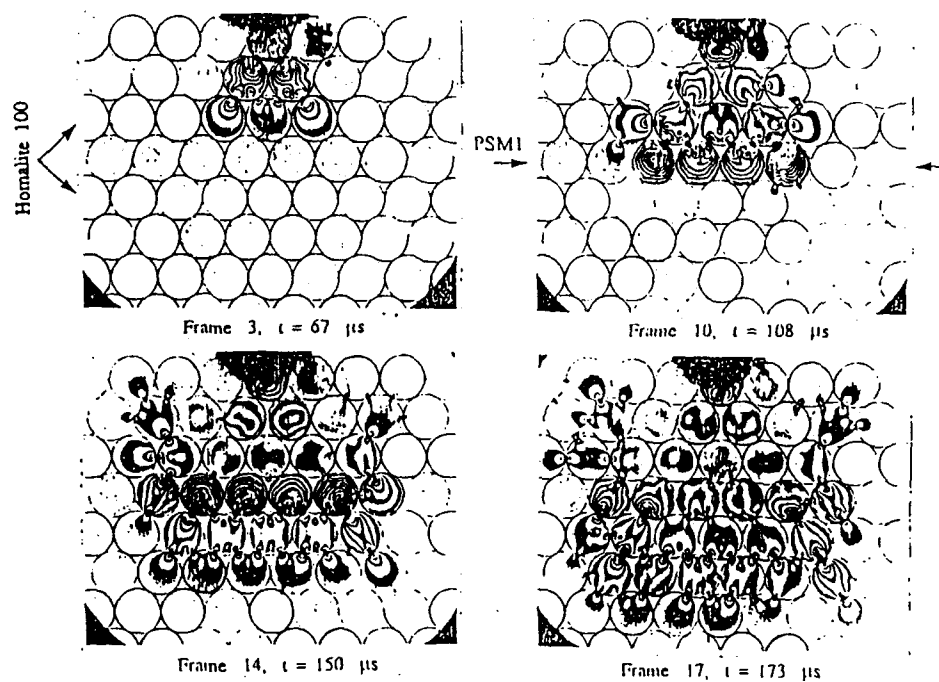
194

Fig. 12.3   Photoelastic fringe patterns of a HCP model
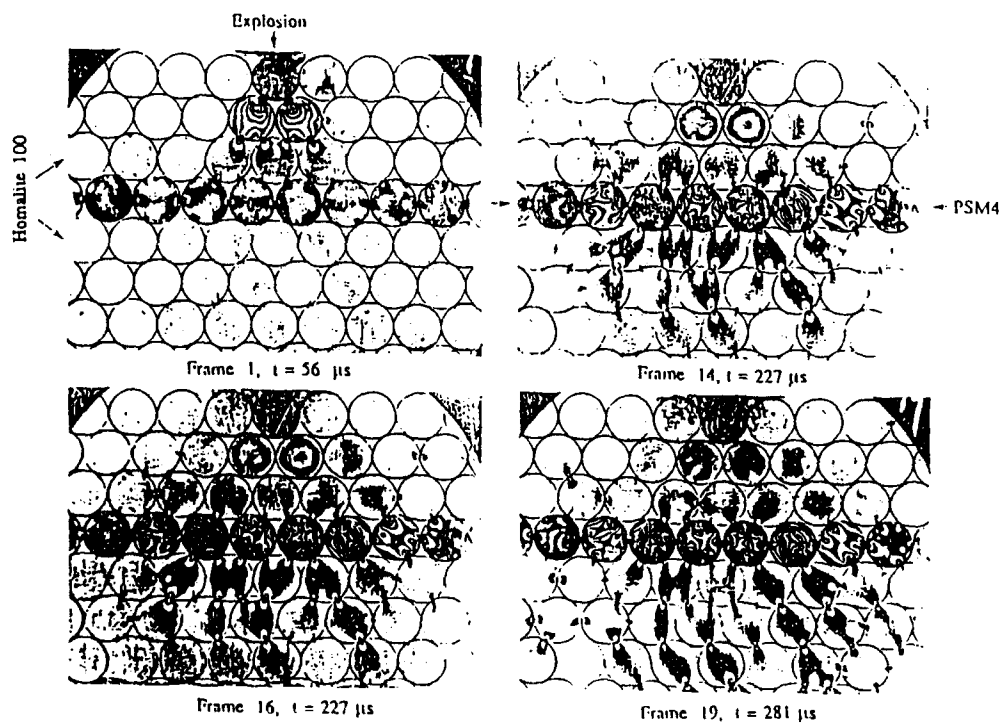with a layer of PSM1 disks

Fig. 12.4   Photoelastic fringe patterns of a HCP model
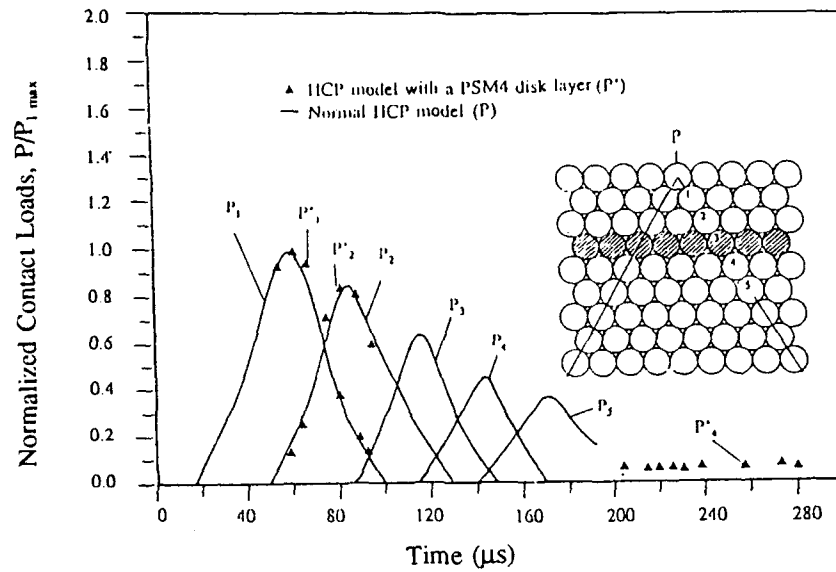with a layer of PSM4 disks

195

Fig. 12.5 Comparison of peak contact loads along the main chain between
the normal HCP model and HCP model with a PSM4 disk layer
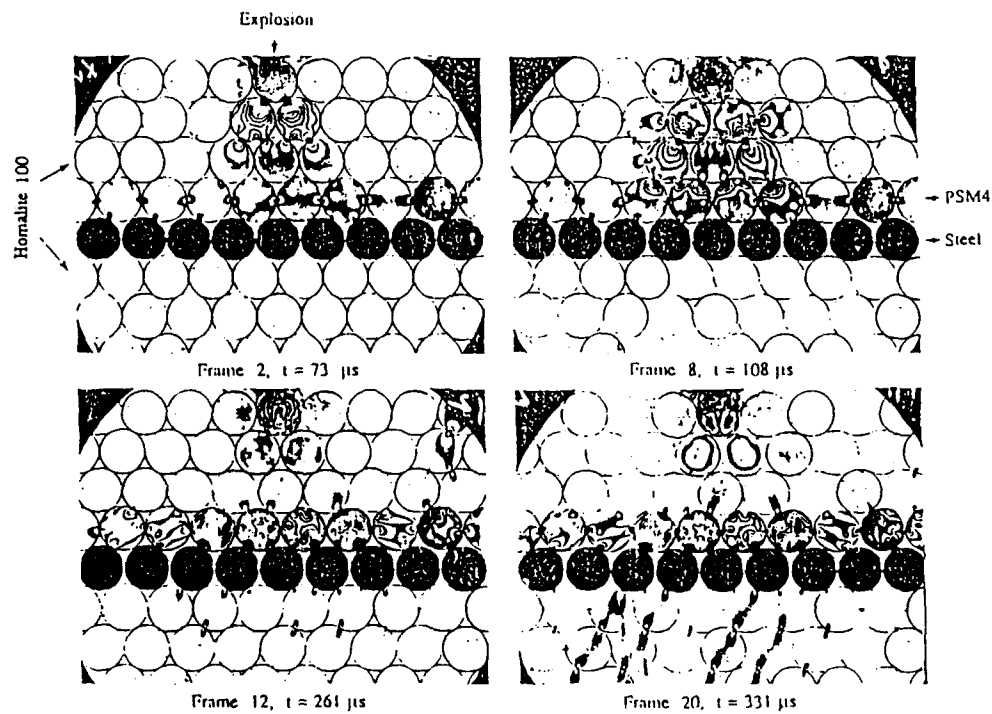
Fig. 12.6 Photoelastic fringe patterns of a HCP model with
a layer of PSM4 and a layer of steel disks

196

Fig. 12.7 Photoelastic fringe patterns of a HCP model with heterogenous disk arrangement

Fig. 12.8 Maximum contact loads obtained from the photoelastic data for a HCP model with heterogenous disk arrangement

Fig. 12.9 Photoelastic fringe patterns of a vertical HCP model with heterogenous disk arrangement

Fig. 12.10 Maximum contact loads obtained from the photoelastic data for a vertical HCP model with heterogenous disk arrangement

Fig. 12.11 Photoelastic fringe patterns of a random packing model with heterogenous disk arrangement
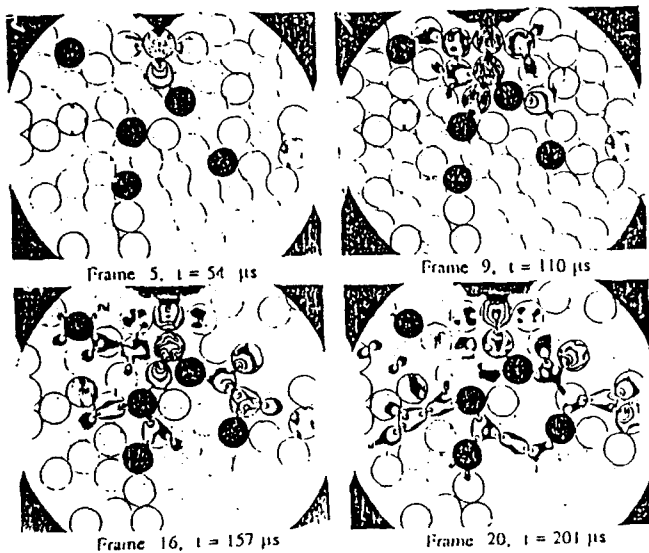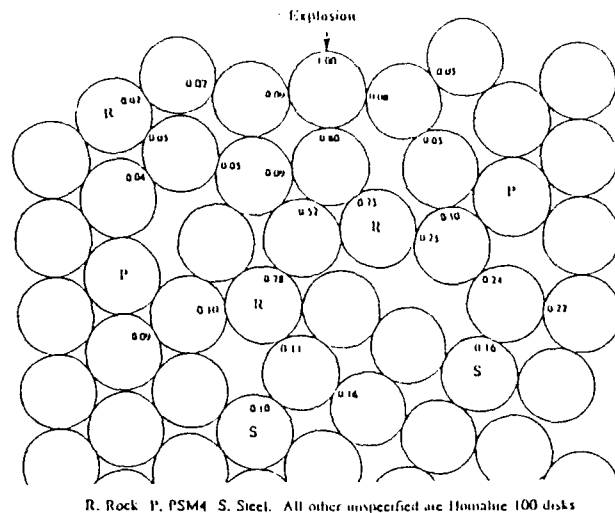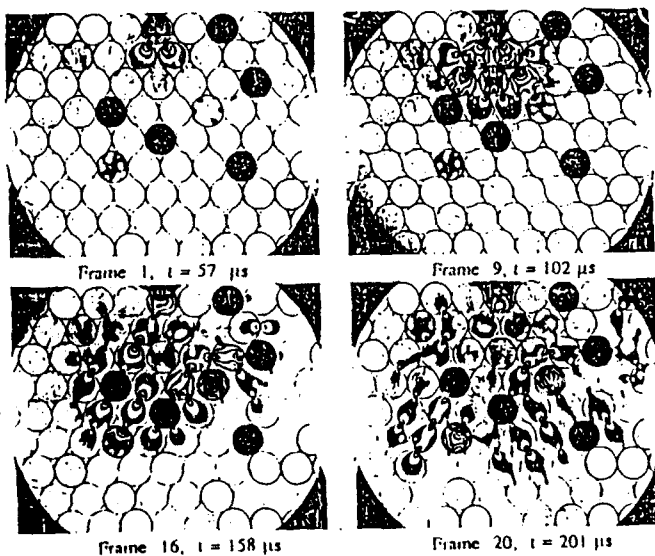
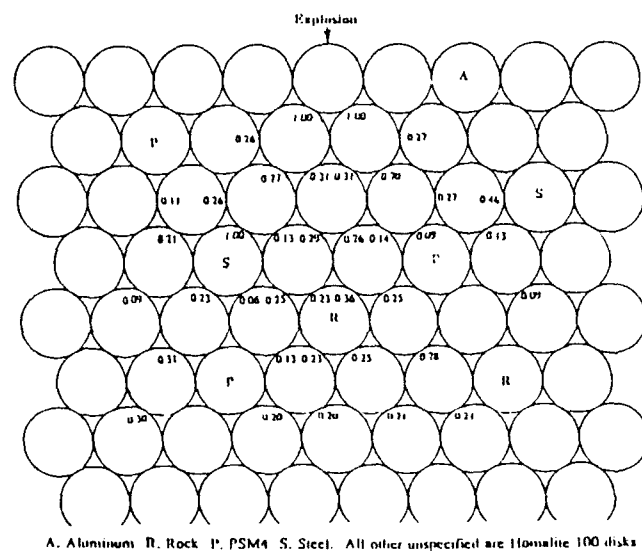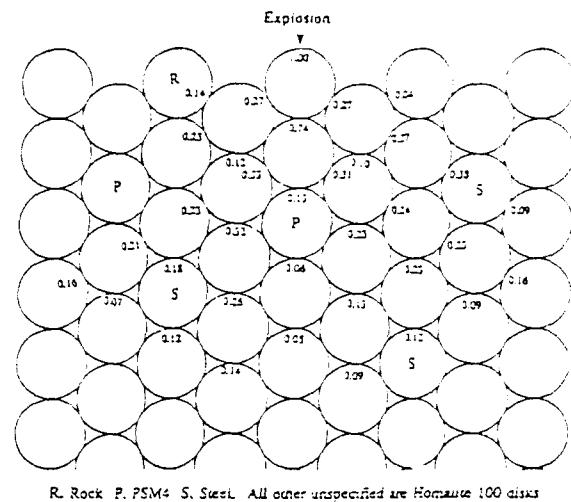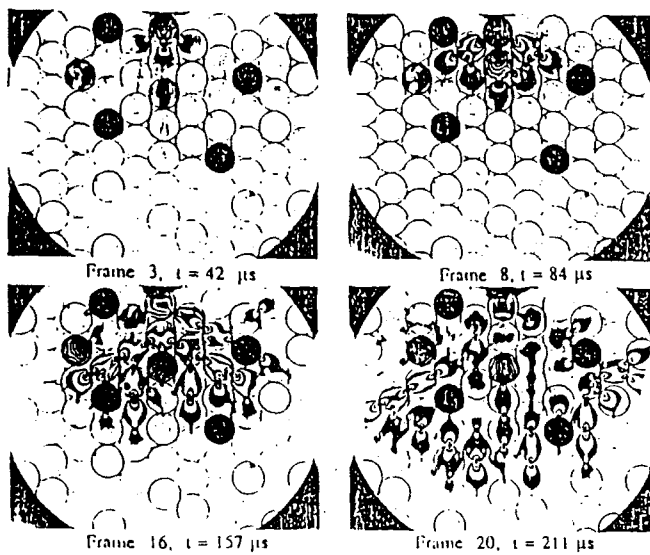Fig. 12.12 Maximum contact loads obtained from the photoelastic data for a random packing model with heterogenous disk arrangement
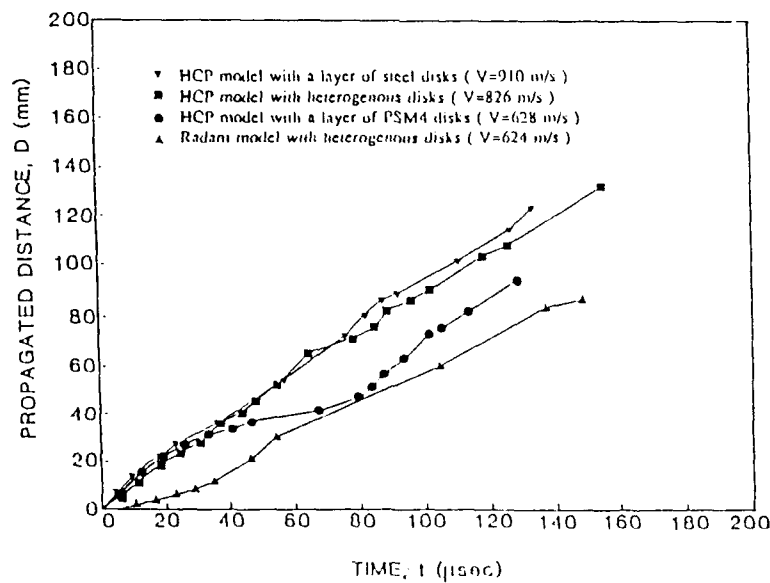

Fig. 12.13 Comparison of wave velocity in the vertical direction for different models

CHAPTER 13

DYNAMIC LOAD TRANSFER IN VIRGIN AND
DAMAGED GRANULAR ROCK MEDIA

An experimental investigation was conducted to study dynamic load transfer in granular rock media. The granular rock media was modeled as one-dimensional chain of disks fabricated from four different types of white Vermont marble. The study focuses on the effect of microstructure on transient pulse propagation. The transient pulse is generated by exploding a small amount of lead azide charge on top of the rock disk assembly. During wave propagation dynamic contact strains are recorded using electrical resistance strain gages. This information is used to calculate wave velocity and attenuation as a function of the cumulative damage in the disk assembly.

13.1 INTRODUCTION

The response of particulate materials to impulsive loading, has been of substantial interest to both engineers and researchers. The stress wave propagation in such a media, due to explosive loading, depends primarily upon the load transfer process by which the mechanical signals are transmitted. This phenomenon is related to the properties, geometry as well as the microstructural arrangements of the particles in the media. As the stress wave passes through the system rearrangement of the particles takes place. Further, depending upon the amplitude of the stress wave, damage can occur in the particles. Thus the transmitted wave carries along with it the information regarding the damage and the microstructural rearrangements of the grains. The wave-propagation characteristics of the resulting media is different as compared to that of the virgin material. Moreover, it has been observed that for real earth materials like sand and rock, this load transfer phenomenon is also a function of the state and history of the applied load.

This chapter presents preliminary work on the wave propagation and load transfer in a one dimensional disk chain assembly. The disks were fabricated from four different grades of white Vermont marble each having a different microstructure. The stress wave is generated by exploding a small amount of lead azide on top of the disk assembly. The dependence of the stress wave velocity and attenuation on the microstructure of the four grades of marble rocks was studied. In general the composition of marble is heterogeneous in nature and the microstructure comprises of preexisting voids,

microcracks and inclusions. In this study, particular attention was paid to the effect of grain size and accumulated damage due to prior loading on wave propagation. Attempt was also made to investigate and quantify the damage that occurs in these one dimensional aggregate of disks under repeated stress wave loading. Tensile splitting tests were performed to estimate the residual strength of the disks. Photomicrographs were taken at different stages of the stress wave loading process. Moreover, the stress wave velocity as well as the wave attenuation were obtained as a function of the accumulated damage in the disk assembly.

13.2 EXPERIMENTAL PROCEDURE

A series of experiments was conducted on a single chain assembly of rock disks to study wave propagation in the rock media as shown in Fig. 13.1. These disks were fabricated from four different cores of Vermont marble having different microstructure as shown in Fig. 13.2. Typical values of the Young's modulus and the Poisson's ratio for the Vermont marble used were 41.3 and 0.23 GPa respectively. The rock disks were 31.75 mm in diameter and 13.7 mm in thickness. The assembly of disks was explosively loaded using 15 mg of Lead Azide in a specially designed charge holder. The resulting dynamic load transfer phenomenon in the disks was studied using electrical resistance strain gages.

The strain gages were bonded on four separate disks in the chain at a distance of 7 mm from the contact point. The strain gages were suitably connected to the Nicolet Oscilloscopes through the bridge amplifiers. The oscilloscopes were triggered when the explosive was detonated. The resulting strain profile was recorded as a function of time. The strain profile was analyzed to obtain the average stress wave velocity, peak contact strain, duration of contact, as well as the stress wave attenuation.

To study and quantify the effect of damage induced in the rock disks due to repeated stress wave loading the residual strength, the wave velocity and the stress wave attenuation were obtained for the single chain of the disk assembly. This average wave velocity and the stress wave attenuation were plotted as a function of the number of times the assembly was loaded.

The residual strength of the disk was measured by an indirect tensile test. In these tests the marble disks were laid vertically on the loading plates of the Instron machine in the compression mode. The load was slowly increased at a very slow rate until the

specimens failed by splitting across the vertical diameter. Assuming linear condition within the core the approximate tensile strength σ_t, was calculated using the equation:

$$\sigma_t = \frac{2\, P_{max}}{\pi\, D\, L} \qquad (13.1)$$

where P_{max} is the applied load at fracture, D is the diameter of the core and L is the length of the core.

To estimate the residual strength of the damaged rock disks 15 mg of lead azide was used to generate the stress wave through the assembly of disks. The tensile tests were carried out on the first two disks taken out from the top of the assembly. Two new disks were placed on top of the disk assembly to replace the damaged disks. The chain assembly, this time was loaded twice, and again the top two disks were taken out and their residual tensile strength obtained. This procedure was continued until the residual tensile strength was obtained for the disks which had been loaded five times.

13.3 ANALYSIS

The wavelength of the stress wave generated by the explosive charge was approximately four times the diameter of the disks as observed in these experiments. This resulted in a quasistatic type of loading around the contact zone (Shukla and Damania, 1987). Hertz contact theory along with the strain gage data were thus used to calculate the contact strains.

Using Hertz contact stress theory, the stress field equations at any point (x=0,z) around the contact region of the two bodies, as shown in Fig. 2.7, are represented as:

$$\sigma_{zz} = -\frac{b^2\, z\, \phi_1}{\pi\, \Delta}$$

$$\sigma_{xx} = -\frac{b\, z}{\pi\, \Delta}\left(\frac{b^2 + 2\, z^2}{b}\phi_1 - \frac{2\, \pi}{b}\right) \qquad (13.2)$$

$$\sigma_{zx} = \frac{2\, z}{b}$$

where ϕ_1, M and Δ are:

$$\phi_1 = \frac{2 \pi M}{(M^2 \sqrt{2 M^2 + 2 z^2 - 2 b^2})}$$

$$M = \sqrt{b^2 + z^2}$$

$$\Delta = R \frac{(1 - v^2)}{E}$$

where R is the principal radius of curvature of the body, E is the modulus, v is the Poisson's ratio and b is the half contact length. For the two dimensional plane stress problem the contact normal strain is given by:

$$\varepsilon_{zz} = \frac{1}{E} (\sigma_{zz} - v \sigma_{xx}) \tag{13.3}$$

Substitution of equation (13.2) in equation (13.3) results in a non-linear equation for normal strain ε_{zz} in terms of the half contact length b as shown below.

$$\varepsilon_{zz} = \frac{- b^2 z \phi_1}{E \pi \Delta} (1 + \frac{2 \pi \Delta v}{b^3 \phi_1}) \tag{13.4}$$

The normal strain is plotted as a function of the normal distance from the contact for different values of the contact length 2b as shown in Fig. 13.3. Thus by experimentally obtaining the normal strain at a known location (x,z) on the disk the half contact length b as well as the contact strain can be calculated. Since the strain gage has a finite size it averages the strain over its grid area. This average strain is not equal to the strain at the grid geometric center. From the plot of the strain vs. distance (Fig. 13.3) it can be seen that steep gradients in the strain exist near the contact point and the strain profiles peak around z=1.0 mm. As the distance normal to the contact point increases the strain gradients reduce and the strain profiles become almost flat after z=6 mm. Thus it is important that the strain gages be placed beyond z=6 mm so as to minimize the averaging error. Further the Hertz contact stress field is valid for a distance approximately equal to 8b from the contact point (Shukla and Damania, 1987). Typical half contact length obtained in the experiments was 1 mm. Thus to meet the above constraints the strain gage

must be placed at a distance of more than 6mm and less than 8mm from the contact point. Fig. 13.4 shows the three dimensional plots of the strain profile as a function of both x and z as the strain gage surface would experience. When the center of the strain gage is placed at 7mm from the contact point the strain gage experiences small strain gradients as compared to being placed 2mm and 4mm from the contact point.

To estimate the error introduced due to the finite size of the strain gages the percentage error was calculated by considering a strain gage with a grid size (L X L) positioned at a height z above the contact point. The percentage error is defined as:

$$Error \ \% = \frac{\varepsilon_G^c - \varepsilon_G^{av}}{\varepsilon_G^c} \ X \ 100 \tag{13.5}$$

The strain ε_G^c at the geometric center of the strain gage is calculated from equation (13.3). The strain gage area is discretized into a grid containing (100 X 100) nodes and the strain at each node is calculated. From this the average strain is obtained. The results are presented in Fig. 13.5, which shows the error due to the averaging effect as a function of the gage grid length, L. The results are plotted for different heights, z above the contact points. The error is higher for strain gages closer to the contact points because of the steep strain gradients. Also the error increases as the strain gage size increases. For the size (2mm X 2mm) and the location of the strain gage used in this study the error is about 2 %.

13.4 RESULTS AND DISCUSSIONS

13.4.1 Wave Propagation in Virgin Rock Disk Assembly

A series of experiments was conducted with strain gages mounted 7mm from the contact point of the disks. Strain versus time plots at the location of the strain gages were recorded. A typical strain gage output profile is shown in Fig. 13.6. Position of the wavefront versus time plots were obtained for marble A, marble C, and marble D disk assemblies. Typical plot is shown in Fig. 13.7. The position of the wavefront was obtained from the strain peaks in the recorded strain profile. The peak in the strain profiles, being clearly defined, were given preference over the arrival times of the waves in the calculation of the wave velocity. Also, the strain profiles being symmetric, the choice of the peak strain avoided any significant error due to the spreading of the strain

profiles due to the material and the geometric dispersion. The stress wave velocity was obtained by drawing a best fit line through the experimental points. The results indicate that a correlation exists between the stress wave velocity and the grain size. It is observed that the average wave velocity is higher for rocks with larger grain size. The average grain size of marble A was the smallest and the stress wave velocity was 1210 m/sec. The grain size of marble C was higher and the corresponding stress wave velocity obtained was 1425 m/sec while marble D had the largest average grain size and a stress wave velocity of 1525 m/sec. This trend is to be expected as the stress wave encounters a fewer number of grain boundaries or obstacles as it propagates through the granular rock material having a larger grain size.

To study the stress wave attenuation in different grades of marble the normalized peak strain was plotted against the stress wave propagation distance as shown in Fig. 13.8. The contact stress was normalized with respect to the stress at the contact between the disks 2 and 3. At the contact point the contact strain increases from zero to a peak value and then gradually decreases towards zero. Some oscillations are seen in the strain profile due to the reflection of waves from the boundaries. A typical duration of the contact was 85 μs. Due to the cumulative effect of the internal losses within the disk, energy spent in closing the contacts, and the reflection effects from the boundaries of the disk the stress wave attenuates rapidly in the first two disks and then gradually as the distance from the explosive loading increases. Again the disk with the smallest grain size shows the steepest drop in contact strain. Marble A shows 50 % drop in its peak strain value as the wave travels through the first two disks. Marble C and Marble D show about 37 % drop in its peak value for the same distance of travel. After this the attenuation in all the three grades of marble is similar and the peak strain drops to 35 % of its initial value as the wave propagates through nine disk diameters.

13.4.2 Wave Propagation in Damaged Rock Disk Assembly

To quantify the damage occurring in the rock disks during wave-propagation, tensile splitting tests were carried out to obtain the residual tensile strength. The residual strength of the first two disks was studied as most of the attenuation in the stress wave occurs in these disks. Table 1 lists the residual tensile strength of the first two disks as a function of the number of stress wave loadings. It was observed that after the passage

of the first stress wave the residual strength of the first disk falls down to 63 % of its value in the virgin state (1125 N/m²). Additional drop of 8 % in the tensile strength occurs after the second loading wave. As the number of stress wave loadings is increased further the residual tensile strength reaches a limiting value of around 600 N/m² (51 %) before the disk fractures.

The tensile strength of the second disk drops down by only 17 % after the first two stress waves. This happens because the cumulative damage occurring in the second disk is relatively small as compared to the first disk as the peak strain value attenuates by almost 40 % by the time the stress wave propagates through the first disk. As the number of shock wave loadings is increased further, the residual strength remains fairly constant until the fourth loading wave after which the tensile strength falls to 60% of the tensile strength value in the virgin state.

The average stress wave velocity in the disk assembly was plotted as function of repeated stress wave loading as shown in Fig. 13.9. The velocity increases from 1080 m/sec in the virgin state to 1400 m/sec after the passage of the first stress wave. As the number of stress wave loadings is increased further the wave velocity undulates about the terminal velocity of 1450 m/sec and eventually falls off as the cumulative damage increases in the disks. The increase in wave velocity, after the first stress wave, is partially due to the fact that as the contacts are established the disks come closer to each other resulting in increased stiffness of the assembly. At the same time as the wave propagates it closes the preexisting voids and microcracks in the disks resulting in a further increase of velocity. As the number of stress wave loadings is increased the cumulative damage in the disks increases resulting in an increase in the number of microcracks. These microcracks impede the progress of the stress waves as it has to travel around these cracks.

The normalized contact strain for the contact point 7-8 under repeated stress wave loading is shown in Fig. 13.10. The contact strain is normalized with respect to the strain obtained at the contact 7-8 after the first stress wave loading. The peak contact strain at contact 7--8 was used as an indicator of the accumulation of the damage in the first seven disks of the assembly under repeated loading. From the plot it can be seen that like in the case of the velocity the contact strain first increases, reaches a terminal level

and then falls off as the damage accumulates in the disks.

As the number of stress wave loadings is increased damage occurs around the contact zone due to high contact stresses and large scale crumbling and pitting is observed near the contact zone. Away from the contact point the grains simply separate along the grain boundaries. Rock grains are made up of crystals having dissimilar orientations and thus having different rates of stress wave propagation. This causes differential stresses to develop along the grain boundaries which tend to pull the grains apart. Fig. 13.11 shows the photomicrographs of the area near the contact zone of the disks after the passage of the first two stress waves. Close examination of the fracture surface also shows fractures which radiate from the contact area. These are caused by the hoop stresses which develop at the front of the divergent stress wave. Spalling is noticed near the lower contact area of the disk. This is caused by the interference of the tail portion of the compressional wave and the front of the same wave which was transformed, on reflection at the free surface into a tension wave. Rocks being strong in compression but weak in tension are particularly prone to spalling.Under repeated loading the microcracks formed due to the grain boundary weakening, radial microfracture and those formed due to spalling combine together to create open cracks on the disk surface as shown in the photomicrograph in Fig. 13.12. The microcracks and the surface crack impede the propagation of the stress wave and lower the stiffness of the disk assembly resulting in the attenuation of the stress waves and reduction of the stress wave velocity.

13.5 CONCLUSIONS

A dynamic strain gage technique was employed to study wave propagation and dynamic load transfer in granular rock media. The rock media was modeled as a one dimensional array of circular disks fabricated from different grades of Vermont marbles having different microstructure. The dynamic data was analyzed to obtain the average wave velocity, stress wave attenuation for both virgin as well as damaged rock media. The residual strength of the disks was estimated after the passage of the stress wave using an indirect tensile test. The damage in the disks was studied by taking optical micrographs of the disk surface. The results indicate that:

1. A correlation exists between the microstructure of the rock material and the stress wave velocity. Larger the grain size of the rock media higher is the stress wave

velocity. For the different grades of marble studied, the wave velocity corresponding to the largest and the smallest grain sizes was 1525 m/sec and 1210 m/sec respectively.

2. Rapid attenuation in the peak contact strains, and thus the amplitude of the stress wave, takes place as the wave propagates through the first three disk diameters. Moreover, it is observed that this rate of decay increases as the grain size of the marble decreases. However, as we move further away from the point of loading all the three grades of marble approach the same rate of attenuation.

3. The stress wave velocity increases sharply by almost 30% after the passage of the first stress wave. Upon repeated explosive loading the stress wave velocity approaches a terminal velocity of 1450 m/sec and eventually falls off as the disk fails by fracturing across the surface.

4. The residual tensile strength of the disk decreases as the number of stress wave loadings was increased. Further, a limiting residual strength value exists which remains fairly constant upon repeated loading until the disk fractures.

Table 13.1 Residual strength as a function of number of stress wave loading

NUMBER OF STRESS WAVES THROUGH THE DISK ASSEMBLY 15mg lead azide	RESIDUAL STRENGTH N/m^2 DISK 1	RESIDUAL STRENGTH N/m^2 DISK 2
VIRGIN	1125	1185
1	710	1160
2	640	980
3	610	1040
4	FRACTURED	830
5	FRACTURED	690

(40x) MARBLE A,   (40x) MARBLE B,

(10x) MARBLE C ,   (10x) MARBLE D,

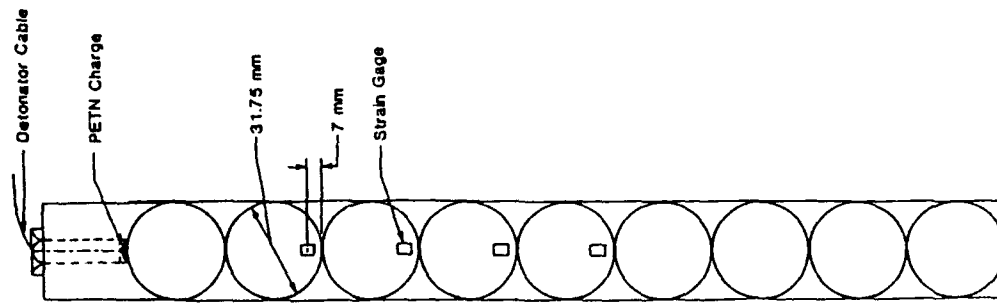Fig. 13.2   Microstructure of the four grades of white Vermont marble

Fig. 13.1   One dimensional marble disk chain assembly showing the position of the explosive charge and the location of the strain gages
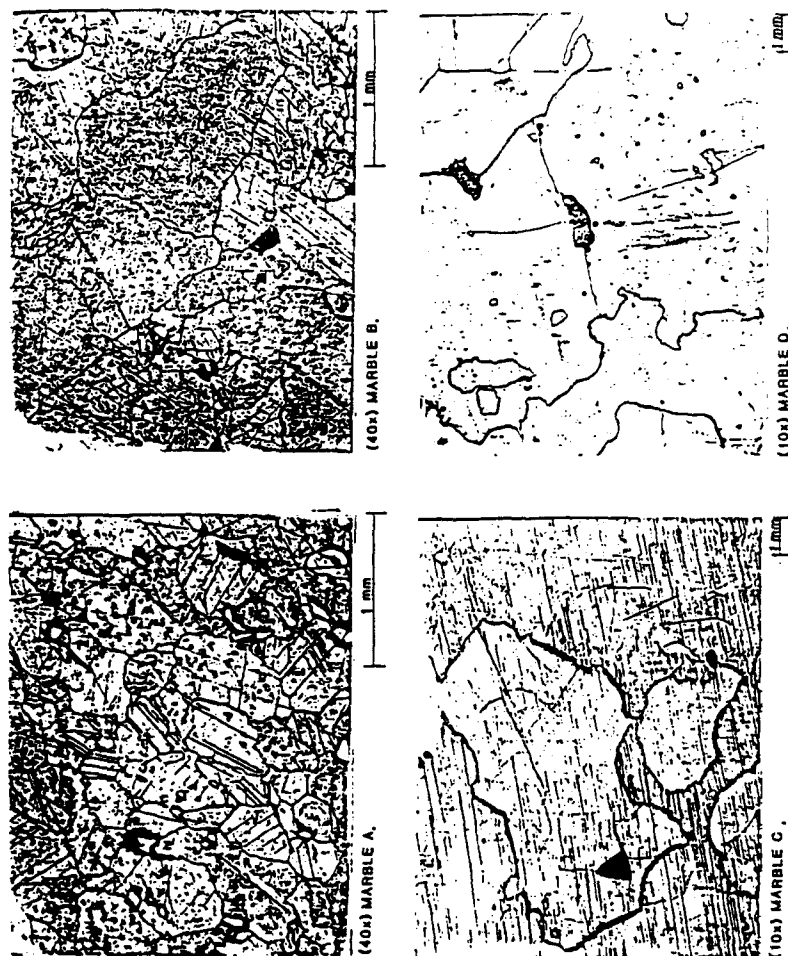
THEORETICAL STRAIN PROFILE

Dynamic Properties of Vermont Marble
Elastic Modulus, E = 41.3 GPa
Poissons Ratio, $V = 0.23$
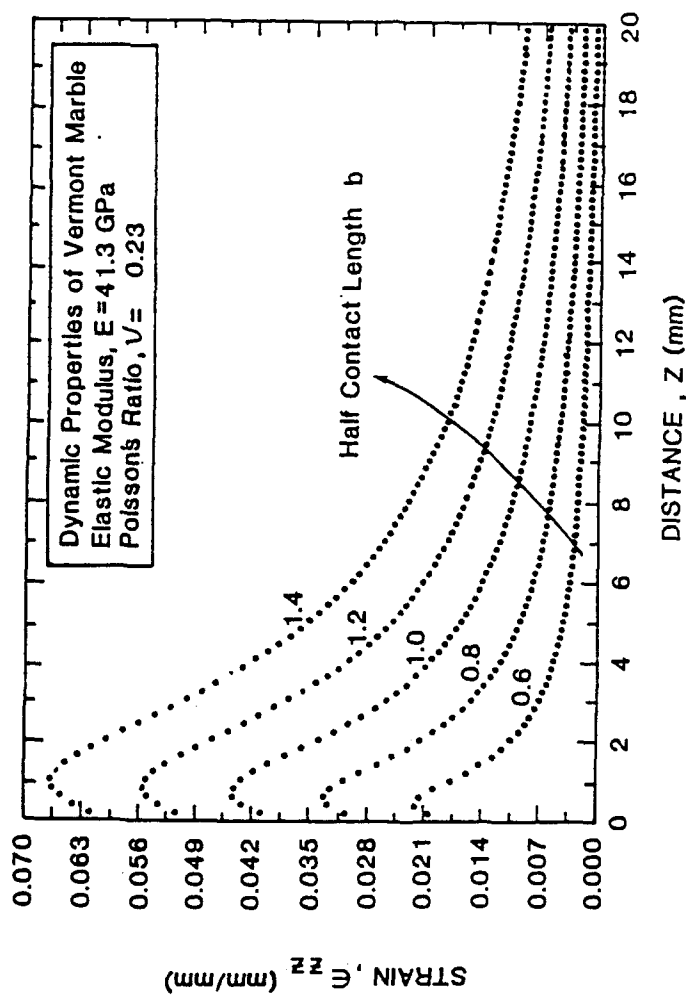
Half Contact Length b

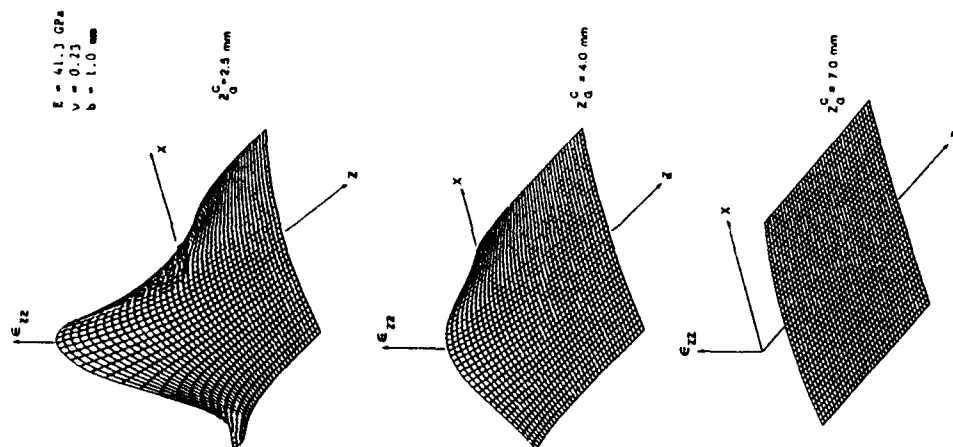Fig. 13.3 Variation of the theoretical strain along the normal distance from the contact point

Fig. 13.4 Three dimensional theoretical strain profiles as seen by the strain gages positioned at three different locations near the contact zone
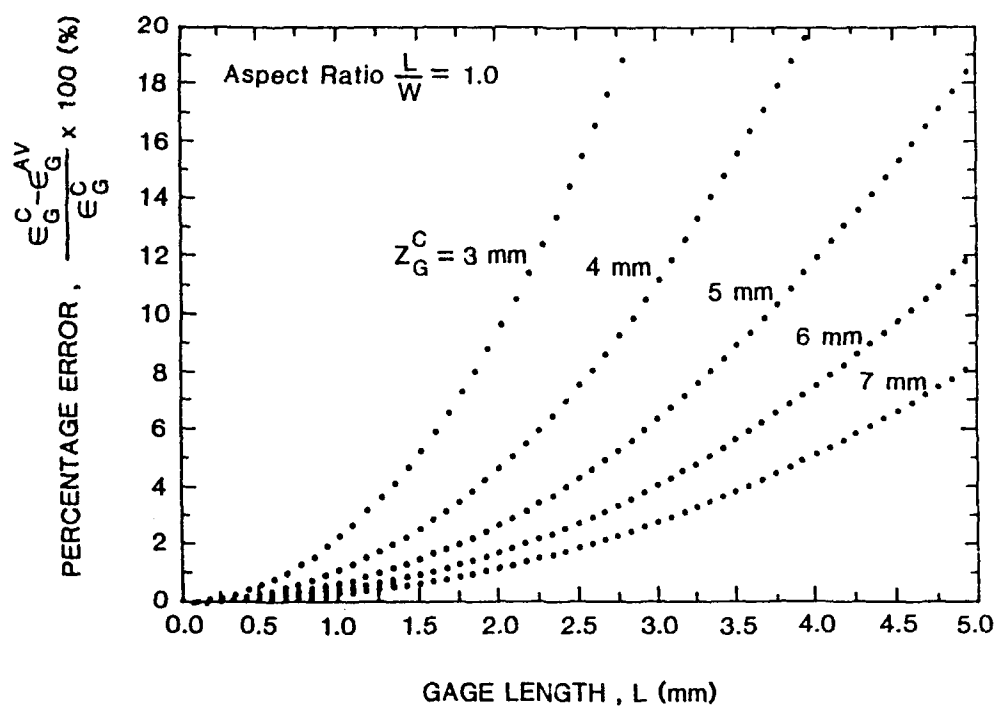
210

Fig. 13.5   Theoretical percentage error as a function of the strain gage length and its location from the contact point
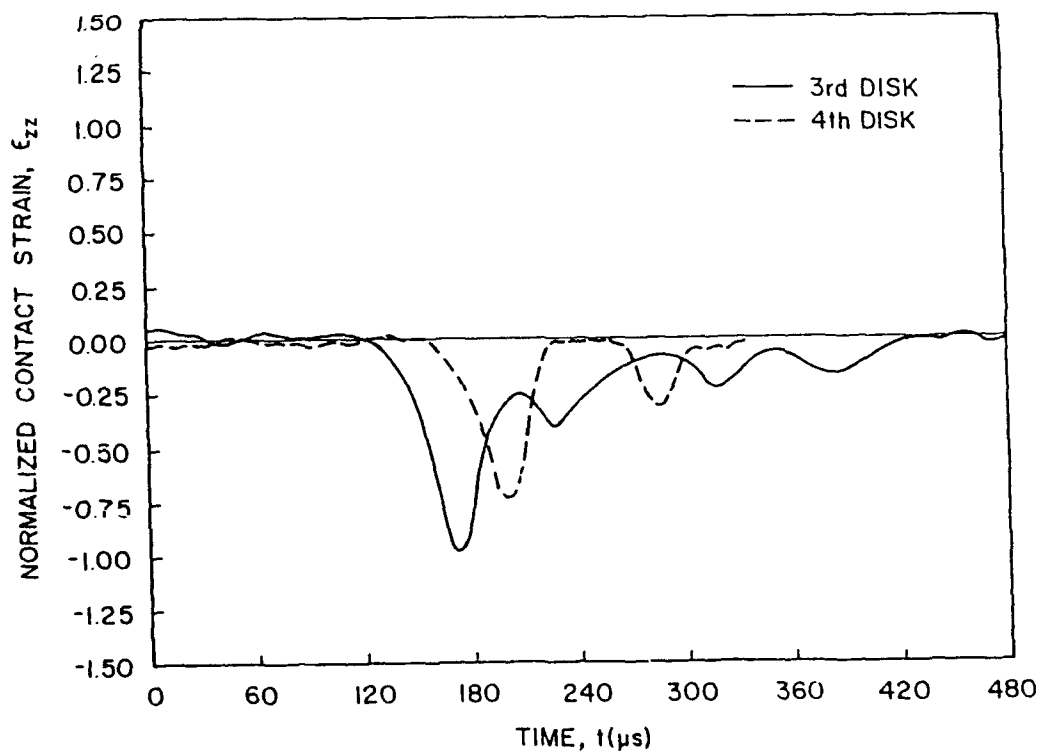
Fig. 13.6   Typical contact strain profile

211

CURVE FIT
o EXPERIMENTAL

POSITION OF WAVEFRONT, D(mm)

350
315
280
245
210
175
140
105
70
35
0

0 30 60 90 120 150 180 210 240 270 300

TIME, t (μsec)
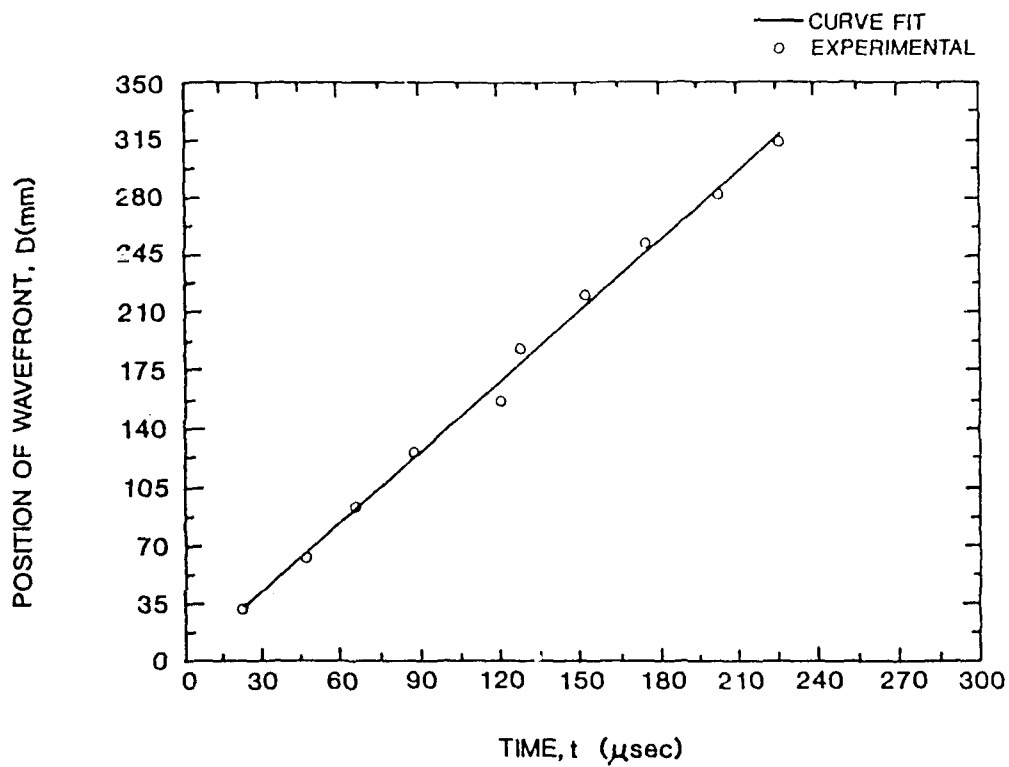
Fig. 13.7 Position of the stress wave versus time used
to obtain the average wave velocity

NORMALIZED PEAK CONTACT STRAIN

1.1
1.0
0.9
0.8
0.7
0.6
0.5
0.4
0.3
0.2
0.1
0.0

o MARBLE A
□ MARBLE C
■ MARBLE D

0.0 50.0 100.0 150.0 200.0 250.0 300.0 350.0 400.0

WAVE PROPAGATION DISTANCE, D (mm)
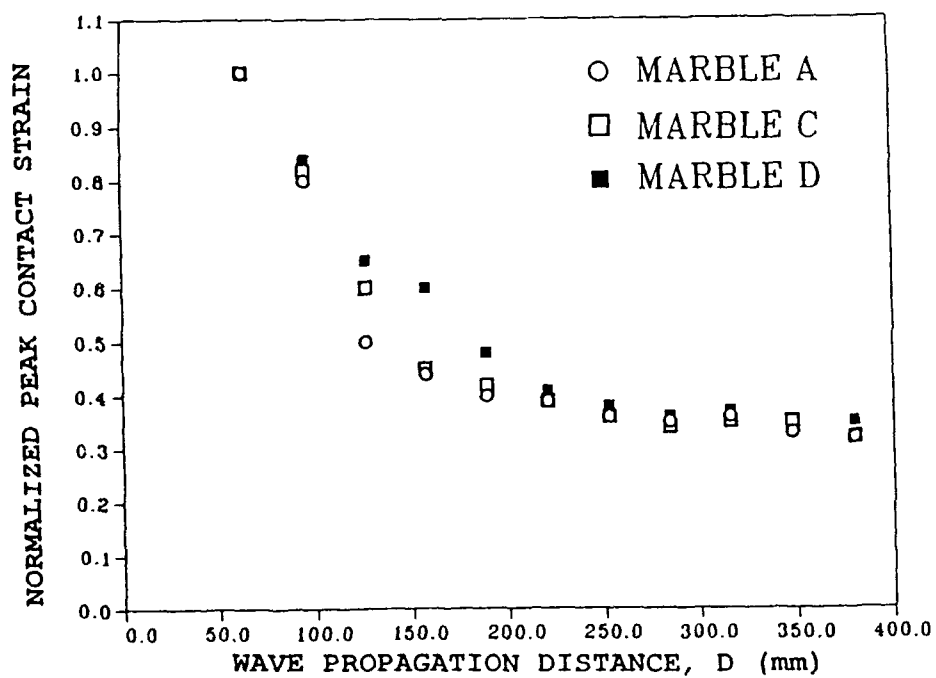
Fig. 13.8 Strain wave attenuation profile for
three different grades of marble

212

Fig. 13.9 Average stress wave velocity as a function
of the repeated stress wave loading

Fig. 13.10 Typical strain wave attenuation profile at
c ntact 7-8 under repeated stress wave loading

213

Fig. 13.11   Photographs showing the damage near the contact zone
of the two disks

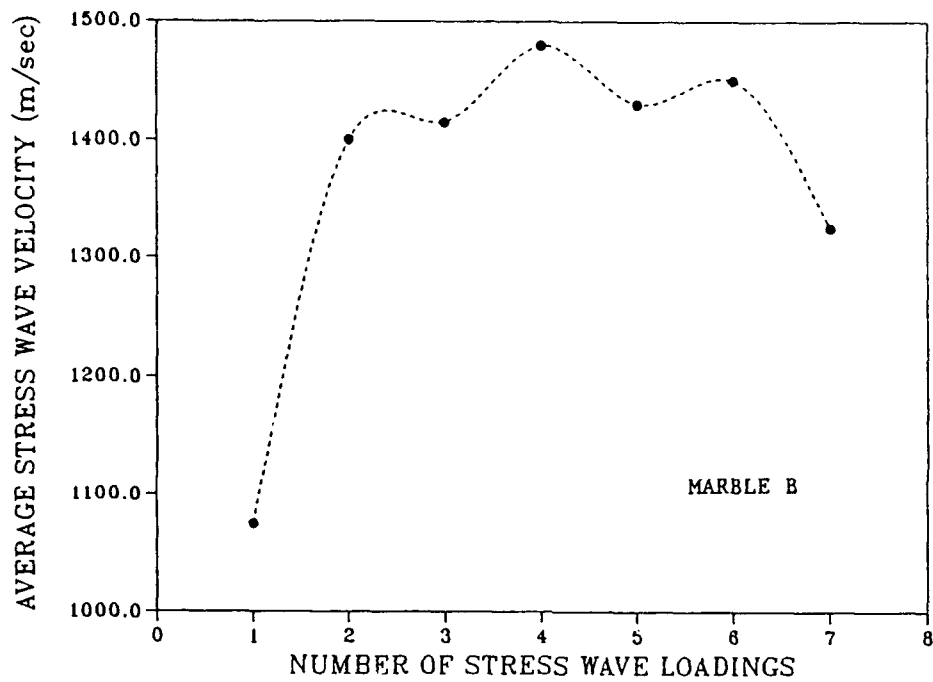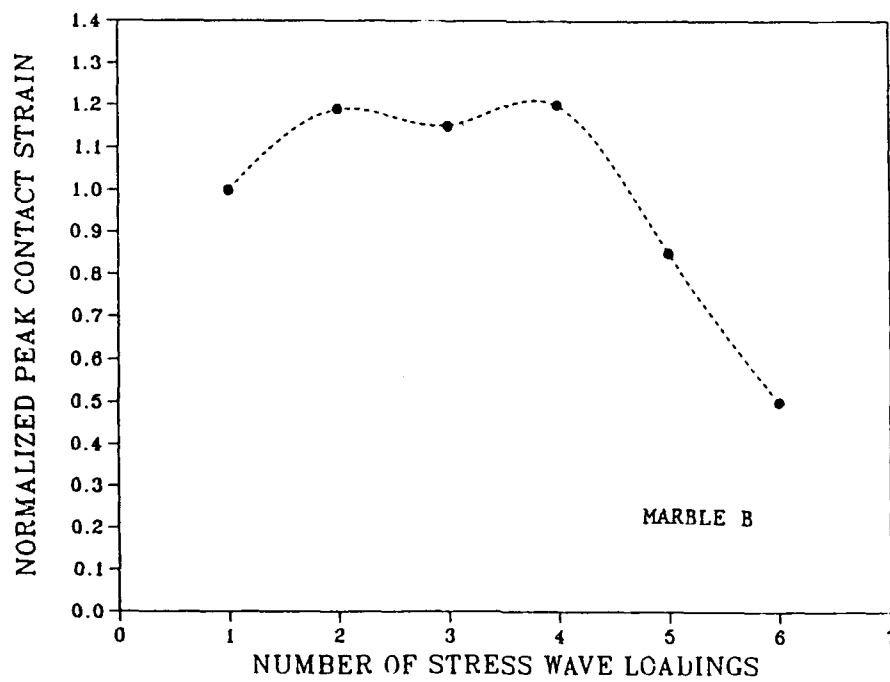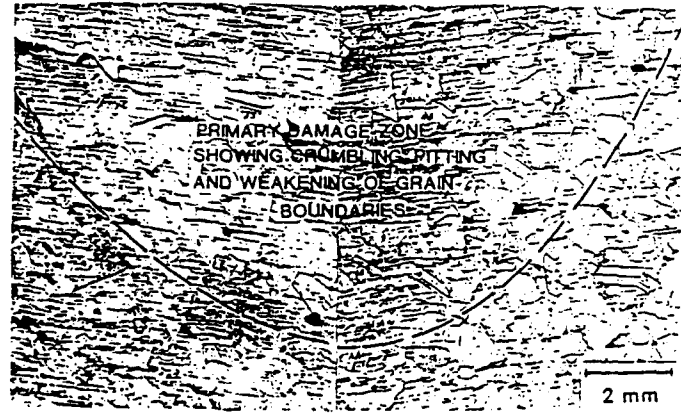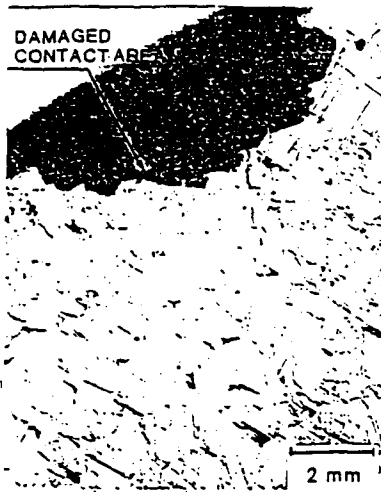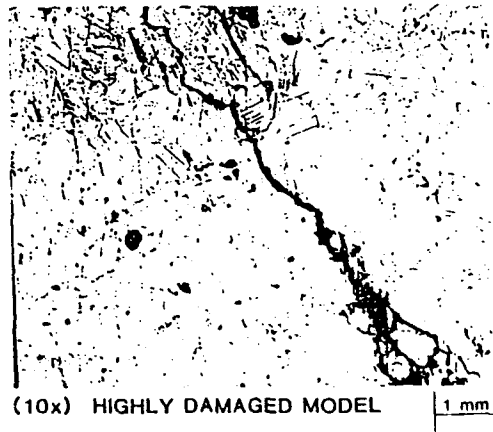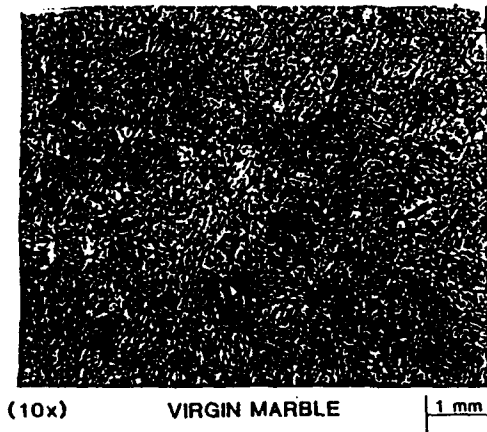Fig. 13.12   Photographs showing a highly damaged disk as
compared to the virgin disk

214

CHAPTER 14

WAVE PROPAGATION IN SATURATED GRANULAR MEDIA

An experimental investigation was conducted using dynamic photoelasticity and high speed photography to study stress wave propagation and dynamic load transfer in fluid-saturated granular media. The stress wave was generated by detonating a small amount of explosive. The granular media was simulated by circular disks fabricated from Homalite 100. In order to compare the effects of fluid viscosity on wave propagation, different fluids such as water, Dow Corning 200 fluids with viscosity 10 cs and 100 cs, were used in this study.

14.1 INTRODUCTION

Wave propagation in a discontinuous media has been of interest to the soil and rock mechanics community. The propagation of elastic wave in the earth's crust is most intimately related to the properties of sand, soil and rocks. The elastic properties of these substances are greatly affected by the amount of water contained in them, packing density, porosity, the size of the particles that form the substances and the binding material which they contain. The equations governing the interaction of the solid and fluid media were first established for quasi-static phenomena by Biot (1941) who extended them to the dynamical case (1962a and 1962b). Then many researchers have done a lot of work on this topic, for example, Sandhu (1968), Prevost (1982).

Current interest in geomechanics is focused on transient phenomena occurring in earthquakes, wave loading and consolidation. For all of these the coupling between the deformation of the 'solid skeleton' of the soil or rock and the motion of the pore fluid is of primary importance. Shukla and Prakash (1990) experimentally investigated wave propagation in fluid-saturated and unsaturated porous media. Ross, et.al. (1989) conducted experiments to determine the effects of particle size, moisture content and peak magnitude on the transmissibility of pressure waves in a granular or soil medium.

However, little attention has been paid to the effect of viscosity of the fluid which saturates the granular media. As a matter of fact, the soil or rock media can be saturated by pure water or crude oil which has different viscosity from each other. This viscosity is believed to affect the shear force transfer between particles. Thus it is proposed not

215

only to investigate the wave propagation in saturated granular media, but also to study the effects of viscosity of pore fluids.

14.2 EXPERIMENTAL PROCEDURE

Experimental models for one and two dimensional arrangements are shown in Figs. 14.1 and 14.2. The fluids were contained in a leak-proof box made from plexiglass sheets. The circular disks were then placed inside the fluids with desired packing geometry. The fluids used in this investigation were water, DOW CORNING 200 fluid 10 cs, DOW CORNING 200 fluid 100 cs. The later two kinds of fluids have ten and one hundred times the viscosity of water, respectively.

The wave propagation phenomena due to explosive loading was studied using the technique of dynamic photoelasticity and high speed photography. This technique has been mentioned before and will not be discussed here. The high speed photographic system operates as a series of high intensity extremely short duration pulses of light and provides 20 photoelastic images at discrete times during the dynamic event. These photographs of the wave propagation process at different stages of development provided the necessary data to obtain the velocity and attenuation of the stress wave.

The sequence of 20 photographs obtained from the high speed camera were analyzed to obtain the wave velocity and the stress wave attenuation in granular media saturated with different fluids. The wave velocity was obtained by plotting the instantaneous position of the wave front with respect to time. The slope of this line gave the average wave velocity. The contact load between two disks was obtained by analyzing the fringe patterns around the contact. The effect of fluids on the fringe pattern appearance is negligible since the fluid layer on the disk surface is very thin.

14.3 Results and Discussions

The first series of experiments was conducted in a one dimensional disk assembly. Fig. 14.3 shows the isochromatic fringes obtained in a single chain granular arrangement saturated with water. The wave front as a function of time is plotted in Fig. 14.4. The slope of the line in Fig. 14.4 gives the average wave velocity about 965 m/s which is little bit lower than the wave velocity of 1050 m/s in the same arrangement without saturation. This small reduction of wave velocity can be explained that between the disks there exists a small layer of fluid through which the wave motion takes more time. The

216

contact load as a function of time is plotted in Fig. 14.5. It can be seen from Fig. 14.5 that the contact load profiles have similar shape as those obtained in a single chain disk assembly without saturation. The amplitude attenuation for four disk distance (127 mm) is about 24% (see Table 14.2). However, it is only around 14% drop of wave amplitude when there is no saturation. This higher drop in wave amplitude is because some of the energy was transferred to the fluid surrounding the disks, especially at the contact.

Fig. 14.6 and 14.7 show the wave propagation in a single chain disk assembly saturated with Dow Corning 200 Fluids with 10cs and 100cs. The wave velocities listed in Table 14.1 are 950 and 940 m/s respectively. The amplitude attenuation are plotted in Fig. 14.8. It seems there is not much difference for wave amplitude attenuation in a single chain disk assembly when saturated with different fluids. However, it does show more attenuation in saturated granular media than that in an unsaturated one.

Fig. 14.9, 14.10 and 14.11 show wave propagation in a hexagonal closed packing granular media saturated with water and Dow Corning 200 Fluids with 10cs and 100cs respectively. The wave velocities listed in Table 14.1 are almost the same compared to the results from 1-D experiments. However, unlike 1-D experimental results, the contact load attenuation in the main chain for saturated granular media is less than that for unsaturated media. It can be seen from the photographs in Fig. 14.9, 14.10 and 14.11 that most energy transfer occurred in the two main chains. However, for unsaturated HCP model as shown in Fig. 14.12 the energy transfer not only occurred in the main chains, but also in the neighboring disks next to the main chain. Since there is a thin layer of fluids in a saturated granular media it is more difficult for the wave to propagate from the main chain disks to the disks with contact angle other than zero degree (In the main chain all the disks have contact angle $0°$). That is why for 2-D problems, the contact load attenuation in the main chain for saturated granular media is less than that in unsaturated one.

14.4 CONCLUSIONS

(1). Wave propagation velocity in granular media decreases by about 5-10% when saturated with fluids.

(2). Wave amplitude in 1-D granular assemblies show 25% higher attenuation when saturated with fluids.

(3). In two-dimensional HCP model, due to saturation, wave mainly propagates through two main chains. Thus, less amplitude attenuation is found compared to the results of unsaturated granular media.

(4). No conclusive information is obtained about the effect of viscosity of the saturating fluids on wave propagation phenomena in granular media.

TABLE 14.1

Wave Velocity (m/s)

Saturated with	air	water	Dow Corning 200 fluids (10 cs)	Dow Corning 200 fluids (100 cs)
1-D	1050	965	950	940
2-D	1010	960	950	900

TABLE 14.2

Contact Load Attenuation
for 4 Disk Distance (127 mm)

Saturated with	air	water	Dow Corning 200 fluids (10 cs)	Dow Corning 200 fluids (100 cs)
1-D	18%	24%	25%	23%
2-D	70%	62%	52%	53%

Fig. 14.2 Saturated experimental arrangement of a 2 - D Homalite 100 disk assembly
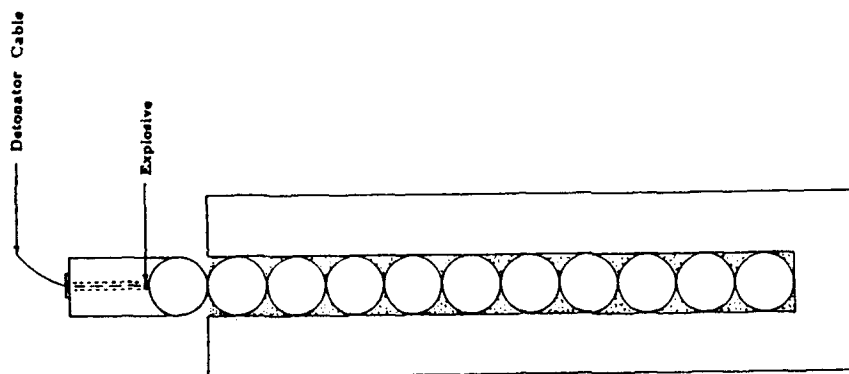
Fig. 14.1 Saturated experimental arrangement of a 1 - D Homalite 100 disk chain

219

Frame 1 | Frame 2 | Frame 3 | Frame 4 | Frame 5 | Frame 6 | Frame 7 | Frame 8 | Frame 9 | Frame 10 | Frame 11 | Frame 12 | Frame 13 | Frame 14 | Frame 15 | Frame 16 | Frame 17 | Frame 18 | Frame 19 | Frame 20
t=138 μs | t=142 μs | t=146 μs | t=152 μs | t=157 μs | t=163 μs | t=168 μs | t=174 μs | t=179 μs | t=185 μs | t=197 μs | t=203 μs | t=208 μs | t=213 μs | t=219 μs | t=225 μs | t=231 μs | t=236 μs | t=243 μs | t=249 μs

Fig. 14.3   Photoelastic fringe patterns of a single chain
model saturated with water
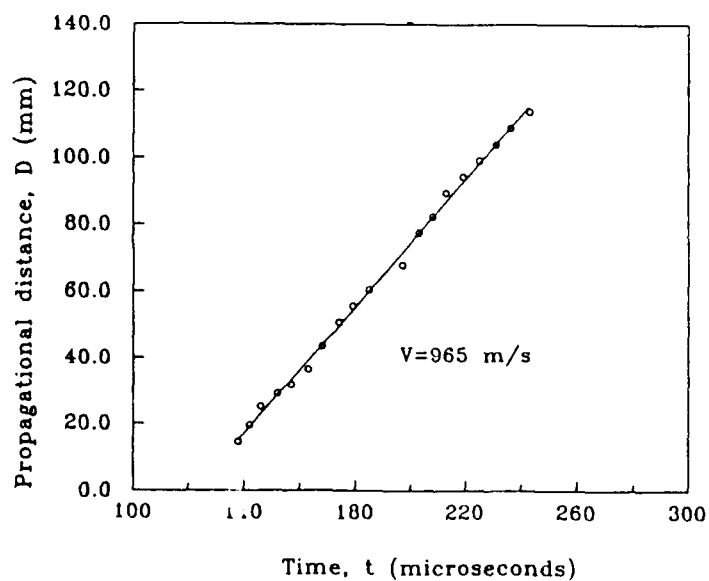
Fig. 14.4   Wave front as a function of time for a single
chain model saturated with water
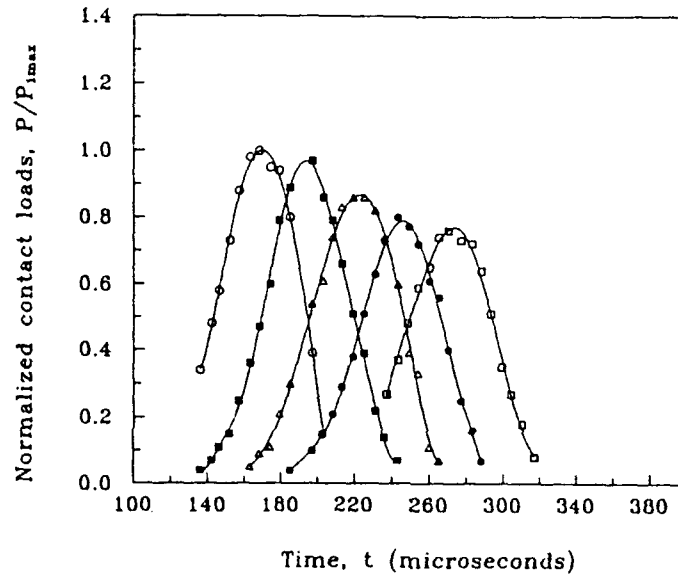
Fig. 14.5 Contact load as a function of time for
a 1 - D disk chain saturated with water
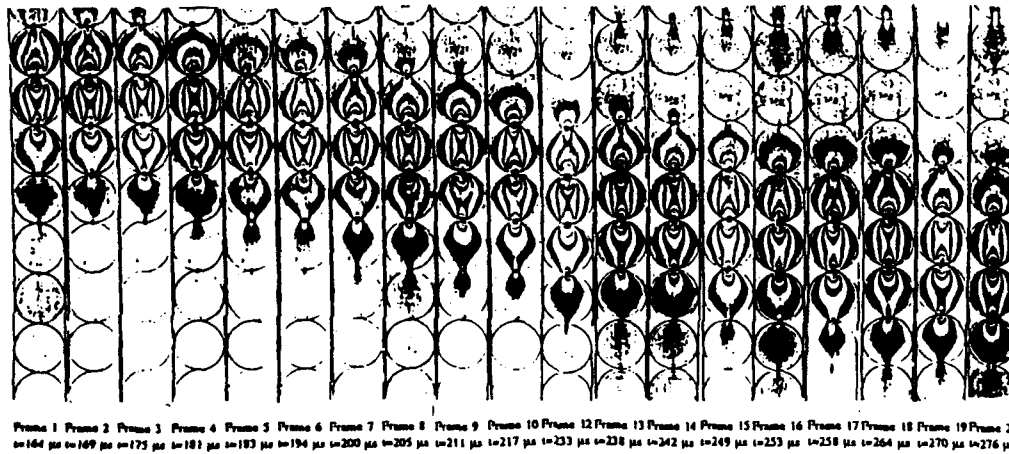
Fig. 14.6 Photoelastic fringe patterns of a single chain model
saturated with Dow Corning 200 fluid (10 centistokes)

221

Frame 1 Frame 2 Frame 3 Frame 4 Frame 5 Frame 6 Frame 7 Frame 8 Frame 9 Frame 10 Frame 11 Frame 13 Frame 14 Frame 15 Frame 16 Frame 17 Frame 18 Frame 19 Frame 20
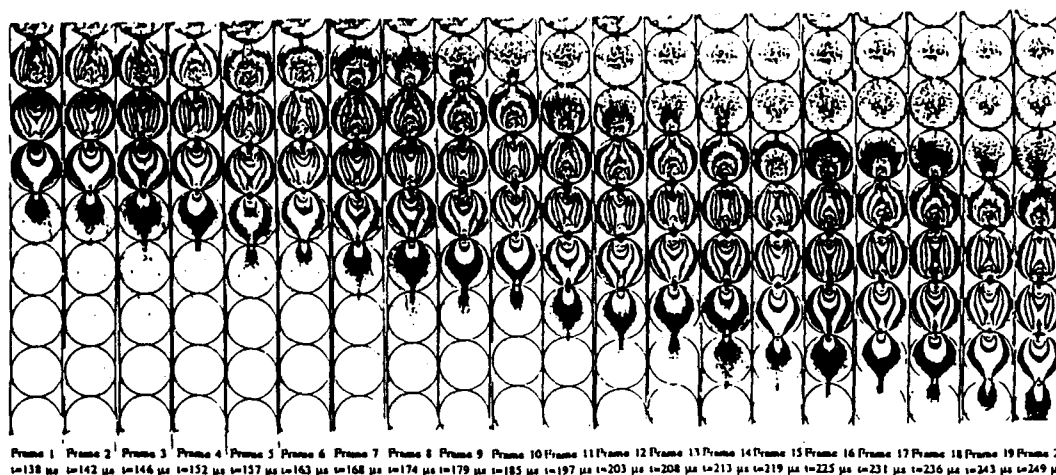t=215 μs t=221 μs t=226 μs t=232 μs t=238 μs t=244 μs t=249 μs t=255 μs t=261 μs t=267 μs t=280 μs t=291 μs t=297 μs t=302 μs t=307 μs t=312 μs t=318 μs t=324 μs t=330 μs
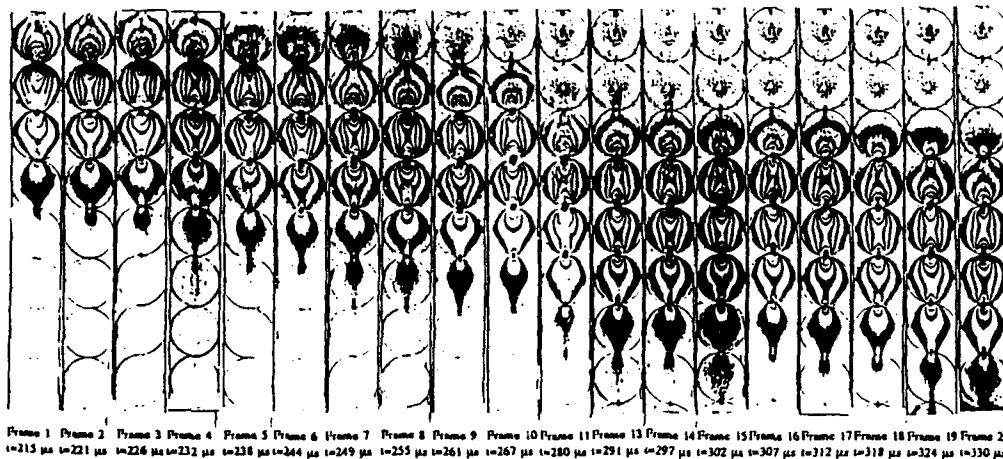
Fig. 14.7   Photoelastic fringe patterns of a single chain model
saturated with Dow Corning 200 fluid (100 centistokes)
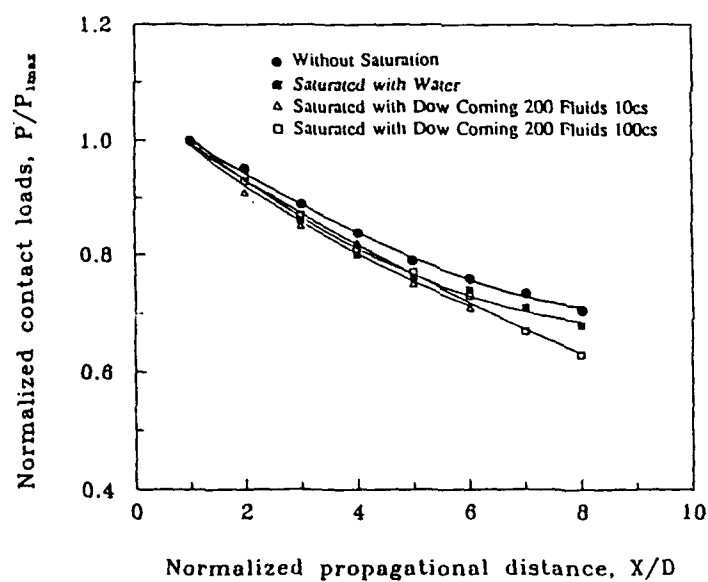
Fig. 14.8   Comparison of wave amplitude attenuation in a 1 - D disk
chain saturated with different fluids

222
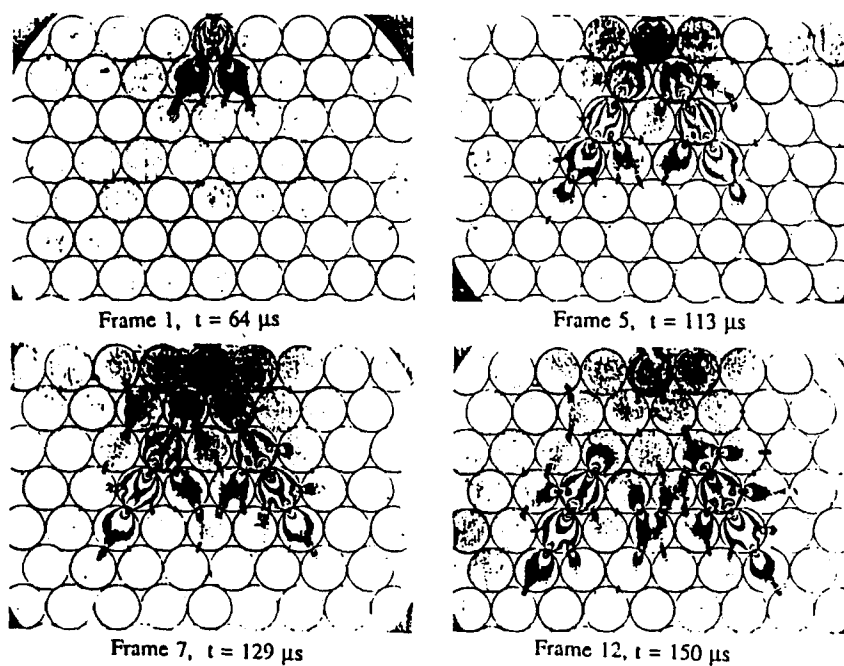
Fig. 14.9 Photoelastic fringe patterns of a HCP model saturated with water
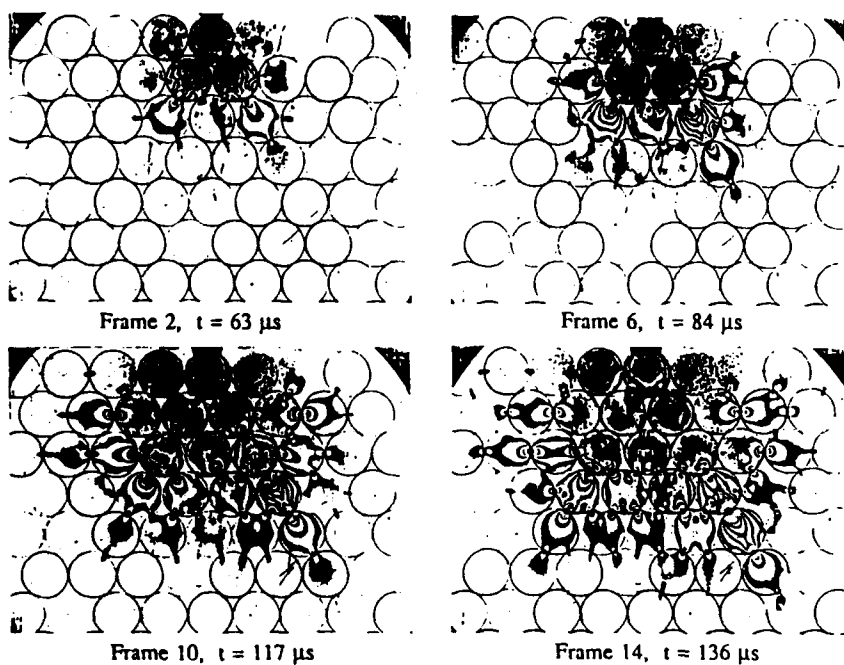
Fig. 14.10 Photoelastic fringe patterns of a HCP model saturated
with Dow Corning 200 fluid (10 centistokes)

Frame 3, t= 68 μs   Frame 6, t = 85 μs

Frame 10, t = 118 μs   Frame 14, t = 135 μs

Fig. 14.11   Photoelastic fringe patterns of a HCP model saturated with Dow Corning 200 fluid (100 centistokes)

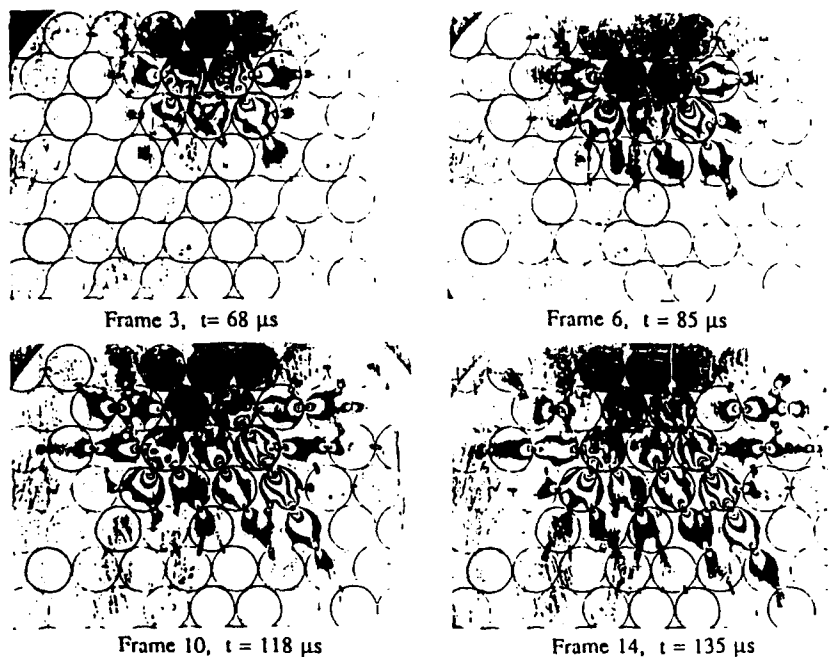FRAME 3, t = 60.6 μs   FRAME 5, t = 72 μs

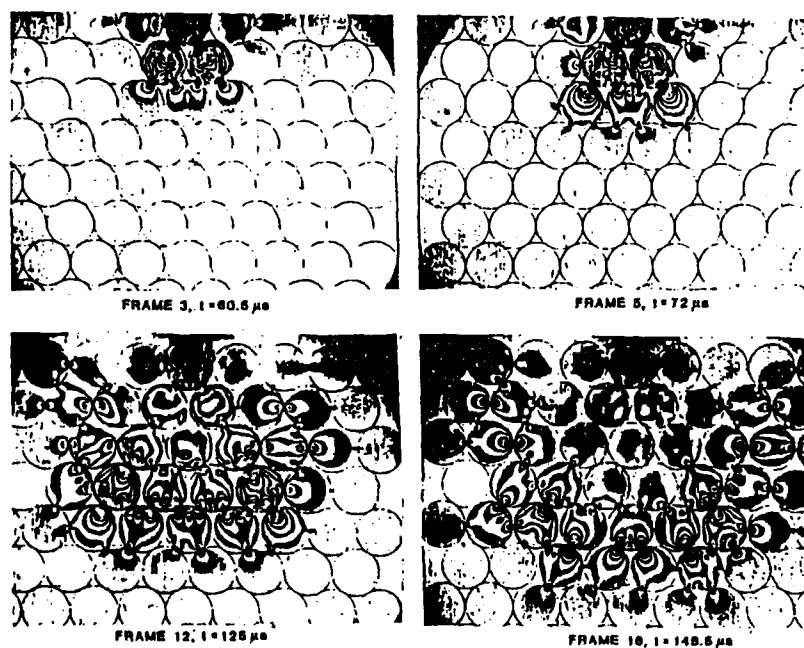FRAME 12, t = 128 μs   FRAME 16, t = 148.5 μs

Fig. 14.12   Photoelastic fringe patterns of a HCP model without saturation

224

CHAPTER 15

CONTINUUM MODELS FOR MATERIALS
WITH LATTICELIKE MICROSTRUCTURE

Within the framework of the finite element method, a general technique is presented to compute the continuum constitutive matrix of an equivalent latticelike microstructural material. The equivalency between the continuum and microstructural stiffness matrices produces an over-determined system which is solved using the Moore-Penrose generalized inverse procedure. Although the resulting solution is *not exact*, it is unique in the least-squares sense. The present study is limited to two-dimensional problems; howevever, the technique can easily be extended to three-dimensions. Several specific examples are given to demonstrate the effectiveness and accuracy of the method.

15.1 INTRODUCTION

The mechanical behavior of materials composed of *granular and/or fiberous microstructures*, is inherently involved with the transmission of loadings along *discrete* paths within the material. This behavior is fundamentally different from that predicted by classical theories of continuum mechanics. It has been observed, see for example Oda, Konishi and Nemat Nasser (1982), that the particular distribution of internal load transfer depends strongly on the material's microstructure. A considerable amount of contemporary research has been conducted in order to understand and explain this complex microstructural behavior. Burt and Dougill (1977) proposed a simple planar pin-jointed truss network to simulate the stress-strain behavior of heterogeneous materials. Based on the fact that granular materials transmit loads only through contact mechanisms, they have been modeled with network theories, e.g. Trollope and Burman (1980), Bagster and Kirk (1985), Bideau et.al. (1986), Thornton and Barnes (1986), and Sadd, Qiu and Boardman (1992). The connection between various lattice gridworks and an equivalent micropolar continuum has been investigated by Banks and Sokolowski (1968), Bazant and Christensen (1972) and Sun and Yang (1975). The relationship between the micromechanics and the overall macro material behavior is a very important and fundamental issue in current materials research. For example, this relationship is needed to understand how localized microstrutural failure will lead to global failure of the entire

225

body, and to predict the effective global properties of a material knowing its microstructure. An example of a microstructural model for a granular material is shown in Figure 15.1. The various contact interactions in the actual material (Figure 15.1a) are modeled using elastic bar elements as shown in the equivalent microstructural system in Figure 15.1b. Other more complex microstructural systems can be constructed to simulate micromechanical behavior.

In addition to this type of research, there has also been considerable interest by the structural mechanics community in the continuum modeling of large repetitive lattice structures. The relationship between a continuum and a gridwork of discrete elements was first examined in some early work (Hrennikoff, 1941, Newmark, 1949) which involved analyzing a continuum by replacing it with an equivalent elastic gridwork. More recently the inverse problem of continuum modelling of repetitive latticelike structures has received considerable attention (Noor et.al., 1978, Kollar and Hegedus, 1985, Renton, 1984, Dow et.al., 1985, Noor and Russell, 1986), and this work has been reviewed by Noor (1988). The ability to replace a large repetitive gridwork with an equivalent continuum provides a means to simplify certain calculations for large space structures. Based on finite element procedures, several methods of computing the properties of an equivalent continuum have been developed. The majority of these methods were developed for beamlike and platelike lattices, where a reduction in dimensionality was an integral part of the equivalency problem.

Current methods of establishing the equivalency between structural and continuum models have been primarily based on stiffness or energy methods (Noor, 1988). These techniques have proposed continuum finite elements with stiffness (constitutive) and strain and/or kinetic energy properties that approximate to some degree of accuracy, the structural system. The present state of research indicates that while satisfactory equivalent continuum models for linear behavior of beamlike and platelike lattices can be developed, methods for general continua still need further refinement and study.

The current article addresses this general problem of developing continuum models for materials with latticelike microstructure. The main objective is to construct a somewhat general technique to compute the constitutive matrix of an equivalent continuum given the microstructural properties. The study is limited to two-dimensional

226

plane problems; however, the technique can easily be extended to three dimensions. After envoking equivalency between the continuum and microstructural stiffness matrices, the resulting over-determined system is solved using the Moore-Penrose generalized inverse procedure. This provides a unique solution in the least-squares sense. Several specific examples are then presented to demonstrate the effectiveness and accuracy of the method.

15.2 FORMULATION OF EQUIVALENT CINTINUUM PROPERTIES

In the method presented here it is assumed that the stiffness matrix of a repeating element of the latticelike microstructure is known. This stiffness matrix may be computed by utilizing the direct stiffness method to assemble each of the discrete element stiffness matrices in the repeating element into a global stiffness matrix. For the type of problems under consideration here the repeating element of the latticelike structure and the element of the equivalent continuum are to have the same degrees of freedom. Therefore, the two elements will exhibit identical behavior if their stiffness matrices are identical. Thus, the stiffness matrix of the element of the equivalent continuum is required to satisfy the equation

$$[K]_t = [K]_c \tag{15.1}$$

where $[K]_t$ and $[K]_c$ are, respectively, the stiffness matrices of the microstructural cell and the equivalent continuum.

Using standard procedures from finite element analysis, the continuum stiffness matrix can be written as

$$[K]_c = \int_\Omega [B]^T [D][B] \, d\Omega, \tag{15.2}$$

where $[B]$ is strain-displacement matrix, $[D]$ is the constitutive matrix containing the material moduli, i.e. $\{\sigma\}=[D]\{\varepsilon\}$, and Ω_e is the element domain. Utilizing Gaussian quadrature to evaluate the integral in equation (15.2), the equivalency equation (15.1) can be rewritten as

$$[K]_t = \sum_{i,j} t_{ij} a_{ij} [B]^T_{ij} [D][B]_{ij} |J_{ij}| \tag{15.3}$$

where t_{ij}, a_{ij}, and $|J_{ij}|$ are, respectively, the thickness, the weighting factor, and the determinant of the Jacobian, all evaluated at the integration point r_i, s_j. The values of the weighting factors and the location of the integration points (which are specified in natural coordinates r and s) are determined by the order of Gaussian quadrature chosen (Bathe, 1982). The values of the strain-displacement matrix and the Jacobian matrix are determined by the continuum finite element selected to model the equivalent continuum. Thus, once the interpolation scheme has been chosen, the value of [D] is the only unknown in equation (15.3). Therefore, equation (15.3) can be used to solve for the constitutive matrix [D] of the equivalent continuum.

At this point it should be noted that equation (15.3) is only valid for a homogeneous equivalent continuum, i.e. the value of [D] is assumed to be the same at each sampling point in the continuum element. It should also be noted that it has been implicitly assumed that a strain energy function exists for the equivalent continuum, which implies that $[D] = [D]^T$. Therefore, it is only necessary to solve for the upper diagonal terms of the constitutive matrix.

Evaluating the right-hand-side of equation (15.3), and rewriting the resulting equation in the standard form utilized for systems of simultaneous equations, we have

$$[A]\{D\} = \{K\} \qquad (15.4)$$

where $\{D\}$ is a vector containing the unknown upper diagonal terms of matrix [D], $\{K\}$ is a vector containing the known terms of the matrix $[K]_t$, and [A] is a known non-square coefficient matrix determined by evaluating the right-hand-side of equation (15.3). Equation (15.4) represents an M^2 by N system of simultaneous equations, where M is the number of degrees of freedom in the equivalent continuum element, and N is the number of unknowns. Since $\{D\}$ contains at most 21 unknowns, it is apparent that equation (15.4) is *severely over-determined*. For example, a plane stress problem which utilizes an equivalent continuum element with eight degrees of freedom would have sixty-four equations and six unknowns. Due to the fact that equation (15.4) is over-determined, standard solution procedures such as Gauss elimination are not applicable, and thus it is not possible to determine an exact solution. Therefore, a residual error vector defined by

$$\{R\} = \{K\}-[A]\{D\}, \tag{15.5}$$

has, in general, entries which are not equal to zero. Since it is not possible to make all of the entries in the residual error vector equal to zero, a solution is sought which minimizes the *size* of this error vector. The approach utilized in this work is to determine a solution which minimizes the sum of the squares of the entries in the residual error vector. It is well known that a solution to such a linear least squares problem yields a residual error vector which is orthogonal to the column space of [A]; see, for example, Stewart (1973). Thus, the residual error vector satisfies the equation

$$[A]^T\{R\} = \{0\}. \tag{15.6}$$

Substituting equation (15.5) into equation (15.6) yields the equation

$$[A]^T[A]\{D\} = [A]^T\{K\} \tag{15.7}$$

where the coefficient matrix ($[A]^T[A]$) is now a square matrix. Since the coefficient matrix in equation (15.7) is a non-singular square matrix, provided [A] has linearly independent columns, the solution for $\{D\}$ can be obtained by simply inverting the coefficient matrix. Thus, the solution for $\{D\}$ can be written as

$$\{D\} = ([A]^T[A])^{-1}[A]^T\{K\} \tag{15.8}$$

where the matrix $([A]^T[A])^{-1}[A]^T$ is known as the *Moore-Penrose generalized inverse* (Stewart, 1973). As mentioned previously, the solution represented by equation (15.8) is not an exact solution. However, provided that [A] has linearly independent columns, it is a unique solution in the least-squares sense.

15.3 EXAMPLES AND DISCUSSION

The method presented in the previous section was utilized, with a bi-linear interpolation scheme and 2 by 2 Gaussian quadrature, to compute equivalent continuum properties for the various repeating cells shown in Figure 15.2. For the sake of

simplicity, two-dimensional examples were chosen to illustrate the effectiveness of the method under consideration; however, it should be noted that this method can also be applied to three-dimensional latticelike structures by simply selecting a different interpolation scheme and a different order of Gaussian quadrature. Equivalent continuum properties for the repeating cells shown in Figures 15.2a and 15.2b were also computed by an alternate method. This alternate method involves relating the force and deformation characteristics of a small segment of the grid to those of a small segment of the equivalent continuum as each is subjected to a homogeneous deformation (Kollar and Hegedus, 1985). The derivation of this alternate method relies heavily on the definition of a homogeneous deformation, i.e. lines which are parallel and straight before deformation remain parallel and straight after deformation. Thus, in analyses where a more general state of deformation must be considered this alternate method may not yield accurate results.

The computed equivalent continuum properties are shown in Table 15.1. The equivalent properties are the upper diagonal terms of the constitutive matrix [D]. It should be noted that the properties of the continuum can easily be expressed in terms of it's elastic constants once the constitutive matrix is known, e.g. the shear modulus is given by $G_{12}=D_{33}$. This alternate representation of the equivalent continuum properties might be desirable for certain anlayses, e.g. computation of the wave speed for dynamics problems.

Table 15.1 also contains a measure of the accuracy of the computed equivalent continuum properties. The error measure was computed by subjecting both the repeating cell and the equivalent continuum element to the nonhomogeneous deformation state shown schematically in Figure 15.3 and then computing the percent difference in the stored strain energy. The displacement vector specified by the selected nonhomogeneous deformation state contains only non-zero terms. Thus, each term in the stiffness matrices will be involved in the strain energy computation. This avoids the possibility of inadvertently accounting for the accurate terms and neglecting the inaccurate terms, or vice versa. It should be noted that the error measure listed in Table 15.1 is not a function of the magnitude of the chosen displacement vector; however, it is a function of the *direction* of the displacement vector. Thus, since the error in stored strain energy is a

function of the *shape* of the chosen deformation state, the same deformation state was utilized for each of the examples examined in this work.

The repeating cells shown in Figure 15.2 are composed of truss elements, i.e. discrete one-dimensional elements which have a single extensional degree of freedom at each node. The stiffness of each truss element is determined by the specified modulus of elasticity, cross-sectional area, and length. Since the length of each element is determined by the configuration of the repeating cell, only two parameters are required to specify the stiffness of each truss element. The truss elements utilized in the repeating cells shown in Figure 15.2 were assigned a modulus of elasticity of 30×10^6 psi. The truss elements utilized in Figures 15.2a and 15.2b were assigned a cross-sectional area equal to either A_1 or A_2, where $A_1 = 0.75$ in^2 and $A_2 = 0.53$ in^2 (See Figure 15.2). Each of the truss elements utilized in the repeating cell of Figure 15.2c was assigned a cross-sectional area equal to 0.75 in^2.

The square lattice with diagonals shown in Figure 15.2a was chosen as an example because it's equivalent continuum properties have been discussed by other researchers (Hrennikoff, 1941, Kollar and Hegedus, 1985). Thus, the accuracy of the method under consideration can be compared to the accuracy of a well known alternate method. By examining the results computed for case 1-1 (see Table 15.1) it is seen that the constitutive matrix computed by the alternative method is that of an isotropic material, i.e. $D_{13} = D_{23} = 0.0$, $D_{11} = D_{22}$, and $D_{11} = D_{12} + 2D_{33}$. This is due to the fact that the alternate method predicts isotropic equivalent continuum properties for the repeating cell shown in Figure 15.2a if the cross-sectional areas A_1 and A_2 are chosen to satisfy the relationship $A_2/A_1 = 1/\sqrt{2}$. The results computed for case 1-1 also show that the alternate method predicts that $D_{12} = D_{33}$; in fact, the alternate method predicts this result for all repeating cells, regardless of the cross-sectional areas chosen. The results computed for case 1-1 also indicate that the equivalent continuum properties computed by the alternate method result in strain energy values which are considerably different than the values computed for the repeating cell. By examining the results computed for case 1-2 it is seen that the present method offers some major advantages over the alternate method. For example, the method under consideration removes the restriction $D_{12} = D_{33}$, and it also results in strain energy values which are considerably more accurate than the values

231

computed with the alternate method. Also, for case 1-2 the present method yields a constitutive matrix for the equivalent continuum which is, like the repeating cell itself, invariant to a 90, 180, or 270 degree rotation, but not invariant to all rotations. That type of orthotropic material behavior seems to be more reasonable than the isotropic behavior predicted by the alternate method.

The example shown in Figure 15.2b was chosen to determine the effect of a change in cell size on the equivalent continuum properties. By examining the results computed for cases 1-3 and 1-4 it is seen that the equivalent continuum properties computed by both the present method and the alternate method are inversely proportional to the size of the repeating cell.

By examining the results computed for case 1-5 (Figure 15.2c), it is seen that the present method yields accurate results regardless of the complexity of the repeating cell. The results computed for case 1-5 may also be interpreted as showing that the repeating cell of Figure 15.2c more closely approximates a continuum than the repeating cells shown in Figures 15.2a and 15.2b.

The examples shown in Figure 15.2 were used to determine how closely the behavior of one element of the equivalent continuum could approximate that of one repeating cell of a latticelike microstructure. The examples of Figure 15.4 were chosen to determine how closely the behavior of a *patch* of elements of the equivalent continuum approximates that of a larger segment of the latticelike structure. The basic repeating cell utilized in each of the examples shown in Figure 15.4 is the same cell which was given in Figure 15.2a; thus, the equivalent continuum properties computed for case 1-2 in Table 15.1 can be utilized in each of the examples shown in Figure 15.4. Table 15.2 shows the percent difference in stored strain energy between the patches of repeating cells and the continuum element models, when each is subjected to the nonhomogeneous deformation state shown in Figure 15.3.

The lattice shown in Figure 15.4a consists of four repeating cells of the type examined in Figure 15.2a. The equivalent continuum model utilized to approximate the behavior of the lattice consists of four continuum elements. As listed for case 2-1 in Table 15.2 the percent difference in stored strain energy computed for the lattice and the patch of continuum elements is 9.0 %. This seems to indicate that the equivalent

continuum model of an entire latticelike structure would be nearly as accurate as the equivalent continuum model of a single repeating cell.

The lattice shown in Figure 15.4b also consists of four repeating cells of the type shown in Figure 15.2a. The equivalent continuum model utilized to approximate the behavior of this lattice consists of one continuum element. As listed for case 2-2 in Table 15.2 the percent difference in stored strain energy for this case is 9.2 %. The results of this example seem to indicate that an entire latticelike structure could be modelled by a relatively small number of continuum elements, with a degree of accuracy that is largely determined by the accuracy of the equivalent continuum properties utilized. Thus, this example illustrates the benefit of the formulation presented in the previous section, as well as the power of equivalent continuum modelling.

15.4 CONCLUSIONS

The results presented in Table 15.1 indicate that the method under consideration yields equivalent continuum properties which are a good approximation to a microstructural repeating cell, e.g. the mean error computed for the repeating cells shown in Figure 15.2 is 3%. The results presented for the repeating cells in Figures 15.2a and 15.2b seem to indicate that for cases which involve nonhomogeneous deformation states the method presented here is significantly more accurate than the previous alternate method examined. The results presented in Table 15.2 seem to indicate that by utilizing the present method to compute the equivalent continuum properties of a repeating cell, an entire latticelike microstructure could be modelled with a reasonable degree of accuracy by using a relatively small number of continuum elements.

TABLE 15.1. Equivalent continuum properties computed for the repeating cells shown in Figure 15.2.

CASE	FIG	METHOD	EQUIVALENT CONTINUUM PROPERTIES(/E)[3]						% ERROR IN STRAIN ENERGY
			D_{11}	D_{12}	D_{13}	D_{22}	D_{23}	D_{33}	
1-1	15.2a	KM[1]	1.125	0.375	0.0	1.125	0.0	0.375	35.4
1-2	15.2a	PM[2]	2.089	0.375	0.0	2.089	0.0	0.482	7.1
1-3	15.2b	KM	0.563	0.188	0.0	0.563	0.0	0.188	35.4
1-4	15.2b	PM	1.045	0.188	0.0	1.045	0.0	0.241	7.1
1-5	15.2c	PM	3.373	1.541	0.0	3.373	0.0	1.385	1.7

[1]Equivalent continuum properties computed by assuming a homogeneous deformation state, see Kollar and Hegedus (1985).

[2]Equivalent continuum properties computed by method described in this work.

[3]Equivalent continuum properties were normalized by dividing them by the modulus of elasticity utilized for the discrete members in the repeating cell.

TABLE 15.2 Computed difference in stored strain energy between a patch of repeating cells and the equivalent continuum models shown in Figure 15.4.

CASE	FIG	EQUIVALENT CONTINUUM PROPERTIES(/E) UTILIZED[1]						% ERROR IN STRAIN ENERGY
		D_{11}	D_{12}	D_{13}	D_{22}	D_{23}	D_{33}	
2-1	15.4a	2.089	0.375	0.0	2.089	0.0	0.482	9.0
2-2	15.4b	2.089	0.375	0.0	2.089	0.0	0.482	9.2

[1]Equivalent continuum properties were normalized by dividing them by the modulus of elasticity utilized for the discrete members in the repeating cell.
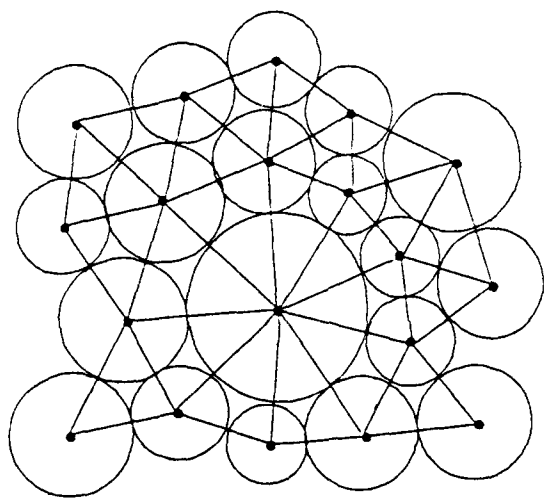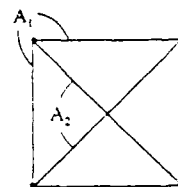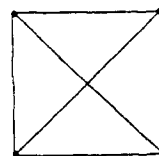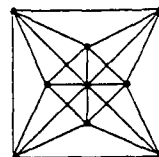
234

Fig. 15.1 Granular media model with a superimposed elastic network

(a) Square 1" x 1" Lattice with Diagonals

(b) Square 2" x 2" Lattice with Diagonals

(c) Square Lattice within a Unit Square Lattice

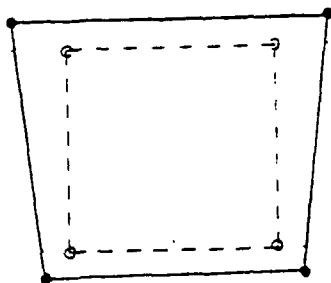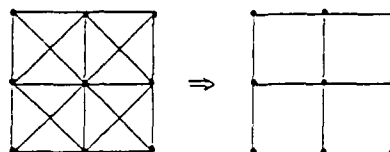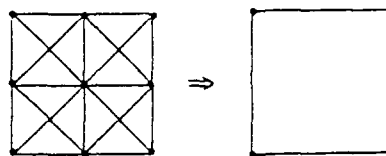Fig. 15.2 Repeating cells examined in the present work

Fig. 15.3 Non-homogeneous deformation state utilized, dotted configuration indicates initial state.

(a) 4 Repeating Cells Modeled by 4 Continuum Elements

(b) 4 Repeating Cells Modeled by 1 Continuum Element

Fig. 15.4 Patches of repeating cells and their equivalent continuum models

CHAPTER 16

WAVE MOTION IN LARGE RANDOM ASSEMBLIES
WITH VARIOUS ANISOTROPY

In order to investigate the effects of granular anisotropy on wave motion in particulate materials, theoretical distinct element studies were conducted on large random assemblies. These particular assemblies were specially generated so as to represent media with various degrees of granular anisotropy. Such anisotropy was measured using the fabric variable of the distribution of the local branch vectors which connect neighboring mass centers of particles in contact. The constructed assemblies were designed so as to produce varying amounts of anisotropy in two orthogonal directions.

16.1 RANDOM MEDIA GENERATION

In order to study large assemblies with varying degrees of fabric anisotropy it was necessary to develop a random particulate media generator computer code. Many different techniques were considered which produced varying degrees of porosity and anisotropy. Three particular schemes are discussed which provided assemblies with desired fabric.

16.1.1 Strongly Anisotropic Particulate Media Generator

This generator produced assemblies with very high degrees of anisotropy with respect to two orthogonal directions. The algorithms employed to generate the assemblies can be described in the following steps.

1. An initial base layer of disks is placed along a horizontal line, with a spacing distance between neighboring disk centers being varied randomly between one and two disk diameters (see Fig. 16.1a).

2. Each pair of neighboring disks in the base layer is then used to generate a new disk making contacting with a base layer pair, see Fig. 16.1b. The position of the new disk is unique, and in this way a new layer of disks is formed.

3. To generate the next layer, a new disk is randomly generated to make contact with the disks in the previous layer. This generation is made by constraining the angle of the branch vectors of each newly constructed contact pair to lie in a particular range ($\pm 15°$ for the cases shown) with respect to the vertical direction,

236

see Fig. 16.1c. Thus this next layer is randomly generated.

4. The next layer of disks is generated in the same fashion as step 2 above, see Fig. 16.1d.

5. The positions of left and right boundary disks of the new layer from step 4 are determined in a special way. Left boundary disks are generated with a randomly generated branch angle in the range (115° - 135°) measured counter-clockwise from the horizontal. Similarly the right boundary disk is generated in the same fashion with a random branch vector angle in the range (45° - 75°).

During any step if a disk generated overlaps with other disks, then a new trial disk will be generated to replace it. Following these steps, large random assemblies of particulate media with pronounced anisotropy can be quickly generated. An example assembly generated by this scheme is shown in Fig.16.2, and Fig.16.3 illustrates the local branch vector distribution as a function of the angular direction.

16.1.2 Moderately Anisotropic Random Media Generator

A second particulate media generator was constructed to produce assemblies with moderately anisotropy. The following construction steps are used to generate these particular granular systems.

1. An initial base layer of contacting disks is formed such that the angle between any pairs of branch vectors of disks in contact is randomly selected in the range ±20° measured from the horizontal, see Fig. 16.4a.

2. To generate the next layer, the left disk of the new layer is randomly set (branch vector ±20° from the vertical) in contact with the left disk of the previous layer. The other disks of the new layer are randomly generated from two groups. One group includes disks that are in contact with their left neighbor as well as with the disk in the previous layer. The second selection group includes disks which are permitted to form contact only with its left neighbor. Thus by randomly selecting disks from these two groups a new layer may be constructed, see Fig. 16.4b. This procedure is then repeated for as many additional layers as desired.

As before, if during any step a disk generated overlaps other disks, then a new disk will be generated to replace it. Fig. 16.5 shows a generated assembly using this

237

moderately anisotropic scheme, and the distribution of local branch vectors for this assembly is displayed in Fig. 16.6.

16.1.3 Weakly Anisotropic Random Media Generator

A final generator was developed to construct assemblies with small anisotropy. The scheme utilized the following procedures.

1. An initial disk forms the starting central point of the assembly. From this first disk a branch angle is randomly generated to determine the position of a new contacting disk, see Fig 16.7a. Similar steps are used to randomly generate the second, third, fourth, and fifth disks which are in contact with the initial generating disk (Fig. 16.7a).

2. From the existing assembly, randomly select a pair of disks. If a new disk can be generated to contact with the two disks and not overlap any other existing disks, this new disk will be added into the existing assembly (see Fig.16.7b). This process is repeated over all possible disk pairs of the existing assembly.

Again as before disk overlaps are not allowed, and random retries are initiated if an overlap is found. Fig. 16.8 illustrates a weakly anisotropic random assembly produced using this algorithm. The local branch vector fabric distribution for this assembly is shown in Fig. 16.9.

16.2 RESULTS AND DISCUSSION

The distinct element method was used to simulate the dynamic response of assemblies generated by the previously described methods, and in this way the effect of granular anisotropy on the wave motion characteristics could be determined. The contact laws used in the modeling were the nonlinear hysteretic normal and tangential laws used in our previous work. The simulations involved the comparison of the propagation of plane waves moving along orthogonal directions in the generated assemblies. The transient nature of loadings was modeled using a triangular time dependent input loading pulse with a peak value of 1000 N and a period of 60 μs. In order to represent a plane-wave input loading, the time-dependent pulses were simultaneously applied on particles along one of the horizontal or vertical boundaries of the assemblies. An imaginary horizontal or vertical line was drawn near the boundary opposite to where the input loadings were applied. If a branch vector of a pair particles in contact is intercepted by

238

this imaginary line, the normal contact load between the particles was recorded. In this fashion, the contribution of the individual particle contacts could be determined, and these recorded loads were then summed and normalized with respect to the sum of the peak values of the input loadings.

Fig. 16.10 shows this wave propagation simulation for the highly anisotropic media. The normalized normal contact load profiles are shown for the case of horizontal and vertical input loadings. It is obvious that for the wave propagating along vertical direction, the attenuation is much smaller than that of a wave travelling along the horizontal direction. Also note that the wave speed as determine by the arrival time of the averaged profile is different for the two propagational directions, with the vertical wave having a significantly higher speed. These results follow qualitatively from the local branch distribution diagram in Fig. 16.3. Since most branch vectors lie along the vertical direction, the load transfer paths in that direction are rather continuous and straight, while just the opposite would be true for load transfer paths along the horizontal direction. Therefore the anisotropic media is a better propagator of waves in the vertical direction.

The normalized normal contact load profiles for a moderately anisotropic random assembly is shown in Fig. 16.11. For this assembly more local branch vectors occur along the horizontal direction, and therefore the distinct element simulations indicate that the horizontal wave attenuation is smaller than that along vertical direction. However, for this case the wave velocities along both directions were found to be almost the same. By checking the load transfer paths along vertical direction, it was found that there was one continuous path along the left vertical boundary, and which contributed most of the energy in the normalized contact load profile. Waves travelling along this special path take about the same time as along a continuous horizontal path. It was determined that if this path was blocked, it would take more time for load to transfer from the bottom to the top of the assembly and the wave speed of the averaged signal would be reduced.

The final simulation was conducted on the weakly anisotropic assembly shown in Fig. 16.8. The normalized normal contact load versus time is shown in Fig. 16.12 for this case. It can now be observed that the differences between the peak transmitted wave profiles and the wave speeds are quite small. This agrees with the local branch vector

distribution diagram which indicates that the assembly is nearly isotropic.

These results indicate that granular anisotropy can have a significant effect on the propagation of waves through such materials. Additional studies of large random assemblies are being undertaken, and a theoretical fabric framework is being developed.
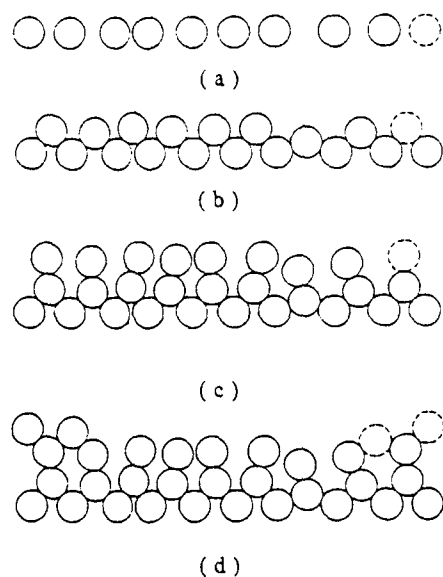
Fig. 16.1 Procedures used to generate strongly
anisotropic random assemblies

Fig. 16.2 A strongly anisotropic random assembly
generated with the steps shown in
Fig. 16.1

Fig. 16.3 The branch vector distribution diagram
of the assembly shown in Fig. 16.2

(a)

(b)

Fig. 16.4 Procedures used to generate moderately
anisotropic random assemblies
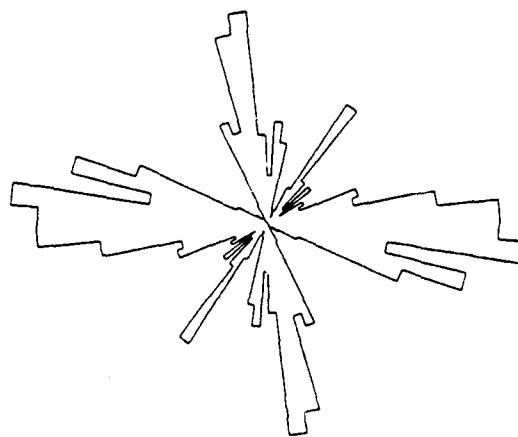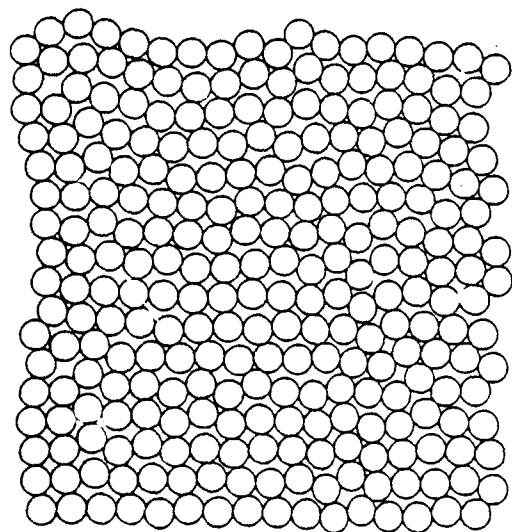
Fig. 16.5 A moderately anisotropic random assembly
generated with the steps shown in
Fig. 16.4

Fig. 16.6 The branch vector distribution diagram
of the assembly shown in Fig. 16.5

(a)

(b)
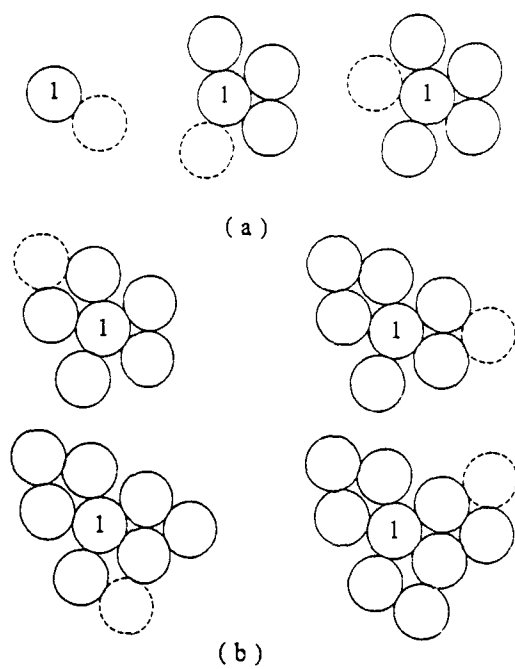
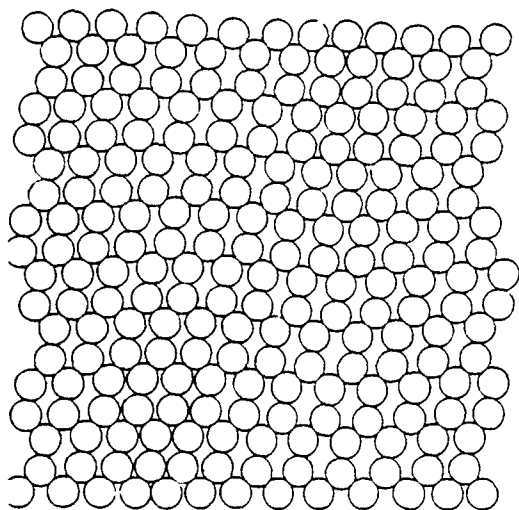Fig. 16.7 Procedures used to generate weakly
anisotropic random assemblies
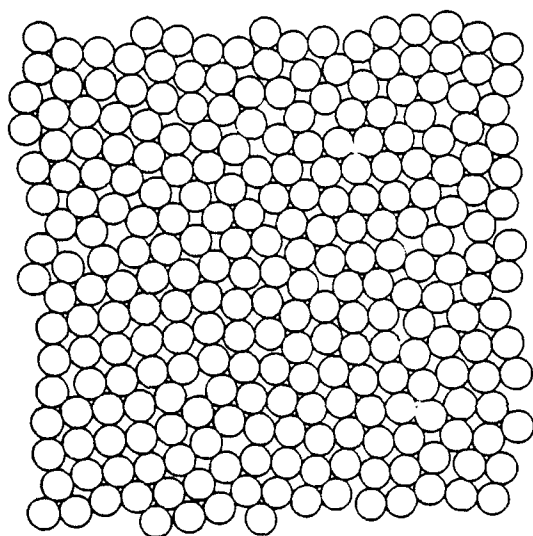
Fig. 16.8 A weakly anisotropic random assembly
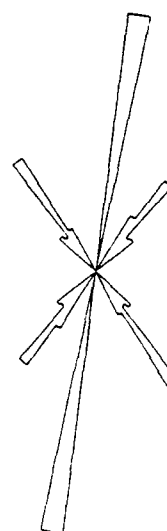generated with the steps shown in
Fig. 16.7

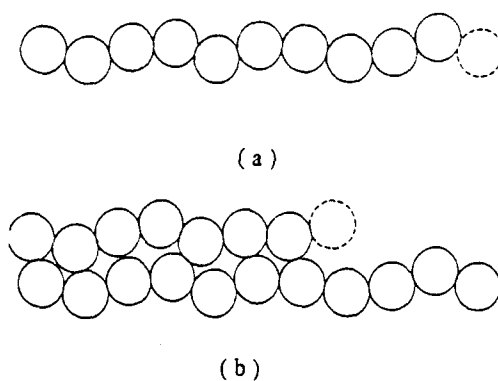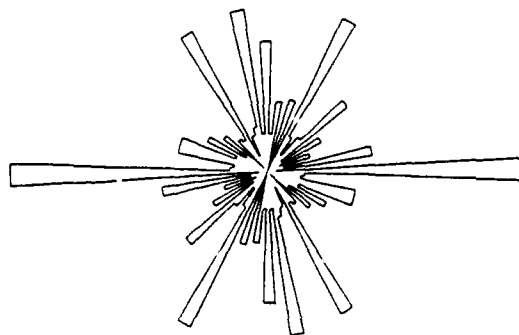Fig. 16.9 The branch vector distribution diagram
of the assembly shown in Fig. 16.8
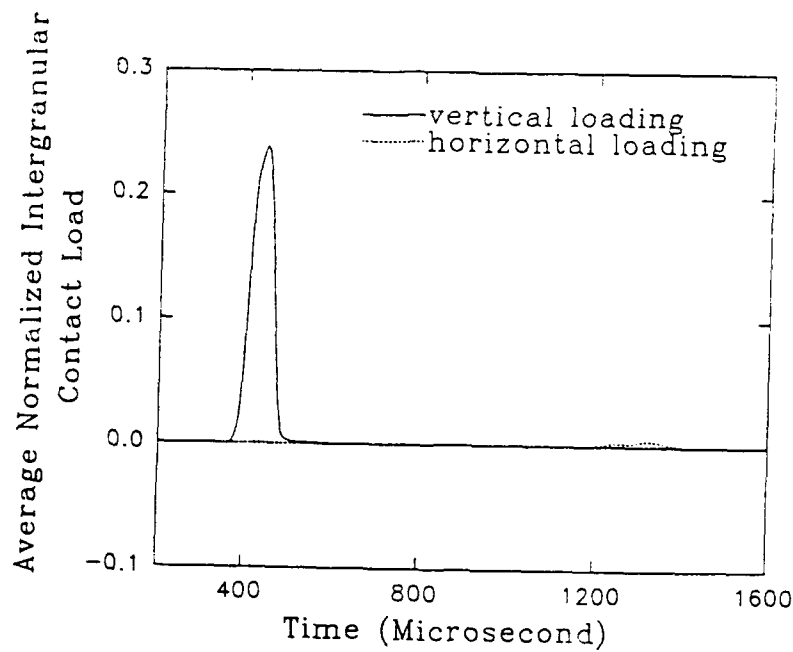
Fig. 16.10 Distinct element predictions of the average normalized normal contact loads versus time for the assembly shown in Fig. 16.2
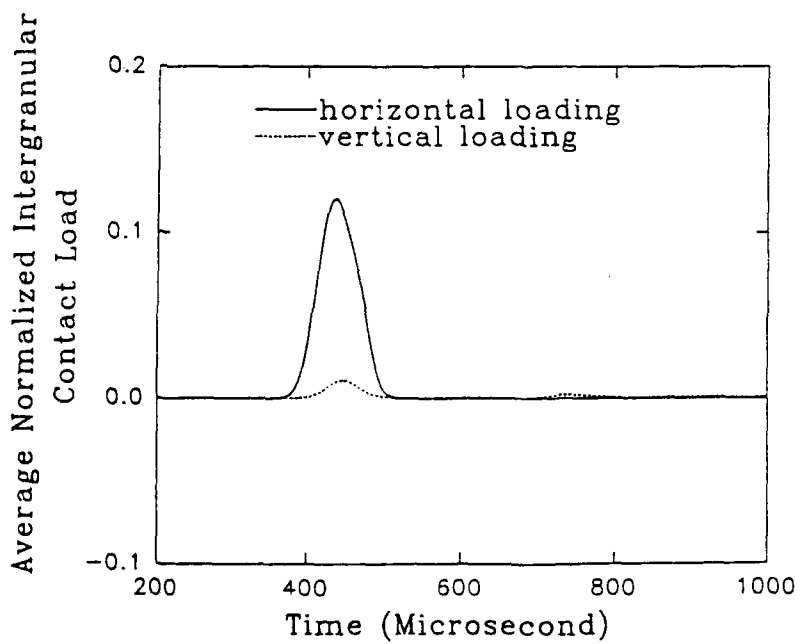
Fig. 16.11 Distinct element predictions of the average normalized normal contact loads versus time for the assembly shown in Fig. 16.5
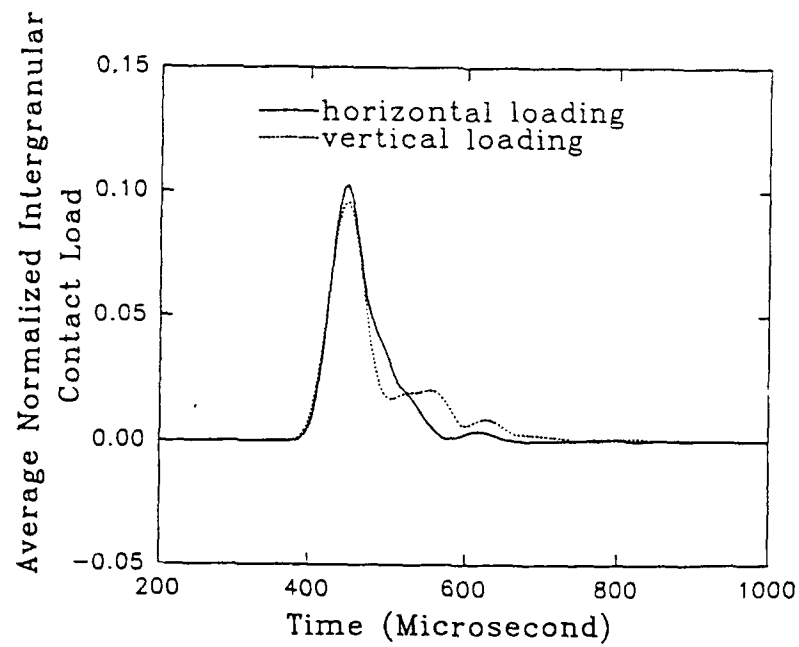
Fig. 16.12 Distinct element predictions of the average normalized normal contact loads versus time for the assembly shown in Fig. 16.9

BIBLIOGRAPHY

Abbott, P.A. and Wang, E.H. (1970) "Dynamic one-dimensional continuum model for transversely cracked rock," Air Force Report AFWL-TR-70-3.

Adley, M. D. and Sadd, M. H. (1992) "Continuum models for materials with latticelike microstructure", *Computers and Structures*, vol.43

Bagster, D.F. and Kirk, R., (1985) "Computer Generation of a Model to Simulate Granular Material Behavior", *Journal of Powder & Bulk Solids Tech.*, vol.9, pp.19-24.

Banks, C.B. and Sokolowski, M., (1968) "On Certain Two-Dimensional Applications of the Couple Stress Theory", *International Journal of Solids Structures*, vol.4, pp.15-29.

Bathe, K.J., (1982) Finite Element Procedures in Engineering Analysis, Prentice-Hall.

Bathurst, R.J. and Rothenburg, L. (1989) "Micromechanical aspects of isotropic granular assemblies with linear contact interaction," *J. Appl. Mech.*, vol.55, pp.17-23.

Bazant, Z. P. and Christensen, M. (1972) "Analogy Between Micropolar Continuum and Grid Frameworks Under Initial Stress', *Int. J. Solids Struct.*, vol.8, pp.327-346

Bazant, Z.P., Krizek, R.J. and Shieh, C.L. (1983) "Hysteretic endochronic theory for sand," *J. Eng. Mech*, vol.109, pp.1073-1095.

Bagster, D.F. and Kirk, R., (1985) "Computer Generation of a Model to Simulate Granular Material Behavior", *Journal of Powder & Bulk Solids Tech.*, vol.9, pp.19-24.

Banks, C.B. and Sokolowski, M., (1968) "On Certain Two-Dimensional Applications of the Couple Stress Theory", *International Journal of Solids Structures*, vol.4, pp.15-29.

Bathe, K.J., (1982) Finite Element Procedures in Engineering Analysis, Prentice-Hall.

Bazant, Z.P. and Christensen, M., (1972) "Analogy Between Micropolar Continuum and Grid Frameworks Under Initial Stress", *International Journal of Solids Structures*, Vol. 8, pp 327-346.

Bazant, Z.P., Belytschko, T.B., and Chang, T.P. (1984) "Continuum Theory for strain-softening," *J. Eng. Mech.*, Vol.110, pp. 1666-1692,

Bideau, D., Gervois, A., Oger, L., and Troadic, J.P., (1986) "Geometrical Properties of Disordered Packings of Hard Disks," *J. Physique* , Vol.47, 1697-1707

Biot, M. A. (1940) "The influence of initial stress on elastic waves", *J. Appli. Phys.*, vol.11, pp.522-530

Biot, M.A., (1941), "General Theory of Three Dimensional Consolidation," *Journal of Applied Physics*, No. 12, pp. 155-164.

Biot, M.A., (1962a), "Mechanics of Deformation and Acoustic Propagation in Porous Media," *Journal of Appllied Physics* No. 33, pp. 1482-1498.

Biot, M.A., (1962b), "Generalized Theory of Acoustic Propagation in Porous Dissipation Media," *Journal of Acoustic Society of America*, No. 34, pp 1254-1264.

Birch, F. (1938) "The effect of pressure upon the elastic parameters of isotropic solid according to

Murnaghan's theory of finite strain",*J. Appli. Phys.*, vol.9,

Bleich, H.H., Matthews, A.T. and Wright, J.P. (1968) "Moving Step Load on the Surface of a Half-Space of Granular Materials," *Int. J. Solids Structures*, Vol.4, pp.243-268.

Boardman, W. (1990) "Wave Propagation in Granular Media Simulated by Elastic Networks," M.S. Thesis, University of Rhode Island

Boresi, Sidebottom, Seely and Smith (1978) Advanced Mechanics of Materials, John and Sons.

Brandt, H. (1955) "A study of the speed in sound of porous granular media," *J. Appl. Mech.*, Vol.22.

Brebbia, C.A., (1985) Topics in Boundary Element Research, Springer-Verlag Berlin, Heidelberg.

Brown, J.W., Murnell, D.W. and Stout, J.H. (1980) "Propagation of Explosive Shock Waves Through Rubble Screens," Misc. Paper SL-80-7, U.S. Army Engineer Waterways Experiment Station, Vickburg, MS.

Burt, N.J. and Dougill, J.W., (1977) " Progressive Failure in a Model Heterogeneous Medium," *J. Eng. Mech. Division*, Proc. ASCE, Vol. 103, pp.365-376

Carroll, M. M. and Holt, A. C. (1972a) "Static and dynamic pore-collapse relation for ductile porous materials," *J. Appl. Phys.*, Vol.43, pp.1626-1636.

Carroll, M.M., and Holt, A.C. (1972b) "Suggested Modification of the P-Model for Porous Materials," *J. Appl. Physics*, Vol.43, pp759-761

Chambre, P. L. (1984) "Speed of plane wave in gross mixture," J. *Acoustic Soc. Amer.*, Vol.26.

Chang, C. S. and Ma, L. (1990) "Modeling of discrete granulates as micropolar continua", *J. of Engineering Mechanics*, vol.116, pp.2703-2721

Chen, Y. C., Ishbashi, I. and Jenkins, J. T. (1988) "Dynamic shear modulus and fabric: part I, depositional and induced anisotropy," *Geotechnique*, Vol.38, No. 1, pp.25-32.

Christoffersen, J., Mehrabadi, M. M. and Nemat-Nasser, S. (1981) "A micromechanical description of granular material behavior," *J. Appl. Mech.*, Vol.48.

Coker, E.G. and Ahmed, M.S., (1921) "Contact Pressures and Stresses," The Institution of Mechanical Engineers, London, England, Vol. 1, pp.365.

Cole, D.M., Koslof, D.D. and Minster, J.B. (1978) "A Numerical Boundary Integral Equation Method for Elastodynamics I.," *Bul. Seismo. Soc. Am.* Vol. 68, pp 1331-1357.

Cowin, S.C. and Satake, M., (1978) Continuum Mechanical and Statistical Approaches in the Mechanics of Granular Materials, Proc. U.S. / Japan Seminar, Gakujutsu Bunken Fukyu-Kai, Tokyo

Cruse, J.A. and Rizzo, F. (1968a) "A Direct Formulation and Numerical Solution of The General Transient Elastodynamic Problems I.," *J. Math. Anal. Appl.* Vol. 22, pp 244-295.

Cruse, J.A., (1968b) "A Direct Formulation and Numerical Solution of The General Transient Elastodynamic Problems II.," *J. Math. Anal. Appl.* Vol. 22, pp 341-355.

Cundall, P. A., Marti, J., Beresford, P., Last, N. and Asgian, M. (1978) "Computer modelling of jointed rock masses," Technical Report N-78-4, U.S. Army Engineering Waterways Experiment Station, Vicksburg, M.S..

247

Cundall, P. A. and Strack, O. D. L. (1979) "A discrete numerical model for granular assemblies," *Geotechnique*, Vol.29, No.1, pp.47-65.

Cundall, P. A. and Strack, O. D. L. (1983) "Modeling of microscopic mechanics in granular material," in Mechanics of Granular Materials: New Methods and Constitutive Relations, J. T. Jenkins and M. Satake, eds., Elsevier Sci. Pub..

Deresiewicz, H. (1958) "Mechanics of granular matter, *Advance in Applied Mechanics*," Vol. V, Academic Press.

Digby, P. J. (1981) "The effective elastic moduli of porous granular rocks", *J. of Applied Mechanics*, vol.48, pp.803-808

Dow, J.O., Su, Z.W., Feng, C.C. and Bodley, C., (1985) "Equivalent Continuum Representation of Structures Composed of Repeated Elements", *AIAA Journal*, Vol. 23, No. 10, pp 1564-1569.

Drescher, A. and De Josselin De Jong, G. (1972) "Photoelasticity Verification of a Mechanical Model for the Flow of a Granular Materials," *Proc. IUTAM-Symposium on Optical Methods in Solid Mechanics*, Poitiers, France.

Drescher, A., (1979) " Application of Photoelasticity to Investigation of Constitutive Laws for Granular Materials," *Proc. IUTAM-Symposium on Optical Methods in Solid Mechanics*, Poitiers, France

Duffy, J. and Mindlin, R. D. (1957) "Stress-strain relations and vibration of a granular medium," *J. Appl. Mech.*

Durbin, F., (1974) "Numerical Inversion of Laplace Transforms : An Efficient Improvement to Dubner and Abate's Method," *Computer J.*, Vol. 17, pp 371-376.

Durelli, A.J. and Wu, D., (1983) "Use of Coefficients of Influence to Solve Some Inverse Problems in Plane Elasticity," *J. of Appl. Mech.*, Vol.50 pp.288-296

Endley, S. N. and Peyrot, H. (1977) "Load distribution in granular media," *J. of the Eng. Mech. Div., ASME.*

Finn, W. D. I., Bransby, P. l. and Pickering, D. J. (1970) "Effects of strain history on liquefaction of sands," *Proc. ASME*, Vol.96, SM6, pp.1917-1934.

Fletcher, E. H. (1971) "Random walk model of ideal granular mass," *J. of the Soil Mechanics and Foundation Division, ASME* Vol.98.

Fu, L.S. (1984) "A New Micro-mechanical Theory for Randomly Inhomogeneous Media," AMD-Vol.62, Wave Propagation in Homogeneous Media and Ultrasonic Non-Destructive Evaluation, ed. by Joh son, G. C., ASME.

Gassman, F. (1951) "Elastic waves through a packing of spheres," *Geophysics*, Vol.16.

Goodman, M. A. and Cowin, S. C. (1972) "A continuum theory for granular materials," *Arch. Rat. Mech. Anal.*, Vol. 44.

Hendron, A.J., (1963) "The Behavior of Sand in One Dimensional Compression," Ph.D., Thesis, University of Illinois

Hertz, H. (1985) "Gesammelte Werke," Leipzig,Germany, Vol. 1, 1985; English translation in miscellaneous papers, 1986

248

Hill, J. M. and Harr, M. E. (1982) "Elastic and particulate media," *J. of the Eng. Mech. Division, ASME,* Vol. 108.

Hrennikoff, A., (1941) "A Solution of Problems of Elasticity by the Framework Method", *Journal of Applied Mechanics,* pp A169-A175.

Hendron, A.J., (1963) "The Behavior of Sand in One Dimensional Compression," Ph.D., Thesis, University of Illinois

Hopkins, M. (1985) "Collisional stresses in a rapidly deforming granular flow," Master's Thesis, Clarkson University, Postdam, NY.

Hudson, J. A. (1968) "The scattering of elastic waves by granular media," *J. Appl. Mech. and Appl. Math,* Vol.21, pp.487-508.

Hughes, D. S. and Cross, J. H. (1951) "Elastic wave velocities in rocks at high pressures and temperatures," *Geophysics,* Vol.14, No.4.

Hughes, D.S. and Kelly, J.L., (1952) "Variation of Elastic Wave Velocity with Saturation in Sandstone," *Geophysics,* Vol.17, pp. 739-752

Huttington, H. B. (1950) *J. Acoust. Soc. Am.* Vol.22, pp.362.

Iida, K. (1939) "The velocity of elastic waves in sand," Bulletin Earthquake Research Institute, Japan, Vol.17.

Ishihara, K. (1978) "Stress history effects on the behavior of sand," *Proc. U.S.-Japan Seminar on Continuum Mechanical and Statistical Approaches in the Mechanics of Granular Materials,* Tokyo, pp.71-90.

Ishihara, K. and Okada, S. (1978) "Yielding of overconsolidated sand", Proc. U.S.-Japan Seminar on Continuum Mechanical and Statistical Approaches in the Mechanics of Granular Materials, Tokyo, 71-90

Jackson, J.G., Ehrgott, J.Q., and Rohani, B. (1980) "Loading Rate Effects on Compressibility of Sand," *J. Geotechnical Eng. Division, ASCE,* Vol.106, pp.839-852

Jenkins, J.T., (1975) "Static Equilibrium of Granular Materials," *J. Appl. Mech.,* Vol.42, pp.603-606

Johnson, K.L., (1985) Contact Mechanics, Cambridge, University Press

Karamanlidis, D. and Stout, R.B. (1989) Wave Propagation In Granular Media, Proc. of the Winter Annual Meeting of the ASME, San Francisco, CA

Kishino, Y. (1988) "Disc model analysis of granular media", in *Micromechanics of Granular Materials.* Ed. by M. Satake and J.T. Jenkins, Elsevier Science Publishers B.V., Amsterdam

Knopoff, L. and Hudson, J. A. (1964) *J. Acoust. Soc. Am.* Vol.36, pp.338.

Kollar, L and Hegedus, I., (1985) Analysis and Design of Space Frames by the Continuum Method, Elsevier Science Publ.

Konishi, J. (1978) "Microscopic model studies on the mechanical behavior of granular materials," *Proc. U.S.-Japan Seminar on Continuum Mechanical and Statistical Approaches in Mechanics of Granular Materials.*

Kuo, C. L. (1983) "Modeling of dynamic deformation mechanisms for granular material," Ph. D. Dissertation, Univ. of Massachusetts.

Krizek, R.J. (1971) "Rheologic behavior of cohesionless soils subjected to dynamic loads," *Transactions of the Society of Rheology*, Vol.15, pp.491-540.

Lee, K. L. and Albaisa, A. (1974) "Earthquake induced settlements in saturated sands," *Proc. ASME*, Vol. 100, GT4, pp. 387-406.

Lin, H.C. and Wu, H.C. (1976) "Strain Rate Effect in the Endochronic Theory of Viscoplasticity," *J. Appl. Mech.*, Vol.43, pp.92-96.

Love, A. E. H. (1927) "The mathematical theory of elasticity", Cambridge Univ. Press, 4th edition, 176-178

Lundberg, G., (1939) "Elastische Beruehrung Zweier Halbraeume," Forschung auf dem Gebiete des ingenieurwesens, Ausgabe A, Vol. 10, September-October, 1939, pp. 201-211

Macelwane, J. B. and Sohon, F. W., (1936) "Introduction to theoretical siesmology, Part I, Dynamics",John Wiley & Sons, New York

Mal, A.K. and Bose, S.K. (1974) "Dynamic Elastic Moduli of a Suspension of Imperfectly Bonded Spheres," *Proc. Camb. Phil. Soc.*, Vol.76, pp.587-600.

Manolis, G.D., (1983) "A Comparative Study on Three Boundary Element Method Approaches to Problems in Elastodynamics," *International Journal for Numerical Methods in Engineering*, Vol. 19, pp 73-91.

Manolis, G.D. and Beskos, D.E., (1988) Boundary Element Methods in Elastodynamis, UNWIN HYMAN.

Martin, Ostsja-Starzewski (1984) "Stress wave propagation in discrete random solids," Wave Phenomenon: Modern Theory and Application, Elsevier Science Publisher, pp.267-278.

Mason, W. P. and Mcskimin, H. J. (1947) *J. Acoust. Soc. Am.* Vol.19, pp.467.

Mei, H. (1989) "A Study of Wave Motion in Granular Materials", M.S. Thesis, University of Rhode Island.

Mindlin, R.D., (1949) "Compliance of Elastic Bodies in Contact," *Journal of Applied Mechanics, Trans ASME*, 1949, 71, pp. 259-268.

Mehrabadi, M.M., Nemat-Nasser, S., and Oda, M., (1982) "On Statistical Description of Stress and Fabric in Granular Materials," *Int. J. Num. Analyt. Methods in Geomech.*, Vol.6 pp.95-108

Mehrabadi, M.M. and Nemat-Nasser, S., (1983) "Stress, Dilatancy, and Fabric in Granular Materials," *Mechanics of Materials*, Vol.2, pp.155-161

Morland, L.W. (1976) "Elastic Anisotropy of Regular Jointed Materials," *Rock Mechanics*, Vol.8, pp.35-48.

Morton, W.B. and Close, L.Z., (1922) "Notes on Hertz's Theory of the Contact of Elastic Bodies", *Phil. Mag., Ser. 6*, 1922, 43, 320.

Mroz, Z. (1980) "Deformation and flow of granular materials," IUTAM conference Proc.

Murnaghan, F.D. (1937) "Finite deformation of an elastic solid," *Am. J. Math.*.

Nachlinger, R.R. and Nunziato, J.W. (1976) "Wave propagation and uniqueness theorems for elastic

materials with internal state variables," *Int. J. Engng. Sci.*, Vol.14, pp.31-38.

Nemat-Nasser, S., (1982) "Fabric and Its Influence on Mechanical Behavior of Granular Materials," in Deformation and Failure of Granular Materials, ed., Vermeer, P.A. and Luger, H.J., A.A. Balkema, pp.77-94

Nemat-Nasser, S. and Mehrabadi, M.M., (1983) "Stress and Fabric in Granular Masses," *Mechanics of Granular Materials: New Models and Constitutive Relation*, pp.1-8

Nemat-Nasser, S. and Mehrabadi, M.M., (1984) "Micro-mechanically Based Rate Constitutive Description for Granular Materials," *Mechanics and Engineering Materials*, ed. by C. S. Resaiand and R. H. Gallagher, John Wiley, New York

Newmark, N.M., (1949) "Numerical Methods of Analysis in Bars, Plates and Elastic Bodies", in Numerical Methods of Analysis in Engineering, L.E. Grinter, Ed., Macmillan, New York.

Noor, A.K., Anderson, M.S. and Greene, W.H., (1978) "Continuum Models for Beam- and Platelike Lattice Structures", *AIAA Journal*, Vol. 16, No. 12, pp 1219-1228.

Noor, A.K. and Russell, W.C., (1986) "Anisotropic Continuum Models for Beamlike Lattice Trusses", *Computer Methods in Applied Mechanics & Engineering*, Vol. 57, No. 3, pp 257-277.

Noor, A.K., (1988) "Continuum Modeling for Repetitive Lattice Structures", *Appllied Mechanics Review*, Vol. 41, No. 7, pp 285-296.

Nunziato, J. and Walsh, E. (1977) "On the influence of void compaction and material non-uniformity on the propagation of one-dimensional acceleration waves in granular materials," *Arch. Rat. Mech. Anal.*, Vol. 64, pp.299-316.

Nunziato, J., Kennedy, J. E. and Walsh, E. (1978a) "The behavior of one dimensional acceleration waves in an inhomogeneous granular solid," *Int. J. Engrg. Science*. Vol.16, pp.291-300.

Nunziato, J., (1978b) "The Propagation of Plane Wave in granular Media," *Powder Tech., Proc. U.S.-Japan Seminar on Continuum Mechanical and Statistical Approaches in the Mechanics of Granular Materials*, Tokyo, pp.291-300

Nunziato, J. and Cowin, S., (1979) "A Nonlinear Theory of Elastic Materials with Voids," *Arch. Rat. Mech. Anal.*, Vol.72, pp.175-201

Oda, M., (1978) "Significance of Fabric in Granular Mechanics," in *Proc. U.S.-Japan Seminar on Continuum Mechanical and Statistical Approaches in the Mechanics of Granular Materials*, ed.Cowin, S.C. and Satake, M., Gaknjutsu Bunken Fukyukai, pp.7-26

Oda, M. Konish, J. and Nemat-Nasser, S. (1980) "Some Experimentally Based Fundamental Results on the Mechanical Behavior of Granular Materials," *Geotechnique*, Vol. 30, pp.479-495.

Oda, M., Nemat-Nasser, S., and Mehrabadi, M.M., (1982) " A statistical Study of Fabric in a Random Assembly of Spherical Granules," *Int. J. Num. and Anal. Meth. Geomech.*, Vol.6, pp.77-94

Oda, M., Konishi, J. and Nemat-Nasser, S. (1982) "Experimental Micromechanical Evaluation of Strength of Granular Materials: Effects of Particle Rolling", *Mechanics of Materials*, Vol.1, pp 269-283

Oda, M., Konishi, J. and Nemat-Nasser, S., (1983) "Experimental Micro_Mechanical Evaluation of Strength

of Granular Materials: Effects of Particle Rolling," in *Mechanics of Granular Materials: New Models and Constitutive Relations*, ed. Jenkins, J.T. and Satake, M., Elsevier Sci. Pub., Vol.1, pp.269-283

Papadakis, E. P. (1961) *J. Acoust. Am.*, Vol.22, pp.1616.

Petrakis, E. and Dobry, R. (1986) "A self consistent estimate of the elastic constants of a random array of equal spheres with application to granular soil under isotropic conditions," Report CE-86-04, Resselaer Polytechnic Institute, Troy, NY.

Petrakis, E. and Dobry, R. (1988) "A Two-Dimensional Numerical Micromechanical Model for a Granular Cohesionless Materials at Small Strains," *Proc. American Physical Society*, New Orleans, LA

Petrakis, E., Dobry, R., and Ng, T. (1988) " Small strain response of random arrays of elastic spheres using a nonlinear distinct element procedure", *Report CE-88-02, Resselaer Polytechnic Institute, Troy, NY.*

Prevost, J.H., (1984), "Nonlinear Transient Phenomena in Saturated Porous Media; The Generalized Biot Formulation and Its Numerical Solution," *International Journal for Numerical and Analytical Method in Geomechanics*, Vol. 8, pp. 71-96.

Read, H.E. and Valanis, K.C. (1979) "An Endochronic Constitutive Model for General Hysteretic Response of Soils," Final Report Research Project 810, Electric Power Research Institute, Palo Alto, California.

Renton, J.D., (1984) "The Beam-Like Behavior of Space Trusses", *AIAA Journal*, Vol. 22, No. 2, pp 273-280.

Rodriguez-Ortiz, J. M. (1974) "Estudio del comportamiento de medios granulares hetergeneos mediante modelos discontinuos analogicos matemeticos, Ph.D. thesis, University Politecnica de Madrid.

Rohani, B., (1970) "Theoretical Studies of Stress Wave Propagation in Laterally Confined Soils," WES Working Draft Report

Rohani, B. and Cargile, J.D., (1984) "A Probabilistic One-Dimensional Ground-Shock Code for Layered Nonlinear Hysteretic Materials," Miscellaneous WES Paper SL-84-6

Ross, C.A., Thomas, P.Y., Charlie, W.A. and Doehring, D.O., (1989), "Transmission of Pressure Waves in Partially Saturated Soils," *Experimental Mechanics*, Vol. 29, No. 1, pp. 83-84.

Rossmanith, H. P. and Shukla, A. (1982) "Photoelastic investigation of dynamic load transfer in granular media," *Acta Mechanics*, Vol.42, pp.211-225.

Sadd, M. H. and Hossain, M. (1986) "A study of explosive wave propagation in granular materials with microstructure," U.S. Army Waterways Experiment Station, Technical Report, SL-86-35.

Sadd, M.H. and Hossain, M.(1988) "Wave Propagation in Distributed Bodies with Applications to Dynamic Soil Behavior," *J. Wave-Material Interaction*, Vol.3, pp311-326

Sadd, M. H., Shukla, A., and Mei, H., (1989a) "Computational and Experimental Modeling of Wave Propagation in Granular Materials," *Proc. of the 4th International Conference on Computational Methods and Experimental Measurements*, pp.325-334, Capri, Italy

Sadd, M. H., Shukla, A., Mei, H., and Zhu, C.Y., (1989b) "The Effect of Voids and Inclusions on Wave Propagation in Granular Materials," in Micromechanics and Inhomogeneity - The Toshio Mura Anniversary Volume, ed. Weng, G.L. Taya, M., and Abe, H., Springer-Verlag, New York

252

Sadd, M. H., Shukla, A., Tai, Q. M., and Xu, Y (1991a) "Micromechanical Constitutive Behavior of Granular Media Under Dynamic loading Conditions," *Proc. of the 3rd international Conference on Constitutive Laws for Engineering Materials: Theory and Application*, University of Arizona

Sadd, M.H., Qiu, L, Boardman, W. and Shukla, A., (1992a) "Modeling Wave Propagation in Granular Media Using Elastic Networks", *Int. J. Rock Mech. and Mining Sci.* Vol.29, pp.161-170

Sadd, M.H., Tai, Q.M. and Shukla, A. (1992b) "Contact Law Effects on Wave Propagation in Particulate Media Using Distinct Element Modeling", submitted to *Intl. Journal of Nonlinear Mechanics.*

Sandhu, R.S., (1968), "Fluid Flow in Saturated Porous Elastic Media," Ph.D thesis, University of California, Berkely.

Satake, M. and Jenkins, J.T., (1982) <u>Mechanics of Granular Materials-New Models and Constitutive Relations</u>, Proc. U.S. / Japan Seminar on New Models and Constitutive Relations in the Mechanics of Granular Materials, Elsevier, Cornell University

Shukla, A. and Nigam, H. (1985) "A numerical analysis of contact stress problem," *J. of Strain Analysis*, Vol.20, No.4.

Shukla, A. and Rossmanith, H.P. (1986) "Dynamic Photoelastic Investigation of Wave Propagation and Energy Transfer Across Contacts", *J. of Strain Analysis*, Vol.21, No.4, pp.213-218

Shukla, A. and Damania, C. (1987) "Experimental investigation of wave velocity and dynamic contact stress in an assembly of discs," *J. Expt. Mech.*, Vol.27, No.3.

Shukla, A. and Zhu, C.Y. and Sadd, M.H. (1988a) "Angular Dependence of Dynamic Load Transfer due to Explosive Loading in Two Dimensional Granular Aggregates," *J. of Strain Analysis*, pp.121-127.

Shukla, A., and Zhu, C.Y., (1988b) "Influence of the Microstructure of Granular Media on Wave Propagation and Dynamic Load Transfer," *J. of Wave-Material Interaction*, Vol.3

Shukla, A. and Prakash, V., (1990), "Wave Propagation in Fluid-Saturated and Unsaturated Porous Media," *Experimental Mechanics*, Vol. 30, No. 1, pp. 80-87.

Shukla, A. and Sadd, M.H., (1990) "Wave Propagation and Dynamic Load Transfer Due to Explosive Loading in Heterogenous Granular Media with Microstructure", AFOSR First Annual Report

Shukla, A. and Sadd, M.H., (1991) "Wave Propagation and Dynamic Load Transfer Due to Explosive Loading in Heterogenous Granular Media with Microstructure", AFOSR Second Annual Report

Shukla, A., Sadd, M. H , and Mei, H. (1991) "Experimental and computational modeling of wave propagation in granular materials", *Experimental Mechanics*, vol.30, pp.377-381

Smith, J.O. and Liu, C.K., "Stresses due to Tangential and Normal Loads on An Elastic Solid with Applications to Some Contact Problems," *Journal of Applied Mechanics*, 1953, 20, pp. 157-166.

Soo, S. L. (1983) "Dynamic interactions of granular materials, Advances in the Mechanics and Flow of Granular Materials," Ed. Shahinpoor, M., Vol. II, Trans. Tech. Pub.

Stewart, G.W., (1973) <u>Introduction to Matrix Computations</u>, Academic Press.

Sun, C.T. and Yang, T.Y., (1975) "A Couple-Stress Theory for Gridwork-Reinforced Media", *Journal of Elasticity*, Vol. 5, No. 1, pp 45-58.

Swrrano, A. A. and Rodriguez-Ortiz, J. M. (1973) "A contribution to the mechanics of heterogeneous granular media, *Proc. Symp. Plasticity and Soil Mech.*, Cambridge.

Takahashi, T. and Sato, Y. (1949) "On the theory of elastic waves in granular substance," Bulletin Earthquake Research Institute, Japan, Vol.27.

Taki, S. and Kitago, S. (1974) "Effect of repeated loading on deformation behavior of dry sand," *Proc. Japan Society of Soil Mechanics and Foundation Engineering*, Vol.14, No.1, pp.95-103.

Thomas, H.R. and Hoersch, V.A., (1930) "Stresses due to the Pressure of One Elastic Solid on Another," *Bulletin of Engineering Experiment Station*, No. 212, University of Illinois, 1930.

Thornton, C. (1985) "Computer simulation deformations of contact under varying oblique forces, *J. of Appl. Mech.*, Trans ASME, Vol. 20, pp.327-344.

Thornton, C. and Barnes, D.J., (1986) "Computer Simulated Deformation of Compact Granular Assemblies", *Acta Mechanica*, Vol. 64, pp 45-61.

Thornton, C. and Randall, C. W. (1988) "Application of theoretical contact mechanics to solid particle system simulations",*Proc. U.S. / Japan Seminar on New Models and Constitutive Relations in the Mechanics of Granular Materials*, Elsevier, Cornell University. 113-142

Ting, J. M., Corkum, B. T., Kauffman, C. R. and Greco, C. (1989) "Discrete numerical model for soil mechanics," *J Geotechnical Engineering*, Vol.115, No.3, pp.379-399.

Ting, J. M. and Corkum, B. T. (1992) "A computational laboratory for discrete element geomechanics", *J. of Computing in Civil Engineering*, American Society for Civil Engineers, Vol.6, pp.129-146

Trent, B.C. (1989) "Numerical Simulation of Wave Propagation Through Cemented Granular Material," in *Wave Propagation in Granular Media, Proc. of the Winter Annual Meeting of ASME*, pp.9-15

Trollope, D.H. and Burman, B.C., (1980) "Physical and Numerical Experiments with Granular Wedges", *Geotechnique*, Vol. 30, pp 137-157.

Varadan, V. K., Varadan, V. V., and Ma, Y. (1983) "Propagation and scattering of elastic waves in discrete random media," *Proc. 20th Annual Meeting of Soc. of Eng. Science*, Univ. of Delaware.

Vermeer, P.A. and Luger, H.J. (1982) <u>Deformation and Failure of Granular Materials</u>, IUTAM Symposium on Deformation and Failure of Granular Materials, Delft, A. A. Balkema

Walton, K. (1987) "The effective elastic moduli of a random packing of spheres," *J. Mech. Phys. Solids*, Vol.35, pp.213-226

Walton, O. R. (1982) "Explicit particle dynamic model for granular materials," Numerical Methods in Geomechanics Edmonton, Z. Eisenstein, ed., A. A. Balkema, Rotterdam, pp.1261-1268.

Walton, O. R., Maddix, D. M., Butkovich, T. R., and Heuze, F. E. (1991) "Redirection of Dynamic compressive waves in materials with nearly orthogonal and random joint sets" *Proc. of ASME Applied Mechanics Conference, Recent Advances in Mechanics of Structured Continua*, Columbus, OH (1991)

Xu, Y. and Shukla, A. (1990), "Stress Wave Velocity in Granular Medium", *Mechanics Research Communication*, Vol. 17(6), pp. 383-391.

Zhu, C.Y., Shukla, A., and Sadd, M. H. (1989) "Use of Load Transfer Coefficients to Predict Dynamic

Loads in Granular Assemblies," in *Wave Propagation in Granular Media. Proc. of the Winter Annual Meeting of ASME*, pp.1-8.

Zhu, C. Y., Shukla, A., and Sadd, M. H. (1991) Prediction of dynamic contact loads in granular assemblies. *J. of Applied Mecha ics*, vol.58, pp.341-346